GEORGIA INSTITUTE OF TECHNOLOGY
Engineering Experiment Station

PROJECT INITIATION

REVISED Date: 2/8/72

Project Title: Eleventh Radome Symposium

Project No.: C-140 (Originally assigned Project No. C-139 in error)

Project Director: N. E. Poulos

Sponsor: Department of Continuing Education

Effective January 21, 1972 Estimated to run until: August 31, 1972

Type Agreement: Amount: $ 500.00

Reports: None

Contact Person: Mr. N. E. Poulos
High Temperature Materials Division
Hinman Building
Campus

Assigned to High Temperature Materials Division

COPIES TO:

- ☐ Project Director
- ☐ Director
- ☐ Associate Director
- ☐ Assistant Director(s)
- ☐ Division Chiefs
- ☐ Branch Head
- ☐ General Office Services
- ☐ Engineering Design Services
- ☐ Photographic Laboratory
- ☐ Research Security Officer
- ☐ Accounting
- ☐ Purchasing
- ☐ Report Section
- ☑ Library
- ☐ Rich Electronic Computer Center
- ☐ Dept. of Continuing Education

C-140

TK 7871.85 .P76 1972

PROCEEDINGS OF THE ELEVENTH SYMPOSIUM ON ELECTROMAGNETIC WINDOWS

AUGUST 2-4 1972

"STATE OF RADOME TECHNOLOGY-1972"

Edited By
N. E. Poulos and J. D. Walton, Jr.

The USAF Avionics Laboratory

GEORGIA TECH
RECEIVED
AUG 14 1972
LIBRARY

ENGINEERING EXPERIMENT STATION
GEORGIA INSTITUTE OF TECHNOLOGY
Atlanta, Georgia 30332

PROCEEDINGS OF THE ELEVENTH SYMPOSIUM

ON

ELECTROMAGNETIC WINDOWS

August 2-4, 1972

"STATE OF RADOME TECHNOLOGY-1972"

Edited By

N. E. Poulos and

J. D. Walton, Jr.

GEORGIA INSTITUTE OF TECHNOLOGY
ATLANTA, GEORGIA 30332

FOREWORD

The Eleventh Electromagnetic Window Symposium marks 16 years of regularly scheduled symposia on electromagnetic windows. This symposium was jointly sponsored by the Avionics Lab, U.S. Air Force, Wright-Patterson Air Force Base, Ohio and the host institution, Georgia Institute of Technology. The organization and the technical quality of the papers presented at the symposium and published in these proceedings were made possible only through the generous cooperation of the U.S. Air Force. In this connection I would like to acknowledge the contributions of Mr. Harold Weber and Mr. Richard Ireland, Avionics Lab, Wright-Patterson Air Force Base, Ohio in organizing and hosting the meeting for the Papers Review Committee. Also, my sincere thanks to each of the following individuals who served on the papers review committee and to their corresponding organizations which made their participation possible:

Mr. H. L. Bassett Georgia Institute of Technology	Mr. R. A. Ireland AFAL, U.S. Air Force	Mr. R. W. Sutton The Boeing Company
Mr. Charles F. Bersch Naval Air Systems Command	Mr. Howard S. Jones Harry Diamond Labs	Mr. Gene Tarrants AFAL/USAF, Retired
Mr. Melvin C. Gilreath NASA/Langley Research Center	Mr. Ken Letson U.S. Army Missile Command	Mr. Arthur J. Thompson The Brunswick Corp.
Lt.Col. W. M. Hart Aerospace Research Labs, WPAFB	Mr. D. L. Loyet Raytheon Company	

Public release for several of the papers was not obtained by the authors from the cognizant organizations in time for publication. However, three abstracts of these papers are presented as the last paper entries in these proceedings. Copies of these papers are to be available during the meeting or by making a request of copies to the respective authors.

I would like to thank the authors for their contributions to the technical program and for their cooperation in our attempt to have the entire proceedings available at the time of the symposium meeting. Finally, my sincere appreciation goes to Mr. J. D. Walton, Jr. for his advice and encouragement for coordinating and organizing the symposium and these proceedings.

N. E. Poulos
Chairman

TABLE OF CONTENTS

TABLE OF CONTENTS (Continued)

TABLE OF CONTENTS (Continued)

TABLE OF CONTENTS (Continued)

LIQUID IMPACT ON ELASTIC SOLID SURFACE

by
Y. C. Huang and F. G. Hammitt

Liquid droplet impingement is a serious and limiting problem at the present time in various technological fields such as large steam turbines, high speed aircraft and helicopters.

The impact between a compressible liquid and rigid solid has been studied analytically in a doctoral dissertation by the first author. The dissertation showed that the pressures and velocities during the important early portion of the impact depend upon liquid impact Mach number and droplet shape. Although liquid pressure build-up commences simultaneously with input, the expansion of the droplet near the contact edge due to the lateral flow is not appreciable during the early stages of the impact. The maximum pressure in this two-dimensional liquid impact problem is found to be less than the one-dimensional maximum pressure. As time elapses, the maximum pressure shifts from the center of the contact area radially outward, while the pressure at the center attenuates to the stagnation pressure.

Our numerical study of liquid-solid impact has been extended to include the effects of an elastic solid boundary. The preliminary results show that the deformation of the target surface due to a spherical liquid droplet impact appears as an annular ring of depression, just as observed in various experimental studies. The results of course depend upon the acoustic impedence ratio between the liquid and solid.

I. Introduction

Liquid droplet impingement is a serious and limiting problem at the present time in various technological fields such as large steam turbines, high speed aircraft and helicopters.

A useful and necessary approach to obtain quickly the engineering information necessary for the continued development of machinery elements such as these is the testing of candidate materials under droplet impingement attack in the laboratory. However, a long-range solution to the problem, allowing the eventual development of predicting ability, requires an analysis of both reaction of the material to a given imposed pressure-time distribution, and also the detailed fluid flow regime during the impact in order to obtain the pressure and velocity distributions on the surface as a function of time.

II. Brief Review of Problem

Liquid droplet impact on a solid surface has been observed for centuries. The first extensive photographic description of this splash phenomena was given by Worthington (1). In more recent years, Dr. Olive Engel (2) also conducted considerable pioneering work on liquid-solid impact research which includes a chemical mapping of radial flow and measurement of impact force as a function of time during collision.

More recently, advanced technology has been able to develop a turbine-driven camera to record photographically the collision process at much higher impact velocity to study the basic mechanism of rain erosion, such as the work of Fyall (3, e.g.).

The first comprehensive numerical investigation of the liquid droplet impact, to our knowledge, was that by Harlow and Shannon (4) at Los Alamos Scientific Laboratory. The Marker-and-Cell (5) technique was used to obtain numerical solutions of the full Navier-Stokes equation for a viscous incompressible fluid.

Another numerical method, also developed at Los Alamos Scientific Laboratory by Amsden (6) was used to study the hypervelocity impact of certain metallic spheres where the effects of compressibility due to melting is important. However, neither method is quite suitable for attacking the rain erosion and turbine droplet impact problem where the practical impact velocities lie between about 1000 and 2500 ft/sec. This velocity range results in intermediate material responses, i.e., the material cannot be considered as a fluid as in the hypervelocity case nor can its deformation (and liquid compressibility) be neglected as is appropriate for very low velocity impacts. A new numerical solution method called Compressible-Cell-and-Marker has therefore been developed by ourselves (7, e.g.).

The response of the target material to an impact ranges from an essentially rigid case with no deformation, to elastic, plastic, viscous or even compressible fluid material response, depending on the impact velocity. The problem treated in its most general aspects requires a detailed investigation of the behavior of different material models under impact. Some compromise must be made between the complexity of the physical problem and the practical difficulties involved in solving the equations governing the model selected.

The first model we examined was that of a rigid solid and a compressible liquid in order to establish a meaningful limiting result. It is to this problem that the doctoral dissertation of the first author (7) was addressed. The dissertation showed that the pressures and velocities during the vital initial portion of the impact depend upon liquid impact Mach number and droplet shape. Although liquid pressure build-up commences simultaneously with impact, the expansion of the droplet near the contact edge due to the lateral flow is not appreciable during the very early stages of the impact. We have discussed these general features of the impact elsewhere (7, 8, e.g.). Our calculation also indicates that a zone of negative pressure appears in the upper region of the droplets where cavitation has been observed, and this particular aspect is also treated elsewhere (7, 9). There is no sudden bursting out of the top surface, because the compression is continuously released, since the drop surface is free to deform. The occurance of negative pressures may result from either the reflection of the compression wave from the top surface or the rarefaction from the side of the droplet. The location of the negative pressure depends upon the initial geometry of the droplet

and the impact Mach number (7, 9). The maximum pressure in this two-dimensional liquid impact problem is found in our calculations to be less than the one-dimensional maximum pressure* for all three different droplet shapes in varying degrees. As time elapses, the maximum pressure shifts from the center of the contact area radially outward, while the pressure at the center attenuates eventually to the steady-state stagnation pressure.

III. Investigation of Liquid Impact on Elastic Solid Boundary

As already mentioned, full surface rigidity provides an asymptotic limiting condition for the liquid impact problem. However, for many real materials important surface deformation during liquid impact for air Mach numbers of the order 1 to 2.5 (water Mach numbers of about 0.25 to 0.6), which is the range of interest for the technological applications previously mentioned, occur.

Liquid impact on an elastic solid boundary is currently under investigation here, using a modified numerical technique to handle this added complexity. Preliminary results show that the deformation of the target surface is then a function of material density, shock wave velocity, and acoustic impedance. A fully rigid surface implies an infinite acoustic impedance. The result for the case of infinite acoustic impedance was checked with the previous result for the case of a fully rigid solid boundary, previously investigated in the doctoral dissertation of the first author, and full agreement was found.

Fig. 1 representing initial results with this new program, shows the deformation of a spherical water droplet impinging on an elastic solid surface such as rubber, whose acoustic impedance is of the same magnitude as that of water. The material surface depression is greatest at the center of the contact area at non-dimensional time $Ct/D = 0.5$, which is about equivalent to 0.5 μsec for a typical rain drop of 2mm diameter at liquid impact Mach Number of 0.2. C is shock-wave velocity in the liquid, t is time, and D is the droplet diameter. The isobar distributions are quite similar to those for a fully rigid solid surface (Fig. 2).

Fig. 3 shows the deformation and isobar distribution for a later stage of the same liquid-solid impact ($Ct/D = 1.25$, i.e. about 1.25 μs for a 2mm drop). The maximum depression has shifted from the contact center toward the contact edge which appears to be an annular ring of depression just as observed in various experimental damage results (3, e.g.).

IV. Conclusions

The current results are still under investigation. The preliminary studies are very encouraging in presenting the first theoretical analysis of deformation of an elastic boundary during liquid impact. A somewhat simplified model of a non-rigid surface is particularly applicable to a soft material coating on a hard backing such as rubber on steel (no

*i.e., less than the "water-hammer" pressure, assuming shock-wave velocity corrected for the increased pressure.

material bending stress was assumed, only material inertia). The acoustic impedance appears to be an important parameter for liquid impacts such as this on an elastic solid surface.

REFERENCES

1. Worthington, A.M., "A Study of Splashes," The MacMillan Company, N.Y. 1963.

2. Engel, O.G., "Waterdrop Collisions with Solid Surface," J. of Research of the National Bureau of Standards, Vol. 54, No. 5, May 1955, pp 281-298.

3. Fyall, A.A., "Single Impact Studies of Rain Erosion," Shell Aviation News, 374, 1969.

4. Harlow, F.H. and Shannon, J.P., "The Splash of a Liquid Drop," J. of Applied Physics, 38, 10, Sept. 1967, pp 3855-8866.

5. Welch, J.E., Harlow, F.H., Shannon, J.P. and Daly, B.J., "The MAC Method," Vol. LA-3425, Los Alamos Scientific Laboratory.

6. Amsden, A.A., "The Particle-in-Cell Method for the Calculation of the Dynamics of Compressible Fluids," Vol. LA-3466, Los Alamos Scientific Laboratory.

7. Huang, Y.C., "Numerical Studies of Unsteady, Two-Dimensional Liquid Impact Phenomena," PhD Thesis, Mech. Engr. Dept., University of Michigan (1971); also available as ORA UMICH Report 03371-8-T, June (1971).

8. Huang, Y.C., Hammitt, F.G., and Yang, W-J, "Computer Simulation of High Speed Collision with Rain Drop," (in review) ASME, 1972; available as ORA UMICH 03371-12-T, Sept. 1971.

9. Huang, Y.C., and Hammitt, F.G., "Cavitation within an Impinging Liquid Droplet," Cavitation Forum, 1972; available also as ORA UMICH 03371-15-I, 1972.

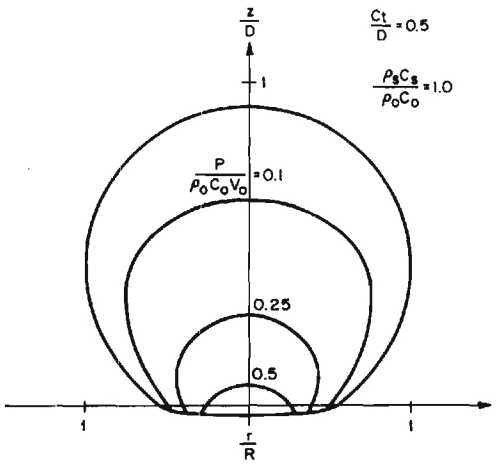

Figure 1. Isobar Distribution in an Initially Spherical Droplet at Time Ct/D = 0.5, for Impact Mach Number of 0.2 on Elastic Boundary, $\rho_s C_s/\rho_w C_w = 1$

3422

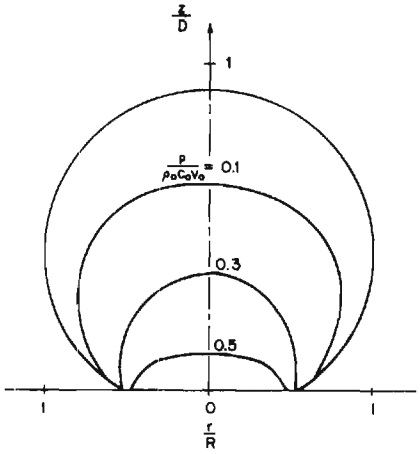

Fig. 2. Isobar Distribution in an Initially Spherical Droplet at Time (Ct/D) = 0.5, for Impact Mach Number of 0.2 and for Free-Slip Boundary Condition.

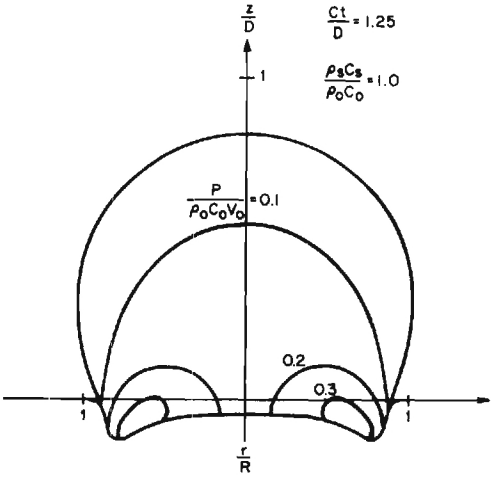

Figure 3. Isobar Distribution in an Initially Spherical Droplet at Time Ct/D = 1.25, for Impact Mach Number of 0.2 on Elastic Boundary, $\rho_s C_s/\rho_w C_w = 1$.

3423

HIGH-POWER BROADBAND CONSTANT-K LENS ANTENNAS FOR AIRBORNE APPLICATIONS

By

W. R. Free, F. L. Cain and E. A. Welsh
Georgia Institute of Technology

This paper describes the results obtained from a study to determine the feasibility of realizing high-power, broadband dielectric lens antennas where the dielectric lens serves as the radome for high velocity airborne applications.

The design objectives for the dielectric lens antennas were a power handling capability of 2 kW average power and a frequency range of 2 to 4 GHz. In addition, it was desirable to have circular polarization, optimum beam steering characteristics, and minimum size and weight. The results from a theoretical study of hemispherical and spherical dielectric lenses indicated that the performance of Constant-K lenses whose dielectric constants range between 3 and 4 compare favorably with the performance of Luneberg lenses. Based on these results and considerations of the increased fabribation difficulties associated with the Luneberg lens, it was concluded that the Constant-K lens was the better choice for a practical high-power, broadband dielectric lens antenna system.

The specifications for spherical and hemispherical Constant-K lenses are shown in Table I. The lens diameter and dielectric constant of each lens are 12 inches and 3.5, respectively. Rebonded fused silica was selected as the lens material. It was chosen primarily on the basis of its low loss tangent, low variation in dielectric constant with temperature, and its availability in a variety of forms such as casting slips, foams, and castable aggregate. For fabrication of the Constant-K lenses, a material with a dielectric constant of 3.5 ± 0.2 was specified. Slip-cast fused silica can normally be processed to fall within the lower bound of this range, but to reach values of 3.5, small additions of rutile ($K = 90$) were required.

After several hemispherical lenses had been fabricated, attempts were begun towards fabricating spheres. Several pouring and tamping schemes were attempted unsuccessfully before a simple technique was developed. Two hemispheres were poured to within 1/2 to 3/8-inch of the top of the mold. After the castable had taken an initial set, the hemispherical molds were clamped together and the remaining 3/4 to 1-inch wide cavity was filled with freshly mixed castable. The resulting sphere had an excellent surface except for a narrow equatorial zone which contained some bubbles. This rough portion of the surface was considered acceptable since it was in the zone to be covered by the mounting ring.

Cavity-backed spiral antennas were mounted on the surfaces of the lenses and utilized as feed antennas. The cavity-backed spiral antennas operated over the 2 to 11 GHz frequency range.

Results from experimental measurements indicate that both the spherical and hemispherical lenses operate satisfactorily over the 2 to 11 GHz frequency range. For the spherical lens, the gain varied from approximately 10 dB at 2 GHz to 26 dB at 11 GHz. The 3-dB beamwidths varied from approximately 20° at 2 GHz to 4.5° at 11 GHz, and the nominal sidelobe levels were approximately -17 dB.

The gain of the hemispherical lens antenna was somewhat lower than the spherical lens due to the reduced aperture. The gain for the hemispherical lens with the feed antenna 45° off boresight varied from 7 dB at 2 GHz to 17 dB at 11 GHz. The 3-dB beamwidths varied from 27° at 2 GHz to 8° at 11 GHz, and the nominal sidelobe levels were approximately -12 dB.

A major attribute of Constant-K lenses is their high power-handling capability, which is particularly important in many ECM applications. Tests involving incident powers up to 2000 watts CW on both the full-spherical lens and hemispherical lens were conducted. The results of the tests verify that these Constant-K lenses can handle high average power without breaking down or altering the characteristics of this type of lens. The high-power measurements indicate that the lens feed system rather than the lens itself appears to be the feature which limits the power-handling capability of a Constant-K lens antenna system.

In performing the high-power tests, both full-spherical and hemispherical lenses were fed by an open-ended waveguide in order to apply the maximum available power to the lens. A special waveguide feed was designed to conform with the lens surface and, in addition, to match the lens to the feed for maximum power transfer by utilizing a dielectric taper insert.

As previously discussed, fabrication of the full-spherical lens necessitated combining two hemispherical lenses; hence a seam resulted. High-power tests were conducted with the input power incident both parallel and perpendicular to the seam, and the results were essentially unaffected by the seam. Fabrication of the hemispherical lens included a ground plane; results indicate that the maximum temperature rise of the hemispherical lens depends on the thermal conductivity of the ground plane. In no case in which the power was applied as long as 75 minutes did the temperature of a Constant-K lens exceed 290°C. In all cases, the maximum temperature of the lens occurred at the feed point on the surface of the lens.

ACKNOWLEDGEMENTS

The work reported in this paper was performed under Air Force Contract F33615-71-C-1497. The authors gratefully acknowledge assistance provided by Mr. E. M. Turner (AFAL/TEM), and Dr. C. E. Ryan, Mr. C. P. Burns, and Mr. J. N. Harris of Georgia Tech.

TABLE I

Spherical and Hemispherical Dielectric Lens Specifications

Specifications
Dielectric Lens Radius = (6.0 ± 0.02) inch
Dielectric Constant = 3.5 ± 0.2
Max. Deviation from Spherical Surface = 0.020 inch
Temperature Requirements:
Withstand temperature of 1500°F to permit firing of printed feeds Withstand lens operating temperature of 500°F
Mounting Structure for Spherical Lens:
Choke ring configuration
Mounting Structure for Hemispherical Lens:
Conducting ground plane bonded to plane containing equator of hemispherical lens and extending beyond lens by 2 inches Ground plane must be strong enough to support weight of lens
All materials must be thermally compatible

PROPERTIES OF HOT PRESSED SILICON NITRIDE

M. L. Torti
D. W. Richerson
Norton Company
Worcester, Massachusetts

INTRODUCTION

Hot pressed silicon nitride has several properties which make it of interest for high temperature radome applications. It is a hard, wear resistant material with high strengths from room temperature to well over 1200°C. It has excellent oxidation resistance to 1400°C, and the combination of low thermal expansion and high strength give it excellent thermal shock resistance. It is an electrical insulator and preliminary electrical property determinations are at least encouraging. This paper reviews the physical and mechanical properties of hot pressed silicon nitride, presents recent electrical and rain erosion test results and comments on size and shape capability.

PHYSICAL AND MECHANICAL PROPERTIES

Representative physical properties are listed in Table I.

TABLE I

HOT PRESSED Si_3N_4

Density g/cc	Elastic Modulus psi@25°C	Coefficient of Thermal Expansion per °C	Thermal Conductivity BTU/hr°F ft @ 25°C	Specific Heat @ 25°C	Hardness Knoop 100
3.2	46×10^6	3.2×10^{-6}	10	0.17	2000

The extremely low coefficient of thermal expansion in combination with good thermal conductivity and high strength, gives the material excellent thermal shock resistance. The density is relatively low, about two-fifths that of steel, and the modulus of elasticity, while higher than that of steel is low for a fully dense high strength ceramic.

Hot pressed silicon nitride billets normally 6" x 6" x 1" are being fabricated by Norton. The silicon nitride starting material has been synthesized in house to yield the standardized product designated as HS-130 containing total metallic impurities of approximately 1.4 percent. This contrasts to an earlier grade, HS-110, containing approximately two percent total metallic impurities. A typical strength distribution, for HS-130 at room temperature is shown in Figure 1. The determinations were carried out in 3 point bending on

1/8" x 1/8" cross section specimens on which the surface had been ground parallel to the long direction of the specimen with a 320 grit diamond wheel. Care was taken to minimize edge chipping but no final polishing or rounding of the edges was carried out. Samples were cut across the 6" x 6" billet to yield a large number of strength determinations. All values are included in the distribution. The low standard deviation obtained is typical of the results which can be obtained with hot pressed silicon nitride fabricated under closely controlled conditions. Figure 2 shows the strengths of this material as a function of temperature in air for the same specimen size and testing procedures as used for the room temperature tests. High temperature strength of HS-130 is strikingly superior to that of the lower purity HS-110.

Not only are the short time high temperature strengths important but the time dependency of this strength is of equal importance. Figure 3 gives the results for stress rupture carried out in air at 1200°C in four point flexural mode on 1/8" x 1/8" cross section samples. The sample subjected to 30,000 psi flexural stress was removed after 250 hours without fracture. The sample which failed at 92 hours under 40,000 psi flexural stress showed approximately one percent flexural creep.

Hot pressed Si_3N_4 has a very fine grain structure as is shown in Figure 4 for a sample prepared by the electron microscope replica technique from a fracture surface. The submicron grain size is typical for this material.

ELECTRICAL PROPERTIES

Electrical properties at room temperature, measured at the Georgia Institute of Technology[1], are given in Table II.

TABLE II

ROOM TEMPERATURE ELECTRICAL PROPERTIES
OF HOT PRESSED Si_3N_4

	HS-130	High Purity
Dielectric Constant	7.2	7.9
Loss Tangent	0.005	0.002
Density gm/cc	3.2	3.01

The dielectric constant, although considerably higher than is normally desired, is still within the useful range and is somewhat lower than had been anticipated based on previous extrapolations. The loss tangent is acceptably low. The high purity hot pressed material is a lower strength, lower density product compared to the HS-130 and does show a slightly lower dielectric constant.

RAIN EROSION TESTS

The high hardness and low porosity of the hot pressed material would indicate good rain erosion resistance. Tests were carried out at Holloman Air Force Base on a rocket sled test facility, under the auspices of the Air Force Materials Lab, at both 45 and 60 degree impingement angles[2]. Samples subjected to 6,000 feet of rain at Mach 3 showed no measurable damage. Testing at higher Mach numbers may be carried out in the future.

SHAPE CAPABILITY

The hot pressing of silicon nitride, which is carried out by the simultaneous applications of high temperatures and high pressures, does impose some limitations upon the shape capabilities. However, flat plates as large as 15" x 4" x 1/2" thick have been fabricated from this material. Large curved shapes, such as torso body armor, are routinely hot pressed from boron carbide and this technology is available to be applied to the hot pressing of silicon nitride. Intricate shapes have been hot pressed from silicon nitride as shown by the small turbine vane in Figure 5. Conversely, shapes can be machined from as-pressed billets such as the large gas turbine vane approximately 6" x 3" as shown in Figure 6.

(1) Private communication, J. D. Walton, Georgia Institute of Technology.

(2) Private communication, G. F. Schmitt, Air Force Materials Lab. WPAFB.

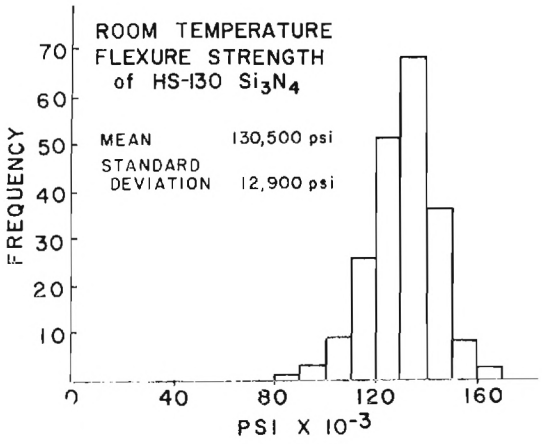

FIGURE 1

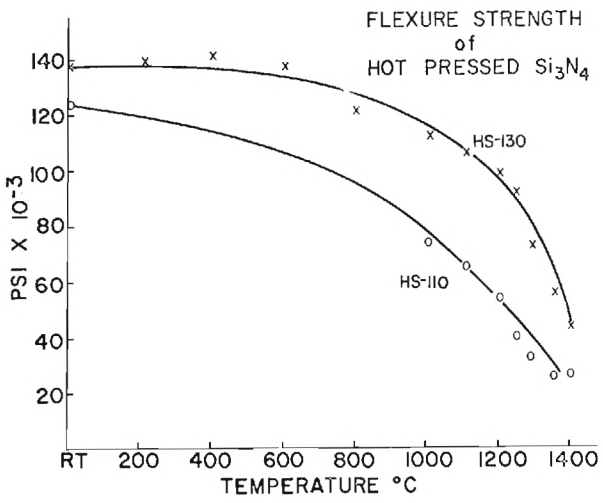

FIGURE 2

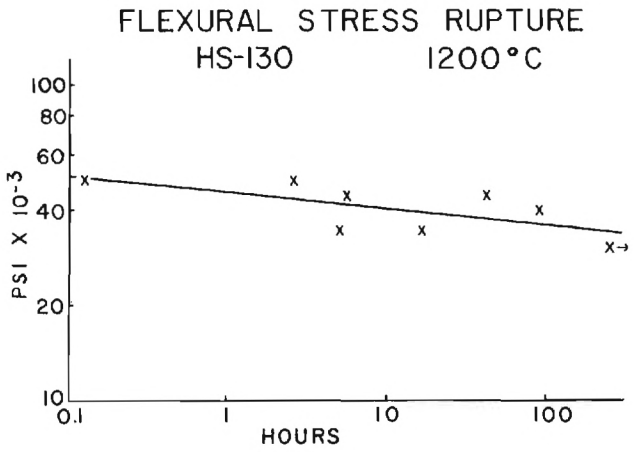

FIGURE 3

FIGURE 4

MICROSTRUCTURE OF HOT PRESSED Si_3N_4

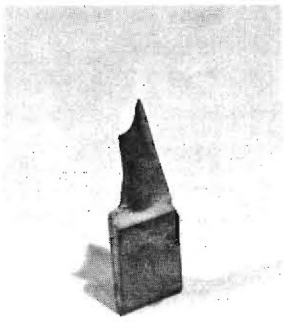

FIGURE 5

HOT PRESSED Si_3N_4 SMALL TURBINE BLADE

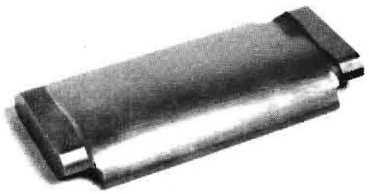

FIGURE 6

HOT PRESSED Si_3N_4 LARGE TURBINE VANE

BROADBAND DESIGNS FOR "A" SANDWICH RADOMES

by

J. E. Hill and W. Bivins
Radiation Systems, Inc., McLean, Virginia

The "A" sandwich radome consists of two thin layers of fiberglass skin separated by a thicker layer of low dielectric constant core material. When an "A" sandwich radome is designed for a wideband application, the maximum loss is solely dependent upon the thickness and dielectric constants of the outer skins. Once the maximum allowable transmission loss and material are specified, the thickness of the skin is completely determined. The thickness of the low dielectric constant core may be determined almost entirely by the required mechanical strength. These simplifications are made possible by the rather good approximation that the loss in the low dielectric constant core material is negligible compared to that in the outer fiberglass skins.

Simple electromagnetic theory can be used to predict the performance of "A" sandwich radomes with an arbitrary number of sandwich layers. These calculations have been performed for a simple "A" sandwich radome over a 1 to 12 GHz bandwidth. The computed curves indicate a maximum transmission loss of less than 1 db over the frequency band for angles of incidence less than or equal to 30°. At a 60° angle of incidence, the maximum transmission loss increases to 1.6 db. Sample radome panels were fabricated in this configuration. Precision transmission loss measurements through the radome sample indicated a maximum deviation from theory of 0.2 db.

GENERAL THEORY ON SANDWICH RADOMES

The transmission loss of a radome is the sum of reflection loss and insertion loss. The insertion loss is the amount of energy absorbed by the radome, and is related to the loss tangent of the radome material. The reflection loss depends upon the dielectric constant of the radome material and the design technique. Due to the currently available low loss material, the insertion loss of the radome becomes insignificant compared to the reflection loss. In this paper, the radome material is assumed lossless, and the object of the radome design is to reduce the reflection loss.

The electromagnetic wave propagation through a homogeneous flat sheet is well understood. The reflection coefficient of a wave passing through a thin dielectric slab is given as:

$$R = \frac{1}{c} (A f t) \qquad (1)$$

where $$A = \frac{\pi (1 - \epsilon_r)}{\epsilon_r \cos \theta} (\epsilon_r \cos^2 \theta - \sin^2 \theta), \text{ for parallel polarization}$$

"ϵ_r" is the relative dielectric constant, "f" is frequency, "c" is the velocity of light of the slab, "θ" is the angle of incidence, and "t" is the thickness of the slab. Equation (1) shows that the magnitude of reflected wave due to a thin slab reflection increases linearly with frequency.

An "A" sandwich radome consists of two thin layers of fiberglass skin and a thicker low dielectric constant core. Assume the core region is an equivalent air region, then its reflection loss may be approximately represented by the vector sum of two individual reflected waves due to the r reflections of skin as follows:

$$\text{Reflection loss of "A" sandwich} = |R| \left[1 + \cos \left(\frac{2\pi d}{\lambda_o \cos\theta} \right) \right] \qquad (2)$$

The relative phase of two reflected waves depends upon the separation between the skin "d" (i.e., the thickness of the core). If the broad frequency band operation is desired and the high operating frequency which makes the core thickness to be electrically large, then these two reflected waves adding in phase at high end of the frequency band cannot be avoided. The reflection loss of "A" sandwich radome over band is $|R|$, where $|R|$ should be evaluated at the high end of the frequency band. By Eq. (1), the maximum loss of "A" sandwich radome is obtained as:

$$\text{Max. Loss of "A" Sandwich} = 2 A f u t / c \qquad (3)$$

"TRIPLE A" SANDWICH DESIGN TECHNIQUE

The "triple A" sandwich radome is constructed with two ordinary "A" sandwich radomes as two equivalent skins and a thick main core at the center as Figure 1 shows. Each equivalent skin produces a reflected wave with magnitude as follows:

$$|R_E| = A t f (1 + \cos k_1 f) \qquad (4)$$

where
$$k_1 = \frac{2\pi d_1}{C \cos\theta} \qquad (4a)$$

"A", "θ", "f", and "C" are defined in Eq. (4). Dimensions "t" and "d", are given in Figure 1.

The optimum design of a "triple A" sandwich radome is to make $|R_E|$ to be minimum over the frequency band of interest. Equation (3) shows an oscillating curve (see Figure 2). All peaks of $|R_E|$ may be obtained under the condition of $\frac{d}{df} |R_E| = 0$. It is required to solve the equation,

$$k_1 f = \frac{1 + \cos k_1 f}{\sin k_1 f} \qquad (5)$$

With the help of graphical method shown in Figure 2, the first solution of Eq. (5) is obtained. It is $k_1 f = 1.32$.

At $k_1 f = 1.32$, the value of $|R_E|$ is optimum, and it can be expressed as

$$|R_E|_{op} = 1.65 \frac{At}{k_1} \tag{6}$$

The next step is to determine the highest possible frequency that $|R_E|$ is still within the limit of $|R_E|$ op. By the graphical method as indicated in Figure 5, the solution found is:

$$k_1 fu = 4.07. \tag{7}$$

Substitute the upper limit of frequency band into Eq. (7) and the value of k_1 is obtained. Therefore, d_1 is determined by Eq. (4a). The substitution of Eq. (7) into Eq. (6) yields

$$|R_E|_{op} = 0.405\ Atfu \tag{8}$$

The maximum loss of a "triple A" sandwich radome can be expressed by

$$\text{Max. Loss of "triple A" sandwich} = 0.81\ Atfu \tag{9}$$

The typical loss characteristics of "triple A" sandwich radome are shown in Figure 6.

Compare Eqs. (3) and (9). It is found that the loss of "triple A" sandwich radome is only 40.5% of "A" sandwich radome loss. Furthermore, since the "triple A" sandwich radome has four layers of fiberglass skin, but the "A" sandwich radome has only two, the thickness of fiberglass skin in both radomes is the same. Therefore, the "triple A" sandwich radome is mechanically much stronger than "A" sandwich radome. If a comparison is made of same mechanical strength, then the thickness of the fiberglass skin in "triple A" sandwich may be reduced and a further loss reduction will result.

The broadband (1-12 GHz) sample radomes, the "triple A" sandwich and the "A" sandwich have been designed to have the same mechanical strength. Their predicted transmission loss characteristics are compared in Figure 5. The design of "triple A" sandwich radome is optimized at wavewidth 0° of incidence, but it still has good performance at an incident angle of 30° and 60°. The transmission loss is computed by an RSi 1130 computer and based on general transmission loss equations of electromagnetic waves passing through a multilayer radome. These two sample radomes have been tested at 9 GHz with various angles of incidence. Figure 6 shows the measured data on both samples and the excellent correlation between theory and empirical results.

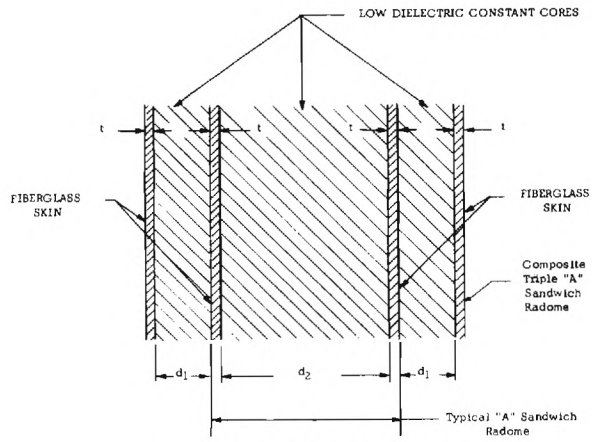

Figure 1. Construction of "A" Sandwich Radome

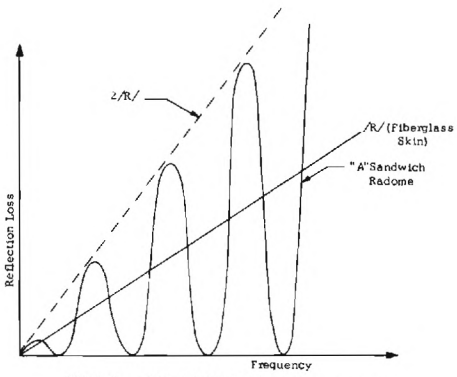

Figure 2. Typical Reflection Loss Characteristics of a Fiberglass Skin and an "A" Sandwich Radome

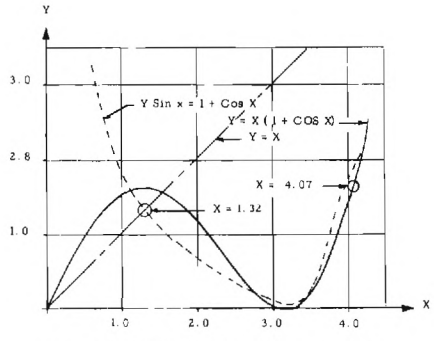

Figure 3. Graphical Solution for Y Sin x = 1 + Cos X. And Y = X (1 + Cos X)

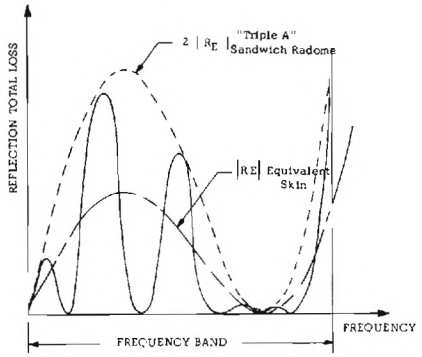

Figure 4. Typical Reflection Characteristics of an Equivalent Skin and a "Triple A" Sandwich Radome

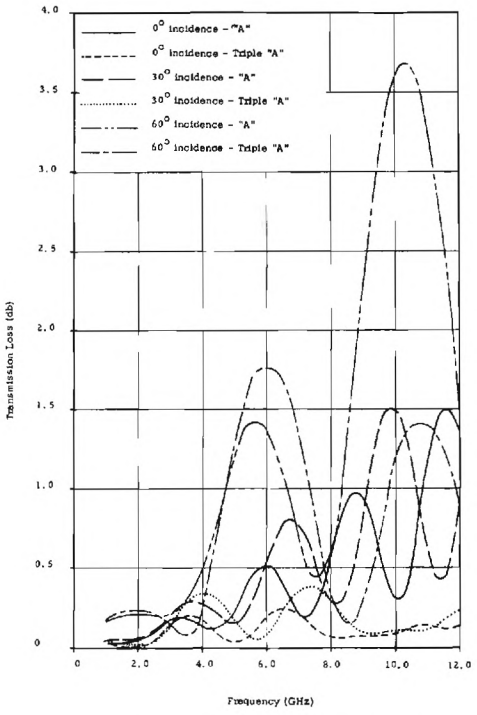

Figure 5. Computed Loss Characteristics of "A" and Triple "A" Radomes at 0°, 30° and 60° of Incidence with Perpendicular Polarization

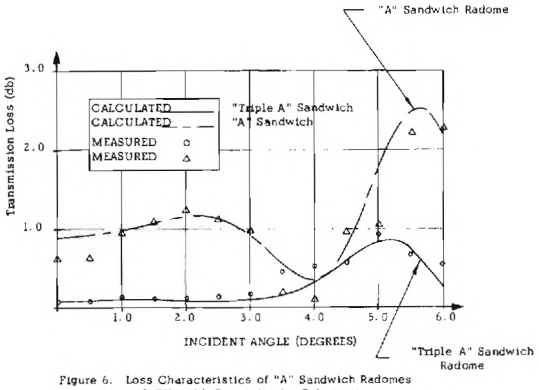

Figure 6. Loss Characteristics of "A" Sandwich Radomes at 9 GHz with Perpendicular Polarization.

HARD METALLIC LENS AND RADOME AT OUT-OF-BAND FREQUENCIES

by

R. B. Dybdal, H. E. King and J. L. Wong

Electronics Research Laboratory
The Aerospace Corporation
El Segundo, California

ABSTRACT

The electrical characteristics of a hardenable metallic lens or radome with a near-unity index of refraction are described. Operating a lens antenna with a near-unity index of refraction either restricts the maximum lens diameter or greatly increases the focal length. When a metallic grating is used as a radome placed in the near field of the antenna, the long focal length requirement of a metallic lens is alleviated and the hardness attributes are retained. The performance of a metallic radome was measured at 10 GHz by using a parallel-plate grating with spacings varied from about 1 to 4 inches. The measured gain, pattern, and sidelobe characteristics are presented. In addition, techniques for suppressing grating lobes are discussed.

I. INTRODUCTION

A metallic lens, constructed from a circular matrix of square waveguides, has been proposed as a hardened ground terminal antenna for a satellite-to-ground communication link (Ref. 1). The electrical performance of a model lens antenna has been evaluated with satisfactory results (Refs. 2,3). Several desirable mechanical properties are inherent in a metallic lens antenna for this application: the lens forms a bridge-like structure with inherent strength to withstand high overpressures, the waveguides filter the EMP and shock waves and reduce the thermal effects. In addition, debris is free to fall through the waveguides (3 to 4 in. openings) and be collected in a debris pit. More recently, considerable interest exists in the establishment of satellite-to-ground links operating in the X- or K-band frequency regime. However, at these frequencies, the waveguide opening size required for debris passage becomes relatively large compared with a wavelength. This imposes a stringent problem in the electrical design (Ref. 4). In this paper the electrical characteristics of a metallic waveguide grating, operated either as a lens or radome, at frequencies other than its normal design frequency range are described.

II. LENS CHARACTERISTICS AT EXTENDED FREQUENCIES

The basic design equation for a plano-concave metallic-lens antenna is given by (Ref. 5) $R = \frac{f(1 - n)}{1 - n \cos \theta}$ where R and θ are the geometrical parameters of the lens, f is the focal length, and n is the index of refraction of the artificial dielectric medium. The index of refraction for a lens composed of rectangular waveguide elements is given by $n = \sqrt{1 - (\lambda/2a)^2}$ where λ is the operating wavelength and a is the

waveguide opening. This expression assumes the waveguide element is operated in its dominant mode. Dominant mode operation of a rectangular waveguide restricts the opening to sizes between one-half and one wavelength, which yields an index of refraction variation between 0 and 0.866.

For the present study, the frequencies of interest are 16 and 35 GHz. This restriction results in waveguide openings that are smaller than the range of opening sizes judged desirable for debris passage. For this reason it is necessary that the waveguide openings be larger than one wavelength. These opening sizes imply operating the waveguides in an overmoded region; i.e., higher-order modes, in addition to the dominant mode, may propagate in an individual waveguide element. Operating the waveguide elements in an overmoded region means that adjacent waveguide elements are separated by more than one wavelength. A consequence of such spacing is the occurrence of grating lobes in the radiation pattern resulting from the periodic nature of the lens structure.

The focal length for a given lens contour may be computed as a function of the index of refraction. The basis of this computation is the thin-lens approximation, which has been previously examined in connection with a 3-ft diameter metallic lens antenna study (Ref. 2). The thin-lens approximation predicts that the focal length varies as $f' = \frac{1 - n}{1 - n'} f$ where f is the focal length corresponding to an index of refraction n. Thus, the required focal length rapidly increases as n' approaches unity. As a numerical example, consider the 3-ft metallic lens, which was designed for operation at 10 GHz with a focal length of 31.2-in and an index of refraction of 0.5. If this antenna were operated at a higher frequency corresponding to an index of refraction of 0.95, the required focal length is 312 in. Such a long focal length imposes both mechanical and electrical design problems. With a long focal length, a larger feed aperture is required, and for a specified beam scan angle the feed has to move a greater transverse distance than that required for a shorter focal length configuration.

III. RADOME CONCEPT

In order to alleviate the long focal length requirement associated with a lens antenna, the concept of employing a metallic waveguide grating as a radome was considered. The geometry is illustrated in Fig. 1. In this radome concept, the desirable hardening properties are retained. In operation, the radome is placed in the near field of the antenna; i.e., the distance between the antenna and the radome is much less than D^2/λ where D is the antenna diameter and λ is the operating wavelength. With this arrangement, the resulting radiation characteristics are determined by both the antenna and the radome. The antenna could be a reflector, an array, or any other suitable radiating structure requiring less hardness. Beam scanning is achieved by applying a proper phase gradient across the radiating aperture of the antenna.

The preferred mechanical configuration for withstanding high overpressures is a bridge-like structure. Such a structure introduces phase errors across the radiating aperture of the radome. Since the radome structure is symmetrical, these phase errors may be compensated for by

adjustment of the applied phase gradient across the antenna aperture. For example, if a reflector antenna is employed, the phase errors may be corrected by refocusing the feed or by shaping the reflector. Other means include the use of an inhomogeneous refractive index for the artificial radome structure; i.e., by allowing the grating spacing to vary with radial position.

The performance of a metallic radome depends on the grating spacing and the characteristics of the illuminating antenna. In order to avoid grating lobes, the individual metallic waveguide elements should be spaced according to $d < \frac{\lambda}{1 + |\sin \theta_m|}$ where λ is the operating wavelength and θ_m is the maximum beam scan angle measured from the antenna axis. However, for the present application, the desired element spacing exceeds the limit specified by this equation. The occurrence of grating lobes in the radiation pattern becomes a major limiting factor on the performance of the metallic radome.

One technique for suppressing grating lobes is to use nonuniform waveguide spacings as illustrated in Fig. 2. This results in a nonperiodic structure, thus destroying the grating lobe phenomenon. The use of nonuniform waveguide spacings also provides the following mechanical and electrical advantages:

1. A nonuniform waveguide spacing means that the refractive index varies with the radial position. This results in a metallic radome with a natural bridge-like structure required for withstanding high overpressures.
2. Phase compensation (through antenna refocusing) is no longer necessary as it would be required for the case with uniform waveguide spacing.

IV. EXPERIMENTAL MEASUREMENTS

The electrical performance of a metallic radome was measured by using a parallel-plate grating as shown in the photograph of Fig. 3. The grating frame was 24" x 24" and the illuminating antenna was an 18" diameter reflector with an f/D of 1/3. The separation between the radome and reflector was 18". Aluminum plates, 6" wide x 1/16" thick, were inserted in the grooves of the frame to form the grating. For convenience all measurements were made at a scaled frequency of 10 GHz with grating spacings varied from about 1 to 4 inches for both TEM (polarization normal to the plates) and TE_{10} (polarization parallel to the plates) modes. In operation, a square-grid grating would be used. The characteristics of a square-grid configuration may be inferred from the parallel-plate data; namely, the E-plane characteristics may be obtained from the TEM-mode data and the H-plane characteristics from the TE_{10}-mode data.

Radiation patterns were recorded for both on-axis and off-axis feed positions. The radiation patterns for on-axis operation in the TEM-mode are essentially independent of the slot spacing as expected; however, grating lobes exist for an off-axis feed, depending upon the scan angle and the slot spacing with respect to the operating wavelength. Grating lobes were always present when the radome was operated in a TE_{10} mode for

the on-axis beam and the slot spacing was greater than one wavelength. Figure 4 summarizes the measured sidelobe and grating lobe levels for the on-axis beam as a function of slot spacing. For the TE_{10} mode there is a fair correlation between the measured grating lobe levels and the theoretical level of approximately -8.6 dB. The grating lobe level increases as the beam is scanned off axis. For a 16° scan, the grating lobe level is approximately 0 dB. Good correlation was observed between the computed and measured grating lobe locations as shown in Fig. 5. The presence of grating lobes means that a significant amount of energy is radiated in directions other than the main lobe, lowering the antenna gain. Figure 6 summarizes the measured gain characteristics for both the on-axis beam and for a 16° beam scan angle (3-3/8 in. off-axis feed). Both TEM and TE_{10} modes exhibit significant gain degradation, relative to the open-frame gain values, when the beam is scanned 16° off the antenna axis. It should be noted that the deterioration in radiation performance is due in part to the aberration effects of the illuminating parabolic reflector.

V. CONCLUSIONS

The electrical performance of a metallic lens or radome, constructed from uniformly spaced waveguides, at frequencies higher than its design band is limited by the presence of grating lobes. However, useful operation can still be provided if some gain degradation can be tolerated. Nonuniform waveguide spacings may be used for suppressing grating lobes. Nonuniform waveguide openings introduce a radial variation of the refractive index, which results in a natural bridge-like design desired for a hardened antenna configuration.

REFERENCES

1. E. M. Polzin, F. E. Cook, H. E. King, "Hardened Metallic Lens Antenna," 1969 IEEE PGAP Intl. Symposium Digest, Austin, Texas, 9-11 Dec. 1969.
2. H. E. King, J. L. Wong, R. B. Dybdal, M. E. Schwartz, "Electrical Characteristics of a Circularly Polarized Metallic Lens Antenna," The Aerospace Corporation, Electronics Research Laboratory, TR-0066(5320) -4, 30 Jan. 1970.
3. H. E. King, J. L. Wong, R. B. Dybdal, M. E. Schwartz, "Experimental Evaluation of a Circularly Polarized Metallic Lens Antenna," IEEE Trans. Antennas & Propagation AP-18, 412-414, May 1970.
4. J. L. Wong, H. E. King, R. B. Dybdal, "Metallic Lens and Radome for X-Band and K-Band Survivable Ground Terminal Antennas," The Aerospace Corporation, Electronics Research Laboratory, TR-0172(2320-01)-1, 15 Aug. 1971.
5. W. E. Kock, "Metal Lens Antennas," Proc. IRE 34, 828-836, Nov. 1946.

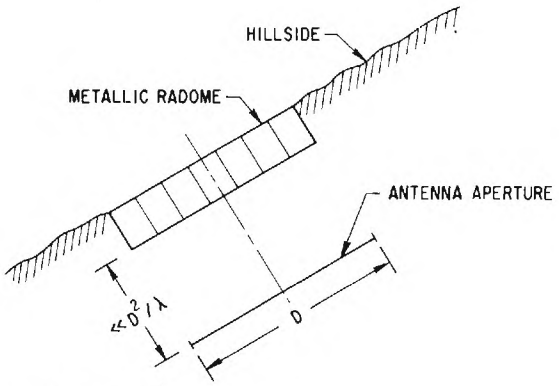

Fig. 1. Metallic radome concept

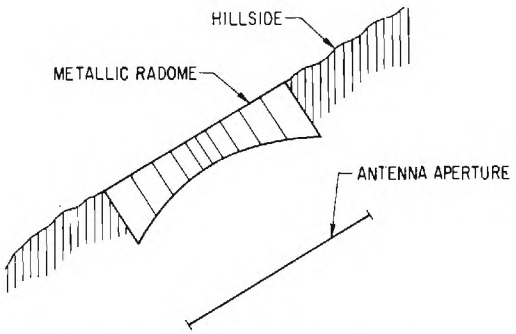

Fig. 2. Bridge-like radome structure employing nonuniformly spaced waveguides

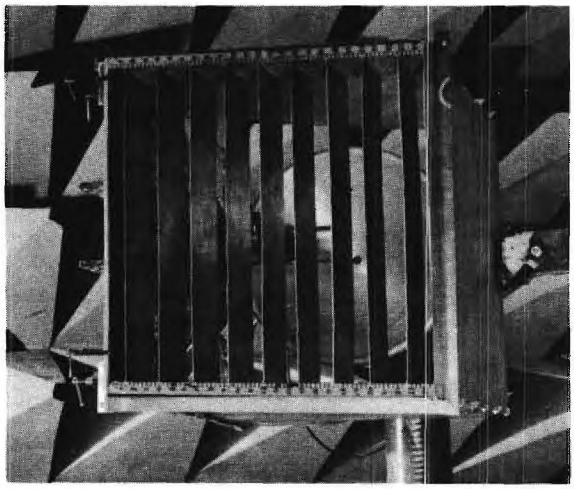

Fig. 3. Photograph of experimental metallic parallel-plate grating with 18-in. diameter antenna

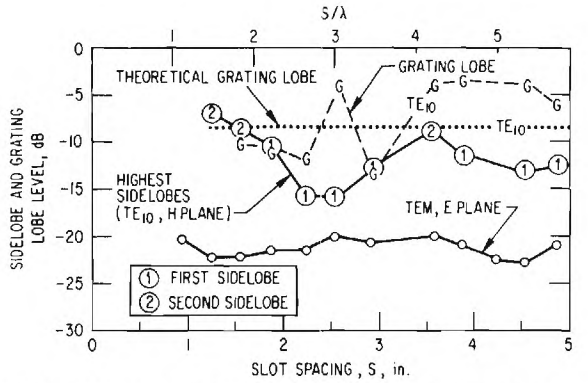

Fig. 4. Measured on-axis sidelobe and grating lobe levels at 10 GHz

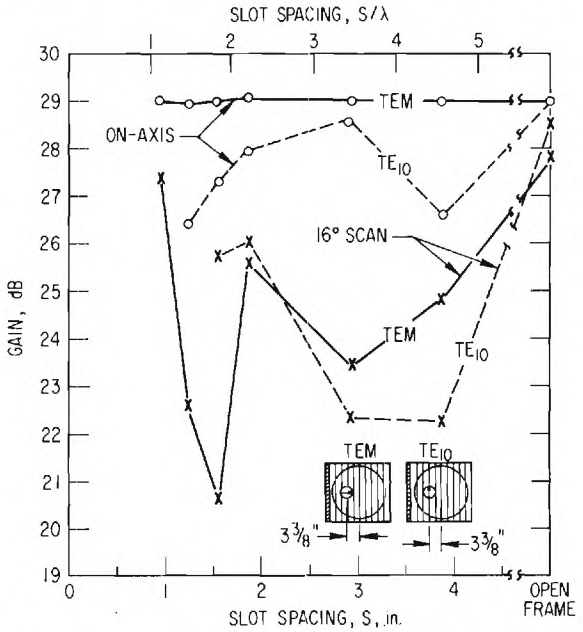

Fig. 5. Gain characteristics as a function of grating spacing for both on-axis and 16° beam scan angle at 10 GHz

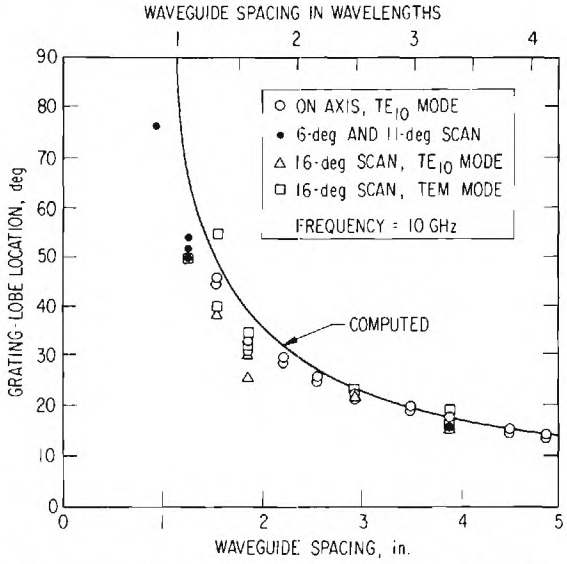

Fig. 6. Computed and measured grating lobe locations at 10 GHz

AN IMPROVED DIELECTRICALLY LOADED, FOAM SANDWICH CONSTRUCTION FOR NOSE RADOMES

A. J. Thompson, Brunswick Corporation, Marion, Virginia

J. R. Rogers, McDonnell Aircraft Company, St. Louis, Missouri

THE DESIGN PROBLEM

The electrical design problem and subsequent analytical/empirical development presented in this paper involved an ogive nose radome (body of revolution in the forward sector) having a $\approx$91 inch length and a $\approx$47 inch base diameter. As shown in Figure 1, this 2:1 fineness ratio radome housed a 36 inch flat plate, vertically polarized array operating in X-band which also served as the mount surface for a 12 element vertically polarized dipole array operating at the standard interrogator frequencies. Scan/offset limits of $\pm$ 65° in azimuth and elevation coupled with $\pm$ 115° roll stabilization yielded a wide range of incidence and polarizing angles. An ILS antenna, serving both the glideslope and localizer functions, was located in the bottom aft region of the radome. In the ILS and IFF bands, the principal electrical requirements were directed toward transmission and pattern distortion control. At X-band, transmission efficiency and beam deflection requirements were stringent, but the most critical parameter was the radiation pattern distortion specification on side lobe intensity where absolute minimization and suppression of radome induced side/reflection lobes were required.

WALL CONSTRUCTION SELECTION

The electrical characteristics, particularly the obvious need for absolute reflection minimization over a relatively narrow bandwidth in conjunction with a high incidence angle range, strongly favored the use of the 1st order (halfwave) electrically homogeneous construction rather than a conventional sandwich, such as the "A" or "C". To achieve an electrically equivalent "halfwave" structure with a much reduced weight, the sandwich structure using a dielectrically loaded foam core was selected. This concept, in which the foam core is loaded to achieve a dielectric constant equivalent to the structural, impact resistant skin laminate, had been successfully developed as outlined in the paper "The Development of a Lightweight Advanced Aircraft Radome Based on Dielectric Loaded Foam Core Sandwich Construction" presented at the Tenth Symposium on Electromagnetic Windows. That achievement, however, was for a higher temperature application and as such the processing and materials costs were high. The cost and processing problem was solved by altering the quartz/polyimide skins to E-glass/epoxy laminates. For outer laminate surface protection, a linear polyurethane paint was used in the mid and aft regions while a 0.030 inch EPDM rain erosion boot was selected for the nose region. This material provides rain erosion protection at the higher temperatures (up to 400°F), but is most impressive electrically with a dielectric constant of 2.5 and loss tangent of 0.010.

CORE MATERIAL DEVELOPMENT

The higher dielectric constant of the E-glass/epoxy skins (4.3 as opposed to 3.2 for quartz/polyimide) required greater core loading to achieve an electrically homogeneous wall, but this, of course, introduced a higher, and unacceptable, loss tangent. Two approaches were investigated in an effort to solve this problem. The first involved the search and development of a good low loss matrix for the syntactic foam while the second examined the necessity for an electrically homogeneous construction. The evaluation of candidate syntactic foam binders resulted in the selection of a silicone matrix system which offered ease of processing and reasonable cost. Most importantly, the loss tangent was lower than that of the other systems for a given dielectric loading. This is illustrated graphically in Figure 2 which shows the mean loss tangent values (for a large series of measurements) as a function of dielectric constant for the selected silicone binder and an epoxy novalac system. Representative flat panels employing these two resins in the foam core verified the general loss tangent trends during transmission efficiency tests, the silicone panel achieving values well over 90% while the epoxy panel appeared to limit maximum transmissivity to about 87%.

Since X-band reflection minimization was deemed the critical control parameter, this characteristic was monitored in assessing the effects of foam dielectric loading variance. With the sandwich facings fixed at 0.030 and 0.050 inches (interior and exterior), the core thickness was varied and the reflection minimum determined for each of a series of fixed dielectric constants. Because of the wide range of antenna scan and stabilization limits, equal weighting was given to the perpendicular and parallel polarization values. A reflection figure of merit, representing this equal weighting, is shown plotted in Figure 3 as a function of core dielectric constant. The 45° incidence angle plot represents the mid-range antenna offsets and includes the linear polyurethane paint while the 65° plot is representative of the radome nose region and, as such, the EPDM boot was included in the wall configuration. Thus, it is concluded that with equal polarization weighting, the most optimum core dielectric is not equivalent to that of the laminate facings ($\varepsilon' = 4.3$), but rather a lower value of about 3.5. Ultimately the target value was fixed at 3.35 since this reduction did not seriously increase the reflection level while the desirable trends of a lower loss tangent and greater latitude in physical thickness tolerance were obtained. Thus, an electrically "hybrid" wall construction had been effected which maintained the good high incidence angle response of the homogeneous construction while achieving some of the broadband characteristics of the conventional "A" sandwich with similar weight savings.

OTHER ELECTRICAL DESIGN ASPECTS

The more conventional design aspects are mentioned only briefly. The ray study yielded average design angles up to 72° in the nose region with components (low power weighting) as high as 83°. The wall thickness configuration was developed using a computerized successive approximation or iterative process based on achieving a reflection minimization taper. Transmission and beam deflection calculations for the final configuration are shown in Figure 4 where they may be compared to the measured values.

The core thickness optimization at X-band produces a significant mismatch at the L-band interrogator frequencies, which may be corrected by a wire grid which is orientated to appear inductive and to tune out the capacitive susceptance of the radome wall designed for the radar band (see for example: "Design of Half-Wave Radomes For Dual-Frequency Operation" by Warren A. Elliott, Volume III, Proceedings of the Symposium on Electromagnetic Windows, June 1968). Such a basic grid configuration consists of small (0.004 inch diameter) wire loops lying on the inner radome surface in station planes.

EMPIRICAL DEVELOPMENT/TESTS

A radome built to the design configuration was subjected to a series of range electrical evaluation and development test measurements in each of the applicable frequency bands.

RADAR BAND

Measured one-way power transmission efficiency values exhibited good agreement with the theoretically calculated values. In illustration Figure 4 shows a comparison at the mid-frequency where the minimum level was around 80% rising to just over 90% at the higher antenna scan angles. At the band extremes, the minimum levels were around 73% (low) and 78% (high), the low material dielectric preventing more severe loss. The obvious asymmetrical performance levels about the mid-frequency were incidently intended since a corresponding imbalance existed in the specification requirements.

Comparison of the measured and calculated beam deflection (Figure 4) is not as impressive; however, the maximum level was limited to about 3 milliradians, a convergent error occurring around 5° to 6° from the nose in the elevation plane.

Antenna radiation patterns were recorded in the radome presence over a 60 db dynamic range with attention being directed to the main beam reflection lobe magnitude. At the low antenna offsets, the reflection lobe was not well defined because of the high antenna free-space level; however, at the higher offsets, the wide angle lobe was quite pronounced. Maximum levels noted at the mid-frequency were -38.5 db for a 30° offset and -41.5 db for a 50° scan angle. Measurements to determine the effects of an IFF band inductive grid showed no discernible degradation of the beam deflection or radiation patterns, however, maximum transmission losses of about 3% were observed for a grid consisting of continuous wire loops on four inch centers. This loss was reduced to around 1% with a grid loop spacing of 8 inches.

INTERROGATOR BAND

The basic wall construction optimized for the radar band presents a serious mismatch at the IFF frequencies as illustrated by the "bare radome" measurement of power transmission efficiency in Figure 5 which shows a minimum level of about 65%. Range measurements indicated that the calculated grid loop spacing of 4 inches provided a proper inductance for matching; it was also determined that the grid loops could be terminated 48 inches aft of the radome tip without degrading the transmission level.

This inductive grid configuration provided a corresponding minimum transmission level of greater than 90% and further experimentation yielded a "2nd order" grid loop spacing of 8 inches which provided an 85% minimum level both curves being shown in Figure 5. The continuous wire loops caused serious distortion of the ILS/glideslope antenna patterns. Consequently, further studies were required which resulted in modification of the wire grid to loops consisting of 6 inch wire segments with 1/2 inch insulated overlaps. This segmented/shunted grid configuration caused no degradation in the good match at the IFF frequencies (see Figure 5), while allowing good pattern reproduction at the glideslope frequencies.

The conventional IFF band inductive grid was then modified by:

1) Utilizing a "second order" loop spacing,
2) Limiting the inductive elements to the forward radome region, and
3) Employing segmented/shunted rather than continuous wire loops.

This grid configuration caused no significant loss in interrogator band performance (noteably transmission and pattern distortion) while providing distinct improvements in the radar and ILS/glideslope electrical response.

ILS BAND

With the ILS antenna mounted on the radome hardware and bulkhead/forward fuselage simulation, the glideslope free-space patterns show smooth characteristics as illustrated by the azimuth scan at a -10° elevation offset in Figure 6. The addition of the radar/IFF array however, produces extreme distortion (as shown in Figure 6) because of its location forward of and in close proximity to the ILS antenna. The addition of the basic radome to this configuration produces no significant changes in the pattern characteristics. Incorporation of a conventional IFF band inductive wire grid in the radome does introduce additional degradation; however, this is effectively minimized by the development modifications. Range studies were thus directed at pattern improvement and ultimately resulted in the inclusion of wire elements in the radome assembly to couple and redirect the glideslope radiation. The director elements envolved consisted of 0.050 inch wires of a 13-3/4 inch length (a particularly critical dimension) lying on the inner radome surface forward of the ILS antenna (4 inch spacing) in station line planes. The pattern gain and shaping was controlled by the number of elements. This then provided for a reconstruction of the glideslope pattern compensating for the radar/IFF array induced distortion, the results of a two director element incorporated array being shown in Figure 6.

SUMMARY

The significance of this work lies in four primary factors:

1) An advancement in dielectrically loaded syntactic foam technology.
2) The inductive grid modifications designed to maintain high interrogator band electrical performance while minimizing electrical degradation in the radar and ILS bands.
3) The development and inclusion in the radome of elements designed to significantly improve the glideslope pattern response.
4) The development of a "hybrid" electrical structure employing a loaded foam core, optimized in dielectric for minimum reflection levels.

FIGURE 1
SIDE VIEW OF RADOME
DEPICTING ENCLOSED ANTENNAS

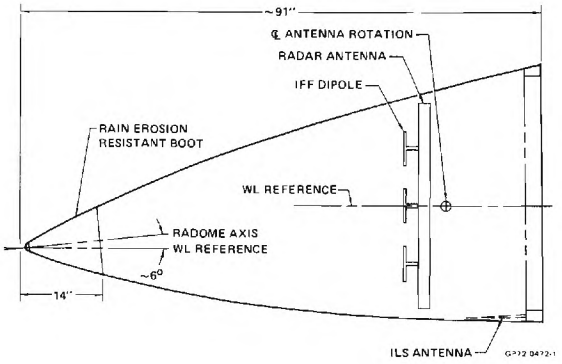

FIGURE 2
LOSS TANGENT OF LOADED SYNTACTIC FOAM
vs RELATIVE DIELECTRIC CONSTANT FOR TWO
CANDIDATE RESIN MATRICES

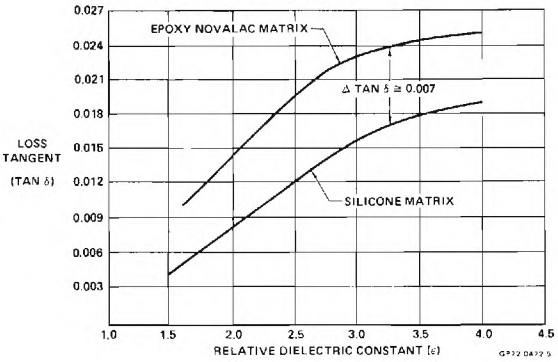

FIGURE 3
MINIMUM REFLECTION LEVEL
vs CORE DIELECTRIC CONSTANT

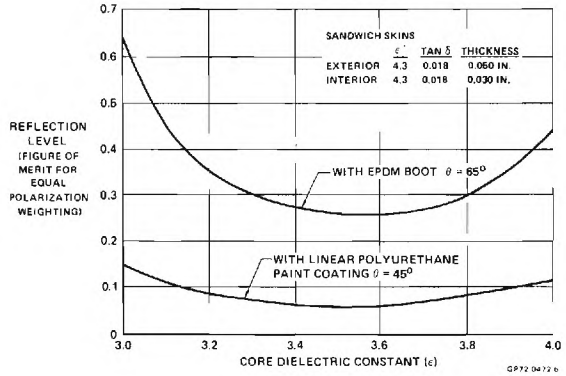

FIGURE 4
MEASURED AND CALCULATED ELECTRICAL PERFORMANCE
(RADAR BAND TRANSMISSION EFFICIENCY
AND BEAM DEFLECTION)

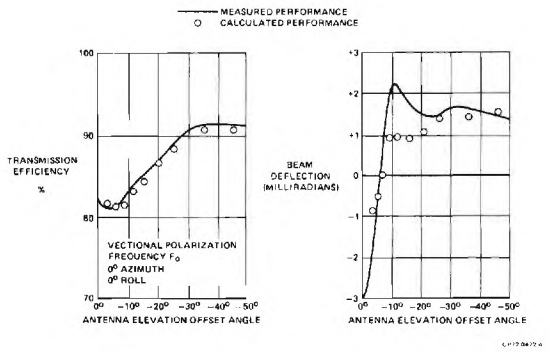

FIGURE 5
INTERROGATOR BAND TRANSMISSION vs
ELEVATION SCAN ANGLE FOR A SERIES OF
RADOME INDUCTIVE GRID CONFIGURATIONS

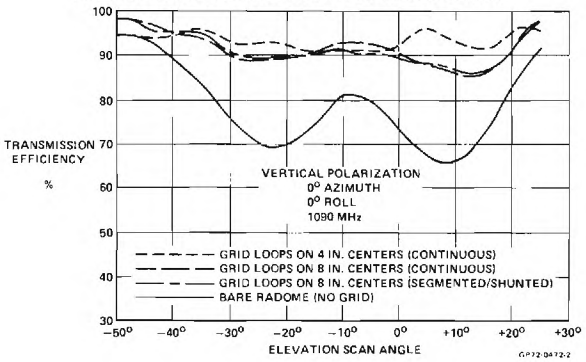

FIGURE 6
AZIMUTH PLANE GLIDESCOPE PATTERNS
AT A −10° ELEVATION OFFSET

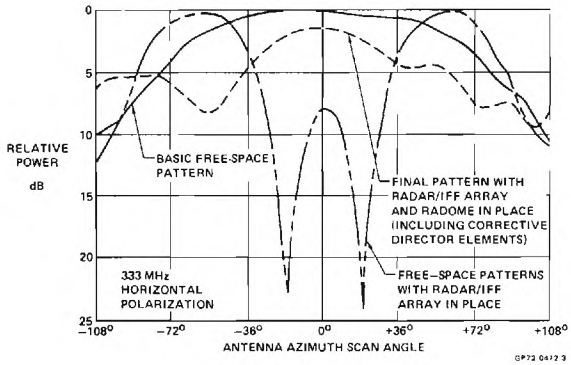

STRUCTURAL DESIGN AND ANALYSIS OF A MATCHED DIELECTRIC FOAM CORE SANDWICH NOSE RADOME

G. J. Vames, Brunswick Corporation, Marion, Virginia

THE DESIGN PROBLEM

A matched dielectric sandwich consists of high density facings and a lower density foam core which is modified so that its dielectric constant matches that of the facings. Thus the composite wall behaves electrically as a solid wall and a significant weight savings is realized.

The sandwich chosen for this radome consisted of E-glass fabric facings impregnated with heat-resistant epoxy resin and silicone foam core. The inner and outer facings were 0.050 and 0.030 inches in thickness, respectively, and the core thickness varied from 0.230 inches at the base to 0.276 inches at the nose. The core density was approximately 30 pounds per cubic foot.

The unique problems associated with analyzing this radome were a result of the mismatch in properties of the facings and the core. While the core material has a significant modulus of elasticity, its strength, especially in tension, is low. This, coupled with the thermal stresses induced by the large mismatch in coefficients of thermal expansion, would indicate that the core stresses could be critical. Therefore, a rigorous analysis of the structure was deemed necessary.

RADOME GEOMETRY AND LOADING

The structure analyzed is an ogival shape with a fineness ratio of approximately 2:1. The overall length is 91 inches and the base diameter 47 inches. The leading edge of the radome is protected with a steel nose cap three inches in length. The base attachment structure consists of an aluminum ring, approximately square in cross-section, containing four combination latch/shear pins. The aftmost 3.5 inches of the radome wall is solid laminate of reduced thickness to accommodate the hardware ring.

The critical load condition results from a negative load factor which produces down bending. The ultimate loads at the radome base are 11,600 pounds shear, 443,000 inch pounds moment, and 8,000 pounds drag. The outer radome surface temperature was taken as 210°F for the forward fourteen inches and 190°F for the aft portion. The radome inner surface temperature was taken as 160°F. The radome geometry and loading are shown in Figure 1.

METHOD OF ANALYSIS

The basic shell stresses resulting from the applied pressure and temperature loadings were determined using the Brunswick Shell Computer Program. This program uses the Sander's modified first approximation theory to analyze thin shell of revolution with arbitrary loading and cross-section parameters. A finite difference method is used to solve the governing differential equations. Axisymmetric boundary conditions are assumed.

Since the radome is attached to the aircraft at four discrete locations, the concentrated stresses at these locations were determined separately. The resultant in-plane axial load at the critical latch/shear pin fitting was divided among the eight fitting attach fasteners. Each fastener load was treated as a point load on a straight boundary; the resultant stress fields from each fastener were superimposed to determine the stress pattern around the fitting.

The buckling resistance of the radome shell was determined using empirical equations developed for conical frustums. Local shell stability at the latch locations was investigated using empirical equations derived for singly curved panels.

SHELL COMPUTER ANALYSIS

Input to the Brunswick Shell Program consists of two general categories: definition of the structure shape and cross-section parameters, and specification of the loadings and boundary conditions. For purposes of this analysis the structure was divided into 500 elements having approximately the same length-to-stiffness ratio. The structure shape was defined by a fourth order polynominal (Figure 2) which is required to be continuous through the second derivative. The cross-sectional properties of each of the three layers were input for each of the 500 elements. The properties required are thickness, modulus of elasticity, Poisson's ratio, and coefficient of thermal expansion. These properties are also input in polynominal form.

The remaining portion of the input is specified by Fourier number. A solution is obtained for each Fourier number input, with the final results being a summation of the individual solutions. In this analysis three Fourier numbers were required to accurately represent the radome circumferential pressure distribution (Figure 3). It can be seen that the first term (P_0) represents the overall drag, the second term (P_1) results in vertical shear and the associated bending moments, and the third term represents a self-equilibrating pressure. Therefore, the distribution of the first two terms versus radome length was input to give the specified drag and shear distributions with the third term being used to give the specified circumferential pressure distribution. Again, these terms were input in polynominal form.

Only the first Fourier number was needed to describe the temperature loading as it was uniform circumferentially. Boundary conditions were

specified for each Fourier number. In general, longitudinal displacements were not allowed at the base and radial displacements were not allowed at the nose or base. Intrawall rotations were allowed at the base only. The restricted deformations of the radome wall at the forward end were due to the metal nose cap.

The computer results are output in the form of internal loads, stresses, and deflections at the desired locations. The stresses in each layer in the axial and circumferential directions are output for each Fourier number and for the total of all Fourier numbers used. This final stress summary is presented in terms of equivalent normal stress derived from the expression:

$$f_{eq} = \sqrt{f_x^2 + f_o^2 - f_x f_o + 3 f_{xo}^2}$$

This stress represents the equivalent uniaxial stress resulting from the biaxial and transverse stresses. The calculated maximum stresses at the upper centerline of the radome are shown in Figure 4. As expected, the minimum margin of safety occurred in the foam core for the basic radome.

CONCENTRATED STRESSES

The combination latch/shear pin fittings are attached to the radome by eight 3/16 inch fasteners. The maximum fitting load occurs at the bottom latches and equal 8180 pounds compression. This load was distributed among the fasteners with each being treated as a point load on a straight boundary. The expression for the internal loads at a point ahead of the applied load is given by:

$$N_x = \frac{2P\cos^4\alpha}{\pi a} \qquad N_o = \frac{2P\sin^2\alpha\cos^2\alpha}{\pi a} \qquad N_{xo} = \frac{2P\sin\alpha\cos^3\alpha}{\pi a}$$

where: a = distance from boundary to point.

α = angle between x axis and a line drawn from load to point.

These internal loads were combined into equivalent normal loads using the same expression as used for the basic shell stresses. These calculations were made on a one inch grid ahead of the fitting and a plot of the load field was made as shown in Figure 5. The calculations were programmed for solution using a time sharing computer as the loads from each of the eight fasteners had to be superimposed at each of the grid points.

The junction between the sandwich portion of the radome and the solid laminate is 4.5 inches from the base. The loads at this juncture were not dissipated to the point where they could be carried by the sandwich skins. Therefore, the solid laminate was extended an additional two inches forward in the area of the fittings. The load plot indicated the required width of the additional solid laminate to be six inches.

BUCKLING ANALYSIS

The stability of the radome was investigated from two standpoints; overall buckling of the basic shell and local instability at the highly loaded attach areas.

The shell analysis was performed using empirical methods derived for thin-walled conical fustums. The conical model used is shown in Figure 6. The methods used were derived from tests made on solid wall models. Therefore, the radome sandwich wall was converted to a solid wall with equivalent extensional and flexural rigidity for purposes of this analysis. The critical internal loads were then calculated for comparison to the applied internal loads. The radome loadings considered were bending, axial compression, shear and hoop compression. The value of the applied internal loads for each of these was taken from the computer analysis. This was simplified by the fact that the results for each Fourier number were calculated separately. It should be noted that these applied internal loads included those resulting from the temperature gradient.

The calculated critical loads were compared to the applied loads to obtain load factors. These factors were then combined using a buckling interaction equation to determine the margin of safety.

The local stability of the radome in the highly loaded attach area was investigated using classic equation for buckling of singly curved panels supported on the straight edges and loaded axially on the curved edges. The applied loadings were taken from the load field plots described above. Both the solid laminate and the sandwich ahead of the fittings were analyzed with the "equivalent solid" method being used in the sandwich analysis. The margin of safety for the solid laminate was significantly lower than that for the sandwich as the solid laminate had been extended to reduce the sandwich stress levels.

SUMMARY

The basic shell analysis indicated that the sandwich facing stresses were of no consequence, but that the foam core stresses were. This is a problem not found with honeycomb core which is loaded only in transverse shear and not influenced by in-plane and thermal loads.

The analysis of the concentrated stresses at the attachments indicated that additional build-up was required. The minimum margin of safety for the radome occurred in the sandwich facings in these areas. This is always a problem with sandwich structures with discrete attach points.

The buckling analysis showed that the overall stability of the shell was more critical than the local stability at the attach points. While the buckling behavior of shells is always hard to predict, the use of a conservative model and the consideration of all loadings, included those which are thermally induced, can give acceptable results.

RADOME GEOMETRY AND LOADING

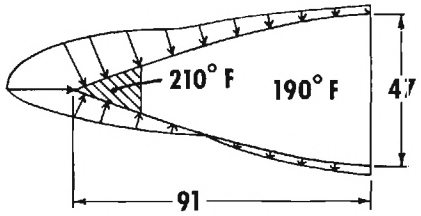

figure 1

Radome Shape Definition

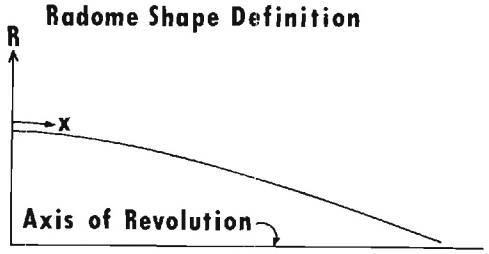

$$R = A_0 + A_1 x + A_2 x^2 + A_3 x^3 + A_4 x^4$$

figure 2

Circumferential Pressure Distribution

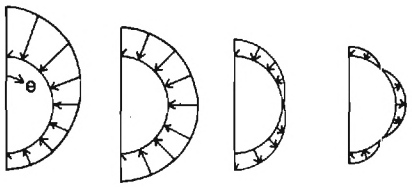

$$P = P_0 + P_1 \cos\theta + P_2 \cos 2\theta$$

figure 3

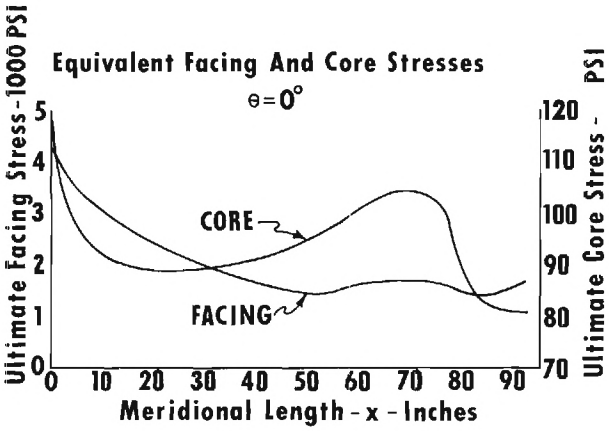

figure 4

Ultimate Load Distribution
at Lower Latch Fitting

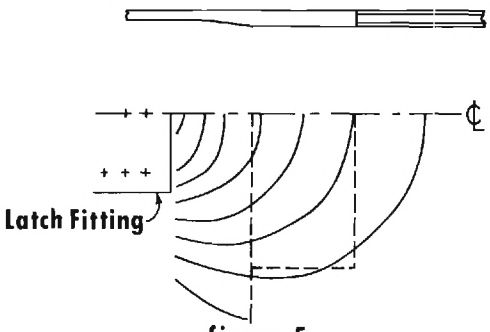

figure 5

Radome Buckling Model

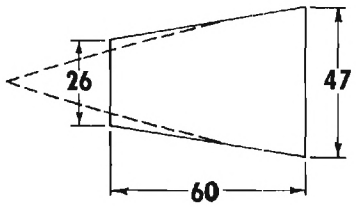

figure 6

COMPUTER DATA REDUCTION SYSTEM
FOR
RADOME ELECTRICAL EVALUATION

John B. Styron, Brunswick Corporation
Stanley Jurczak, Grumman Aerospace Corporation

INTRODUCTION

This paper describes the electrical testing and subsequent data reduction techniques utilized in evaluation and production acceptance testing of F-14 nose radomes. Radome electrical testing is performed using a conventional null-seeker and positioner system in conjunction with a digital computer. Transmission efficiency and boresight error performance is first measured as a continuous function of antenna scan angle. This data is digitized and stored in the computer concurrent with each test scan. Upon completion of each test scan, the computer is programmed to evaluate the data against required specification values. Parameters evaluated include average and minimum transmission efficiency, boresight error magnitudes, and boresight error rates of change as functions of both radial and roll scan angles. A hard copy print out is provided showing differences between specification requirements and measured values. The computer system also plots curves for transmission efficiency and vector sum boresight error.

RADOME TEST REQUIREMENTS

The radar system antenna used in the F-14A nose radome is a flat plate waveguide array approximately 3 feet in diameter. Radome specifications require that transmission efficiency and boresight error measurements be performed on each unit produced using the system antenna. The measured data must then be evaluated for the following specification parameters over all possible antenna scan angles.

Transmission Efficiency	Window Area
Minimum	All
Average	±10 Degree Angle
Average	±10 to ±70 Degree Angle

Boresight Error Rate Of Change As A Function Of Antenna Scan Angle

Boresight Error Components	Antenna Scan Direction
Roll	Radial
Roll	Roll
Radial	Radial
Radial	Roll

Boresight Error Magnitude	Window Area
Maximum Vector Sum Of Roll and Radial Components	0 - 15°
	15 - 40°
	40 - 70°

TEST SYSTEM

A conventional three (3) axis radome positioner and automatic null seeker test system is used for transmission efficiency and boresight error measurements. The radome positioner is shown in Figure 1. Only two axes, Azimuth and Roll, are used however for these tests. The radar system antenna is mounted on a polarization positioner which is attached to a fixed post. The radome is mounted to the roll axis of the positioner through a hinging mechanism which allows the radome to be swung away from the antenna for calibration. The automatic null seeker as shown in Figure 2 is located on a down range tower at a range distance of 4000 inches. The null seeker transmitting antenna is also mounted on a polarization positioner. The control console, shown in Figure 3, is located in the main tower with the radome positioner. All controls for the test system are located at the console including positioner axis driver, system antenna roll, null seeker antenna polarization, and null seeker servo driver. A two (2) plane R-F bridge with video detection is used in conjunction with the null seeker to facilitate boresight error measurements.

Measurements are made on the radome by first aligning the antenna with the radome removed, and performing the various calibration functions as required for transmission efficiency and both planes of boresight error. The radome is then placed over the system antenna and rotated from 0 to 70 degrees in azimuth generating the transmission efficiency and boresight error data. The next scan is run after repositioning the system antenna, radome, and null seeker antenna to a 4° roll position. These measurements are continued at 4° roll increments until a full 360° of roll is completed (90 scans).

DATA ACQUISITION AND EVALUATION SYSTEM

A block diagram of the data acquisition and evaluation system is shown in Figure 4. This system utilizes an H.P. 2114A Computer with 8K memory. Data acquisition and interfacing with the computer is provided by an analog to digital subsystem (H.P. 2310C). Four (4) of the eight (8) channels available in this subsystem are used in these tests. These are, Null Seeker Horizontal and Vertical Displacement (boresight error), Radome Positioner Azimuth Angle, and Transmission Coefficient. These data inputs are provided as D-C Analog Voltage to the H.P. 2310C. Conversion to digital is accomplished automatically and this data is retained in sample-and-hold amplifiers of each channel for later use by the computer. Each channel is continuously up-dated with an aperture time of 100 nano seconds.

The computer is programmed and controlled through the H-P 2754B teleprinter. The teleprinter also provides a print-out of all parameters evaluated. The computer and analog to digital converter are shown in Figure 5. Figure 6 shows the teleprinter and plotter. The computer program provides for sampling of transmission and boresight error data at 1/2 degree intervals of radome scan from 0 to 70 degrees. To perform radome measurements, the radome positioner is first positioned at an angle just outside the 0 to 70 degree range (approximately 0 to -5 degrees). The Computer Program is then initiated by depressing the "RUN" button. When the computer is started, it immediately begins testing for azimuth angle. The scan of the radome positioner is next started. When a voltage corresponding to 0 degrees of radome position angle is reached, the three channels of transmission and boresight data are loaded into the computer and stored. The computer then begins testing for the next angle (1/2 degree) and when the positioner reaches this point, transmission and boresight data is again transferred to the computer. All three data points are read into the computer in less than 100 microseconds. This sampling is continued until the radome positioner completes the 70 degree scan. 141 data points are thus stored for each parameter (transmission efficiency, vertical boresight error, horizontal boresight error) during each radome scan.

The last data point received in the computer (70° point) initiates the calculation of the various parameters for comparison with specification requirements. The specification requirement values are stored in the computer and comparisons are made with measured values after each calculation. Calculations of all parameters and deviations from the specified requirements are made at the completion of each scan with the exception of boresight error rate of change relative to roll angle. This calculation requires that data from the second or adjacent scan (4° roll interval) be available for comparison with the first scan on a point-by-point basis. To accomplish this, data from the first scan is stored in the computer, and all calculations are made except roll rates. The boresight error components of this scan are also stored in another area of the computer. Data from the second scan replaces the data from the first scan, and at that point calculations of all parameters are made including roll rates. Each suceeding scan then replaces data from the previous scan such that it is only necessary to retain data from two scans at any time. After each suceeding scan, the teleprinter prints out the values of each parameter evaluated and/or the deviation (either + or -) from the specification requirements. The plotter also plots transmission efficiency, two components of boresight error, and vector sum boresight error as a function of scan angle. The total time required for testing each scan using this system, including data evaluation, print-out and curve plotting, is approximately 2 minutes.

SUMMARY

The test system and evaluation system as described above has been very successful in the evaluation of nose radomes produced for the F-14A aircraft. The computerized data reduction and evaluation system has provided a considerable savings in time and effort to the program. The speed of operation is not limited by the computer or data acquisition system but rather by the response of the null seeker used. This system also makes it possible to determine immediately after testing, the acceptability of each radome. The system is also designed to be operated by a single technician after programming. In the design of the system, a relay output register was also included to facilitate automatic radome positioner scanning and control. This device has not been utilized to date, however. The computer and all peripheral equipment have proven to be very reliable in approximately two years of operation.

ACKNOWLEDGEMENT

The authors gratefully acknowledge the assistance provided by Mr. Barry Firebaugh in programming of the computer system and Mr. Robert Francisco in the testing of F-14 radomes, and others associated with this program.

FIGURE 1
RADOME POSITIONER

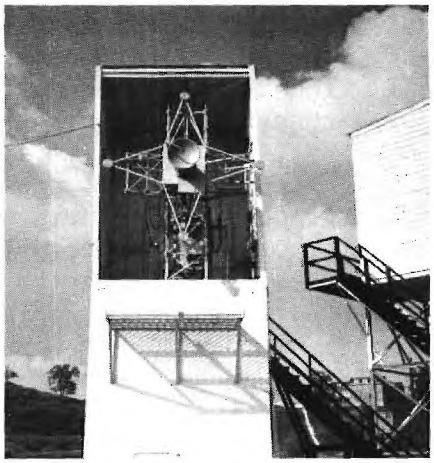

FIGURE 2
NULL SEEKER

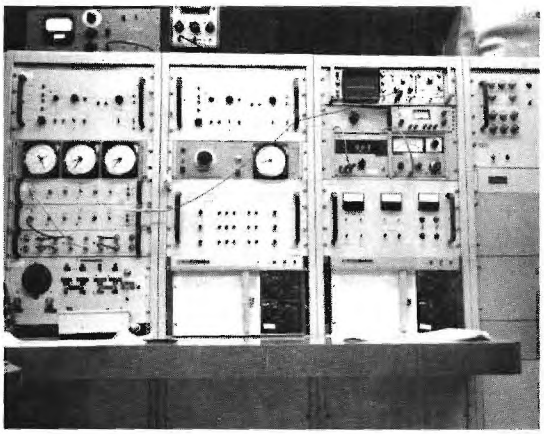

FIGURE 3
CONSOLE

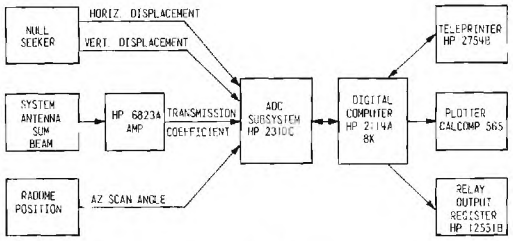

FIGURE 4
DATA ACQUISITION AND EVALUATION SYSTEM

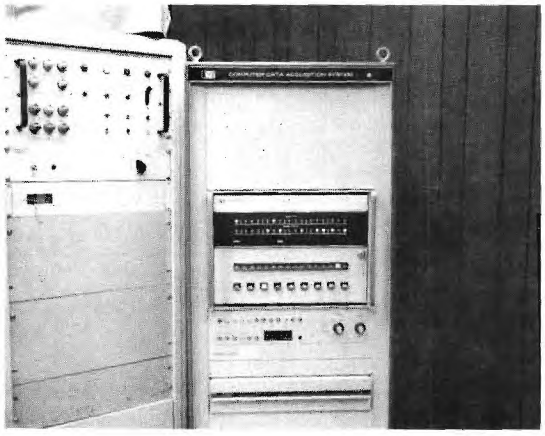

FIGURE 5
COMPUTER

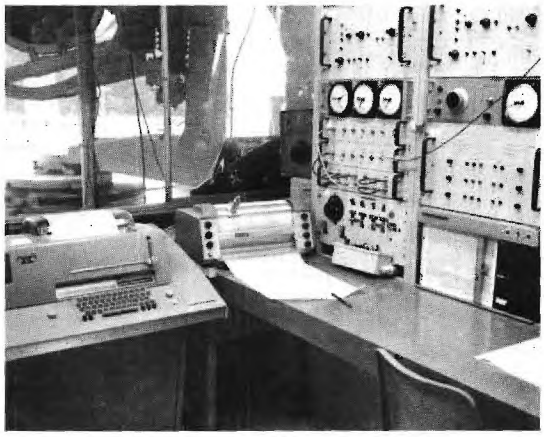

FIGURE 6
PLOTTER

EXPERIMENTAL AND COMPUTATIONAL METHODS IN MICROWAVE HOLOGRAPHY FOR ANTENNAS AND RADOMES

E. L. Rope and G. Tricoles

(General Dynamics Electro Dynamic Division, San Diego, Calif. 92112)

Following its origin in optics, holography is being developed for microwaves.* Some applications are to image formation, especially for objects in optically opaque surroundings; for example, fog penetration and the location of concealed weapons are being investigated. Other applications are diagnostic; for example the analysis of plasmas, antennas, and radomes. Classifications are not rigid for images have been formed to study ionospheric reflections of radio waves.

APPLICATIONS TO RADOMES

New avionic systems have created new radome problems. The problems are quite diverse and special, but we mention two that are significant but quite distinct. First, low sidelobe levels are necessary to reduce clutter in doppler radars; radomes can increase sidelobes, and they can cause boresight error. Second, wide bandwidth antennas are being developed. These antennas usually are small; they have wide antenna patterns that are severely distorted by reflections.

These new applications motivate improvements in methods for analyzing radomes. Of course both computational and experimental methods should be developed. In this paper experiment work is emphasized but some theoretical work is included.

Figure 1 illustrates reflections. The reflections increase sidelobe levels of narrow-beam antennas and distort broad-beam patterns. The field consists of a direct wave that passes through only one side of the radomes and a second wave that is reflected from the opposite side after propagation through the directly

---

* Holography originated in optics as an imaging process. Images are formed in two steps. The first is hologram formation. A beam illuminates an object that scatters a field onto a photographic plate, and a coherent beam also illuminates the plate. The developed plate is a hologram. Images are formed in the second step when the hologram is illuminated. Holograms are interferograms so that holography is similar to interferometry with the added aspect of image formation and optical data processing. The separation into two steps permits data processing during the intervening period.

illuminated side. The two fields are coherent and interfere to produce fringes. These fringes are illustrated in Figure 2. Both measured and computed values are shown.

Computations were based on two distinct physical models; both were approximate. As a first approximation, the field at P in Figure 1 is

$$E(P) = T_P(P_{D)}\, E^I(P) + R(P_R)\, T_P(P_Q)\, E^I(P_R)\, e^{ik_o p}, \qquad (1)$$

where $T_P(P_D)$ is the complex-valued, amplitude transmittance of a flat sheet for plane waves, $T_P(P_Q)$ is the same but evaluated at P_Q, $E^I(P_R)$ is the incident field at P_R; p is the path between P_R and P, and k_o is $2\pi/\lambda_o$ where λ_o is the wave length in air.

Figure 2 shows results of computations based on Eq. 1. The oscillations have, to a good approximation, the spacing of those measured. However, the amplitude of the variations is much greater for the measured case than for the computed. As a second approximation to the field at P, we include the directional properties of the receiving antenna. We assume that

$$E(P) = T_P(P_D)\, E^I(P)\, |P(\phi_{RD})| + R(P_R)\, T_P(P_Q)\, E^I(P_R)\, e^{ik_o p}\, |P(\phi_{RR})| \qquad (2)$$

where $P(\phi_{RD})$ and $P(\phi_{RP})$ are the values of the amplitude pattern for the angles of arrival of the direct ray and the reflected ray, with both angles evaluated at P. Values computed with Eq. 2 are graphed in Figure 2. Notice that the fluctuations have magnitude more nearly those measured.

The form of Equation 1 and 2 illustrates one of the goals of the work; namely to describe the field diffracted by a radome as a sequence of terms corresponding to distinct mechanisms.

In addition to reflections and refraction, radomes cause vertex scattering and guided waves; however, for brevity these mechanisms are not discussed in this paper.

Fringes such as those in Figure 2 can be recorded and displayed to form microwave holograms. Visible images were formed from microwave holograms by reconstructing with microwaves. Visible images were also formed from scale reduced optical holograms with laser light. The images are photographs of the

reflecting regions of radomes. The images are directly useful in visualizing reflecting regions. In addition the holograms are useful because they aid in locating quarter wave matching layers that reduce sidelobe levels. Figure 3 shows an example.

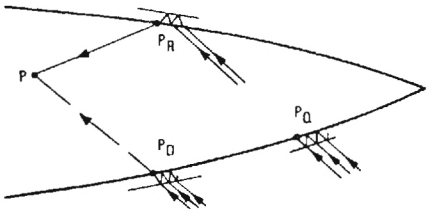

Figure 1. Reflection Geometry. Energy reaches point P directly with multiple reflections near P_D and by reflections from near P_R after propagation through the wall near P_Q.

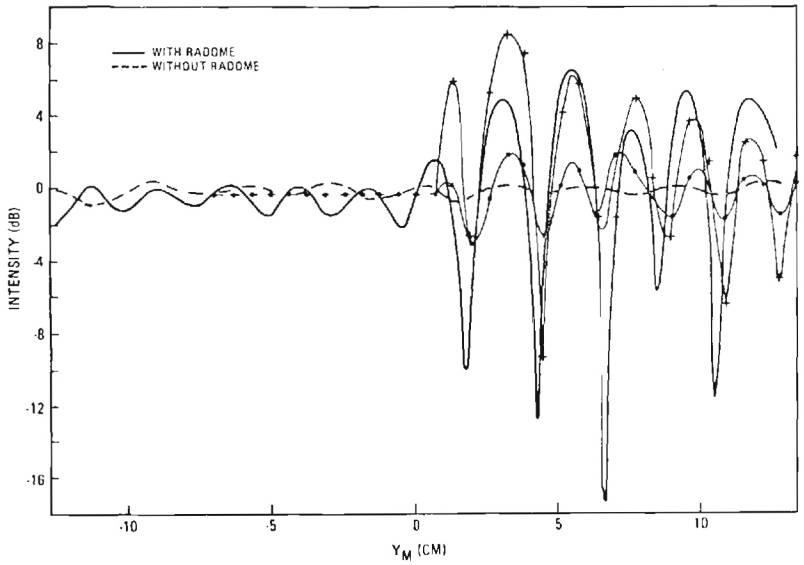

Figure 2. Measured and Computer Power. ϕ_R is -36°. Measurements with 2 by 2.8 wavelength probe, on the plane X = 5 cm. Measured: without radome, (---); with axially-symmetric radome (——). Computed with Equation 1 (·); with Equation (+).

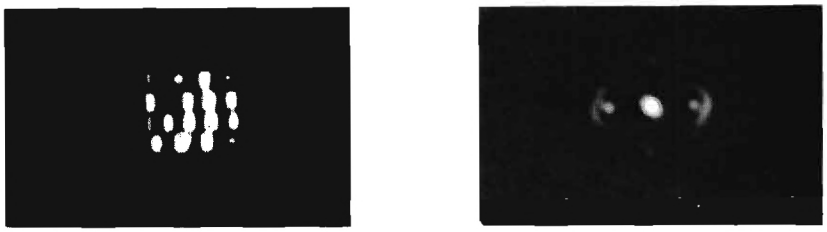

Figure 3. Hologram and a Pair of Images of the Reflecting Parts of a Radome. Holograms were formed at 16 GHz and reduced to 1/250 scale for reconstruction at 6328Å.

AWACS RADAR RADOME ELECTROMAGNETIC DEVELOPMENT

T. Larry Norin
The Boeing Company
Seattle, Washington

INTRODUCTION

This paper presents in summary the results of electromagnetic analytical/experimental work that has been accomplished at Boeing towards the development of a radar radome for the USAF Airborne Warning and Control System (AWACS). Ten 1/7 scale model radomes of various types and shapes have been designed, fabricated and tested. This model work led to the selection of a single full-size design configuration of which six radome units have been fabricated and tested at Boeing. Presently, four of these radomes make up two rotodomes which house respectively, very low sidelobe radar antennas for competing Hughes and Westinghouse AWACS radars.

OBJECTIVES/DESIGN GOALS

Radome electromagnetic performance requirements were not discretely defined. However, electromagnetic objectives and design goals were established with regard to the normal consideration of minimizing degradation to the antenna radiation pattern (main lobe and side lobes) over the operating frequency bandwidth. The radome design problem was aggravated to a considerable extent by concern about antenna sidelobes as low as 60 dB below the antenna peak of beam. The radome design was to be accomplished while maximizing structural integrity and minimizing adverse aerodynamic effects. Such considerations required trades based upon overall AWACS effectiveness and cost considerations. A fall-out of such considerations yielded the following basic radome electromagnetic performance design goals:

- Total power reflections from the radome not to exceed 1% at the radar center frequency (f_o).
- Total power reflections from the radome not to exceed 2% over the frequency range $f_o \pm 150$ MHz.
- The average one-way power gain reduction due to the radome should not exceed 0.7 dB.
- The increase in the azimuth half-power beamwidth due to the radome should be 10% or less.
- The increase in the elevation half-power beamwidth due to the radome should be 20% or less.
- The increase in the average radiation level due to the radome below the antenna (toward the ground) should be 2 dB or less.

DESIGN CONSIDERATIONS

The radome design parameters were size and shape, location, wall construction, radar antenna configuration, and operating frequencies. These parameters were then used to develop a radome with the guidance of the above mentioned electromagnetic performance design goals.

1) Size and Shape

The radome size, related to antenna configuration, was based upon a 6 x 30 foot rotodome. The candidate shapes were: a symmetrical biconvex, symmetrical ellipsoid, several cambered ellipsoids and an aerodynamically chosen asymmetric shape. A brief sketch of the elevation cross section of each of these shapes is given in Figures 1 and 2. The plan-form view of each shape, when forming a complete rotodome, is a circle.

2) Rotodome Location

The rotodome central waterline is 14 feet above the fuselage of the Boeing 707-320 type aircraft at aircraft body station 1120. Figure 3 is a photo of one of the AWACS aircraft in flight.

3) Wall Construction

Radome wall construction is a function of minimum structural requirements, weight, and electromagnetic performance criteria. Once minimum structural requirements were satisfied, electromagnetic considerations were the basic factors used to select the final wall configuration. "C" sandwich type construction as shown in Figure 4 was the final wall selection. The one-half wavelength solid wall radome was structurally inadequate and a multiple half wavelength wall was too heavy, too lossy and too narrow in bandwidth when using cost-effective materials. The "A" sandwich did not have the desired structural redundancy nor the low reflection characteristics versus incidence angle that are exhibited by the "C" sandwich.

4) Radar Antennas

The antennas supplied by the respective radar contractors required a cross-sectional area within the radome of an approximate elliptical shape 5 x 27 feet. The antennas were both two dimensional waveguide slot arrays, arranged to be horizontally polarized.

5) Operating Frequency

The radome was to operate in the "S" band region over a frequency band designated as $f_o \pm 150$ MHz.

RADOME MATERIALS

The radome sandwich consists of the materials tabulated in Figure 4 along with their respective dielectric properties as measured using resonant cavity and/or network analyzer techniques. Microwave absorber materials are also used in the radome to aid in reducing sidelobe levels. The use of absorber materials and metallic shields have been, and continue to be, investigated with regard to their applicability to radiation pattern sidelobe reduction.

DESIGN AND CALCULATED PERFORMANCE

A symmetrical 6 x 30 foot ellipsoidal rotodome shape was selected based on scale model radiation pattern testing and analyses traded against aerodynamic and structural considerations. A constant thickness "C" sandwich wall construction was chosen as the most "cost-effective" after consideration was given to the possibility of a tapered wall (skins and/or core) thickness to correct for radome reflections (impedance matching) or insertion phase delay. This decision was based upon the fact that a wall taper used to correct for phase errors disrupts the low power reflection characteristics of the constant thickness design; while wall thickness corrections used to further improve the basic impedance characteristics of the constant thickness design results in even greater phase errors. Essentially, what would be desired here is a practical technique for impedance and phase matching at the same time over all incidence angles. Incidence angles here vary from zero (normal) to greater than 85 degrees.

The selected design approach was to utilize the antenna nearfield aperture power distribution as the basis for a weighted computer ray analysis to determine by iterative process the radome wall thickness that provides the minimum total reflected power. Figure 5 is a plot of optimum total wall thickness (T_t) versus fiberglass skin thickness to achieve minimum total power reflection from the radome.

The following table summarizes the final radome wall design component thickness and associated tolerances.

RADOME WALL COMPONENT	EFFECTIVE ELECTRICAL THICKNESS (INCHES)
Fiberglass Skins	0.060 ± 0.006
Honeycomb Core	*0.850 ± 0.010
Core to Skin Adhesive	0.010 ± 0.001
Environmental Coating Primer	0.0015 ± 0.0005
Erosion/Thermal Protecting Coating	0.011 ± 0.001
Anti-Static Coating	0.0015 ± 0.0005
TOTAL RADOME THICKNESS	1.994 ± 0.050

* Fabrication thickness is 0.035" greater due to core embedding into fiberglass skins and adhesive layer.

The radome wall thickness was chosen to minimize total reflected power from the ellipsoidal radome shape within the required operating frequency band. Emphasis in the design was placed on elevation beam tilt angles from -10° to $+10^{\circ}$. The following tables summarize the calculated power transmission, total reflected power and power absorption for the selected radome design.

MINIMUM POWER TRANSMISSION ($-10^{\circ} \leq$ Elev. Scan $\leq +10^{\circ}$)			
Frequency	f_o - 150 MHz	f_o	f_o + 150 MHz
Power Transmission	90.0%	90.5%	89.5%

TOTAL POWER REFLECTION						
Frequency	f_o - 150 MHz		f_o		f_o + 150 MHz	
Elevation Scan	0°	$\pm 10^{\circ}$	0°	$\pm 10^{\circ}$	0°	$\pm 10^{\circ}$
Total Power Reflection	2.1%	0.9%	1.2%	1.0%	1.6%	2.1%

MAXIMUM POWER ABSORPTION ($-10^{\circ} \leq$ Elev. Scan $\leq +10^{\circ}$)			
Frequency	f_o - 150 MHz	f_o	f_o + 150 MHz
Power Absorption	8.0%	8.5%	9.0%

Estimated total one-way gain reduction due to reflection, absorption and insertion phase delay characteristics of the radome are given below.

ESTIMATED TOTAL MAINBEAM GAIN REDUCTION			
Frequency	f_o - 150 MHz	f_o	f_o + 150 MHz
Peak Loss (0° Elev. Scan)	0.6 dB	0.9 dB	1.3 dB
Average Loss (-10° to $+10^{\circ}$ Elev. Scan)	0.5 dB	0.6 dB	0.8 dB

Microwave absorber was used inside the radome to aid in reducing lower hemisphere elevation sidelobes. The selection of an absorber material configuration was done after evaluation of numerous candidate materials and for the most part an empirical approach to configuring an optimum absorber layout. It was not anticipated that the final absorber configuration would impact the above calculated performance.

TESTING

Tests that have been performed during this program include dielectric properties of materials, flat panel power transmission, absorber material properties, lightning damage susceptibility and protection methods, RF dielectric heating, 1/7 scale model and full size radiation patterns and boresight tests. The dielectric properties and flat panel tests were used to confirm basic material electromagnetic properties. The radiation pattern tests were used to establish sidelobe levels in the radome and to generate data for radar performance analysis.

The basic AWACS radar antenna radiation patterns are classified and proprietary to the respective radar contractors and therefore are not presented here. However, the following table gives the reader some idea of sidelobe control obtained with the AWACS radome with its low power reflection design and the use of microwave absorber materials.

RADOME IMPACT ON ANTENNA SIDELOBES		
SIDELOBE LEVEL WITHOUT RADOME (ONE-WAY)	* TYPICALLY RAISED DUE TO RADOME BY:	
	AZIMUTH	ELEVATION
-30 dB	0	+ 1.0 dB
-40 dB	0	+ 1.0 dB
-50 dB	+ 1.0 dB	+ 1.0 dB
-60 dB	+ 3.0 dB	+ 3.0 dB

* There are cases where sidelobes are higher and lower

Figure 6 shows in summary, plots of typical main beam gain reduction and beam broadening due to the radome and absorber materials as obtained from full-size hardware radiation pattern tests. One notes in Figure 6 the absorber material impact on gain and beamwidth at elevation scan angles below -7.5°.

CONCLUSIONS

The radome design presently being used for the AWACS radar is a compromise design based upon aerodynamic, structural and electromagnetic considerations. Without compromising present aerodynamic and mechanical design constraints and within state-of-the-art electromagnetic design and fabrication constraints, the present radome design is nearly the ultimate. The primary limitation from the radar performance standpoint is radome shape. A radome shape with lower angles of incidence or perhaps a flatter upper surface to project radome power reflections more towards the radar horizon might be advantageous. Radar flight tests are presently being conducted which will provide information for updating radar performance versus airplane performance trades to help verify or modify the radome design for optimum system performance.

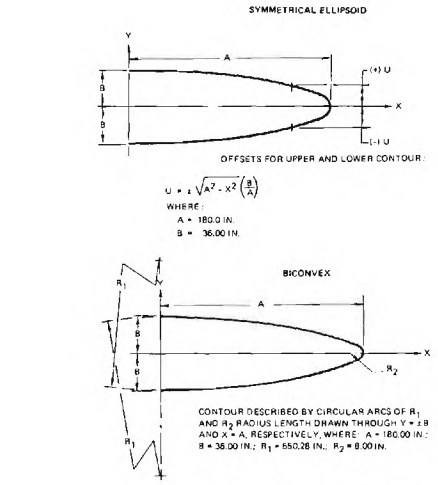

Figure 1: CANDIDATE RADOME SHAPES — SYMMETRICAL

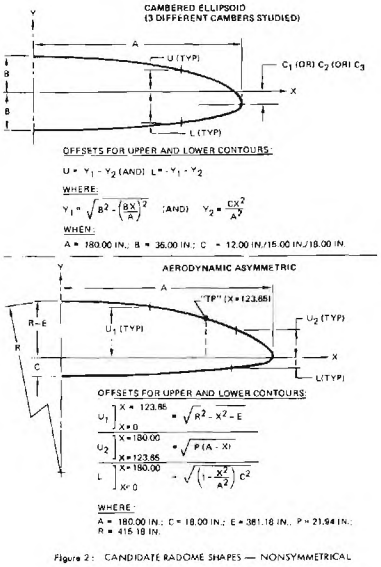

Figure 2: CANDIDATE RADOME SHAPES — NONSYMMETRICAL

Figure 3: USAF/BOEING AIRBORNE WARNING AND CONTROL SYSTEM

RADOME WALL THICKNESS CROSS SECTION

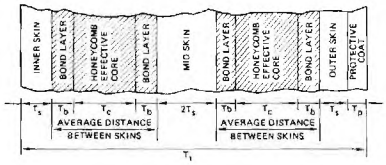

RADOME MATERIAL DIELECTRIC PROPERTIES

MATERIAL DESCRIPTION	DENSITY (GM/CC)	ϵ'	TAN δ
FIBERGLASS SKIN LAMINATE (S-462 GLASS/F-181 EPOXY RESIN)	1.85	4.3	0.017
HONEYCOMB CORE (4.0 LB/FT^3 HRP)	0.068	1.1	0.003
CORE TO SKIN ADHESIVE (BMS-145 TYPE I EPOXY-NOVOLAC)	1.40	3.7	0.03
ENVIRONMENTAL COATING PRIMER (OLIN RM-115P)	1.11	3.3	0.07
EROSION/THERMAL PROTECTION COATING (OLIN RM-115W, POLYURETHANE WITH 10% TiO_2)	1.18	3.4	0.10
ANTI-STATIC COATING (OLIN RM-115AS: POLYURETHANE WITH 5% CARBON)	1.11	8.0 – 7.2	0.2 - 0.4

Figure 4: RADOME WALL CONSTRUCTION

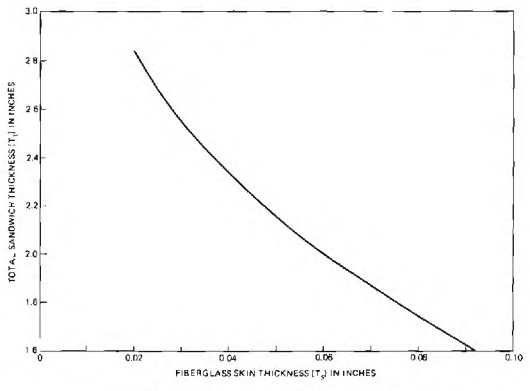

Figure 5: OPTIMUM TOTAL THICKNESS VERSUS SKIN THICKNESS

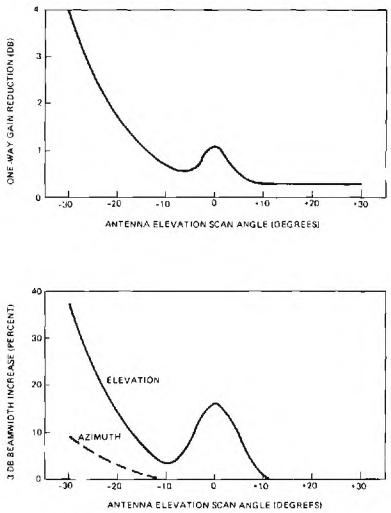

Figure 6: MEASURED GAIN REDUCTION AND BEAM BROADENING

SYSTEM AND RADOME DESIGN CONSIDERATIONS FOR A TACTICAL BALLISTIC MISSILE SYSTEM

by
Dr. William J. Craft and Norman E. Singletary
Martin Marietta, Orlando, Florida

Desired system characteristics can severely restrict the design capability of a missile radome. These factors and their influence on radome design for a tactical ballistic missile system are presented and the tradeoffs with regard to radome design are discussed.

SYSTEM CONSIDERATIONS

The ballistic range requirement for a typical surface to surface terminally guided missile subjects the radome to a severe environment in terms of external loads in combination with the thermal environment during the reentry and terminally guided portion of the trajectory.

As an example, consider a typical system having a range of 400 nautical miles. The burnout velocity/reentry velocity associated with this range is typically 8000 feet per second. This velocity regime results in an external thermal environment considerably greater than that experienced by current tactical missile, i.e., SAM-D, Improved Standard Missile, etc. A radome maximum surface temperature of 2650°F can be expected in the vicinity of the nose. In addition to this thermal environment, the utilization of terminal guidance, which is employed to obtain significant improvement in missile delivery accuracy, requires that sufficient reentry vehicle maneuver capability be provided to insure accurate and rapid response to guidance commands within the available flight time. Thus in addition to the thermal environment, aerodynamic and inertia loads associated with these maneuver requirements must be considered in the radome design conditions. Typical values for lateral maneuver capability could range from 20 to 50 g's.

Additional system considerations include all weather capability and high impact velocity to minimize vulnerability of the reentry vehicle. All weather capability implies that the selected radome material in combination with the radome shape provide adequate rain erosion resistance. Of course, the above requirements must be met with acceptable electronic performance of the radome.

The designer's primary parameters for resolution of the radome design include material, and shape/fineness ratio. These parameters in turn impact back through the system requirements to a limited degree. In contrast, however, certain system characteristics can strongly affect the radome design and tradeoff studies are required to determine the best solution to the problem. For example, Fig. 1 shows for a given radome shape and reentry body ballistic coefficient that the melt point of slip cast fused silica (SCFS) is reached at ballistic missile performance corresponding to approximately 475 nautical miles. However, the use of a reentry vehicle having a lower ballistic coefficient can provide a considerable reduction in peak surface temperature or permit an increase in range for the surface temperature. This would reduce the radome design

problem. The use of a reduced ballistic coefficient vehicle, however, could result in failure to meet system requirements such as velocity available for maneuver and impact velocity; therefore, the tradeoffs must be thoroughly investigated.

These system considerations are not the primary subject of this paper and will not be considered further. The detail design aspects of a radome suitable for application to a terminally guided surface-to-surface missile of medium range is now addressed. The results which follow reflect work performed at Martin Marietta/Orlando over the past year in the areas of radome design.

DETAIL DESIGN

The first consideration given a candidate radome material is its melting point. This value is an indicator of its potential velocity range capability. An unprotected radome could survive greater ranges only to the extent that ablation or sublimation could remove energy while not thinning the radome too severely. For the ballistic missile performance being studied, it was desired to limit radome material candidates to those having melting points above 3000°F. With this constraint, available radome materials are limited to SCFS, Silicon Nitride, Alumina, Beryllia, and Boron Nitride. For the application being considered, state-of-the-art limitations precluded Boron Nitride, Silicon Nitride and perhaps Beryllia and thermal shock requirements eliminated Alumina. Thus consideration was steered initially to SCFS for which the maximum surface temperature is shown in Fig. 1 vs. range for a 20° cone. These data are for the radome surface immediately aft of a rain protective nose cap.

With SCFS as the candidate material, a full wave wall thickness of approximately 0.5 inch was required. This thickness also provides for high lateral load capability and thermal insulation. The radome base diameter in each case is 18.3 inches. Tactical usage and field maintenance dictated that the radome should be removable. This consideration in conjunction with the problems of high outer temperatures at the radome base lead to an inner attachment concept as depicted by Fig. 2, Concept A. Because hoop tensile stresses in SCFS might develop due to an inner attachment (due to thermal expansion mismatch), a low expansion nickel-iron alloy, (Invar) was considered. A flight load equivalent to 50,000 in lbs bending moment was chosen as a reference for this geometry but failure was analytically predicted without any consideration being given to thermal stresses from this bending exceeded 3000 psi when this ring was assumed screwed to a mating surface and for such boundary conditions a stress concentration factor of over 5 was found. This checks the result Dunham & Zike Ref. 1 obtained by using similar geometries and finite element computer programs, (Ref. 2 and 3). At this point it was decided that: 1) For a mechanically weak material, the attachment concept is of great importance. 2) An attachment is desired which does not produce wide variations in the SCFS stresses as a function of the boundary conditions. That is, a deflection insensitive method of attachment is desired. 3) Sharp geometric corners are to be avoided in any attachment in the vicinity of

of the ceramic radome, 4) The stiffness expansion product ($E\alpha$) of the joint should be low to avoid thermal mismatch stresses.

With this in mind, the authors chose the design of Fig. 2, Concept B. This attachment utilizes a series of shear bolts at the end of the skirt in lieu of the previously considered screw attachment.

At this point a study was conducted to develop sensitivity tables of the maximum SCFS tensile stress related to the deflection boundary condition, the bondline modulus and thickness, Fig. 3, 4, and 5 respectively. These results indicate that the maximum tensile stress in the slip case fused silica is very sensitive to all these conditions when used in conjunction with an Invar joint. The final design, which evolved by considerable analysis and study is greatly improved in that the sensitivities of the bond and deflection have been significantly reduced.

The final design (Figure 6) evolved through thickening the silica, incorporating a spherical bond, and substituting fiberglass for Invar. The geometry changes reduced axial stress and placed the bond more nearly in pure shear. The material change further reduced deflection sensitivities and joint stresses. The stress reduction is demonstrated in Tables I and II, where the Figure 6 geometry was used with both fiberglass and Invar. The mechanical load of Table I is equivalent to a 90,000 in. lbs. bending moment.

There remains some uncertainty in equating these stresses to a realistic fracture stress as is commonly obtained in modulus of rupture and tensile specimens. For the computation of margins of safety, the highest tensile component of the principal direction stress tensor was compared to uniaxial tensile data. This neglects compressive failure and is otherwise tantamount to the Lame-Navier Fracture theory. Other theories commonly used are those of Tresca and Saint-Venant or Von Mises-Hencky which are thought unacceptable for brittle ceramics (Ref. 4-7).

Other analysis on SCFS radomes has included rain erosion prediction based on experimental data from G. Schmitt (Ref. 8 and 9). For an indication of the thickness of SCFS which might be removed by flying through a moderate to heavy storm, Schmitt's formula was used. The removal rate was integrated through the rain field for trajectories and ranges consistent with maximum surface temperatures below melt. For conical shapes, the worst predicted erosion was 0.013 in. for a 24° slope and the least was 0.0067 in. at 15°.

An evaluation of EM properties was not emphasized since transmission characteristics are of secondary importance when compared to radome survival. In a tactical system however, EM properties must receive due consideration. Similarly, rain erosion and thermal shock, being essentially determined by the choice of the radome material, must also be considered in the design task.

In summary it can be concluded that: 1) Slip Cast Fused Silica is the best presently available material for reentry heating trajectories.
2) SCFS radomes with wall thickness of approximately 0.5 inch can be designed to withstand reasonable maneuver requirements imposed by terminal guidance in spite of relatively low material strength and internal

missile components will be provided adequate thermal protection because of the inherent low thermal conductivity of silica.

TABLE I

Maximum Thermal Gradient in Joint Area Plus Flight Mechanicals

	Adhesive Stresses			
	Bi-Directional Ring		Invar Ring	
σ_r Min/Max	-358	204	-597	264
σ_θ Min/Max	-157	229	-302	270
σ_z Min/Max	-185	387	-316	322
τ_{rz} Min/Max	-119	[127]	[-176]	106
	SCFS Stresses			
σ_r Min/Max	-462	1048	-462	1048
σ_θ Min/Max	-3495	885	-3643	885
σ_z Min/Max	-1908	[986]	-2554	[1337]
τ_{rz} Min/Max	-709	602	-710	602

All Stresses in psi.

TABLE II

Cool Down From 325°F Cure Temperature to Room Temperature. (.03" Bond Line)

	Adhesive Stresses			
	Bi-Directional Ring		Invar Ring	
σ_r Min/Max	-100	146	-120	47
σ_θ Min/Max	143	436	196	385
σ_z Min/Max	-116	[604]	216	[380]
τ_{rz} Min/Max	[-239]	115	[-82]	-31
	SCFS Stresses			
σ_r Min/Max	-124	150	-27	38
σ_θ Min/Max	-2050	196	-557	[118]
σ_z Min/Max	-1260	[484]	-176	62
τ_{rz} Min/Max	-157	326	-69	76

All Stresses in psi.

REFERENCES

1. Dunham, R. S. and Zike, J. H., "Stress Analysis of the SAM-D Fused Silica Radome/Invar Ring Joint," DA Project No. 1X63302D212, Report No. RK-TM-70-1, U. S. Army Missile Command, Redstone Arsenal, Alabama, 3 Aug 1970
2. Stress Analysis of Solid Propellant Grains Under Transverse Acceleration Loads, Report No. S-116 Rohm and Haas, 1967
3. Heat Conduction and Stress Analysis of Solid Propellent Rocket Nozzles by J. J. Brisbane, Technical Report S-198 Rohm and Haas Company, Feb 1969
4. Ely, R. E., "Stress Results for Ceramic Materials Under Multiaxial Stresses," Report No. RR-TR-68-1, U. S. Army Missile Command, Redstone Arsenal, Alabama, April 1968
5. Brontman, L. T., and Cornish, R. H., "Effect of Polyaxial Stress States on Failure Strength of Alumina Ceramics," Journal of American Ceramic Society, 48, No. 10, pp 519-524, 21 Oct 1965
6. Marin, J., "New Evaluation for Multiaxial Stress Properties of Ceramic Materials," Experimental Mechanics, 6, No. 3, March 1966, pp 162-170
7. Hoffman, O. and Sachs, G, "Introduction to the Theory of Plasticity for Engineers," McGraw-Hill Book Co., 1953
8. Schmitt, G. F. and Krahill, A. H.; "Velocity-Erosion Rate Relationships of Materials in Rain at Supersonic Speeds," ARML-TR-70-44, October 1970
9. List, R. L., "Smithsonian Meteorological Tables," Sixth Revised Edition, Published by the Smithsonian Institute, April 1966

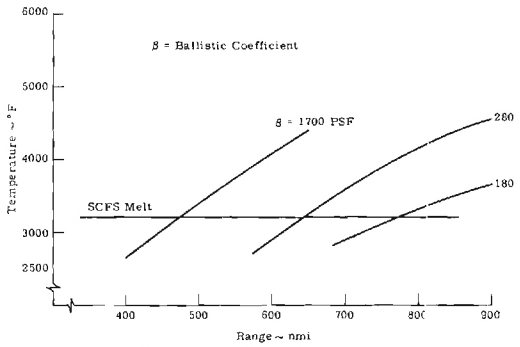

Figure 1. Peak Radome Surface Temperature of S.C.F.S. versus Range

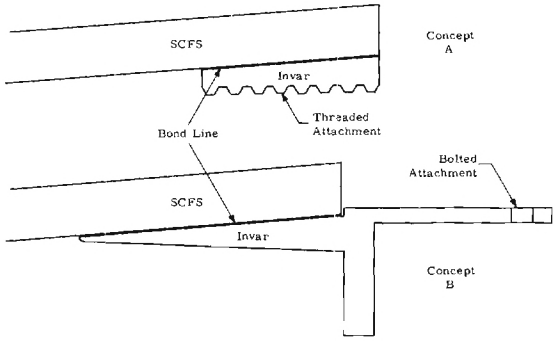

Figure 2. Preliminary Attachment Ring Concepts

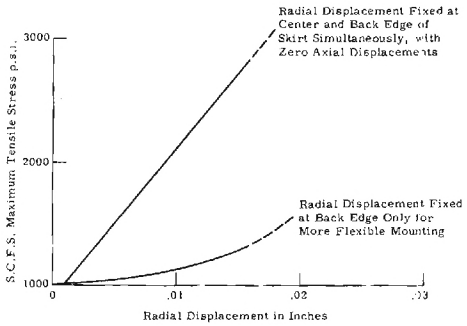

Figure 3. Displacement Boundary Effects on Maximum Tensile Stress in S.C.F.S. for Invar Joint B

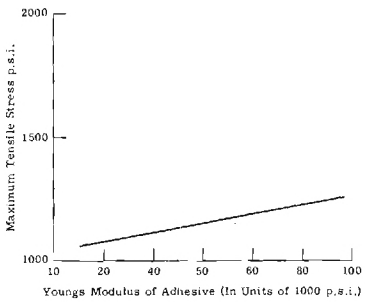

Figure 4. Maximum Tensile Stress in S.C.F.S. versus Adhesive Modulus with Invar Joint B

Figure 5. Bondline Thickness versus Maximum Tensile Stress in S.C.F.S. with Invar Joint B

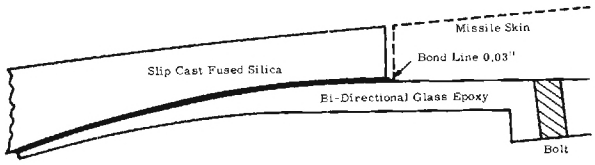

Figure 6. Final Attachment Ring Concept

Cold-Sprayed Fused Silica Radomes

by F. P. Meyer and G. M. Harris

INTRODUCTION

Fused silica has proven to be the prime ceramic material for high velocity missile radome applications. Its unexcelled thermal shock resistance and its low and stable dielectric constant give it excellent properties as a ceramic radome material. Future requirements for very large and thin-walled structures have pushed the state-of-the-art to the limit of present capability of producing radome structures by conventional ceramic processing techniques.

Presently, fused silica radomes are formed using the slip casting process (1). This process is well documented and many various size radome shapes have successfully been made with it. As the size of the radome increases however, the fabrication difficulties increase and there is a sharp rise in the scrap rate for the process.

Previous work by Gannon et al (2) had shown that a medium density fused silica shape could be fabricated by spraying a slurry of silica powder containing colloidal silica as a binder phase onto a heated metal substrate and carefully drying the material. Bodies up to 60% of theoretical density could be fabricated with high green strength attributable to the binder used. With a few adaptations it was felt that this process could be used for fabricating large fused silica radome shapes and that impregnation processes could be developed for densification and strengthening of the preform to produce an acceptable radome. The ease with which the spraying process can be mechanized for high production rates and the excellent green strength of the material were major considerations in selecting this process.

PROCEDURE

The basic cold-spraying process for radome fabrication is shown in Figure 1. Similar to porcelain enamel spraying, a silica slip is pressure fed to a conventional air spray gun in which it is atomized and the fine spray made to impinge upon a rotating mandrel. The outside surface of the mandrel is machined to define the interior surface of the radome. Continual drying of the surface by four ribbon burners dries the spray upon contact and substantial thicknesses of ceramic may be built up.

Fused Silica Slip

The slip used in the cold-spraying process is made entirely of inexpensive commercially available materials; fused silica powder, colloidal silica and water. The fused silica powder is purchased as minus 200 mesh Glasgrain from Glassrock Products and the colloidal silica is a 30% by weight suspension produces by E. I. du Pont Co. as LUDOX AS.

Best spraying results to date have been with a slip containing 58% by weight fused silica powder, 40% by weight colloidal silica solution and 2% water. This gives a total silica content of 70% by weight. The pH of the slip is maintained at 8.5 and the specific gravity is 1.62 ± .05 gm/cc.

The slip may be mixed in the spray tank by adding the fused silica powder to the liquid under moderate agitation. The slip may be sprayed immediately and is stable up to 8 hours or until agitation is stopped.

Spray Equipment

The fused silica slip is cold-sprayed using a conventional pressure feed paint spray outfit. The slip is contained in a five gallon pressure feed tank equipped with an air driven agitator. The slip is fed to the spray gun under a gauge pressure of 16-18 psi. The hand spray gun has a specially reinforced body, heavy duty packings and a high hardness fluid tip and needle for use with highly abrasive materials.

Cold-Spray Process

The mandrel used in the cold-spray process is machined from hardened steel. It is 17 inches high and 7 inches in base O. D. with an 80 inch radius ogive shape. This mandrel is rotated at approximately 35 rpm for spraying.

Ribbon burners are positioned vertically on either side of the mandrel and held approximately 3 inches from the surface.

A silicone base mold release agent is sprayed onto the surface of the mandrel and air dried for 10 minutes. The mandrel is then rotated in the heat of the burners for 3 minutes to preheat the surface.

During spraying the gun is held approximately 12 to 15 inches from the mandrel surface and rapid vertical strokes are made while keeping the gun perpendicular to the ogive at all times. Care must be taken to allow the freshly sprayed surface to dry properly and so spraying is done only on an up-stroke and occaissionally an entire stroke is ommitted.

Best spraying results have been obtained using a fluid nozzle of 0.070 inches I. D. and compressed air delivered to the gun at 45 psi for atomization of the slip. Upon completion of the cold-spraying operation the burners are shut off and the radome and mandrel are allowed to cool for 10 to 20 minutes. The steel mandrel will shrink away from the interior surface and the ceramic radome is lifted off.

Impregnation Process

In the as-sprayed condition the radome will average 55 to 60% of theoretical density. The first impregnation step is simply a soak in the colloidal silica solution. The radome is inverted in a large vat of colloidal silica and the liquid is allowed to permeate thru the body. When the entire inside surface has been wetted the radome is removed and dried.

Step two in the impregnation is a vacuum treatment as shown in Figure 2. The radome is sealed into the bottom fixture with wax so that a vacuum may be applied to the interior volume. Colloidal silica solution is then admitted to completely immerse the radome. After the accumulation of approximately 50 ml. of solution in a collection trap in the vacuum line the impregnation is terminated. The radome is then removed from the wax and dried.

DISCUSSION OF RESULTS

The cold-spray process has been used successfully to fabricate 18 inch high ogive-shaped radomes with up to 1 inch wall thickness. An as-sprayed radome is shown in Figure 3.

As-sprayed, a radome is 55% dense. The use of the colloidal silica binder in the slip imparts excellent green strength to the body however, and the radome will withstand rough handling in this condition. Subsequent impregnations greatly increase the green strength.

Drying shrinkage for a radome fabricated by the cold-spraying process is virtually non-existent. The heat from the ribbon burners drives off nearly all free water from the spray as it collects on the mandrel. The binder phase then holds the particles against the surface and its strength is such as to prevent any shrinkage of the ceramic shell during this drying operation. The inner surface of the radome conforms exactly to the outer surface of the mandrel.

The simple soak type impregnation increases the radome density to 65% of theoretical. Vacuum impregnation further densifies the ceramic to 1.48 gm/cc or 68% of theoretical.

Several commercially available soluble silicate systems were tried as alternate impregnants in this work but none functioned as well as the colloidal silica. The combination of low viscosity and reasonably high silica content for this solution proved it to be the best impregnant.

Repeating either of the impregnations steps failed to increase the density to any degree. Surface porosity was sealed rather quickly and penetration of the liquid is impossible. The vacuum treatment used as a second step was far better than using another soak cycle and future work will be to pressurize the colloidal silica solution and drive the liquid into the radome with greater force.

The radome is 68% dense after impregnation and has a flexural strength of 1400 psi. The surface finish on the interior of the radome is not affected by the impregnation and only the exterior surface requires machining.

Samples from an impregnated radome were fired at 2250°F for three hours and their final density was 1.70 gm/cc, 78.0% of theoretical.

CONCLUSIONS

Large thin-walled fused silica radomes can successfully be fabricated using the cold-spray process. Although porous in the as-sprayed condition, the structures are exceptionally high in green strength and subsequent impregnation greatly increases this strength so that machining may be done before firing.

Impregnation of the porous radome structure produces a green body 68% of theoretical density and upon firing the density is increased to 78%.

Improvements must be made in the densification of the as-sprayed radome. Work must be devoted to improving the vacuum technique or else some other method for densification must be employed (cold isostatic compaction).

ACKNOWLEDGEMENT

The authors wish to express their sincere appreciation to Mr. John J. Coppi for his hard work and his skill and knowledge of the cold-spraying process.

REFERENCES

1. Walton, J. D. Jr., Section V. Fabrication Processes, of Chapter 5. Inorganic Radomes, pp 298-320, Radome Engineering Handbook, Edited by J. D. Walton, Jr., Marcel Dekker, Inc., New York, New York, 1970.

2. Gannon, R. E., G. M. Harris and Thomas Vasilos, "The Effect of Porosity on Mechanical, Thermal and Dielectric Properties of Fused Silica", Bull. Amer. Cer. Soc., Vol. 44, No. 5, pp 460-462, May 1965.

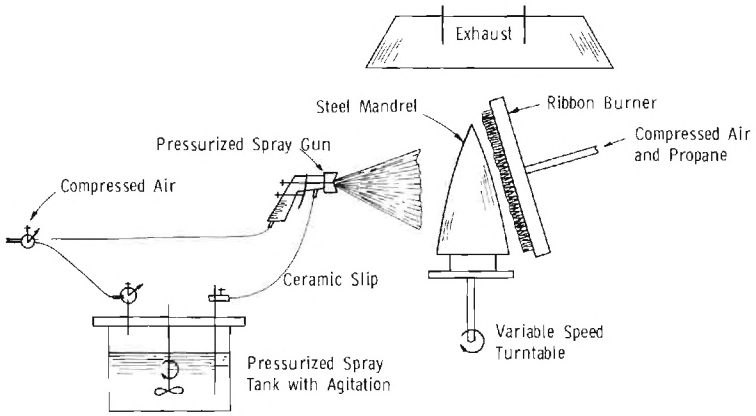

Figure 1. COLD-SPRAY PROCESS FOR FUSED SILICA RADOME FABRICATION

ARMY MATERIALS AND MECHANICS RESEARCH CENTER

19-066-564/AMC-72

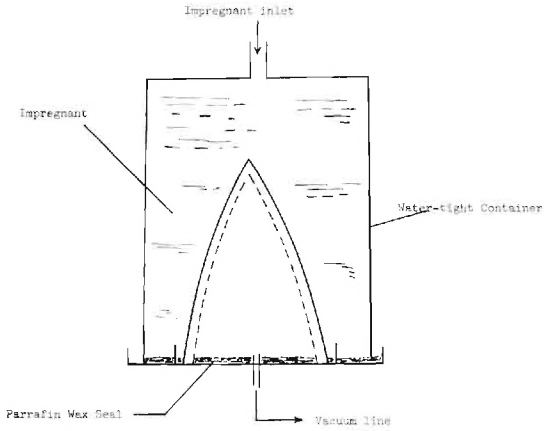

Figure 2. Vacuum Impregnation Treatment

Figure 3. Fused Silica Radome (As-Sprayed)

ARMY MATERIALS AND MECHANICS RESEARCH CENTER

19-066-1028/AMC-71

SYNTHESIS OF ELEVATED TEMPERATURE RESISTANT, EROSION RESISTANT POLYMERIC COATINGS

By

G. F. Schmitt, Jr.
Air Force Materials Laboratory
Wright-Patterson AFB, Ohio

I. Background

Operation of aircraft and missiles in rainy environments has resulted in rain erosion problems on numerous components of those systems. Rain erosion has been a particular problem on radomes and other exterior plastic parts of aircraft and missiles because those components are nonmetallic (to be compatible with the radar), made of fiber-reinforced constructions (which are prone to erosion damage), and are typically located in positions on the aircraft which are subject to rain exposure. These problems are primarily subsonic in nature because current aircraft do not operate supersonically, if at all possible, in rain environments. However, because of aerodynamic heating associated with supersonic flight, erosion resistant coatings with long term (hundreds of hours) thermal stability at temperatures up to 500°F are required for advanced systems.

Protection of aircraft radomes in the Air Force currently utilizes MIL-C-83231 polyurethane rain erosion resistant coatings which have been described at the last EM Window Symposium (Reference 1). The outstanding performance of the polyurethanes in actual service has eliminated erosion problems on many aircraft and service times in excess of two years for these polyurethane coatings are common. However, the polyurethanes are limited in service temperature to 300°F for long times and 350°F for shorter periods (up to 24 hours). At temperatures above 400°F, the polyurethane erosion coatings lose their elastomeric character and their erosion resistance very rapidly.

Outstanding erosion resistance is not the only requirement for a coating to be used in actual service. Other requirements include a) good dielectric transmission properties for radar transmission; b) antistatic properties for reduction of precipitation static on large radomes; c) good weatherability including retention of rain erosion resistance, transmission and surface resistivity after prolonged outdoor exposure; d) application techniques and cure properties which are compatible with repair of radomes at field activities. Repair of the coatings themselves as well as strippability, if the coating must be removed, are also required.

In-house research at AFML has long emphasized high temperature polymeric erosion coatings and continual evaluations of candidate elastomeric/polymeric coatings have been conducted (Reference 2). A variety of thermally stable polymers including silicones, polyimides, amide-imides, fluorosilicones, carboxy-nitroso, silphenylene-dimethylsiloxane

and other polymers which are elastomeric or thermally stable or both have been investigated with little success. Until recently, the ability to develop a coating which has long term (hundreds of hours) stability at 400°F or 500°F, and possess substantial subsonic resistance to rain erosion and meets all of the other requirements as discussed above had not appeared within the state-of-the-art. However, the newly developed fluorocarbon coating as reported herein does meet the requirements for advanced aircraft radome protection.

II. Development of Fluoroelastomer Coatings

Previous research at AFML on fluoroelastomers for high temperature sealants had proven the long term thermal capability of these polymers for retention of physical properties. With this as a background, erosion resistant coatings were formulated and optimized with carbon black pigment for color and conductivity purposes), magnesium oxide filler (which serves as a stabilizer for the curing reactions) and cross-linking agents. Fluoroelastomers used were commercially available ones such as Viton from duPont and Fluorel from 3M Company.

One of the keys to developing and optimizing the fluoroelastomer coatings which exhibited the greatest erosion resistance was the extensive use of the rotating arm apparatus to characterize the dynamic response of these coatings to the rain environment. The rotating arm was located at the Air Force Materials Laboratory. In these experiments the coated materials specimens are fastened on the tips of a propeller-like blade, spun at velocities of 500 MPH typically, through artificial rain (at AFML, 1.0 inch/hour simulated intensity of 1.8 mm diameter drops) which impinges on the surface. The specimens are exposed in this environment until failure of the coating by penetration to the substrate, which is determined by observation of the specimens while running through use of a stroboscopic light and closed circuit TV camera. The performance of coatings in the rotating arm apparatus has been correlated to actual flight test results both as to rankings of various materials and the actual modes of failure of the materials themselves. The apparatus has been previously described (Reference 3).

Since, as previously mentioned, the principal components to be protected are constructed of reinforced plastics, glass fiber-reinforced plastic laminates (typically glass-epoxy or glass-polyimide) were used as the substrates in the rotating arm experiments. Not only are these laminate substrates representative of the actual radome constructions which need to be protected, but their use was essential to assessing the performance of the fluoroelastomer coatings being developed. The dynamic response of the coating over the substrate to the high loading rates associated with droplet impingement has been found to be dependent on both the coating and substrate properties. For example, if aluminum substrates were used instead of the glass-reinforced laminates, the resulting erosion response of the coating is not representative of its overall

protective ability for laminate (i.e. radome) substrates but is only indicative of the coating strength and erosion resistance itself.

The coating penetration phenomenon caused by continued droplet impingement on the surface varies for different types of coatings. For example, neoprene coatings gradually wear away with a true erosion phenomenon on the surface. Epoxy or polyester coatings possess no erosion resistance at all and fail by brittle rupture of the coating. Polyurethanes do not erode on the surface but suffer localized failures at a weak spot in the substrate under the coating or at a defect in the coating surface after prolonged exposure. The fluoroelastomer coating erodes away on the surface in a manner similar to the neoprene. Examples of coating failures are shown in Figure 1.

Prior to the development of this fluoroelastomer elevated temperature resistant rain erosion coating, the AFML had formulated and evaluated high temperature premolded rubber boot materials, including epichlorohydrin and ethylene propylene rubbers, for potential application to aircraft requiring high temperature performance radome protection. Based on AFML rotating arm rain erosion evaluations, these boot materials have shown promise with regard to their erosion performance. However, boots are not as good as coatings from the standpoint of field application and repair. Application of the boot will require elevated temperature curing of a thermally stable adhesive which bonds the boot to the radome surface. For field repair, replacement of the entire boot will be required. Also, the coating has better rain erosion performance.

The erosion performance of these coatings as a function of thickness is compared to that of the polyurethane and neoprene in Figure 2. As may be seen, the fluoroelastomer provides erosion resistance of 50% greater than the MIL-C-7439B neoprene and improves with thermal aging. It is not as erosion resistant as the polyurethane and would not be used for applications where the thermal requirements do not exceed the capability of the polyurethane.

However, if long times at temperatures above 350°F are required the fluoroelastomer coating is the only polymeric erosion coating which can withstand these conditions and maintain its erosion resistance. A graph demonstrating the retention of erosion resistance by the fluoroelastomer coating is shown in Figure 3. As illustrated therein, the coating improves slightly in erosion resistance after 24 hours at 400°F or 500°F which serves as a post cure even though the fluoroelastomer cures at room temperature. Even after 200 hours at temperature, there is little decrease in time-to-failure and what reduction is observed is due to loss in substrate (epoxy or polyimide) properties not because of changes in the coating itself. This has been confirmed by physical properties measurements on free films of the coating which show no change in tensile strength, elongation or modulus after 672 hours at 400°F. Note also in Figure 3, the new fluoroelastomer coating possesses approximately 50% more erosion resistance at only 12 mil thickness compared to the performance of the 30 mil thick high temperature boot materials. The 12

mils thickness is a minimum for attainment of any substantial erosion resistance; at thinner sections, elastomeric coatings of any kind fail rapidly in the rain environment.

As the temperature increases above 550°F, the fluoroelastomer embrittles and after exposure for 24 hours at 600°F, the coating is no longer elastomeric or erosion resistant. This data is summarized in Figure 4. The substrates had to be changed from glass-epoxy (at 400°F) to glass-polyimide (at 500°F), to aluminum at 550°F or 600°F) to prevent substrate degradation with thermal exposure from confusing the results.

To obtain a proper level of surface resistivity for the antistatic coating, 0.5-15 megohms, the fluoroelastomer coatings were pigmented with sufficient conductive carbon black to attain this resistivity. Greater or lesser amounts resulted in too much or too little conductivity. In addition, the magnesium oxide used in the base coat had to be changed in the conductive top coat because it masked out the carbon black even at higher loading levels and prevented attainment of proper surface resistivity levels. Another magnesium oxide was found to be conductive. This topcoat is applied in a 2 mil thickness over the base coating which is 10 mils thick. This approach maximized the erosion resistance of the antistatic coating system since the use of higher loaded fluoroelastomer only would result in less resistance (because the presence of a high loading of pigment or filler invariably reduces the performance) and would reduce the transmission properties.

The transmission properties of the Type I and Type II (antistatic) coatings were measured at X-band (9.375 GHz) after application and found to be 94% and 90.5% respectively. After six months exposure in Florida, the coatings were found to retain transmission values of 92% and 90% or greater and to maintain their resistivity at 0.5-15 megohms. The dielectric constant and loss tangent at X-band and room temperature are 3.77 and 0.055 respectively.

The erosion resistance of the fluoroelastomer coatings was unchanged after six months of Florida weathering. The fluoroelastomer coating is spray applied and cures at room temperature within 48 hours to full physical properties and erosion resistance.

III. Future Applications of the High Temperature Fluoroelastomers

Service tests of the fluoroelastomer coatings including electrical tests and actual flight testing are scheduled for summer 1972. The combination of demonstrated subsonic erosion resistance, radar transmission properties, ease of application and thermal stability up to 500°F make this new fluoroelastomer coating a prime candidate for protection of radomes on high speed aircraft which will develop high surface temperatures due to aerodynamic heating and will encounter rain subsonically. The types of aircraft on which the MIL-C-83231 polyurethane and the new fluoroelastomer erosion coatings can be used are shown in Figure 5 as a function of temperature.

Further development is well along to provide the necessary data to prepare a military specification on the coating. Also, to satisfy thermal flash requirements, a white version of this coating is being developed (the current coating is black). Initial erosion evaluations, dielectric transmission tests and thermal flash tests are extremely promising for the white fluoroelastomer. Tests are also underway at supersonic speeds (up to Mach 2.5) to determine its potential for use on missile radomes which are expected to encounter rain at supersonic speeds up to Mach 2.5.

On the basis of rain erosion evaluations using the rotating arm apparatus in simulated rain, the new fluoroelastomer coating has demonstrated at least 50% of the erosion resistance of the best current coating, a polyurethane coating as covered in MIL-C-83231, while offering at least 200°F increase in thermal stability over the polyurethane. To provide a basis or measure of what this offers in erosion protection for actual service, recent reports from SEA have shown that the polyurethane coating has functioned for over one (1) year with very little or no damage. Also, SAC has experienced that the polyurethane coating will last at least 2500 flight hours on KC-135 radomes before requiring repair or replacement. Considering this, the new fluoroelastomer coating is expected to provide service life of at least six (6) months or up to 800 flight hours including elevated temperature exposure (up to 500°F continuous service) with little or no repairs. Further planned modifications of the coating are expected to further extend these lifetimes. However, because of the excellent demonstrated performance of the polyurethane coating, it is not intended that the new fluoroelastomer will replace the polyurethane for applications below 300°F.

IV. Conclusions

1. A new fluoroelastomer rain erosion resistant coating has been developed which possesses a long term thermal stability (hundreds of hours) up to 500°F.
2. The fluoroelastomer coating withstands rainfall conditions of 1 inch/hour at 500 MPH for an average of 55-60 minutes. The coatings demonstrate one way power transmission of 94% (at 9.275 GHz) and surface resistivity of 0.5-15 megohms. They can be applied to full 12 mils thickness in 3 hours using conventional spray techniques, cure at room temperature, and maintain erosion resistance, transmission and antistatic properties after outdoor exposure of six months or longer.
3. With the use of the MIL-C-83231 polyurethane coating for rain erosion protection of aircraft systems where the temperature does not exceed 300°F for long periods and the use of the new fluoroelastomer coating for higher temperature radome erosion protection, these two coatings provide a significant capability for aircraft radome subsonic rain erosion resistance.

References

1. G. F. Schmitt, Jr. "Polyurethane Coatings for Subsonic Radome Rain Erosion Protection, Proceedings of the Tenth Symposium of Electromagnetic Windows, 29-31 July 1970, Georgia Institute of Technology, Atlanta, Georgia, pp. 74-79.

2. G. F. Schmitt, Jr. "Erosion Behavior of Polymeric Coatings and Composites at Subsonic Velocities" Proceedings of the Third International Conference on Rain Erosion and Associated Phenomena, 11-13 August 1970, Royal Aircraft Establishment, Farnborough, England, Volume I, pp. 107-146.

3. C. J. Hurley and G. F. Schmitt, Jr. Development and Calibration of a Mach 1.2 Rain Erosion Test Apparatus, AFML-TR-70-240, October 1970.

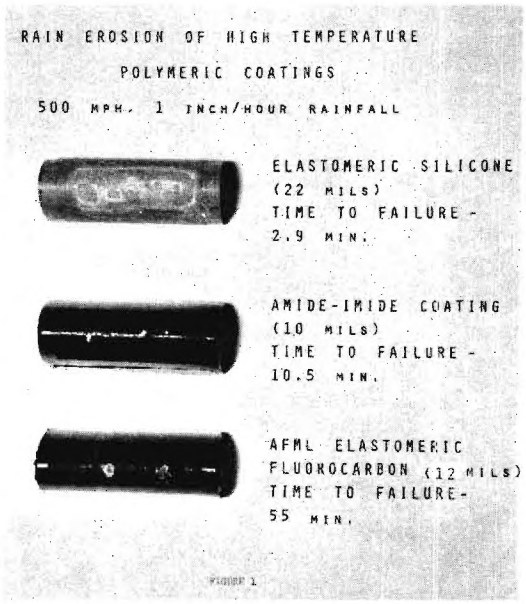

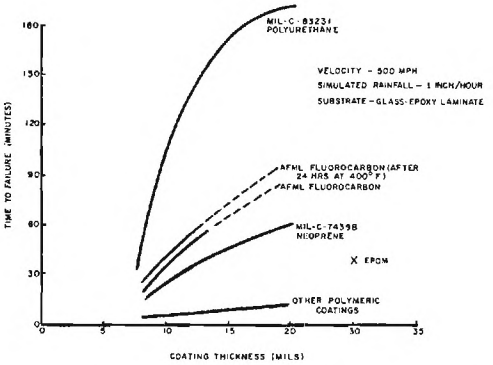

Figure 2. Comparison of Polymeric Coatings Performance In Rotating Arm Apparatus

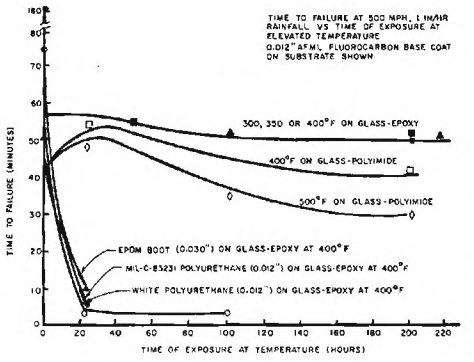

Figure 3. Erosion Resistance as a Function of Thermal Exposure

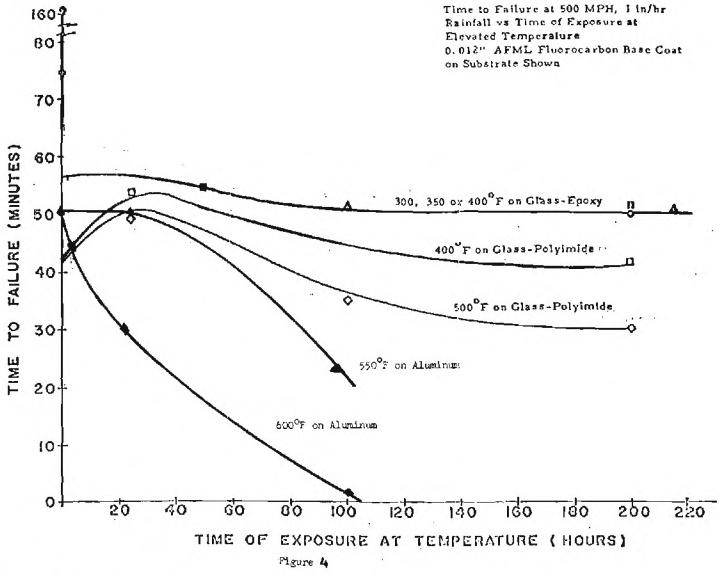

Figure 4

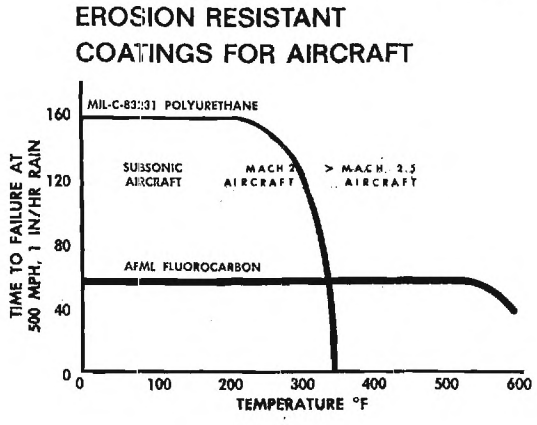

FIGURE 5

MANUFACTURING METHODS FOR HIGH TEMPERATURE REINFORCED PLASTIC AIRCRAFT RADOMES

S.A. Moorefield and P. W. Harruff
Technical Products Division
Brunswick Corporation
Marion, Virginia
24354

ACKNOWLEDGEMENTS

This program is supported by the Air Force Materials Laboratory under the direction of Mr. S. Litvak of the Fabrication Branch (LTF), Manufacturing Technology Division, Contract No. F33615-71-C-1380. The authors wish to express their appreciation also to L. C. Hoots, J. A. Marshall and G. W. Eastridge for their support and contribution to this paper.

ABSTRACT

Characteristics of a new radome materials system are described. Polyimide/quartz fabric skins with a dielectrically matched syntactic foam core form the basis for lightweight radomes. The current state-of-the-art in fabricating panels and scaled-up items is discussed. Plans for manufacturing and testing full-scale aircraft nose radomes are outlined.

INTRODUCTION

As the speed, size and performance capabilities of advanced aircraft increase, the demand for radomes with correspondingly improved structural and environmental resistance capabilities also increases. At the same time, the requirements for high levels of transmission efficiency and improved broadband capabilities must be met.

Within recent years, new high temperature resistant resins such as the polyimides have made it possible to foresee radomes capable of operating for long periods at temperatures up to 600°F. When combined with quartz fiber reinforcements, low dielectric constant and loss composites ($\sim$ 3.2 and 0.005 respectively at 9.375 GHz) are achieved.

It is recognized that the best electrical performance at any given frequency can be achieved with the half-wave radome wall configuration, particularly in the case of streamlined shapes. Solid laminates of the optimum electrical thickness are, however, much heavier than necessary to meet the structural requirements. One approach to reducing the weight is to replace part of the thickness with a low density syntactic foam core, loaded to the same dielectric constant as the laminate material. In this way, a lightweight sandwich construction is achieved which appears electrically as a half-wave wall.

With this concept in mind, Brunswick Corporation developed a high temperature resistant syntactic foam formulation, using conventional

polyimide resins, with filler materials for light weight and for dielectric loading. With this core material and low void polyimide*/quartz fabric skins, a prototype F4J radome was fabricated under a contract to McDonnell Aircraft. Electrical performance of this unit was outstanding[1].

Based upon the demonstrated feasibility of fabricating large lightweight radomes with 600°F capability, a program was funded by the Manufacturing Technology Division, Air Force Materials Laboratory, to establish new or improved manufacturing processes for fabricating large radome structures. The goals of this program are to achieve a high degree of reliability and reproducibility of such configurations, while effecting the maximum reduction of materials and manufacturing costs. Phase I efforts, discussed in this paper, have included the optimization of fabrication processes, fabrication of scale-up items, and evaluation of fabricated parts to verify the adequacy of the materials and processes to meet the structural, environmental and electrical requirements of future radome systems.

PROPERTIES OF MATERIALS

Typical mechanical, physical and electrical properties of sandwich components and the assembled sandwich are shown in Table I, measured at room temperature after sandwich fabrication. Figure 1 depicts a typical radome wall construction designed for X-band. Dielectric constant of the foam core can be adjusted as desired by the addition of more or less filler material.

Of particular interest is the stability of electrical properties at elevated temperatures. Dielectric constant and loss tangent of the quartz/polyimide laminated skins, foam core and miscellaneous materials were measured at temperatures up to 1000°F for the laminate and to 600°F for other components, using the ASTM D-2520 shorted wave guide method. Average results for several runs are shown in Table II.

MANUFACTURING PROCESS: STATE-OF-THE-ART

Although the basic methods for fabricating large radomes with these polyimide-based materials were demonstrated in the F4J radome, this work also showed a need for improved processing techniques. In this current effort, understanding and control of major material and process variables has been established. Specifications have been written to assure that the performance properties can be achieved from each material used in the construction. Process controls have been established, and manufacturing time reduced. Significant advances include:

Fabrication of Large Foam Tiles - Prior to this current program, the maximum size of a sandwich core tile was about one square foot. Severe cracking during cure and postcure of larger sizes was a limiting factor. However, the incorporation of 1/4" long chopped fibers into the mixture, and careful control of drying and curing processes resulted in significant reduction in the frequency and severity of cracks. Currently, tiles

*BPI-373 Polyimide Prepreg, Brunswick Corporation, Marion, Virginia

as large as 16 square feet are common, both in flat or curved configurations, with a high level of confidence that no cracking will occur. Previously, 72 individual tiles were required to form the core of an F4J radome. Today, a much larger radome will use no more than eight tiles. This ability will reduce the manufacturing time and cost substantially.

Maintaining Low Void Content of Skins - The Brunswick-developed polyimide prepreg system, designated BPI-373, can produce a low porosity laminate (< 5%) rarely achieved with other polyimide systems. Lower void content reduces the rate of strength degradation at elevated temperatures, as reported by Askins[2]. In order to achieve a void content level below 5%, however, it is necessary to maintain close control over the prepreg volatiles content and curing conditions. Figure 2 shows the effect of residual volatile materials in the prepreg upon final laminate void content, under one set of curing conditions.

Rain Erosion and Lightning Protection - Integrated into this radome manufacturing development effort is a program to include advanced protective materials and concepts. Application techniques for the latest rain erosion-resistant coating, an Air Force developed fluoroelastomer designated AF-C-934, have been established. This coating has been found to retain excellent erosion-resistant properties on glass-polyimide substrates after 200 hours' exposure at 500°F. In addition, the recently developed "button" type lightning diverter strips[3] are being evaluated for use on these radome wall substrates. Techniques for fabricating the diverter strips are being undertaken by Douglas, the developer of the concept, with polyimide-based laminates as the circuit board carrier material. Prior to this program, only low temperature (epoxy) materials have been used. Other components of the strips, such as the resistance coating and metallic button coating, are being upgraded for 600°F capabilities.

Radome Assembly Processes - Procedures have been established during this program to fabricate the elements of the polyimide foam core sandwich and assemble them into large structures. Of particular significance is the use of conventional tooling and facilities, which maintains the processing costs at a relatively low level for future production consideration.

Figure 3 illustrates the major operations involved to produce a finished radome, less attach hardware. Each step of the manufacturing process is monitored to assure structural and electrical performance. Cured foam core tiles are checked for density, dielectric constant and loss at the primary radome design frequency. Skin samples are checked for density, void content and resin content. Each of the two grinding operations shown in Figure 3 are followed by one-horn interferometer scanning to assure the correct dielectric thickness. Non-destructive test methods such as X-ray, ultrasonic and photochromic coating analysis are being evaluated for use in detecting internal defects which might have an effect upon structural integrity.

Large-Scale Test Articles - Prior to attempting to fabricate full-scale aircraft radomes, several large items have been prepared for evaluation

of the processes developed and the performance of the materials. Shown in Figures 4 and 5 are a sub-scale radome, about 30" long, and a 19" dia. x 32" long cylinder, respectively. In addition, panels of up to 4' x 4' have been fabricated to test one-way power transmission and insertion phase delay, before and after exposure to several environmental conditions in accordance with MIL-E-5272. Following these scans, mechanical properties of test coupons will be determined before and after thermal aging of up to 1000 hours at temperatures of 400°F, 500°F and 600°F. This work is currently in progress.

Future Plans - Assuming that the testing of scale-up items described above indicates no serious problems, these processes and materials will be used to fabricate two full-scale aircraft nose radomes. At this time, plans are to use an ogive configuration of about 92" in length and a fineness ratio of about 2:1, typical of advanced supersonic fighter aircraft nose radomes. These units will be complete with erosion-resistant coating and lightning diverter strips of the "button" type.

Radome testing will be extensive. Electrical testing will include X-band transmission and beam deflection, full radar patterns at X-band and L-band, and X-band and L-band VSWR (power reflection). All of these tests will be conducted on the radome shell with and without lightning strips, before and after environmental/dynamic and lightning tests. The latter tests include vibration, shock, acceleration and altitude (70,000 ft) cycling. Following the lightning tests, to be conducted by Lightning Transients Research Institute (LTRI), one unit will be subjected to static loading at 600°F in combined modes of shear, bending and simulated drag.

CONCLUSIONS

Materials and processes have been established which should prove applicable to large radome structures. With these materials and techniques readily usable by the radome industry, the prospects are good that future supersonic aerospace vehicles will incorporate radomes with the polyimide-based lightweight foam sandwich construction.

REFERENCES

(1) Moorefield, S.A. and Rogers, J.R., "The Development of a Lightweight Advanced Aircraft Radome Based on Dielectric Loaded Foam Core Sandwich Construction", Proceedings of Tenth Symposium on E-M Windows, July 29-31, 1970.

(2) Askins, D.R., "Effect of Environmental Pressure on the Thermal Degradation of Glass Reinforced Plastic Laminates, Part III: Investigation of Low Void Content Polyimide Laminates", Technical Report AFML-TR-68-322, Air Force Materials Laboratory, Wright-Patterson Air Force Base, Ohio (February 1972).

(3) Amason, M.P., and Cassell, G.J., "Radome Lightning Protection Techniques", presented at Symposium on USAF Antenna Research and Development, University of Illinois, 1970.

TABLE I

TYPICAL PROPERTIES OF COMPONENTS OF SYNTACTIC FOAM CORE SANDWICH

PROPERTY[1]	MATERIAL				
	SKINS	CORE[2]	ADHESIVE	EROSION COATING	SANDWICH
DIELECTRIC CONSTANT @ X-BAND	3.2-3.3	3.1	3.1	~3.8	3.1
TAN δ @ X-BAND	.003-.006	.012	.012	.05-.07	.009
DENSITY - GM/CC - LB/FT3	1.7 -	- 18-21	1.7 -	1.9 -	- -
RESIN CONTENT, % WT.	35	-	-	-	-
VOIDS, % VOL.	<5	-	-	-	-
COMPRESSIVE STR., PSI @ R.T.	60,000	>500	-	-	>500
SHEAR STRENGTH, PSI @ R.T.	5,000 (INTERLAM.)	-	2,500 (METAL-METAL LAP)	-	>300 (CORE)
FLEXURAL: STRENGTH, PSI @ R.T. MODULUS, 10^6 PSI @ R.T.	 90,000 2.4	 - -	 - -	 - -	 - -
FLATWISE TENSILE STRENGTH, PSI @ R.T.	-	>600	-	-	-

NOTES: (1) TESTS PER FEDERAL TEST METHOD STANDARDS 401, 406, OR MMM-A-132 AS APPLICABLE

(2) CORE PROPERTIES AFTER BEING BONDED INTO SANDWICH.

TABLE II

TYPICAL DIELECTRIC PROPERTIES OF RADOME WALL COMPONENTS

MATERIAL	TEST TEMP	DIELECTRIC PROPERTIES @ 9.375 GHz	
		DIELECTRIC CONSTANT	LOSS TANGENT
POLYIMIDE/ QUARTZ LAMINATE	R.T. 400°F 500°F 600°F 1000°F	3.29 3.32 3.31 3.25 3.4	.005 .005 .003 .002 <.001
POLYIMIDE SYNTACTIC FOAM CORE	R.T. 400°F 500°F 600°F	3.08 3.10 3.11 3.11	.012 .011 .012 .012
POLYIMIDE ADHESIVE	R.T. 400°F 500 F 600 F	3.12 3.06 3.09 3 13	.014 .008 .008 .011
FLUOROELASTOMER COATING	R.T.	~ 3.8	.05-.07

FIGURE 1

TYPICAL RADOME WALL CONSTRUCTION

FIGURE 2

EFFECT OF PREPREG VOLATILES ON FINAL VOID CONTENT

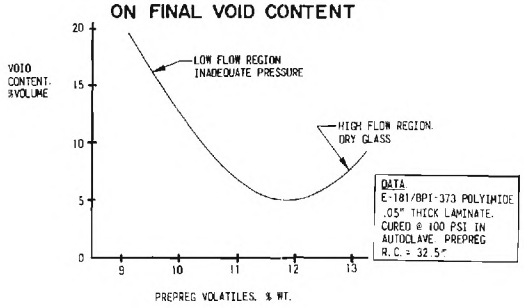

FIGURE 3

RADOME MANUFACTURING SEQUENCE

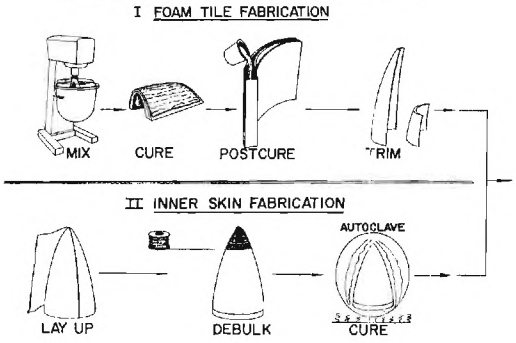

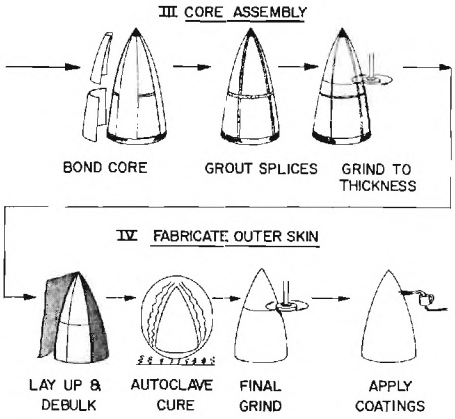

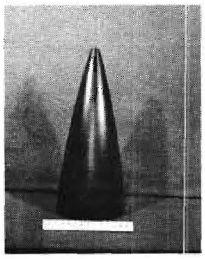

FIGURE 4
POLYIMIDE/QUARTZ SUBSCALE RADOME
WITH POLYIMIDE FOAM CORE

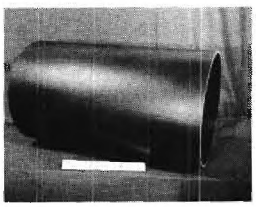

FIGURE 5
19" DIA X 32"L CYLINDER.
POLYIMIDE FOAM SANDWICH CONSTRUCTION

PERTURBATION OF THE ANTENNA-RADOME INTERACTION

by
Abul Maksud Sayied*
Precision & Quality Research Systems
88 Holworthy Street, Cambridge, Mass. 02138

The Antenna-Radome System interact both through volume-type electromagnetic phenomenon present within the radome and surface-type electromagnetic phenomenon present in the form of a guided wave propagating parallel to the inner walls of the radome. In this note we announce an analysis of the antenna-radome interaction and its perturbation due to the introduction of various geometrics of artificial dielectric layers and multilayers on the inner walls of the radome.

The antenna-radome system together with artificial dielectric layers (referred to as ARD System) is a hypercomplex electromagnetic structure whose description using the mathematical machineries of Maxwells equations involve several types of mathematical complexities:

(a) We are involved with mixed type boundary value problems i.e. boundary value problems which are elliptic (and hence require a Dirichlet type boundary condition) on some parts of the boundary and which are hyperbolic (and hence require a Cauchy type boundary condition) on other parts of the boundary.

(b) The geometric boundaries of the various sub-systems of the antenna-radome system together with artificial dielectric layers (or multilayers) are themselves not simple and are comparable or incomparable in size to the electromagnetic wave-length.

(c) The artificial dielectrics have electromagnetic properties which themselves require complex statistical analysis (Analysis of the electromagnetic properties of artificial dielectrics and their technical uses by A. M. Sayied to be published in P & Q Research Systems Reports).

The analytical techniques adopted for the electromagnetic analysis of ARD-System is the introduction of the mathematical motion of the functional dielectric parameter together with a system of equations derived from Maxwells equations and Liouville's equation in strong analogy to those found useful in the discussion of "Many-Body Problem in accelerators due to high beam intensity" by A. M. Sayied Brookhaven National Laboratory. Advanced Accelerator Development Division Report No. AADD-73, July 24, 1964, issued March, 1965, Pages 1 - 33.

---

* On absence at School of Physics and Mathematics,
University of Science of Malaysia,
Penang, Malaysia.

THE PLANE WAVE SPECTRUM-SURFACE INTEGRATION TECHNIQUE FOR RADOME BORESIGHT ANALYSIS *

R.C. Rudduck and D.C.F. Wu **
ElectroScience Laboratory
Department of Electrical Engineering
The Ohio State University
Columbus, Ohio 43212
9 June 1972

**Now at Amecon Div., Litton Systems, Inc.,
College Park, Md.

I. INTRODUCTION

Accurate prediction of radome boresight error has proven difficult even after years of effort by many researchers. Achievement of small boresight error at all look angles is a major design goal of an antenna-radome system. The boresight error of a well-designed system will be less than a few tenths of a degree. The purpose of this paper is to report an accurate boresight analysis for practical three-dimensional antenna-radome systems.

The basic approach of the radome analysis is the same as that of Paris[1] in that the antenna near fields are accurately analyzed in a point-by-point calculation of the fields transmitted through the entire radome surface. However, the analysis of practical three-dimensional antenna-radome combinations has been impractical for medium and large antennas, i.e., on the order of $75\lambda^2$ or larger. The principal difficulty encountered is the excessive computation time required for the large number of antenna near field calculations. The key feature of the approach taken by the authors is the use of the Plane Wave Spectrum (PWS) formulation for calculation of the antenna near fields[2]. The PWS formulation provides much improved efficiency over conventional near field analyses and makes possible calculation of radome boresight for large antennas.

II. ANTENNA NEAR FIELD CALCULATIONS

The plane wave spectrum formulation is based on the Fourier transform of the aperture field[3,4]. The near field of a circularly symmetric aperture can be represented in terms of a spectrum $F(k_\rho)$ of one variable as

*The work reported in this paper was supported in part by Contract N00019-70-C-0252 between Department of the Navy, Naval Air Systems Command, Washington, D.C. and The Ohio State University Research Foundation.

$$(1) \qquad E_y(\rho,\phi,z) = \frac{1}{2\pi} \int_0^\infty F(k_\rho)\, J_0(k_\rho \rho)\, e^{-jk_z z}\, k_\rho\, dk_\rho$$

$$(2) \qquad E_z(\rho,\phi,z) = \frac{j \sin\phi}{2\pi} \int_0^\infty F(k_\rho)\, J_1(k_\rho \rho)\, e^{-jk_z z}\, \frac{k_\rho^2}{k_z}\, dk_\rho$$

where (ρ,ϕ,z) are the cylindrical coordinates of the near field point, and k_ρ and k_z are the spectral wavenumbers with respect to the ρ and z coordinates, respectively. The circular symmetry property was used to great advantage by Bailey and Swift [5] in the analysis of the aperture admittance of circular waveguides. The spectrum of the uniform circular aperture corresponds to the well-known radiation pattern result

$$(3) \qquad F(k_\rho) = 2\pi a \frac{J_1(k_\rho a)}{k_\rho}$$

where a is the aperture radius.

The PWS formulation for antenna near field calculations is about 5 times more efficient than conventional aperture integration techniques for a 10λ diameter antenna; and is increasingly more advantageous for larger apertures[6].

Some typical near field distributions are shown in Figs. 2 through 4 for the 10λ diameter uniform circular aperture used in the radome boresight calculations discussed below. Both phase and magnitude distributions of the y-component of the electric field are compared on plane surfaces spaced 2λ, 10λ and 20λ from the aperture antenna. As seen in Fig. 2 the fields at 2λ away from a circular aperture antenna are almost the same as a two-dimensional strip antenna. However, the finiteness of the circular aperture antenna becomes apparent as the distance away from the aperture is increased. Thus it is seen from Figs. 3 and 4 that the main lobe of the circular aperture antenna is shaping up faster than that of the two-dimensional strip antenna as the distance from the aperture antennas increases.

III. RADOME ANALYSIS

The basic approach for analysis of the three-dimensional antenna-radome combination can be divided into the following steps:

1. The near fields of the antenna which are incident upon the radome are calculated.

2. The transmission through the radome is calculated.

3. The radome boresight is determined from the beam maximum of the distorted antenna pattern which is calculated from the transmitted field.

A brief explanation of each step is given below.

The radome analysis and computer program were developed for cylindrically symmetric radomes defined in terms of ogival sections. For a given look angle and gimbal location, each computation point on the radome surface is related to the antenna coordinates through a coordinate transformation to obtain the incident field on the radome at each point.

The transmission through the radome wall is analyzed by using the approximation of a local plane wave incident on a plane sheet. The incident Poynting vector is calculated from the knowledge of both the electric and magnetic near fields of the antenna. This gives the angle of incidence at each point and permits the incident wave to be resolved into the usual components perpendicular and parallel to the plane of incidence. The electric and magnetic field components tangential to the radome surface are then calculated using the plane wave transmission coefficients for perpendicular and parallel polarizations.

The third step in the analysis consists of performing an integration over the radome surface to determine the distortion of the radiation pattern. In the computer program that was developed only the distortion of the main beam and thus the boresight error are calculated. The analysis can readily be extended to calculate antenna sidelobes. The boresight error is evaluated in this analysis from the deviation of the radiated beam maximum.

Boresight error calculations using the three-dimensional Plane Wave Spectrum - Surface Integration (PWS-SI) analysis have been obtained for two ogive radomes with half-wavelength wall design and with fineness ratios 1:1 and 2:1 are shown in Figs. 5 and 6, respectively. The corresponding measured boresight error data shown in the figures were supplied by the U.S. Naval Air Development Center at Johnsville, Pennsylvania. It is noted from Fig. 5 that there is essentially no boresight error in the nose-on region for the radome with fineness ratio 1:1. However the boresight error for the radome with 2:1 fineness ratio peaks up at look angles around 10 to 15 degrees. Considering that some experimental error may be present in the measured results, it is concluded that the PWS-SI method is a powerful technique in analyzing three-dimensional antenna-radome combinations.

IV. CONCLUSIONS

The research presented here offers a practical method for determining boresight errors in an antenna-radome system. The Plane Wave Spectrum-Surface Integration (PWS-SI) analysis contains the diffraction mechanisms necessary to accurately treat practical antenna-radome problems. The Plane Wave Spectrum analysis offers accurate and efficient methods for calculating

near-fields of large aperture antennas. Good agreement between theory and measured boresight data is obtained.

In the recent developments of antenna-radome systems, considerable attention is being given to the prediction of antenna sidelobes and backlobes. As an extension of this research, steps may be included in the PWS-SI technique to calculate the influence of the radome on sidelobe and backlobe levels for practical three-dimensional antenna-radome combinations. Useful applications include radome systems in the R and D stage as well as operational radomes with boresight or other deficiencies.

REFERENCES

1. Paris, D.T. [1970 IEEE Trans. AP-18, p. 7].

2. Wu, D.C.F. and Rudduck, R.C. [1970 Proc. Sympos. E.M. Windows, Geo. Tech., July 29].

3. Booker and Clemmow [1950 JIEE (London), 97, p. 11].

4. Brown, J. [1958 JIEE (London), 105, Part C, p. 343].

5. Bailey and Swift [1968 IEEE Trans. AP-16, p. 386].

6. Wu, D.C.F. and Rudduck, R.C. [1971 Report 2969-4, Ohio State University Research Foundation].

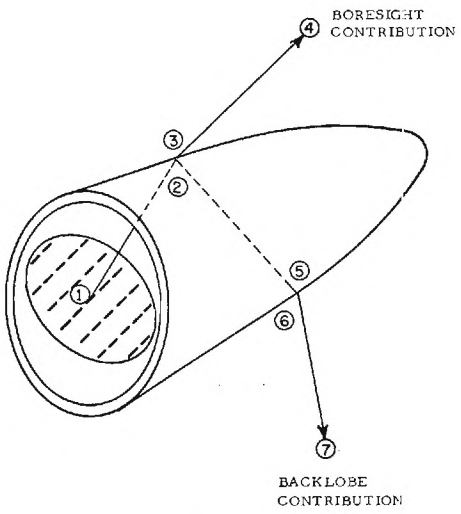

FIG. 1. 3-D ANTENNA-RADOME SYSTEM.

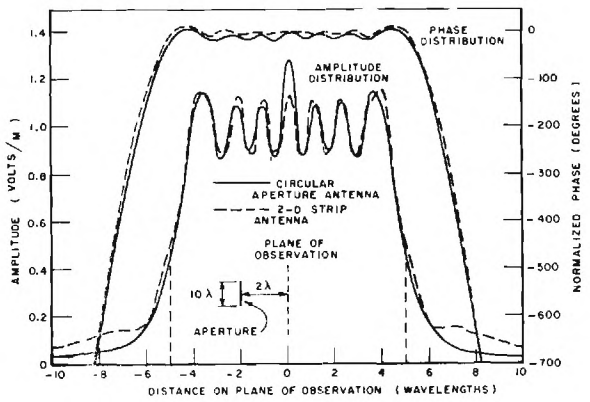

FIG. 2. NEAR FIELD AT 2λ FROM A UNIFORM CIRCULAR APERTURE OF 10λ DIAMETER.

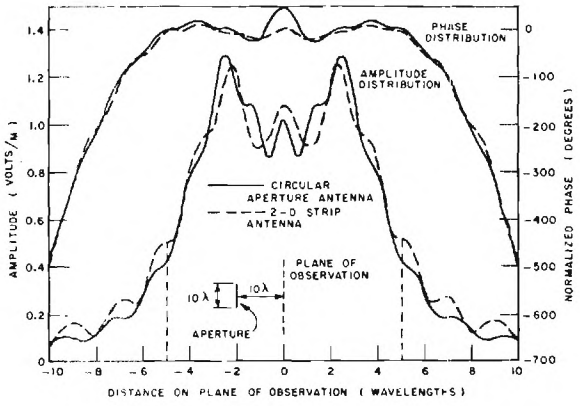

FIG. 3. NEAR FIELD AT 10λ FROM A UNIFORM CIRCULAR APERTURE OF 10λ DIAMETER.

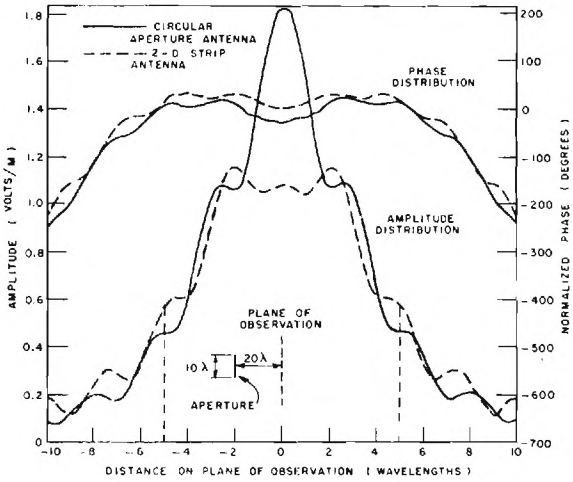

FIG. 4. NEAR FIELD AT 20λ FROM A UNIFORM CIRCULAR APERTURE OF 10λ DIAMETER.

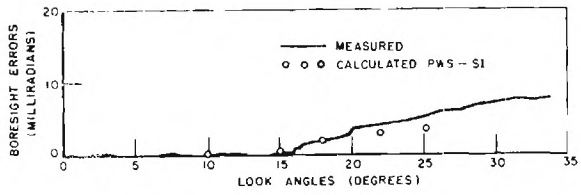

FIG. 5. BORESIGHT ERROR FOR AN OGIVE RADOME WITH 1:1 FINENESS RATIO. PERPENDICULAR POLARIZATION.

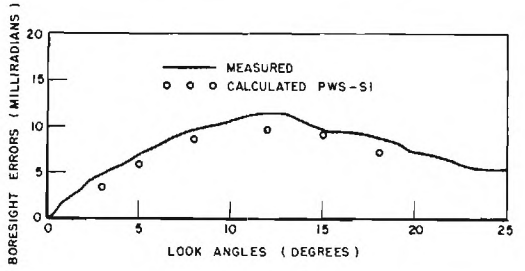

FIG. 6. BORESIGHT ERROR FOR AN OGIVE RADOME WITH 2:1 FINENESS RATIO. PERPENDICULAR POLARIZATION.

BANDPASS CONICAL RADOME

C. C. Chen

Hughes Aircraft Company
Ground Systems Group
Fullerton, California 92634

In conventional airborne radar systems, the antenna is located in the nose fuselage of the aircraft or missile. The antenna and the bulkhead on which it is mounted can present large radar cross sections to hostile radars over a wide frequency range when viewed from certain angles. By using a bandpass radome or cover, it is possible to reduce significantly the RCS of the antenna and bulkhead while still allowing the antenna system to operate properly within its prescribed frequency ranges. Recent advances in the capability of computing the transmission and reflection coefficient from a flat conducting sheet perforated with various shapes of apertures [1-3] make it possible to design a bandpass structure which satisfies the above requirements.

The calculated and measured transmission losses for a thin slotted brass sheet with a dielectric backing are shown in Figure 1 for three different angles of incidence. There is very close agreement between the computed and experimental results. This flat panel computation has been used to approximate the design of a conical radome. Figure 2 shows an X-band conical radome which has a 41.8 degree half cone angle, and a 30-inch base diameter. The wall of the radome is constructed from a perforated thin, conductive sheet backed by a .018 inch thick fiberglass with dielectric constant of 4; four different sizes of rectangular slots on the conical surface were designed according to their respective looking angle in each sector of the cone. The slots are uniformly spaced on the conical surface and they are so oriented to pass a linearly polarized wave. This conical radome was attached to a 30-inch dish, conical-scan fire control antenna to test the transmittivity of the radome. The E and H-plane radiation patterns of the dish with and without the radome are shown in Figure 3. Within the designed passband, the dish patterns with radome show negligible loss in gain and the first sidelobe is about 2 dB higher than the pattern without the radome. However, all sidelobes are still more than 24 dB below the peak in the H-plane and 22 dB in the E-plane. Off the designed passband the slotted radome is detuned from resonance and behaves like a conducting cone. In this experiment, it is observed that: first, the curved surface near the vertex of this cone causes little gain degradation. Second, there is little edge effect of the radome since the base edge of this cone was attached to the rim of the dish. Third, at frequency, slightly off the passband, the radome forms a cavity, therefore, the gain of the antenna becomes oscillatory with the change of frequency.

The reflectivity and transmissibility of a perforated plate depends on the polarization and the angle of incidence. In order to reduce the polarization sensitivity, a sandwiched conducting screen perforated with circular holes arranged in a hexagonal lattice was chosen. The calculated transmission loss

and insertion phase delay for an infinite flat plate as a function of incident angle are presented in Figure 4. The maximum transmission loss is less than .6 dB and insertion phase delay less than 35 degrees for both polarizations within a 60 degree incidence from normal to the plate. At a few percent lower frequency, transmissibility of this plate is improved for a perpendicularly polarized incidence, and deteriorated for a parallely polarized incidence. Shifts of resonant frequency and changes of bandwidth in the opposite sense for the two orthogonal polarizations as a function of incident angle limit many useful applications of this perforate plate. Other structures such as multi-layer panel and center-loaded slots are under investigation.

References

1. C. C. Chen, "Transmission through a conducting screen perforated periodically with apertures," IEEE Transactions on Microwave Theory and Techniques, Vol. MTT-18, No. 9, September 1970.

2. C. C. Chen, "Diffraction of electromagnetic waves by a conducting screen perforated periodically with circular holes," IEEE Transactions on Microwave Theory and Techniques, Vol. MTT-19, No. 5, May 1971.

3. B. A. Munk, R. G. Kouyoumjian, and L. Peters, Jr., "Reflection properties of periodic surfaces of loaded dipoles," IEEE Transactions on Antennas and Propagation, Vol. AP-19, No. 5, September 1971.

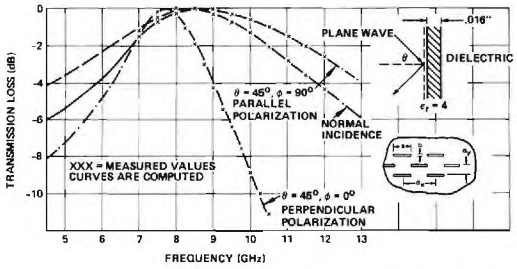

Figure 1. Comparison of Measured and Computed Transmission Losses ($a = 2/3\ d_x$, $b = 1/10\ d_x$, $d_x = .9375"$, $d_y = 1/3\ d_x$).

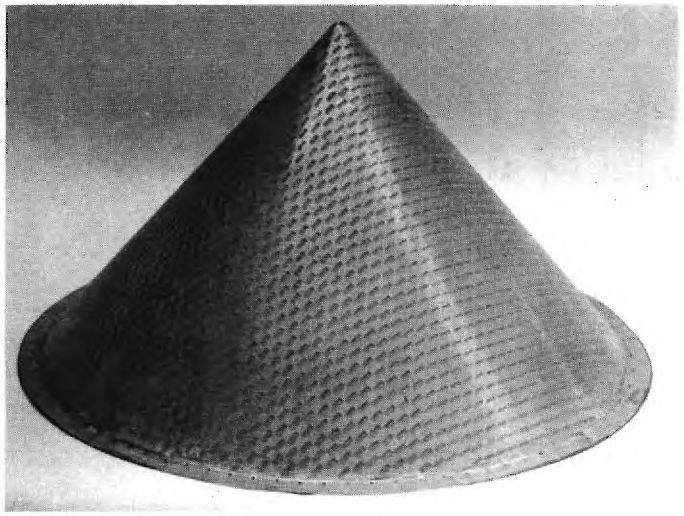

Figure 2. Bandpass Conical Radome.

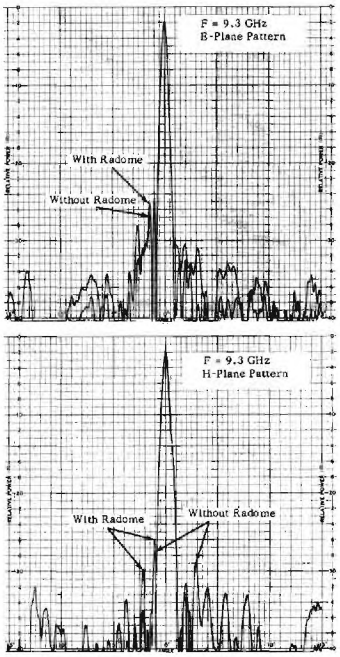

Figure 3. Radiation Patterns in E and H Plane with and without Bandpass Radome.

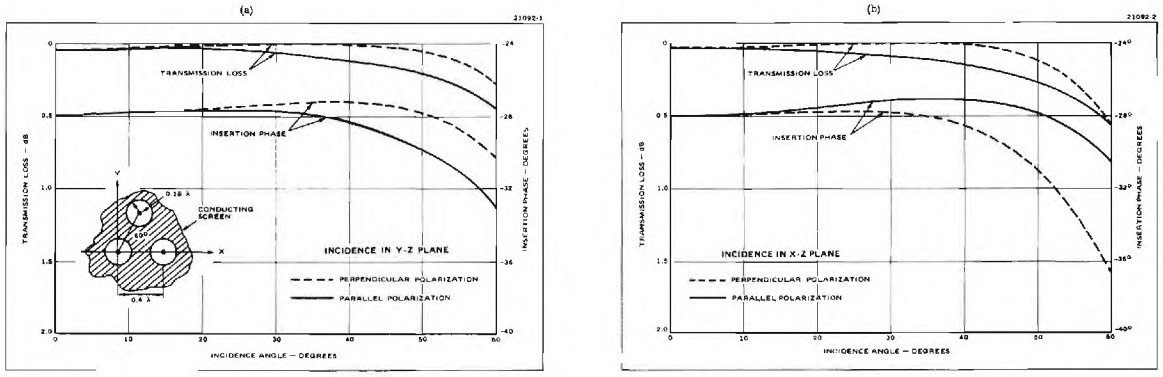

Figure 4. Transmission Loss and Insertion Phase Delay of a Flat Perforated Screen Sandwiched between Two Dielectric Sheets of $\epsilon_r = 4$, 0.043λ Thick.

SOME EXPERIMENTAL RESULTS OF DIELECTRIC AND METALLIC LOADING OF RADOMES

R H J CARY ROYAL RADAR ESTABLISHMENT MALVERN UK

1 REACTIVE LOADING OF A HELICOPTER BLADE ANTENNA-RADOME

Long microwave antennas have been included in the front and trailing edges of helicopter blades to give narrow azimuthal beams scanned by the rotation of the blades. Various vertical beamwidths typically 35^{o} to 80^{o} have been employed. Ref. 1. A particular requirement arose which required optimising gain of such an antenna by limiting the vertical pattern. The front edge was not preferred structurally, nor from erosion damage, nor from having space to optimise gain. The rear blade was offered with the possibility of replacing the outer metallic surface by a dielectric resin-glass fibre laminate of near 0.95 mm thickness, and the internal supporting metallic honeycomb to be replaced by preferably, a dielectric honeycomb or possibly a lightweight foam material. The antenna source, which was expected to be some waveguide linear array system was to be located (Fig. 1a) preferably as near the centre of gravity as possible.

1.1 Choice of Internal Structure: The waveguide linear array source divorced from the helicopter blade would have a wide vertical beam. An arrangement as in Fig. 1(a) with an X(I) band source, within the internal structure of dielectric honeycomb permittivity near 1.06 and without the external skins, gave some beaming in the vertical plane. Higher permittivities, using expanded foams, of 1.2 and 1.3 gave considerably more beaming and the choice of beamwidth to suit the application, Fig. 1(b). At K_u (J) band the honeycomb gave more beaming and again higher permittivity foams gave narrower beams.

The foam material, though lightweight, still added considerable weight overall, due to the long length of the antenna, and the additional weights required to balance the blade individually and further weights to balance the blades as a group.

The use of an artificial dielectric in the form of dielectric thin sheets on which were imprinted metallic shapes, were employed in various sizes and distances to give the required permittivity at the particular waveband, and to replace the foam material. Ref. 2. The artificial dielectric sheets formed an integral part of the lightweight dielectric honeycomb support structure and in consequence added negligible weight to the blade. An example of the permittivity and loss tangent of this form of artificial dielectric is shown in Fig. 1(c). Spaced crosses were found to have less loss than discs, and were suitable for both polarisations.

1.2 Matching the Outer Skins: The external 0.95 mm skins of permittivity 4, require matching from the internal material to that of air. Due to the high angles of incidence (84^{o}), without matching resulted in severe distortion of the beam and losses.

For matching perpendicular polarisation inductances may be used, which may take the form of a grid of parallel wires parallel to the E vector. With the source in Fig. 1(a) with E vector horizontal, an X(I) band design for instance, where the internal structure permittivity was 1.3, required 0.05 mm diameter wires spaced 10 mm apart, placed inside the laminate 0.5 mm from the outer surface, and lying longitudinally along the blade.

For parallel polarisation capacitive matching of the skins is required. An example at X(I) Band with the E vector vertical, an inner structure of permittivity 1.3, the match consisted of capacitive metallic crosses giving the necessary shunting susceptance placed 0.5 mm from the outer surface of the skin.

For circular polarisation inductive wires used to match the perpendicular polarised component have to be adjusted to also neutralise the effect of the necessary capacities used to match the parallel polarised component. The wires being orthogonal to the E vector do not affect the parallel polarisation. While this method of combining matching ensured good transmission, the phase of the different components was such as to tend to mar its circularity. This was corrected by generating a somewhat elliptical polarisation such that it was converted to circular through the radome.

1.3 Beam Shift in the Vertical Plane: The rotor blades as they rotate change often their attitude with respect to the horizontal. Where the angle change is large, to maintain the relatively narrow vertical beam pointing at the desired vertical angle it may be necessary to incorporate a double source into which by switching power or controlling phase from one source to the other, the beam can be maintained at a particular horizontal angle in the vertical plane.

1.4 Conclusion: This type of antenna-radome construction employing an artificial dielectric in the skin support structure, and matching of the outer skins can give a narrow beam in the vertical plane with increased gain, with minimum weight added and may be applicable not only to helicopter blade antennas but also to rotodome constructions.

2 REACTIVE LOADING OF A WIDEBAND CIRCULAR POLARISED AIRCRAFT RADOME

A circular polarised antenna system covering nearly a 4:1 frequency range at microwavelengths required to be housed in a radome whose shape was such that the angles of incidence were mainly less than 72^{o}.

Because of the narrow band properties of the solid type radome, an A sandwich construction was considered, with skins, permittivity of 4.2 and thickness 0.11 mm, and a foam core permittivity 1.2, whose thickness was varied for optimum transmission and minimum ellipticity. Matching the skins individually with lumped inductances in their centre is known to improve their wideband performance. A grid of wires as a lumped inductance in the centre of the core was found to give even better matching and closer Insertion Phase Difference between perpendicular and parallel polarisation, and improved circularity and the advantage of only one layer of lumped susceptance.

Values of circular polarised transmission efficiency at different frequencies and angles of incidence are shown in the following Table 1 for skins of permittivity 4.2 and core 1.2 without any inductive matching. A considerable improvement was obtained by using resin-quartz cloth with a skin permittivity of 3.2 without inductive matching as shown in the table, and a further improvement of transmission by including inductive matching in the core is shown, with the resultant ellipticity.

TABLE 1 % TRANSMISSION & ELLIPTICITY AT ANGLES OF INCIDENCE

SKIN ε	CORE ε	ANGLE OF INCIDENCE	INDUCTIVE MATCHING WIRES	% TRANSMISSION & ELLIPTICITY							
				f_1		$2f_1$		$3f_1$		$4f_1$	
				%	E	%	E	%	E	%	E
4.2	1.2	70°	-	66	1.6	68	1.42	62	1.68	58	2
3.2	1.2		-	73	1.45	72	1.4	80	1.52	72	1.88
3.2	1.2		YES	94	1.42	76	1.2	86	1.37	80	1.5
4.2	1.2		-	75	1.36	86	1.32	63	1.56	55	2
3.2	1.2	60°	-	83	1.3	90	1.25	80	1.3	74	1.8
3.2	1.2		YES	95	1.3	92	1.1	86	1.16	81	1.4
4.2	1.2		-	86	1.3	86	1.15	75	1.3	58	1.8
3.2	1.2	30°	-	88	1.15	92	1.13	78	1.25	70	1.5
3.2	1.2		YES	90	1.15	93	1.1	82	1.2	72	1.4

TABLE 2 RADOME % TRANSMISSION & ELLIPTICITY

3.2	1.2	UP TO 72°	YES	92	1.2	85	1.15	84	1.2	77	1.4

The inclusion of the inductive matching on the radome could take the form of circumferencial thin wire rings laid in the centre of the core medium, each ring spaced to give the necessary loading at that point on the radome. This arrangement was found satisfactory as the wires are mainly parallel to the E vector for perpendicular polarisation and gave the necessary matching. Transmission of parallel polarisation through the A sandwich of the given dimensions did not require inductive matching and the wires being perpendicular to the E vector in this case did not interfere with its performance.

The values of the matching inductances were such that they could be obtained by a wire of near 0.05 mm dia., variably spaced near 15 mm. This was found to give the improved transmission and ellipticity, but due to the spacing and the angles of incidence resulted in diffraction lobes being produced and resultant losses in the main beam, when this occurred. The spacing could be reduced such that diffraction lobes were not produced, by making the wires thinner. An impractical diameter of near 0.002 mm was required to give typically the necessary inductance. The problem was solved by coiling 0.05 mm dia. wire on a thin walled 0.84 mm dia. dielectric tube, and the required inductance was obtained by varying the number of turns, typically one per mm. Fig. 2.

The radome was constructed on a male mould on which was built the inside skin and then the foam core. Grooves were machined round the radome from nose towards the base at the necessary non-diffracting spacing, to a depth such that the coiled wires on their formers were set in the middle of the foamed core. The grooves were then sealed with a low permittivity filler and the outer skin and finally the rain erosion coating applied. The result of the measurement on the radome in Table 2 indicated over the frequency band and scan angles, that the power transmission was not less than 77%, and the ellipticity (V.E.R.) was less than 1.2 over most of the band.

3 A DIELECTRIC LOADED MULTI-BAND RADOME

Design solutions to an X(I), K_u (J) multi-band, not harmonically related radome may be obtained by choosing the permittivity of the centre section of a radome to suit the ratio of the frequency bands. Ref. 3. As an example, for a ratio of X(I) to K_u (J) band of say, 1.89, a solution can be found by making the radome as a B sandwich, the external layers having a permittivity of 4 and the centre of 5.4. See Fig. 3 where maximum transmission for perpendicular polarisation at various angles of incidence is plotted against skin and core thickness to wavelength, from which the necessary thickness of skin and core can be determined.

The permittivity of 4 was obtained by conventional resin glass-fibre construction and the radome centre loaded to give 5.4. Models with titanium dioxide and lightweight artificial dielectric loading were experimented with, to the shape requirements of an advanced aircraft. Comparison of the theoretical and practical transmission loss, ellipticity and aberration at X and K_u band for circular polarisation at various scan angles and frequencies showed close agreement as shown typically in Fig. 3(a), (b), (c). A compromise in design in thickness was necessary as the practical best conditions of transmission, ellipticity and aberration did not coincide as shown typically in Fig. 3(d) for frequencies at X Band.

4 REFERENCES

1 Bell Helicopter Company, "Helicopter Rotor Blade Radar Antenna", Report No. 299-099-285.

2 Cary R H J, "Loaded Dielectric Materials for Radomes", Second International Conference on Electromagnetic Windows, Paris, September 1971.

3 Cary R H J, "Design of Multi-band Radomes", IEE Conference, Publication No. 77 "Aerospace Antennas", June 1971.

Contributed by permission of Director RRE Copyright Controller H.B.M.S.O.

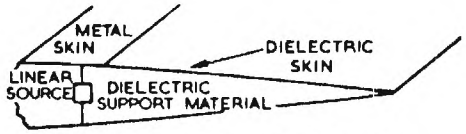

REAR SECTION OF BLADE FIG. 1(a)

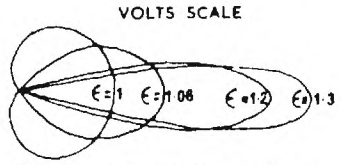

VERTICAL PATTERNS WITH DIFFERENT PERMITTIVITY SUPPORT MATERIAL FIG 1(b)

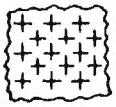

LAYERS OF METALLIC CROSSES
LAYER SPACING 7mm
CROSS SIZE 4mm
CROSS SPACING 7mm
ε = 1·3 TAN δ 0·003 (X BAND)

ARTIFICIAL DIELECTRIC FIG. 1(c)

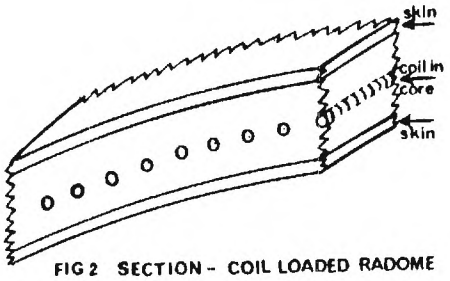

FIG 2 SECTION - COIL LOADED RADOME

ANGLE OF SCAN IN AZIMUTH PLANE (10° ELEVATION)

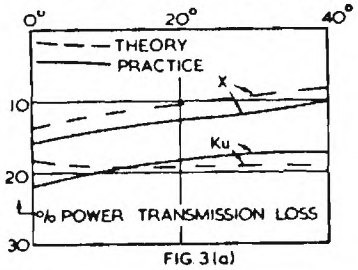

FIG 3(a)

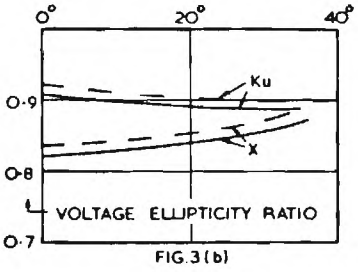

FIG. 3(b)

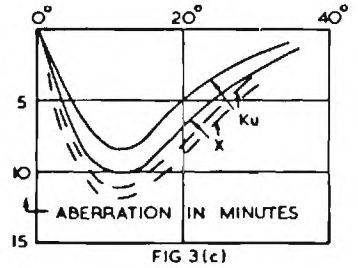

FIG 3(c)

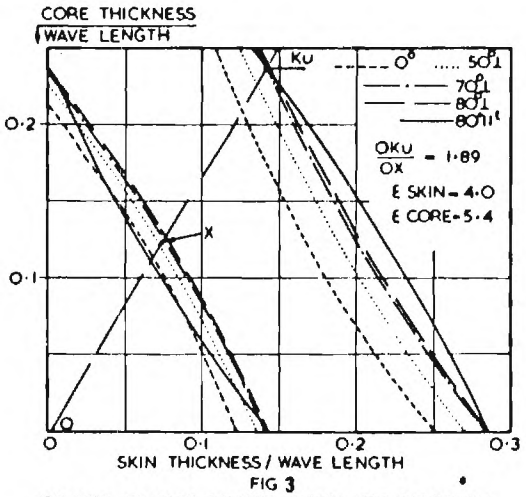

FIG 3

CURVES OF MAX. TRANSMISSION FOR SANDWICH RADOME

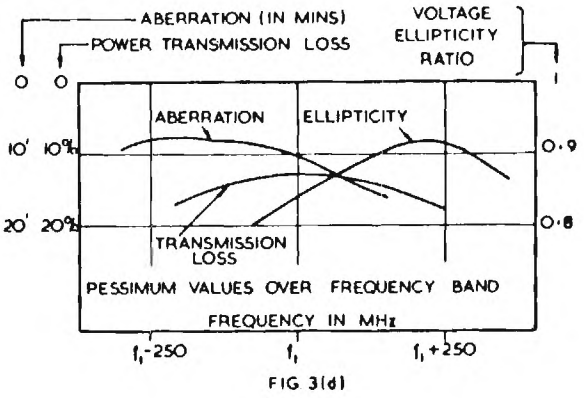

FIG. 3(d)

FIG. 3(a) (b) (c) (d)

CHARACTERISTICS OF AN X – Ku BAND RADOME

PERFORATED METALLIC RADOMES

T. E. Fiscus and G. Tricoles

(General Dynamics Electro Dynamic Division, San Diego, Calif. 92112)

Radomes are usually dielectric objects, but perforated metallic layers are being developed for inclusion in or addition to radomes. There are several reasons for including metal. Dielectric radomes lose strength at elevated temperatures of supersonic flight. A combination of metal and dielectric may be lighter than a halfwave, all-dielectric radome. The bandwidth of a radome with metal can be made narrow with the possibility of reducing the radar cross section of the antenna-radome region. Metal layers outside a radome may provide protection against lightning and hail.

Methods for designing radomes with perforated metallic layers are very well developed in some respects but not in others. Very accurate theoretical descriptions and numerical techniques have been developed, but only for flat structures.* Moreover, this analysis is for periodic structures. No theory has apparently been developed for curved structures such as cones, ogives, or hemispheres. The approach is usually experimental; however, the radomes that have been developed so far are blunt, such as a hemisphere, or if they are pointed, incidence angles are relatively low, approximately 50°. In addition, experimental evaluations have been limited; antennas have been large in terms of wavelengths; the aspect and polarization dependence of observed quantities has been restricted. The boresight error properties of curved radomes have apparently not been evaluated.

The most practical approach to designing perforated radomes seems to be to consider the radome as locally flat. This approach is widely used to design dielectric radomes. However for a perforated radome, curvature may change the interactions of adjacent apertures.

A perforated radome will probably be periodic so it may have grating lobes. To prevent grating lobes, aperture spacings could be reduced, but in a finite lattice of apertures the spacing criterion depends on the number of apertures. For a radome, the spacing criterion may depend on the curvature.

This paper describes an experimental study of the effects of curvature on the performance of dielectric-coated, perforated metallic radomes. Initially, flat structures were fabricated, and their complex-value transmittances were measured.

---

* C.C. Chen, Digest IEEE/G-AP Symposium 1971, p. 153 (IEEE Cat. No. 71C 39ap)

The results agreed well with those computed by Chen. Both square and hexagonal lattices were considered.

To test curvature in one plane, a hemi-cylindrical radome was fabricated. The lattice was square with columns of apertures parallel to the axes of the cone and rows on diameters. Transmittance was measured with a small probe antenna moved in the radome-bounded region with a very-nearly plane wave incident outside. The results were compared with those for the flat structure before it was formed into the cylinder. We first defined an incidence angle for each probe position by considering the ray through the probe. When the probe was at the center of the cylinder the incidence angle was zero. As the probe neared the cylinder, the incidence angles increased to approximately 67°. For low incidence angles, less than 50° to 55°, the probing measurements agreed with the flat sheet data. However, for high incidence angles the discrepancies were as much a 1 dB. Measurements with a large antenna would have averaged these variations over the aperture. The discrepancies also would not be observed with an antenna that was large but only 3/4 the size of the cylinder. The measurements can be interpreted as showning a defect in a design theory that uses a single ray and that treats the radome as locally flat. However, the measurements do not necessarily imply that flat sheet theory is inadequate because a prediction based on a surface integration may be accurate. In either case, the data to show that curvature is a factor.

The transmittance of the panel with the square lattice depended on its orientation within its plane; therefore a panel with a hexagonal lattice was fabricated. Its transmittance was relatively independent of orientation and direction of wave polarization.

Several conical radomes were fabricated with hexagonal lattices of perforations. The first was a cone with 30° half angle. It was formed by rolling a flat metallic sheet into a cone. The transmittance averaged approximately -1 dB over gimbal angles. Minimum values depended on wave polarization relative to the seams; -2 dB was obtained when the electric field was parallel to the seams; -1.5 dB was obtained for the orthogonal polarization.

Additional conical radomes were fabricated; these had 20° half angles. These radomes were fabricated by first forming a dielectric cone, attaching circular, masking tape discs, and spraying with metal paint. A final dielectric layer was then added. This procedure gave uniform radomes. The radomes were fabricated with two shapes. One was a truncated cone with length 12.6 in. The other was identical except for a hemispherical region at the tip; radius was 1 in.

Antenna patterns were measured for two horn antennas. One antenna was small; its aperture was 1 1/2 in. × 2 in. The other was larger; its aperture was 5 in. × 6 in. Frequency was 14.5 GHz. E and H plane patterns of the larger

antenna are shown in Figure 1 with and without a conical radome. Figure 2 shows patterns for the small antenna. For zero gimbal angle the aperture plane of the smaller antenna was 1 7/8 in. forward of the radome base; the larger antenna was 7/8 in. forward.

Figure 1 shows that a conical, perforated metallic radome can give high transmittance and little sidelobe level increase. Figure 2 shows, on comparison with Figure 1, that the results depend on antenna size.

Power transmittance was measured with the smaller (1 1/2 in. × 2 in.) aperture while the radome was gimballed. Figure 3 shows the transmittance of the conical, 20° half-angle radome. The minimum transmittance for horizontal polarization is 1/4 dB higher than the value for vertical polarization. The transmittance of the radome with the rounded tip is shown in Figure 4. The minimum value was increased to -1.8 dB by adding dielectric tape to the rounded portion. Here we have another effect of curvature. It may be possible to further increase transmittance by further modifying the dielectric on the tip; however, a change in the lattice pattern may be necessary. One reason for the relatively low transmittance of the rounded-tip radome is a phase error caused by incidence angle variations. The added dielectric reduces this phase error.

The field near a conical radome was probed to explain the source of the transmittance minima. Equal intensity contours were plotted. The data can be interpreted as a set of Moire patterns that represent interference between a field radiated by the antenna directly through the radome and a second field that has properties of a reflected field. The field is being further investigated to determine the mechanism; the possibility of a reflected grating lobe is being investigated; so far the data discourage this interpretation. Figure 5 shows wavefronts for the field scattered by the radome; construction from a Moire diagram. The arrows show rays normal to the wavefronts.

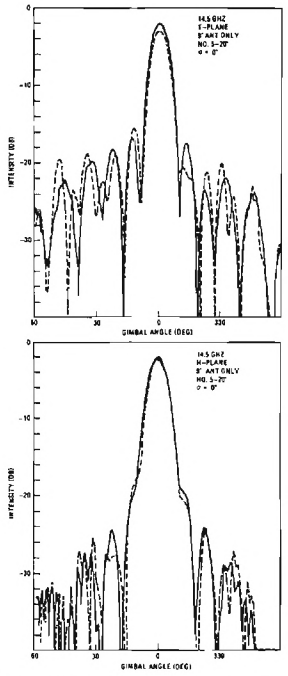

Figure 1. Patterns of 5 × 6 in. Aperture Horn Antenna With and Without Conical 20° Radome

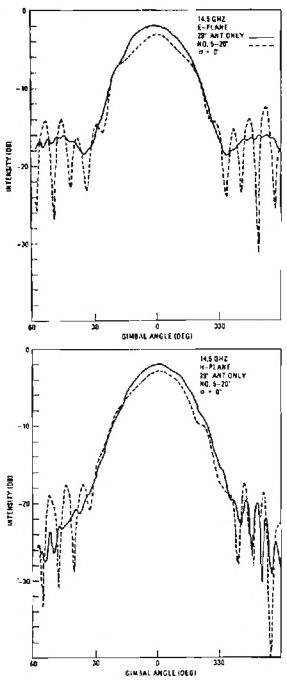

Figure 2. Patterns of 1.5 × 2 in. Aperture Horn Antenna With and Without Conical 20° Radome

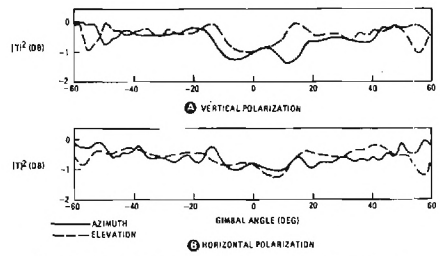

Figure 3. Power Transmittance of Conical Perforated Radome. Frequency 14.5 GHz

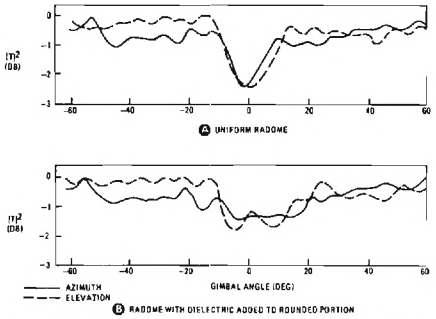

Figure 4. Power Transmittance of Perforated Radome with Rounded Tip; Frequency 14.5 GHz

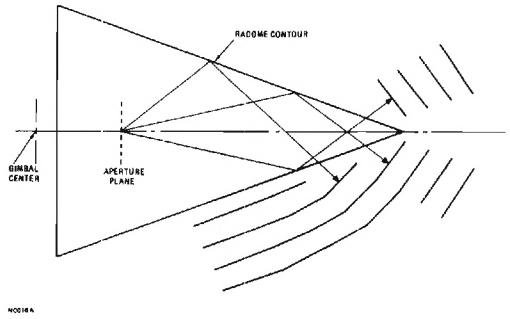

Figure 5. Wavefronts for the Field Scattered by the Radome; Construction from a Moire diagram. The arrows show rays normal to the wavefronts.

CHARACTERIZATION OF MATERIALS FOR HIGH POWER IR LASER WINDOWS

D. F. Stevison, C. L. Strecker, W. J. Ekman
Air Force Materials Laboratory, WPAFB
and
J. R. Schneider
University of Dayton Research Institute

The recent development of high power lasers, especially the electrical and gas dynamic lasers, has created the need for optical components which are capable of withstanding high power levels and power densities. One of the critical problems is to provide a physical barrier or window, transparent to infrared radiation (10.6μm), between the laser optical components and the environment. These windows must also have good thermal and mechanical properties if they are to be reliable under the rigors of ordinary handling and use in the field.

In response to this need, the Air Force Materials Laboratory has been working for the past year on a laser window program to develop and characterize candidate materials potentially useful in high power CO_2 laser systems. AFML will also be responsible for scaleup of candidate materials to full size windows for incorporation into test systems. The short lead time for development and scaleup has restricted the selection of materials to those possessing both good optical properties at 10.6μm and a reasonably advanced stage of development. These considerations suggested a concentration on ZnSe and CdTe. Since neither material was clearly superior to the other and since no one materials process was clearly more promising, it was necessary to undertake simultaneous and parallel approaches on both these materials. Samples resulting from the materials processes investigated must provide an optimum of low absorption at 10.6μm, low scatter, good thermal and mechanical properties, durability in the environment, optical homogeneity, and potential for large size. As a result of these initial efforts, a selection of materials and processes will be made for further development and scaleup.

A means of evaluating sample windows produced from the materials development contracts was required in order that the materials and processes could be properly assessed. The purpose of this experimental evaluation is twofold: to serve as a means of evaluating the effects of changes in the materials process parameters on the material properties in order that an iterative program of materials optimization can be accomplished, and to provide values for material parameters which can be used for engineering design studies. The experimental program discussed consists of two distinct efforts: an optical evaluation program, and a program for the thermal, electrical, mechanical, and physical characterization of these window materials. Both evaluation programs are conducted on a contractual basis by the University of Dayton Research Institute at AFML.

To meet the responsibility of development of laser window materials, a number of materials process investigations were undertaken by contractual efforts with six independent material fabrication firms. Existing Air Force crystal growing laboratories provided input to the materials evaluation efforts. Samples were also procured from manufacturers that have existing processes to provide commercially available materials.

The six materials development processes which were chosen for investigations into the techniques of growth of the candidate window materials, CdTe and ZnSe, are summarized in Table I. In terms of good optical quality ($\beta<.005cm^{-1}$) and scalability, the chemical vapor deposition (ZnSe), physical vapor deposition (CdTe, sonic casting (CdTe), and directional solidification (CdTe) have shown promise. Although the modified Bridgman process has provided CdTe samples with an absorption coefficient less than .005 cm^{-1}, the system in its present configuration is not readily scalable to large sizes. The usual mottled appearance together with inclusions and/or agglomerates, many of unknown origin, has plagued the hot pressing method. The liquid epitaxy growth process has not lended itself to CdTe; crystalline CdTe was found to form from the growth substrates, but Te-rich solution was entrained beginning at the substrate-layer interface.

The overriding consideration given to the experimental facility was that a system of meaningful, reproducible measurements could be made and recorded in such a way that valid comparisons could be made with specimens studied during the evolution of the material's development efforts. Because of this primary mission, no innovative or unusual techniques were selected for implementation. The attempt has been to do straightforward, careful measurements.

In order to systematically handle the large number of samples involved in the optical evaluation program, it is essential that the samples be identified and carefully logged in. Physical characteristics such as size, material, and geometrical data, as well as information supplied by the manufacturer are entered into a sample log book that is kept for each sample. A series of surface and near IR transmission photographs are used to aid identification. A conventional photometric IR scan from 2 to 50 μm is taken to provide an initial assessment of the optical transmission quality near the 10.6 μm region of interest.

Calorimetry is a sensitive method of measuring low absorption coefficients, especially when the source is a laser. While it could take a variety of forms, the method utilizes the determination of the heat due to the power absorbed from the beam that passes through the sample. In the adiabatic calorimeter technique used in this laboratory, the thermal rise of the sample resulting from absorbed laser power is determined. The sample is mounted by insulating pins in a vacuum chamber in approximate thermal isolation. A thermocouple is attached to the sample to record its temperature rise.

Experimentally, the power absorbed in the sample is determined from temperature rise ΔT by $P_{abs} = mc(\Delta T/\Delta t)$ where m is the mass of the sample, c is the specific heat of the sample, and Δt is the time during which the sample is absorbing energy from the beam. The attenuation of radiation passing through matter follows the law, $P_z = P_o \exp(-\beta Z)$ which for small absorption coefficient becomes $\beta = P_{abs}/ZP_o$. Radiation impinging on an uncoated window sample undergoes multiple reflections off the surfaces of the window, and with the coherent radiation may involve interference effects. Summing the effects of multiple reflection, P_o can be related to the transmitted power through the reflection and transmission coefficients of the surfaces (and thus the refractive index). Consequently, for the experimental arrangement of the adiabatic calorimeter, the absorption coefficient can be expressed in terms of measurable parameters as

$$\beta = \frac{mc}{L}\left(\frac{2n}{1+n^2}\right)\frac{\Delta T/\Delta t}{P_{trans}}$$

The data from this calorimetric absorption coefficient experiment consists of the graphical record of temperature as a function of time before, during, and following the passage of the beam through the test samples together with the determination of the transmitted power. The remaining parameters are obtained from other measurements. Figure I shows a typical experimental record. By controlling the incident laser power, the temperature rise during irradiation is permitted to increase only about 1 degree above the ambient temperature. This has provided reliable data that require minimal corrections for heat loss. Calorimetric data is reproducible to within a few percent and the absorption coefficient is evaluated to be accurate to within 10 or 20 percent.

In order to examine the variations in absorptance across the surface of samples of window material, an experimental apparatus to measure small changes of absorptance and a mechanism for transporting the samples within the beam to form a raster scan, has been employed. The measurement of absorptance is done by the use of a dual-frequency, dual-beam ratiometric system. Figure II shows the apparatus in block form. The source is a 3 watt stable CO_2 laser and a single pyroelectric detector is used. The beam is modulated near the laser at approximately 100 Hz. A 13 Hz mirror chopper is used as a beam splitter and gives rise to the low frequency signal observed when the attenuation in the sample path increases over that in the reference path. The instrument can be calibrated to read absorptance directly. Source and detector variations are eliminated by taking the ratio of the low frequency signal to the high frequency signal using a ratiometric lock-in amplifier.

A quantitative determination of dn/dT is obtained from multiple internal reflection interference. Knowing the thermal expansion coefficient, the variation in transmitted intensity permits a calculation of dn/dT by monitoring the transmitted power as the sample temperature is changed. The change of fringe order, for a given temperature change is recorded. This test requires samples with optically flat and parallel faces.

Additional optical properties tests are also performed. Interferometers operating at CO_2 and He-Ne wavelengths using all reflecting optics and utilizing a reflection diffraction grating as a beam splitter are used for observation of variations in optical path homogeneity. Apparatus for both differential scattering cross section measurements and for total scattering is available. An experimental device was also designed to provide input data for thermal lensing investigations. In this test a NaCl beam splitter permits a small fraction of an intense laser beam to be brought to a focus by an off-axis paraboloid mirror. The image intensity is examined by moving an apertured detector through the focus along the optic axis. The experiment is performed with and then without a window material sample in the high intensity beam. The material thermal lensing can be related to the measured change in focal position when the sample is inserted.

To provide for the measurement of the thermal, mechanical, and electrical parameters, a contractual program was arranged which is designed to provide standard measurements. In addition to generating engineering data,

emphasis has also been placed on obtaining meaningful feedback of information to the materials process development. The more pertinent parameters measured are thermal diffusivity, specific heat, thermal expansion, and flexural strength. Scanning electron and electron microprobe analysis is employed for material homogeneity and structural defect analysis. Electrical resistivity and Hall mobility are measured as a function of temperature.

Thermal diffusivity is measured from room temperature to 200°C by the flash technique. A ruby laser is used as a pulsed energy source and the backface temperature response of the sample is sensed by a thermocouple. The thermocouple output is then displayed as a function of time on a storage oscilliscope which is photographed for a permanent record of the temperature-time history. This technique, when used at temperatures below 1000°C, provides a measure of thermal diffusivity accurate to within ±5%.

An isothermal drop calorimeter is used for measurements of specific heat in the temperature range of -40°C to +200°C. This is a relatively standard procedure in which a sample is equilibrated at a specified temperature and then transferred to a receiver at a different temperature. A measurement of the heat content of the sample is then obtained as a function of the corresponding temperature change of the receiver as it comes into thermal equilibrium with the sample. With reasonable care this method can provide specific heat measurements with an accuracy of ±10%.

Four-point flexure tests are undertaken to obtain strength data of the sample materials. The fixture incorporates the basic design features recommended by the NATO Advisory Group for Aerospace Research and Development and is designed to minimize error arising from misalignment, friction effects, specimen twist and taper, and contact point wedging.

Some of the parameters of interest for CdTe and ZnSe are listed in Tables II and III, respectively. The measured parameters are listed by materials process since the materials' properties are quite often related to the method by which it was produced. The numbers are typical results and are not necessarily attainable in every process run.

Significant progress has been made in the quality of these semiconductor materials as a result of the AFML Laser Window Program. At the start of this program CdTe was available in small sizes only, but now there are several sources of good optical quality CdTe in much larger sizes with absorption coefficients an order of magnitude lower. Similarly, polycrystalline ZnSe has shown dramatic improvement. The absorption coefficient is nearly two orders of magnitude lower and the flexural strength is nearly doubled in currently produced large samples. These materials have yielded somewhat to the attempts to optimize their optical and physical properties by controlled adjustment of the materials fabrication processes. The improved technology resulting from this program is expected to benefit many other IR research and development programs.

Obviously the program we describe represents the efforts of many scientists and technicians both in government laboratories and at a variety of firms under contract to the Air Force. We wish to acknowledge however, John Detrio, Paul Greason, John Wurst and G. Edward Kuhl for their distinctive activities in the evaluation programs and in the assimilation of information at AFML.

TABLE I. AFML MATERIALS DEVELOPMENT EFFORT

PROCESS	MATERIAL
PHYSICAL VAPOR DEPOSITION	CdTe, ZnTe*, CdSe*
MODIFIED BRIDGEMAN	CdTe
LIQUID EPITAXY	CdTe*
CHEMICAL VAPOR DEPOSITION	ZnSe, CdTe*
SONIC CASTING	CdTe
HOT PRESSING	ZnSe, CdTe*
DIRECTIONAL SOLIDIFICATION	CdTe

*-DISCONTINUED

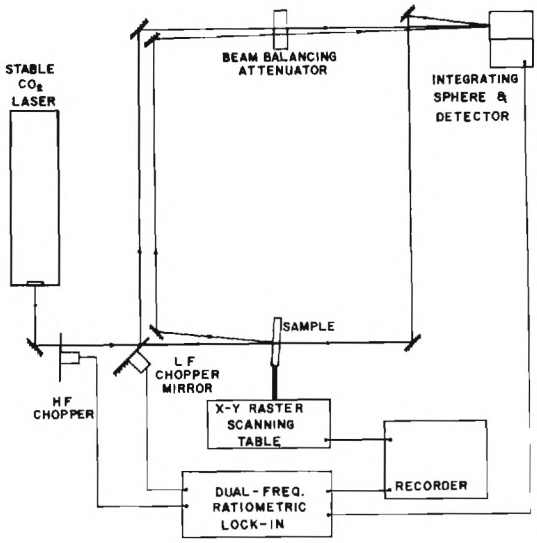

FIGURE II. ABSORPTANCE UNIT

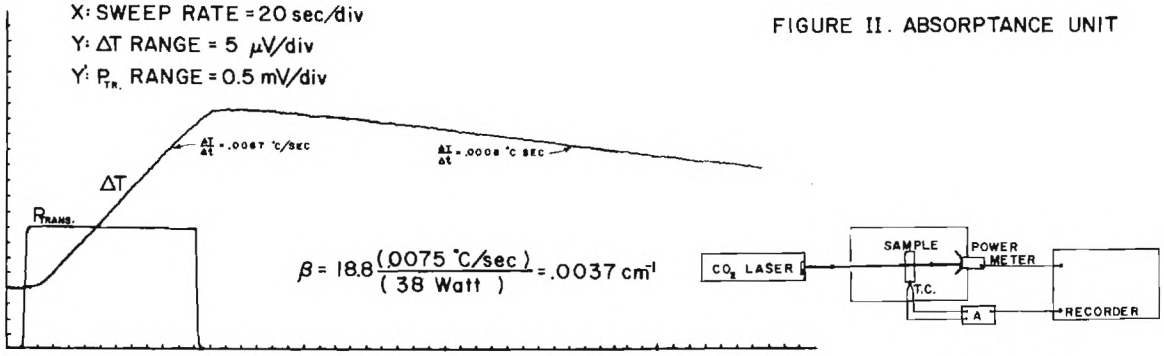

FIGURE I. THERMAL RISE CURVE; CdTe, SAMPLE CT55D5-67

CALORIMETER

TABLE II
CdTe PROPERTIES

TABLE III
ZnSe PROPERTIES

PROPERTY	PHYS. VAP. DEPOSIT.	MODIF. BRIDGM.	SONIC CASTING	HOT PRESS.	DIRECT. SOLIDIF.	CHEM. VAP. DEPOSIT.	HOT PRESS.
ABSORPTION (cm^{-1})	.001	.0025	.003	.2	.001	.005	.035
TRANSMISSION (%)	68	68	68		68	74	72
INDEX OF REFRACTION	2.67	2.67	2.67	2.67	2.67	2.35	2.35
dn/dT ($10^{-5}/°C$)	10.6	—	—	—	—	5.6	—
LINEAR EXPANSION ($10^{-6}/°C$)	4.6	—	—	4.2	—	7.8	7.4
THERMAL CONDUCTIVITY ($W/cm°C$)	.11	.11	.01	.09	—	.12	.16
SPECIFIC HEAT ($cal/gm°C$)	.055	—	.055	—	—	.085	.085
ELECTRICAL RESISTIVITY (Ω-cm)	10^5	10^7	10^9	—	10^6	10^{12}	10^{12}
FLEXURAL STRENGTH (psi)	2000	3000	3500	5000	—	7300	6000
HARDNESS (Knoop)	40	—	—	—	—	95	—
DENSITY (gm/cm^3)	5.86	5.86	5.86	5.86	5.86	5.27	5.27
GRAIN SIZE (cm)	2-3	3-5	.2-.4	.01-.02	1-2	.02	.05-.1

Rain Erosion of Infrared Transmitting Materials

G. Hoff & H. Rieger, Dornier System GmbH

1. Introduction

Infrared domes at airplanes or missiles belong to the components of these aircrafts which are mostly exposed to rain erosion. The increased frequency of rain erosion damages at such infrared domes is essentially conditioned by two factors: Firstly the exposed position of these infrared domes at the airplane or missile and secondly the relatively bad erosion resistance of the infrared transmitting window materials.

With regard to their application, different demands are made on these infrared transmitting window materials. The most important demands are: sufficient optical transmittance in wave length range up to abt. 5 µm, good thermo-shock behaviour as well as good resistance against rain erosion, hail erosion and sand erosion.

The present paper deals exclusively with the investigation of rain erosion behaviour of infrared transmitting materials. In this connection not only the material loss but, for the first time, also the change of the optical transmittance as a function of various erosion parameters have been investigated.

The performed tests can be subdivided into two groups:

1. material tests to determine the influence of the material on rain erosion and
2. parameter investigations to demonstrate the dependence of rain erosion on test parameters, such as velocity or drop size.

2. Test Facility to Perform Erosion Tests up to M = 1.4

Fig. 1 shows a schematic picture of the test facility to perform rain erosion tests up to M = 1.4. It is a rotating arm operating at normal pressure which obtains a maximum velocity of 1.4 Mach. The specimen is fixed at the outer end of the arm. Rain is produced by injecting drops from oscillating nozzles at eight different points of the circular path. The following test parameters can definitely be varied: velocity, drop size, angle of impact and, within certain limits, also temperature.

3. Test Results

3.1 Measurements of Weight Loss. The erosion process is normally investigated by determining the weight loss as a function of the exposure time to rain. Fig. 2 represents the erosion curves for various infrared transmitting materials at a velocity of 400 m/sec, for drops of 1.2 mm diameter. The weight loss is plotted as ordinate and the exposure time as abscissa in logarithmic scale. The curves of this diagram show the different erosion resistance of the single infrared transmitting materials. Of all materials tested in this case, pure quartz glass has the lowest and sapphire the highest rain erosion resistance. For instance, the tested quartz glass is used as infrared window in the F 104, the Starfighter of the German Airforce, where it is subject to very strong rain erosion so that on the average two infrared windows at one airplane per year have to be exchanged. This special erosion problem could be solved by using sapphire as infrared material which could easily be realized with the existing window size. It would even be

economic when considering that sapphire has a higher rain erosion resistance than the aluminium alloy with which the airplane has been constructed, and that the costs for one sapphire window are only abt. four times as much as for the quartz window.

In the direction of decreasing rain erosion resistance sapphire is followed by specially sintered magnesium oxide, yttrium oxide, silicon and a number of calcium aluminate glasses. It can be seen that the rain erosion resistance of all calcium aluminate glasses which can partly also be used as infrared window materials, is distinctly inferior to that of silicon. The infrared dome of the sidewinder consists mostly of silicon.

There is no strict correlation between the erosion test parameters and the mechanical characteristic values for the infrared transmitting materials. Fig. 3 shows, however, the tendency that rain erosion resistance of infrared transmitting materials increases with rising microhardness. The incubation time has been plotted against microhardness as a measure for rain erosion resistance.

Fig. 4 shows that rain erosion depends not only on microhardness but also on internal stress. The erosion curves of an annealed and an unannealed sapphire are represented in this figure. It can distinctly be seen that erosion resistance of sapphire can be increased by an appropriate thermal treatment. Reducing the internal stress during annealing causes an improvement of the erosion stability. Corresponding improvements of erosion resistance due to thermal treatments have also been observed with other infrared transmitting glasses.

With sapphire, the erosion behaviour depends moreover on crystal orientation. Fig. 5 shows two erosion curves of two differently orientated single crystals. This proves that sapphire crystals the c-axis of which is parallel to the surface show a remarkably higher erosion resistance than sapphire crystals the c-axis of which is perpendicular to the surface.

3.2 Investigation on Light Transmittance. The test results shown up to now give an idea of the weight loss during rain erosion. With window materials, weight loss is less interesting than the change of optical properties due to rain erosion. For this reason, the change of light transmittance as a function of exposure time in the rain has been determined parallel to the measurements of weight loss.

Measurement of light transmittance was mainly performed in the visible region by applying a photometer of a microscope. Supplementary investigations have been made by a spectral photometer in the infrared region up to 5 µ. Fig. 6 to 9 show distinctly the high reduction of light transmittance with increasing exposure time to rain.

These investigations show the result which is important for the application of infrared transmitting window materials that there is a strong decrease of light transmittance already within the incubation region of the weight loss curves. At the end of the incubation period, the light transmittance is usually only abt. 10 to 20 % of the initial value with most of the infrared transmitting materials tested. The shape of the curves shows that the decrease of light transmittance is decisive at the beginning of the exposure to rain, while there is only little

damage as soon as the incubation period is exceeded.

The behaviour of sapphire represents a certain exception. Fig. 9 shows that, compared with other tested infrared transmitting materials, sapphire has a considerably lower decrease of transmittance. At the end of incubation period, sapphire transmittance values represent still 75% of the initial value. The strongly inhomogenous erosion is the reason for this divergent behaviour. Fig. 10 shows the comparison of an eroded sapphire specimen and an eroded quartz glass specimen. While the quartz glass surface erodes regularly, erosion of sapphire occurs only on single points. The influence of the different kind of erosion on the optical properties of these both materials is also shown by the legibility of the letters under both specimen.

At this point it may be added that corresponding investigations conducted in the infrared spectral region furnished practically the same results. Small quantitative differences occur only at the beginning of erosion. In the infrared region, the decrease of transmittance is a little lower than in the visible spectral region.

3.3 Dependence of Rain Erosion of Infrared Transmitting Materials on Different Test Parameters. Material destruction due to rain erosion depends, on a large scale, on flight velocity and strength of the rain.

The dependence of rain erosion of infrared transmitting materials on drop diameter and specimen velocity is indicated as example for parametric investigations as follows:

Fig. 11 and 12 are examples for the influence of drop size on the destruction of quartz glass and silicon. The weight loss for different drop diameters is plotted against the water column of impacting water in these figures. Would there be no drop size effect on the rain erosion, the erosion curves measured for different drop sizes would coincide with this kind of representation. Fig. 11 and 12 show that there is a considerable dependence of drop size on rain erosion. The present investigations show that highest erosion occurs with drops of 0.9 mm diameter, and lowest erosion with drops of 1.2 mm diameter. At this point, it cannot be commented on the reasons for this behaviour in detail. They have already been discussed in an earlier paper [1].

From all test parameters, velocity has the strongest effect on rain erosion. Fig. 13 serves for demonstration of velocity dependence of rain erosion. This figure shows the erosion curves of quartz glass measured at different velocities, the extraordinary increase of erosion with rising velocity is distinctly to be seen.

Fig. 14 gives an idea of the velocity dependence of rain erosion of various infrared transmitting materials. Incubation time has there been plotted double logarithmically against the velocity for various materials. This kind of representation shows that in the velocity region between 300 m/sec and 450 m/sec the curves resulting therefrom can very well be approximated by a straight line with a few exceptions. This means that the velocity dependence of incubation time can be represented by an exponential function of the type

$$t_K = \frac{a}{v^n} .$$

The coefficients n for the various infrared transmitting materials are summarized in table 1; they range between n = 3.7 and n = 7.0.

Table 1

material	SiO_2	Ge	calcium aluminate	MgF_2	Si	Y_2O_3	MgO	Al_2O_3
n	3,7	6	6	5	5,7	6,1	5,0	7,0

It has to be mentioned that due to lacking test results of sapphire, the velocity dependence of incubation time of sintered Al_2O_3 has been indicated in fig. 14.

The results of these parameter investigations show that, for infrared transmitting window materials, it is extremely necessary to detect the velocity dependence of rain erosion up to the region of operation velocities of modern aircrafts and missiles.

3.4 Test Facility to Perform Rain Erosion Tests up to 1000 m/sec. The steady increase of velocity of aircrafts and guided missiles as well as the critical demands for low level flight and all-weather usefulness require urgently a quantitative measurement of rain erosion test parameters of the various material qualities up to a velocity of M = 3.

Up to now complete rain erosion data are available only up to a velocity of M = 1.4. Therefore, in 1969 Dornier System had been ordered by the Ministry of Defence of the Federal Republic of Germany with the development and construction of a rain erosion test stand for velocities up to 1000 m/sec. For this test stand the successful principle of the rotating arm had been conserved. To solve the problems of high driving power, sound generation and heat transmission from the test stand, this stand had been designed for a test range of 1 to 30 Torr.

A double arm rotor of 240 cm diameter designed as so-called arm of same strength runs in a vacuum container of 320 cm diameter. The cylindrical specimen of 16.8 mm diameter to be tested are fixed at the end of the arm. Drive is made by an electro-motor of 80 kW with a speed stability of 1 °/oo.

Rain is produced by injection nozzles. Drop size, rain density and exposure time to rain can be varied regardless of each other in a large range. The water vapor being produced by spraying is freezed in an ice condenser.

The M = 3 test stand is so designed that specimen size and arm diameter are identical with the rain erosion test stand for M = 1.4 in operation at Dornier System since 1960.

It is therefore possible to get a quantitative connection of rain erosion test parameters measured in vacuum with thosemeasured at normal pressure in a velocity range of M = 1 to M = 1.4.

[1] H. Rieger, Investigation of the influence of various test parameters on material destruction at drop impact.
Proc. 3rd Int. Conf. Rain Erosion and Associated Phenomena 1970, Ed. A.A. Fyall and R.B. King, RAE, England

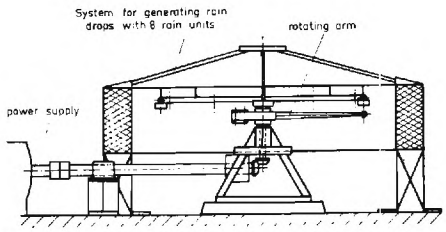

Fig. 1 Schematic Representation of Mach 1.4 Rotating Arm

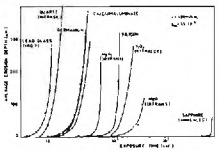

Fig. 2 Erosion Curves of Various Infrared Transmitting Materials

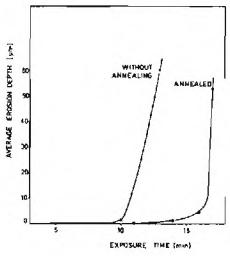

Fig. 4 Influence of Heat Treatments on Rain Erosion of Sapphire

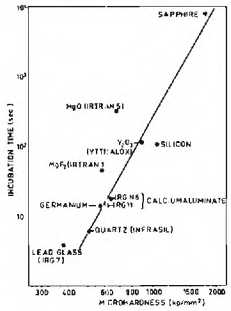

Fig. 3 Connection between Incubation Time and Microhardness

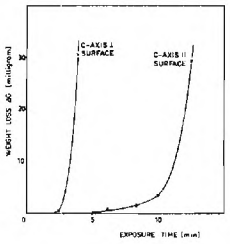

Fig. 5 Influence of Crystal Orientation on Rain Erosion of Sapphire

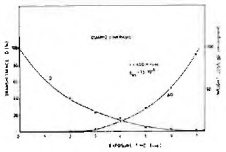

Fig. 6 Light Transmittance and Weight Loss as a Function of Exposure Time for Quartz Glass

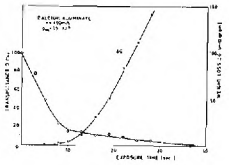

Fig. 7 Light Transmittance and Weight Loss as a Function of Exposure Time for Calcium Aluminate

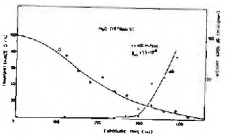

Fig. 8 Light Transmittance and Weight Loss as a Function of Exposure Time for Magnesium Oxide

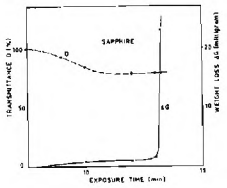

Fig. 9 Light Transmittance and Weight Loss as a Function of Exposure Time for Sapphire

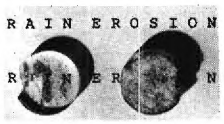

Fig. 10 Destruction Picture of Sapphire (left) and Quartz Glass (right)

Test Conditions:

Sapphire:

velocity	v	= 400 m/sec
drop diam.	d	= 1.2 mm
water volume concentration	γ_{WL}	= $1.2 \cdot 10^{-5}$
exposure time	t	= 15 min

Quartz Glass:

	v	= 400 m/sec
	d	= 1.2 mm
	γ_{WL}	= $1.5 \cdot 10^{-6}$
	t	= 8 sec

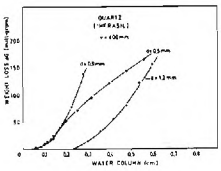

Fig. 11 Influence of Drop Size on Rain Erosion of Quartz Glass

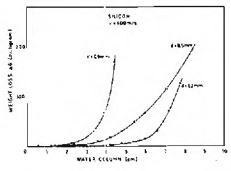

Fig. 12 Influence of Drop Size on Rain Erosion of Silicon

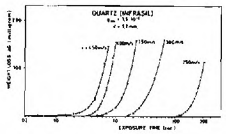

Fig. 13 Influence of Velocity on Rain Erosion of Quartz Glass

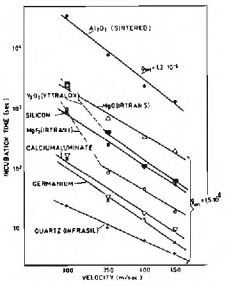

Fig. 14 Dependence of Incubation Time on Velocity for Various Infrared Transmitting Materials

THIN SKIN RADOME HARDENED BY VENTING

W D Delany

Admiralty Surface Weapons Establishment, Portsmouth

United Kingdom

ABSTRACT

A single skin circularly symmetrical radome has been developed which has an increased resistance to air blast damage. Several features have been incorporated in the design, the main one of which has been to vent the radome from the underside during the air blast positive phase in order to reduce the differential pressure to zero as rapidly as possible. Experiments have been carried out in an air blast simulator on 4 ft 6 in and 6 ft diameter models at various overpressures. Some results are given as photographs of tests on vented and unvented radomes of the damage sustained at various overpressures. Graphs show pressure V time at a number of points inside the radome. A 16 mm film taken with a camera at 1000 frames/second shows sequences of these tests, viewed from the direction of the blast, and also from the side.

INTRODUCTION

Circularly symmetrical radomes of spherical or bell-jar shape are generally very susceptible to air blast, as they are difficult to reinforce internally if an all round field of view is required. The purpose of most radomes is to provide an environment which is proof against the natural elements for the operational use and maintenance of the antenna, the mechanical strength of the antenna being usually such that much higher overpressures can be withstood. If this were not so it would not in most cases be difficult to increase the mechanical strength of the antenna at least to sustain static overpressure if not dynamic pressure. In Naval ships the items susceptible to air blast are radomes, and the problem of increasing their strength without paying a high price in terms of loss of electrical performance has recently been studied. A GRP single thin skin structure was chosen for the basic work, as if damaged it is not susceptible to water absorption, and is readily repairable. The results could possibly also be applied generally, for instance to alternative forms of construction such as sandwich layer.

EFFECTS OF AIR BLAST

The three main effects of air blast on a radome, which behaves as a diffraction type structure, are:

a. Reflected pressure The blast wave in striking the surface facing ground zero crushes or fractures the skin, causing the drag coefficient of the entire structure to be unpredictably increased, making it susceptible to:

b. Dynamic pressure is the air particle movement following the blast wave. The destructive effect on the front surface depends mainly on the time of duration, is the total energy of the blast source. High tensile loading on the lower front face just above the flange occurs as a result of the overturning moment on the structure as a whole.

c. Static overpressure The pressure which applies uniformly over the entire surface during the positive phase and has a crushing effect on the radome as a whole.

DESIGN OF RADOME

Figure 1 shows the main features of the design and Figure 2 is a photograph of the radome. The main features are:

a. Shape The near cylindrical shape of the radome as compared with a frustum of a sphere ensures that the stresses in the lower regions of the skin, due to the bending moment on the structure as a whole, are carried in simple tension, for which GRP is most suited. Also, this shape enables filament winding to be used as the manufacturing process, by which the glass content can be raised to 80% (ie optimum) for hoop/longitudinal winding, and 65% for helical winding.

b. Thickened skin at base This reduces stress concentrations still further in this highly critical area, which is subject to shear loading due to the reflected pressure, in addition to the tensile loading due to the bending moment.

c. Clamping rings are used instead of an integral flange. The stresses are carried by compressed rubber pads acting in shear to internal and external metal rings. There is thus no complication in manufacture of the radome, and its strength is fully maintained; stress concentrations are also avoided by this method of attachment.

d. Annular Deflector This forms the pedestal on which the radar antenna is mounted. It is enclosed in an open framework supporting the radome, which may be covered externally by a low strength fabric, or by internally-opening flexible doors, or by louvred shutters. The internal environment is protected at all times by this arrangement until the arrival of the air blast front.

RESULTS

Tests to date have been carried out in the air blast simulator at Atomic Weapons Research Establishment, UK, on radomes of 4 ft 6 in diameter and 6 ft diameter, for the purpose of determining:

a. The changing pressure distribution over the external and internal surfaces, and various points inside the structure during the air blast positive phase. For these tests a thick walled moulding was specially made that would not be damaged at the high test overpressures. Pressure transducers in the experiment were disposed as shown in Figure 3. The results of these measurements are in Figure 4.

b. Ditto, but with an open top (ie a frustum of a cone only).

c. Target response of thin walled radome with vent closed all round.

d. Comparison of response of radomes with open vent, made with various combinations of glass filament winding, including hoop, longitudinal, and 45° helical.

e. Ditto, comparing rigid epoxy and flexible epoxy laminates.

For tests c, d, e, photographic recordings were made by ciné-cameras at 1000 frames/second, one placed on the blast side, and one at side elevation to the target. In general, tests were started at 4 lb/in^2 overpressure level, and repeated at increasing intervals of 1 lb/in^2 until moderate damage or destruction occurred. The sequence of photographs Figures 5 and 6 show typical deflections of the front surface for unvented and vented conditions during the positive phase at 7 lb/in^2 overpressure.

CONCLUSIONS

a. The best filament winding combination was found to be hoop/longitudinal/hoop in equal thicknesses. Helical winding was found to be very uneven for a thin wall moulding, and local weaknesses resulted in failure at lower values of overpressure. It also resulted in the laminate having a lower glass content.

b. Unvented radomes failed at 4 lb/in^2 overpressure: similarly constructed unvented radomes withstood overpressures up to 7 lb/in^2.

c. The degree of damage sustained up to 9 lb/in^2 would probably allow operational use of the radar antenna, although its environment would not be protected.

d. Flexible resin mouldings suffered approximately the same damage as equivalent rigid resin moundings at about 8 lb/in^2 overpressure, but they deflected more, and the antenna would be at higher risk. The surface crazed more generally, rather then locally, as for the rigid resin mouldings.

e. Pressure inside the radome equalised with the reflected pressure within 10 millisecs of the blast wave striking the radome.

f. After the first 10 millisecs, the internal pressure was sensibly equal to the external overpressure.

g. Panels in the upper surface of the radome designed to blow off, or to be rupturable, would cause failure of the entire radome by increased drag.

h. The design feature of gradually thickening the wall near the base is completely successful. No failures occurred in this region in any tests.

ACKNOWLEDGEMENT

This paper is published by permission of the UK Ministry of Defence (Navy). Acknowledgement is made also to AWRE, Foulness, UK for the use of results obtained in testing radomes in the air blast simulator.

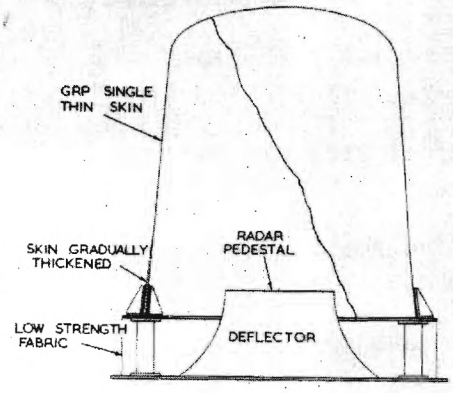

FIGURE 1.
MAIN FEATURES OF RADOME DESIGN

FIG. 2.
RADOME BEFORE TEST

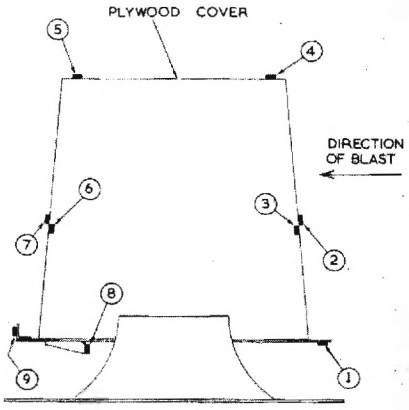

FIGURE 3.
DISPOSITION OF PRESSURE TRANSDUCERS.

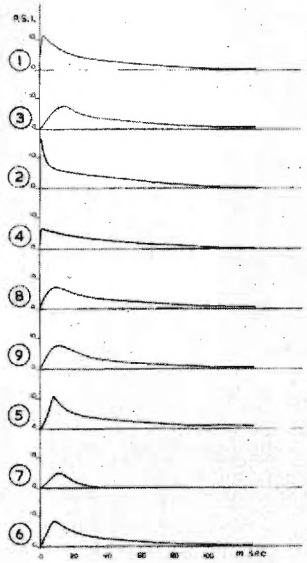

FIGURE 4.
PRESSURE / TIME RECORDINGS.

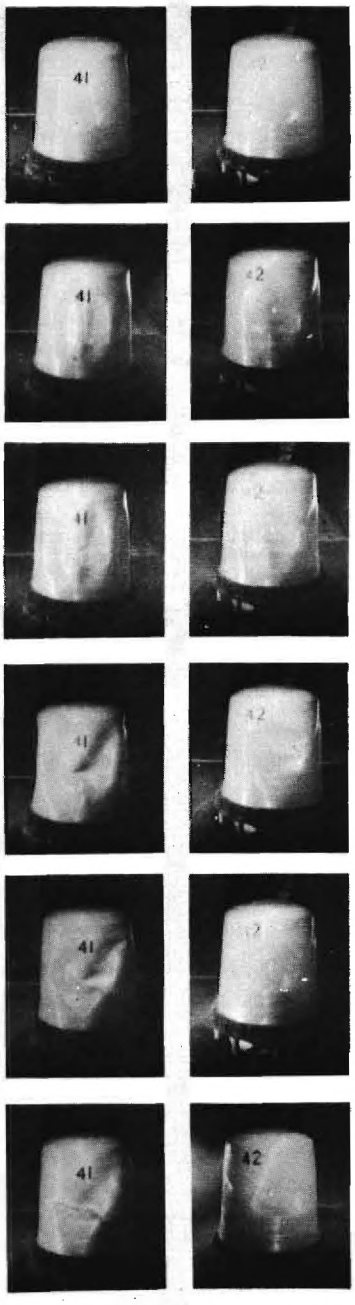

FIG. 5.
UNVENTED RADOME

FIG. 6.
VENTED RADOME

RADOMES AT 7 P.S.I. OVERPRESSURE VIEWED FROM DIRECTION OF BLAST

REACTION SINTERED SILICON NITRIDE AS A HYPERSONIC RADOME MATERIAL

By

J. D. Walton, Jr.
Engineering Experiment Station
Georgia Institute of Technology

I. INTRODUCTION

Silicon nitride has been the object of intensive study and development during the past decade. Primary attention has been given to developing this material for high temperature structural applications such as gas reactor heat exchangers, high temperature bearings, leading edges, and gas turbine components 1/. Although there has been intermittent interest in reaction sintered silicon nitride as a possible radome material 2/, it generally has been considered that the electrical properties are not adequate for this application 3/.

Although the dielectric properties were questionable, the Engineering Experiment Station became interested in reaction sintered silicon nitride as a potential radome material since it should have adequate thermal shock resistance to survive Mach 6-7 flight and have superior rain erosion resistance to slip-cast fused silica. However, the problem remained of determining whether or not reaction sintered silicon nitride could be produced with adequate high temperature dielectric properties. After a search for the needed high temperature dielectric property data proved unsuccessful, the decision was made to prepare samples of reaction sintered silicon nitride under carefully controlled conditions and to determine the dielectric constant and loss tangent of this material as a function of temperature.

II. MATERIAL PREPARATION

Reaction sintered silicon nitride was prepared from nominally 98 per cent pure -200 mesh silicon powder with a maximum iron content of one per cent. This material was dry milled in one gallon ceramic ball mills for 96 hours and was suitable for isostatic pressing or slip casting without the need of lubricants, binders or suspending agents. Slip casting was accomplished using a 70 per cent solids suspension of silicon powder in water.

The preformed silicon part was sintered in a mullite tube which was evacuated and back-filled with dry nitrogen which was allowed to flow continuously as the tube was heated to 2350° F for 50 hours and then to 2650° F for 10 hours.

The density of the final product depended upon the method of fabrication. Isostatic pressing at 30,000 psi provided a density of 2.50 gm/cc, and slip casting gave 2.35 gm/cc. By gelling the slip it was possible to achieve a density of 2.14 gm/cc.

III. REQUIREMENTS FOR HYPERSONIC RADOMES

The criteria used at the Engineering Experiment Station for selection of a hypersonic radome material, in order of decreasing importance, are: (1) dielectric properties, (2) thermal shock resistance, (3) rain erosion resistance, (4) fabricability, (5) weight, and (6) economics. The following sections will consider the first four items with respect to current data related to the capabilities and limitations of reaction sintered silicon nitride for hypersonic radome applications. Table I presents pertinent thermal, mechanical and electrical property data for eight ceramic radome materials 4/.

1. Dielectric Properties

Figure 1 shows dielectric constant versus per cent pores for dielectric constants of 4, 7 and 10 at zero per cent pores. These data were calculated using the formula

$$\epsilon = \epsilon_o^{1-P} \qquad (1)$$

where ϵ_o is the dielectric constant of the 100 per cent dense material and P is the volume fraction of pores. Also shown in Figure 1 are the dielectric constants for reaction sintered silicon nitride with 21, 26 and 33 per cent pores (2.5, 2.35, and 2.14 gm/cc) prepared as described in Section II. These data were obtained at 9.8 GHz using the short circuit waveguide technique 5/. The Admirality Materials Laboratory data were furnished by Godfrey and are for 2.45 gm/cc material prepared by the flame spray process 6/.

Figures 2 and 3 show dielectric constant and loss tangent as a function of temperature for the dielectric materials listed in Table I. Data are also shown for reaction sintered silicon nitride with densities of 2.50 and 2.35 gm/cc prepared by Georgia Tech and 2.45 gm/cc prepared by the Admirality Materials Laboratory.

Dielectric property data up to and above the decomposition temperature (3400° F) are required in order to establish the flight velocity limit for hypersonic applications. Such data will be obtained using the high temperature dielectric facility developed at Georgia Tech 7/.

2. Thermal Shock Resistance

Figure 4 shows the maximum temperature, above ambient, to which each material in Table I can be heated and survive the associated thermal shock (ah). In this figure (a) is the wall thickness and (h) is the heat transfer coefficient. Also shown are recovery temperatures which would result from a sea level flight of a 15 degree half angle cone at three different Mach numbers. The h values used are those occurring at a point 5 inches from the tip.

3. Rain Erosion Resistance

Essentially no quantitative rain erosion data exist for well

characterized reaction sintered silicon nitride. Fyall states that "A specimen 0.25 inches thick, tested at 500 miles/h in 1 in/h rain showed moderate to severe erosion, depending on the surface being ground or unground respectively, in 360-480 minutes. While obviously inferior to high quality aluminas, these characteristics place the material somewhat on a par with the nucleated glass ceramic, Pyroceram 9606" 8/. Godfrey reports that the normal component of velocity to cause damage simulating rain impact for flame sprayed silicon nitride is 2500 ft/sec 6/.

It should be pointed out that the radome shape, as related to impact angle, can be designed to reduce the rain erosion damage to any material. Therefore, if a sufficiently small cone angle is used for the forward portion of the radome, and if a protective tip is employed, many materials including slip-cast fused silica and boron nitride can survive encounter with rain at hypersonic velocities. However, intrinsic rain erosion resistance of the material used will determine the maximum allowable impact angle and therefore the maneuverability of the vehicle in rain.

4. Fabricability

Reaction sintering should provide the most practical and economical process for fabricating silicon nitride radomes. Because of the porosity which accompanies this process reaction sintering provides a material with a lower dielectric constant than that obtained by hot pressing.

Although porosity presents certain problems such as reduced strength and moisture absorption, these problems are not considered serious. For example, sealing with organic sealants has proven successful in the case of slip-cast fused silica (about 12 per cent pores). The strength of reaction sintered silicon nitride at 20 per cent porosity appears more than adequate for radome applications.

For ease of machining the compacted silicon powder radome may be partially sintered at about 1900° F, removed from the furnace, and machined using conventional metal working techniques. The machined radome is then returned to the furnace for completion of the nitridation cycle. The dimensional change from the compacted silicon powder body to the hard-fired reaction sintered state is less than 1 per cent 9/.

IV. CONCLUSIONS

1. The dielectric constant and loss tangent of reaction sintered silicon nitride suggest that this material should be suitable for high temperature radome applications to temperatures at least as high as 2000° F.

2. The thermal shock resistance of reaction sintered silicon nitride should be adequate for radome flight velocities as high as Mach 6 and perhaps to Mach 7.

3. Although rain erosion data are incomplete, it is estimated that reaction sintered silicon nitride should be equivalent to Pyroceram Code 9606 with respect to threshold damage velocity. At higher velocities it is possible that reaction sintered silicon

nitride might exceed that of dense ceramics since its porous structure should permit incremental erosion rather than gross material failure.

4. The reaction sintering process provides an excellent means of fabricating silicon nitride radomes. Slip casting, isostatic pressing or injection molding should each be capable of producing satisfactory radomes.

5. Because of the excellent dimensional tolerance that can be obtained through the reaction sintering process, and the ease with which partially nitrided silicon nitride can be machined, the economics of producing radomes from this material should be as good or better than any other ceramic radome material.

REFERENCES

1. D.J. Godfrey and E.R.W. May, "The Resistance of Silicon Nitride Ceramics to Thermal Shock and Other Hostile Environments" Ceramics in Severe Environments, W.W. Kriegel and H. Palmour III Ed., Materials Science Research, Vol. 5, pp 149-162, Plenum Press, New York, 1971.

2. W.M. Wells, "Silicon Nitride as a High Temperature Radome Material," UCRL-7795, Lawrence Radiation Laboratory, May 19, 1964.

3. D.J. Godfrey, "The Fabrication Properties of Silicon Nitride Ceramics and Their Relevance to Aerospace Applications," Jour. Brit. Interplanetary Soc., Vol. 22, pp 353-368, 1969.

4. J.D. Walton, "The State of Techonolgy of Ceramic Radomes, Their Use and Possibilities for the Future," Volume II, Proceedings of the Second International Conference on Electromagnetic Windows, Paris, France, September 8-10, 1971.

5. T.W. Dakin and C.N. Works, "Microwave Dielectric Measurements," J. Appl. Physics, Vol. 18, pp 789-796, September, 1947.

6. D.J. Godfrey, private communication, November 22, 1971.

7. H.L. Bassett, S.H. Bomar, Jr., G.K. Huddleston and A.C. Merritt, "High Temperature Complex Permittivity Measurements on Reentry Vehicle Antenna Window Materials," Techincal Report No. AFWL-TR-71-189, Air Force Weapons Laboratory, January, 1972.

8. A.A. Fyall, private communication, November 25, 1971.

9. P. Popper, et al., "The Preparation Properties and Structure of Silicon Nitride," Trans. Brit. Ceram. Soc., September, 1961.

SELECTED PROPERTIES OF CANDIDATE CERAMIC RADOME MATERIALS

	Single Oxides			Mixed Oxides		Nitrides		
				Cordierite ($2MgO \cdot 2Al_2O_3 \cdot 5SiO_2$)		Boron Nitride (BN)		Silicon Nitride (Si_3N_4)
	High Purity Alumina (Al_2O_3)	Beryllia (BeO)	Slip-Cast Fused Silica (SiO_2)	Pyroceram Code 9606	Rayceram III	Hot Pressed	IPBN	Reaction Sintered
Major phase per cent	99-99.5	> 99	99.8	unknown	unknown	98-99	99.9	unknown
Density (gm/cm^3)	3.7-3.9	2.85-2.95	2.1	2.6	2.45	1.9-2.0	1.25	2.5
Per Cent Theoretical Density	95-98	95-98	95	100	98	84-88	55	80
Water Absorption per cent	0	0	1.5	0	0	0-3**	0	20
Flexural Strength (10^3 psi)	45	35	6.5	20*	18	17	14	25
Young's Modulus (10^6 psi)	52	50	8.7	17.2	17	13	1.75	15
Thermal Conductivity (Btu/ft-hr-°F)	18	120	0.5	2.16	≈ 2	11	16	6
Coefficient of Thermal Expansion (10^{-6} in/in°F)	4.6	4.6	0.3	3.2	1.45	3.1	2.1	1.4
Specific heat (cal/gm-°C)	0.27	0.26	0.18	0.18	0.19	0.33	0.29	0.2
Poisson's ratio	0.28	0.34	0.15	0.24	0.27	unknown	0.23	0.25
Dielectric constant at 8-10 GHz	9.5	6.6	3.3	5.65	4.8	4.1	3.2	5.6
Loss Tangent at 8-10 GHz x 10^3	0.1	0.5	0.4	0.2	2.0	0.1	0.2	2.0

*Abraded surface. **Hydration.

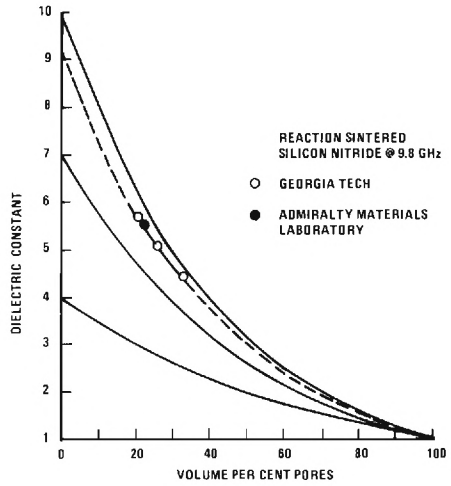

Figure 1. Dielectric Constant vs Volume Per Cent Pores for Dielectric Constant Values of 4, 7 and 10 at Zero Per Cent Porosity.

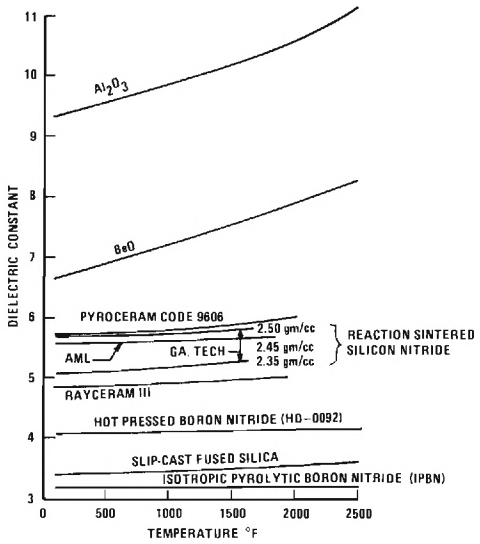

Figure 2. Dielectric Constant vs Temperature for the Dielectric Materials Shown in Table I.

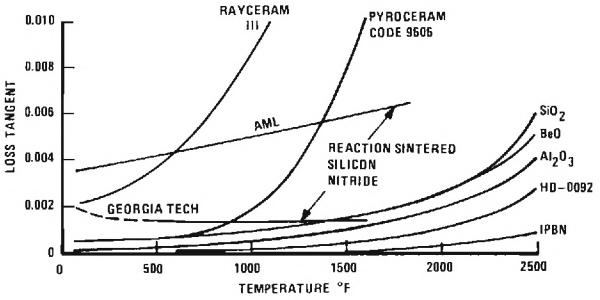

Figure 3. Loss Tangent vs Temperature for the Eight Dielectric Materials Shown in Table I.

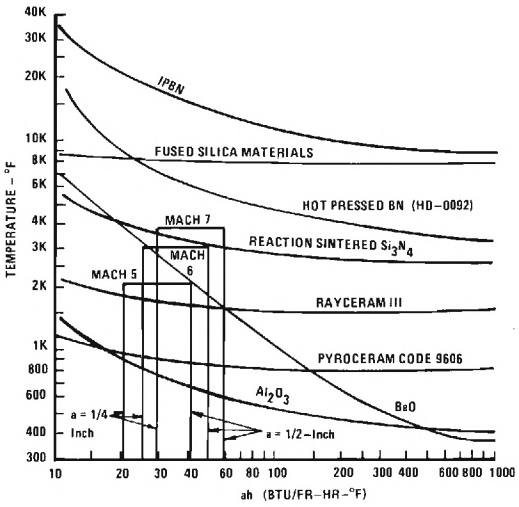

Figure 4. Recovery Temperature vs Heat Transfer Rate for Ceramic Radome Materials.

End-Oriented, Fiber-Reinforced Plastics Composites as Rain Erosion Resistant Radome Materials

by
Boyce G. Kimmel, Hughes Aircraft Company, Culver City, California
Maxwell Stander, Naval Air Systems Command, Washington, D.C.

Rain erosion tests performed for the U.S. Navy by the University of Cincinnati* have demonstrated clearly the marked superiority in rain erosion resistance of plastics composites utilizing end-oriented reinforcing fibers instead of the conventional glass fabric reinforcements. Such materials would find wide application in the fabrication of radomes and leading edge structures for high performance aircraft.

An end-oriented composite is one in which the reinforcing fibers are oriented perpendicular to a designated surface. Glass-epoxy composites with this end-oriented construction when exposed to simulated rain at subsonic velocities, have been observed to erode relatively slowly and uniformly. Surface recession for such composites seems to occur by the erosion of matrix from between fibers and the shearing of fibers left protruding above the surrounding matrix (Figures 1 and 2). A far less frequently occurring type of erosion at near-sonic velocities involves deep pitting in widely separated areas with no indication that the location of these pits corresponds to imperfections in the composite structure prior to testing (Figure 3).

End-oriented, fiber-reinforced plastics composites are being evaluated as rain erosion resistant materials by Hughes Aircraft Company under the sponsorship of the Naval Air Systems Command. This evaluation includes studies of the effect on the rain erosion resistance, as determined by whirling arm tests, of such variables as matrix, reinforcement, reinforcement configuration, and fiber loading. Most of the effort to date has involved the evaluation of unidirectionally reinforced, end-oriented composites. However, highly directional composites with a large fraction of end-oriented fibers fabricated from three-dimensional fabrics and directional fabrics and tapes have also been evaluated.

All of the rain erosion tests were run in the whirling arm facility operated by Dornier System GmbH, Friedrichshafen, West Germany.

Dornier's apparatus consists essentially of a rotor driven by a powerful electric motor. The rotor is contained inside a chamber which may be partically evacuated as required for high testing speeds. A water injection system is used to form water droplets of the desired size and quantity. The specimen holder can be adjusted to allow impact angles ranging from 15° to 90°.

The specimens consist of circular discs 0.660 inch in diameter by 0.200 inch maximum thickness. The specimen is secured to a specimen holder at the end of the rotor by means of a retaining ring. During the test, one face of the specimen is subjected to simulated rain erosion under controlled test conditions. All of the materials evaluated to date in this program were tested under the following conditions:

- Test velocity - from 300 to 466 meters/second (nominally Mach 0.9 to Mach 1.5)

*Progress Report, Dept. of Mechanical Engineering, University of Cincinnati, "Testing of Rain Erosion Resistance" Sept. 19, 1968.

- Droplet diameter - 1.2 mm
- Impact angle - 30° to 90°
- Rain density - 1.2×10^{-5} (equivalent to a rainfall rate of 7.5 inches per hour)

Prior to testing, the weight and thickness of each specimen are measured and recorded. The responses measured for a given exposure time are weight loss and erosion depth. However, many specimens erode in a manner to make measurement of erosion depth meaningless. In addition, the specimens are examined visually and by means of a scanning electron microscope for extent and nature of damage due to erosion. In most cases, repeated weight loss measurements of the same specimen are not made for various exposure times. Usually, the erosion resulting from a single arbitrary exposure time is used to compare the relative rain erosion resistance of the various composites tested.

Matrices evaluated in combination with end-oriented glass or Nomex fibers include rigid epoxies, flexibilized epoxies, polyurethanes, a polyimide, a polybutadiene and a polyphenylene oxide. Reinforcements evaluated include E glass, S glass, quartz, Nomex, Dacron, PRD-49 in the form of rovings or yarn. Reinforcement configurations evaluated include, in addition to unidirectional, end-oriented fibers, those obtained by machining composites fabricated from three-dimensional fabrics and highly directional tapes and fabrics.

The rain erosion test results obtained thus far indicate the following:

- End-oriented composites are substantially more rain erosion resistant than the corresponding fabric-reinforced composites
- Polymeric fibers such as Nomex and Dacron are superior to glass fibers
- Flexibilized matrices such as flexibilized epoxies and polyurethanes are superior to rigid epoxy matrices
- High fiber loadings increase rain erosion resistance, this effect being more pronounced in the case of glass fibers, less pronounced for Nomex fibers
- Three-dimensionally reinforced composites with a high degree of end-orientation are inferior to pure, unidirectional end-oriented composites, although 3-D polymeric fiber constructions are sufficiently rain erosion resistant to merit further evaluation

The following tables summarize the principal rain erosion test results obtained to date. Table 1 shows the increased rain erosion resistance of the unidirectionally-reinforced, end-oriented construction compared with that of the fabric-reinforced composite and various 3-D composites.

Table 1. Effect of Reinforcement and Reinforcement Configuration on Relative Rain Erosion Resistance (Matrix: Epon 828/MPDA; Test Conditions: 30 sec and 333 meters/sec)

Reinforcement Description	Fiber Content, Vol-%	Void Content, Percent	Average Weight Loss, mg	Degree of Erosion
181 E glass fabric, not end-oriented	51.2	0	622*	Deep
			411**	Deep
E glass roving, end-oriented	73.9	0	13	Light
143 E glass, end-oriented	51.3	1.2	657	Deep
7575 E glass, end-oriented	53.2	0	624	Deep
3-D E glass, angle interlock	59.7	0	416	Deep
3-D Nylon 6/6, angle interlock	66.0	0	145	Moderate
S glass Omniweave (GE)	42.3	3.3	896	Extreme
Nomex Omniweave (GE)	53.8	13.5	63	Moderate

* Tested on machined surface.
** Tested on molded surface.

Table 2 compares the rain erosion resistance of end-oriented composites reinforced with several types of fiber. The composites reinforced with the polymeric fibers are clearly more rain erosion resistant than those reinforced with E glass. Composites reinforced with polymeric fibers do not undergo spallation as do composites reinforced with glass fibers (Figure 4 shows a typical Nomex-reinforced composite after rain erosion testing). High fiber loadings appear to be necessary to achieve rain erosion resistance with E glass fibers. However, a relatively wide range in fiber loadings is permissible for the Nomex fibers. Quartz fibers are far inferior to glass fibers.

Table 2. Effect of Reinforcement and Fiber Content on Rain Erosion Resistance of Unidirectional, End-Oriented Composites (Matrix: Epon 828/MPDA)

Reinforcement	Fiber Content, Vol-%	Void Content, Percent	Velocity, meters/sec	Exposure Time, sec	Average Weight Loss, mg	Degree of Erosion
Nomex yarn	78.6	3.6	333	30	1.6	Slight
			333	60	1.0	
	64.0	2.4	333	30	0.4	Very slight no spallation
			333	60	4.4	Slight
	52.4	2.0	333	30	4.1	Slight
			333	60	9.1	Slight
	51.5	0	333	30	8.0	Slight
Dacron yarn	75.3	0	300	30	0.9	Very slight
			300	60	2.0	Very slight
PRD-49	65.6	0.6	333	30	20	Moderate
ECG glass roving	50.0	0	333	30	94	Deep
	56.9	0	333	30	263	Extreme
	65.5	1.1	333	30	98	Deep
	69.8	0.1	333	30	222	Deep
	73.9	0	333	30	13	Light

Table 2 (continued)

Rein-force-ment	Fiber Content, Vol-%	Void Content, Percent	Velocity, meters/sec	Exposure Time, sec	Average Weight Loss, mg	Degree of Erosion
Quartz	71.8	2.1	333	30	1206	Extreme
roving			333	15	354	

Table 3 compares the rain erosion resistance of glass fiber-reinforced, end-oriented composites containing various matrices. The results show clearly the improved erosion resistance obtained by the use of an epoxy-polyamide formulation or a polyurethane. Figures 5 and 6 shed some light on the difference in behavior of composites containing, respectively, a rigid and flexibilized matrix. The polyphenylene oxide and polyimide tested exhibited very poor erosion resistance.

Table 3. Relative Rain Erosion Resistance of Unidirectional, End-Oriented Composites with Various Matrices (ECG or SCG Roving)

Matrix-Roving	Fiber Content, Vol-%	Void Content, Percent	Velocity, meters/sec	Exposure Time, sec	Average Weight Loss, mg	Degree of Erosion
Epon 828/MPDA-ECG	73.9	0	333	30	13	Light
Epon 828/HV-SCG	74.3	0	333	30	72	Deep
Epon 825/ Versamid 140-SCG	77.7	0.8	333	30	4.5	Light
			466	5	4	
PR 1547-SCG (polyurethane)	59.7	0	333	30	6	Slight
P13N-ECG (polyimide)	66.9	0.5	333	30	523	Deep
Epon 828/Hycar/ piperidine-ECG	75.3	0	333	30	84	Deep
PPO 534-801-ECG (polyphenylene oxide)	74.2	5.8	333	30	-	(destroyed)
FCR 1261-ECG (polybutadiene)	77.3	0.4	333	30	522	Extreme

The feasibility of fabricating radome structures containing end-oriented, fibrous reinforcements is being studied. Efforts to date include the winding of highly directional glass and Nomex tapes on a small conical mandrel. Two methods were used: winding with pre-impregnated tape and dry winding followed by vacuum-pressure impregnation of the wound material on the mandrel. The latter method was highly successful and based on the limited effort thus far, it can be predicted that radome structures with end-oriented reinforcements are achievable by a tape wrapping technique.

ACKNOWLEDGEMENT

The assistance of Dr. Mariner Norr of the Naval Ordnance Laboratory, White Oak, Maryland in preparing the scanning electron micrographs used in this presentation is gratefully acknowledged.

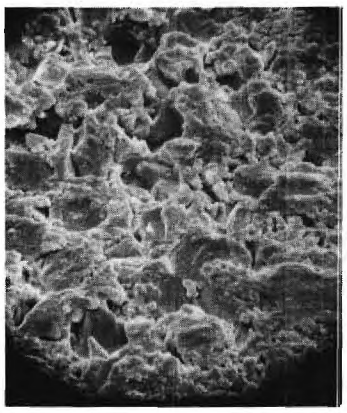

Figure 1. End-Oriented Composite Before Erosion (Kimmel-Standen)

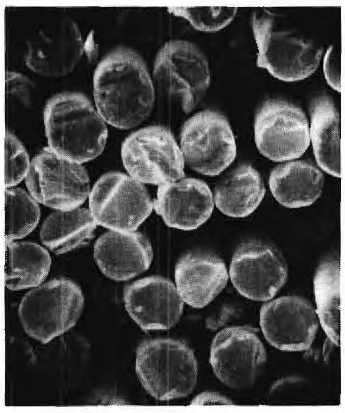

Figure 2. End-Oriented Composite After Erosion (Kimmel-Standen)

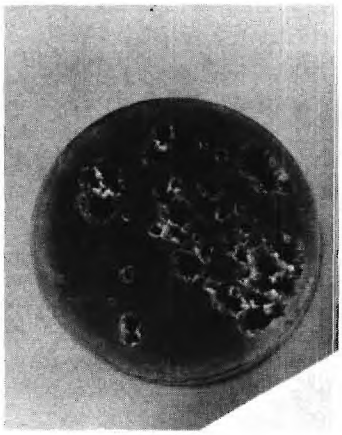

Figure 3. Glass Fiber-Reinforced, End-Oriented Composite (Kimmel-Standen)

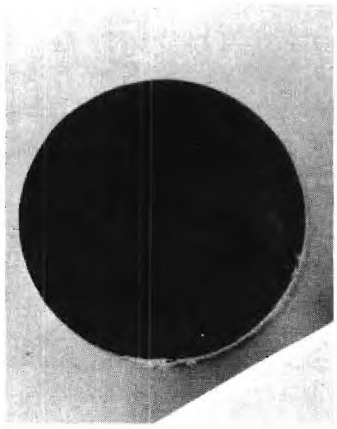

Figure 4. Nomex Fiber-Reinforced, End-Oriented Composite (Kimmel-Standen)

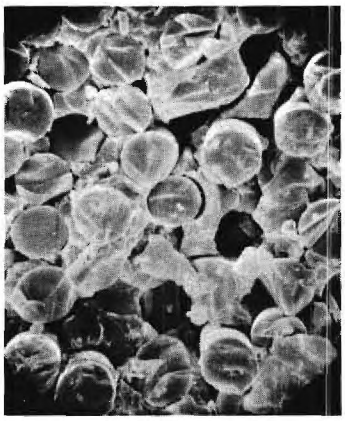

Figure 5. End-Oriented Composite With Rigid Epoxy Matrix (Kimmel-Standen)

Figure 6. End-Oriented Composite With Flexibilized Epoxy Matrix (Kimmel-Standen)

STUDIES OF DISCRETE WATER DROP IMPACT IN CERAMIC MATERIALS

BY
JOHN L. LANKFORD
ROBERT A. LEVERANCE

NAVAL ORDNANCE LABORATORY
SILVER SPRING, MARYLAND

INTRODUCTION

The problem of high-velocity water-impact damage has been under investigation for many years. As long ago as 1877, articles appeared in Proceedings of the Royal Society in England, discussing damage to low-pressure blades in steam turbines by water droplets in the wet steam.

Early investigations were carried out with water jet and wheel apparatus, cavitation "generators," and other means of providing damage environments.

In recent years the problem has taken on additional importance, because as flight speeds of missiles and aircraft increase, the damage to electronic windows, leading edges and nose cone heat shields has become severe. The requirement for all-weather capability in tactical aircraft and missiles dictates the need for solution of the problem of rain damage in critical components.

At very low impact velocities where the material is treated as a nondeforming solid and the fluid is treated as incompressible, results have been predicted successfully.

Progress has also been made at very high velocities where the material can be evaluated by hydrodynamic methods, and relations between impacting energy and certain material properties can be made to correlate with material loss in some cases.

In the velocity range representing impacts from high subsonic velocities to about 3000 feet per second, however, the material cannot be considered as a fluid, nor can its deformation and interaction with the impacting drop be neglected or generally predicted. In this region, the need for controlled experimental data is particularly critical.

The Naval Ordnance Systems Command (ORD 035) has supported a joint effort at NOL and the High Temperature Materials Division at Georgia Institute of Technology to evaluate the effect of water drop impact in this critical range of velocities. Preliminary work has been completed on several control materials and on some characterized forms of slip-cast fused silica (SCFS) (ref. (1)).

The program results included in this paper are limited to normal impacts on disc-shaped specimens 1/2 inch in diameter and 1/2 inch thick. These were held in polyethylene sabots and fired into controlled water drop patterns. Details of the technique and the apparatus for 1.2 mm drops will be found in ref. (1). Impact was monitored photographically,

and specimen and sabot were nondestructively captured after impact. A schematic of the apparatus for normal impact at atmospheric pressure is shown in Figure 1.

The 1.2 mm drops were highly spherical before encounter with the shock wave, and distortions of the drop were predicted as well as observed. This evaluation is discussed in some detail in ref. (1). Two phases of distortion and impact are indicated in the photographs of Figure 2.

The 2 mm drops were more difficult to control, and, initially, some of the drops were nonspherical. Distortion through the shock was less for this drop size, however, and no measurable effect on damage was observed due to the variation in original drop shape.

Effort is continuing on stabilization and definition of drop condition at impact with 2 mm and larger drop sizes.

The use of other techniques for introduction of the drop (ref. (2)) can be substituted if necessary. Very well-controlled and definitive experiments of discrete impact have been carried out on many materials by A. A. Fyall, et al, of RAE (ref. (2)). That work has been limited in velocity for several reasons, and catching damage in some materials had begun to appear at upper velocities with that technique.

The technique presented here was developed to obtain information through a closely spaced range of velocities from subsonic up to approximately 3000 feet per second, in order to supply much-needed experimental data on several materials in that velocity range.

Preliminary effort was directed toward establishing the effect of discrete impact under controlled conditions of drop size and velocity with the object of defining and presenting damage "thresholds" or characteristic damage patterns if such were found to exist. Preliminary work indicated that distinct patterns did exist and that, initially, these patterns and thresholds could be semi-quantitatively evaluated by simple low-magnification photographs and by observation of the material after impact with several lighting techniques. An example of this type of damage classification is shown in Figure 3 for untreated SCFS impacted by 1.2 mm drops. More exact definition of the quantitative damage is being conducted during the present phase of the program, as indicated in Figure 4. This work on detailed measurement of damage areas by several techniques will not be included in this paper, but should provide data for quantitative analysis and evaluation when completed.

UNTREATED SCFS

Typical preliminary results for untreated SCFS are presented in Figures 3 and 5. This material was developed and characterized by Georgia Institute of Technology, ref. (1). Three distinct thresholds were apparent. Early damage appeared as very small pits appearing at random locations within the impact area. This damage characteristic appeared to be somewhat dependent upon smoothness of original surface

and variation in individual specimens (see Fig. 4). The general data were well ordered and consistent, however, when consideration of experimental scatter and repeatability were taken into account. The results can be summarized by a plot like Figure 5. Here the damage characteristics or regimes have been indicated as influenced by velocity and drop size, while the thresholds as influenced by individual specimens and experimental scatter have been shown as bands between areas of different damage characteristics. The trends indicated in Figure 5 were repeated for several series of specimens and included samples from three lots of material. The total number of specimens fired at each condition are not sufficient for meaningful statistical evaluation, and additional firings would be desirable. The data repeat well enough within the limits shown in Figure 5 to be considered significant and representative. In one or two cases at each drop size, a ringed crater formation did appear at lower velocities than indicated on Figure 5. The infrequency of this result and the fact that it was not repeated when additional shots were made under the same conditions led to the preliminary conclusion that a particularly weak spot in the material was the reason for such inconsistency.

Preliminary results with the 1.2 mm drop size in untreated SCFS indicated no visible damage below approximately 1300 feet per second while some pitting always appeared above 1500 feet per second. As velocity was increased with the 1.2 mm drops, pitting became heavier and more general over the impact area. Above approximately 2100 feet per second definite craters appeared over the extent of the impact area ($\sim$ 1mm in diameter). The floors of these craters were irregular or generally flat in contour. With the exceptions noted, above approximately 2600 feet per second the craters always showed a ringed depression around their periphery with a hump or raised section in the center. The general nature of these damage characteristics is indicated in Figures 3, 4, and 5.

The preliminary results with 2 mm drops were similar to those for the smaller drops in that the same sequence and type of damage patterns appeared. A definite effect of drop size is apparent, however, since all thresholds appeared at lower velocities with the larger drops. This supports results from several experiments, indicating that damage increases with drop diameter at a given velocity beyond the simple increase in impact area.

More thorough and detailed quantitative measurements in the damage areas should provide valuable data for correlation and analysis. The visual damage thresholds and characteristics defined by preliminary results already indicate that data of the type indicated in Figure 5 should precede and complement erosion testing and evaluation of brittle materials in the velocity range covered by this investigation. Variations in velocity and nonuniformity in simulated rain fields could exceed thresholds in ceramic materials and cause failure or damage by discrete impact that cannot be readily understood or explained in terms of "average" or mean erosion rate. The need for experimental data on discrete impact under controlled conditions is also apparent even for some materials that will also be studied in an erosion or fatigue environment.

RESULTS WITH OTHER MATERIALS

Space does not permit presentation of results with other impacting and specimen materials. Preliminary work with lead spheres in several materials is reported in ref. (1).

Results with plastic spheres, lead spheres, and water encapsulated in wax have indicated that although some similarity in impact with materials other than water can be observed, satisfactory correlation between impact with solids and liquids in this velocity range has not been accomplished.

Preliminary results with treated SCFS indicate that damage thresholds are significantly influenced by treating the material (see Fig. 6).

REFERENCES

(1) Lankford, J. L., and Leverance, R. A., "Determination of Threshold Damage in Radome Materials by Discrete Impact in a Ballistics Range," NOLTR 71-113, Naval Ordnance Laboratory, Silver Spring, Maryland, 30 Jun 1971.

(2) Fyall, A. A., and Smith, P., "Single Impact Studies of Rain Erosion, Part I, Preliminary Evaluation," Royal Aircraft Establishment, Technical Report 69086, Farnborough, Hants, England, Apr 1969.

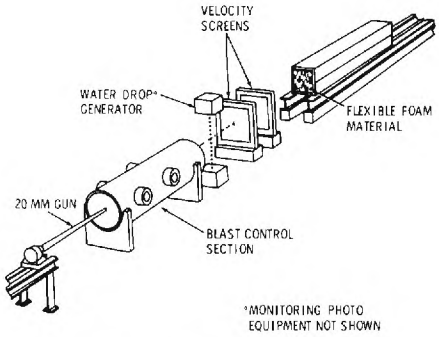

FIG. 1 EXPERIMENTAL APPARATUS FOR DISCRETE IMPACT STUDIES (ATMOSPHERIC TEST)

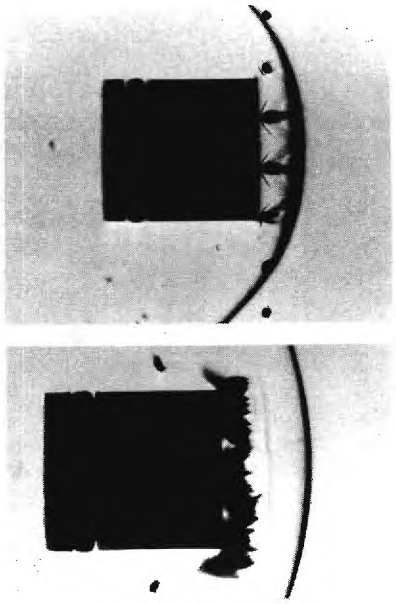

FIG. 2 DROP IMPACT PHOTOGRAPHS

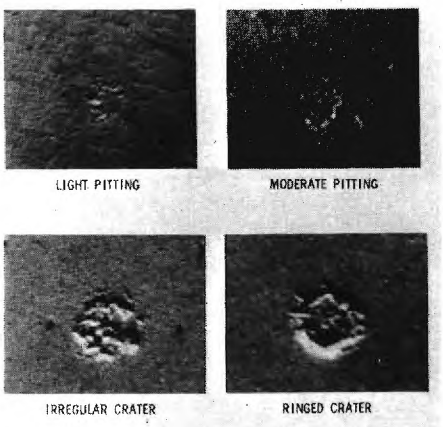

FIG. 3 CHARACTERISTIC DAMAGE IN S.C.F.S. (UNTREATED) 1.2MM DROPS

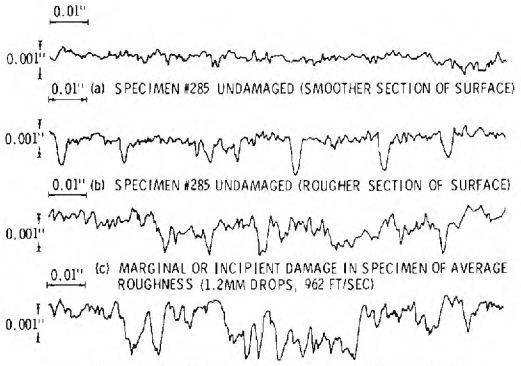

FIG. 4 SURFACE PROFILES IN SLIP CAST FUSED SILICA (UNTREATED MATERIAL - VARIATIONS IN ORIGINAL SURFACES COMPARED WITH INCIPIENT DAMAGE)

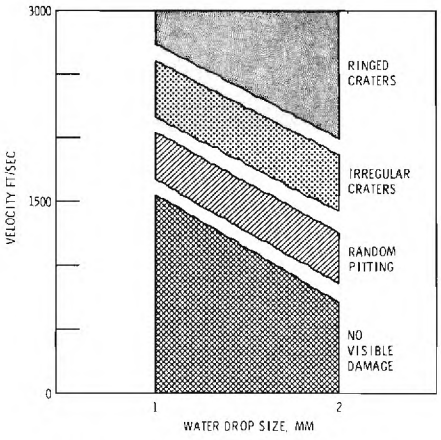

FIG. 5 DAMAGE THRESHOLDS IN (SCFS) (UNTREATED)

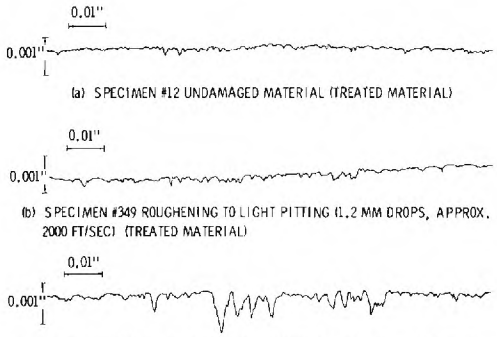

FIG.6 SURFACE PROFILES IN SLIP CAST FUSED SILICA (INCIPIENT DAMAGE TREATED MATERIAL)

EFFECTS OF SIMULATED ICING ON RADOME AND ANTENNA RADIATION PATTERNS

R. W. Wesley
Missile Systems Division

P. G. Accardi
Los Angeles Division

North American Rockwell Corporation

INTRODUCTION AND SUMMARY

The objective in this test program was to gather quantitative data regarding the degradation to the antenna radiation pattern when ice accumulates on an aircraft radome. The type of ice and the geometry of the accumulation are determined by the meteorological conditions, the speed and altitude of the aircraft, and the radome shape.

The program tested only one ice formation (simulated with wax) on a streamlined radome with a constrained lens antenna designed and fabricated by the Missile Systems Division for the Air Force Avionics Laboratory. Use of the antenna for this program was authorized by R. A. Ireland, Project Engineer, at WPAFB. The tests run consisted of antenna principal plane patterns, boresight shift, and one-way power transmission. The data were taken for the "clean" radome and for the "iced" radome, the former supplying the reference data.

With the ice accumulation, peak side lobes increased more than 10 decibels (db), maximum boresight error increased from approximately 3 milliradians to as much as 18 milliradians for in-plane error and increased from approximately 3 milliradians to as much as 14 milliradians for cross-talk error. Average one-way power transmission decreased from approximately 89 percent to 61 percent.

Because the impact of antenna performance degradation on total system performance is a function of overall system requirements, effort in this test program was oriented toward antenna performance only. The impact of the measured degradation on a total system would have to be determined for the specific system being considered.

TEST DESCRIPTION AND RESULTS

The antenna used in the test program is a low side lobe, high-gain, dual-plane monopulse space-fed transmission lens consisting of an array of slots coupled to a true time-delay collimating circuit. It is an X-band, linearly polarized (vertical for these tests) antenna with an approximately 30-inch aperture diameter, a gain of about 34 db, and a beam width of slightly over 3 degrees. The side lobes are less than -30 db in free space. For the tests, the antenna was mechanically scanned on an elevation-over-azimuth gimbal which was attached to the radome holding fixture (figure 1).

The radome used is a solid, constant-thickness half-wave wall fabricated with Selectron 5003 resin and fiberglass laminates. The radome is 86 inches long and has a 39-inch base diameter. For the tests, the radome was mounted on a hinged ring on the holding fixture. The holding fixture was attached to an azimuth-over-elevation antenna pattern positioner used for positioning and scanning the radome. The hinged ring allowed the radome to be swung open (to approximately 165 degrees) to check the free-space antenna pattern when required.

The ice configuration selected for simulation in these tests represents the accumulation which would occur in a 30-minute prelanding loiter between sea level and 22,000 feet in moderate icing conditions (0.5 gram/m^3 water content at 15° F). The configuration is shown in figures 2 and 3. The average thickness was approximately five-eighths inch; the tip was approximately 5 inches long and equally large in diameter. The ice was simulated with a methyl hydroxystearate wax (Paracin 1, Baker Castor Oil Company), which has a melting point of approximately 125° F and a dielectric constant of approximately 2.8 at X-band. The dielectric constant of ice at X-band and 10° F is given as 3.17 in Dielectric Materials and Applications, by von Hippel, and is estimated to be approximately 3.3 at 15° F. Loss tangents were not compared. The Paracin was selected because, of the readily available materials, its dielectric constant was the closest to that of ice, and it could be easily formed to the geometry of the ice accumulation and easily applied to and removed from the radome. The wax was melted to a molasses-like viscosity and applied to the nose of the radome in the approximate thickness and geometry being simulated.

The tests reported in this paper were run at a frequency of 9,400 MHz, and consisted of recording principal plane sum and difference patterns, boresight error, and one-way power transmission for both the clean and the iced radome. Table I is a summary of information from the test data for comparison of the clean and iced radome performances. Boresight error and power transmission data were measured at discrete antenna scan angles as shown.

Typical results of the tests are shown in figures 4, 5, and 6. Figures 4 and 5 are the H-plane and E-plane sum patterns, respectively, at 0-degrees elevation and 0-degrees azimuth, showing both the clean and iced radome data. These data plots have been smoothed for clarity of reproduction. Figure 6 is a comparison of the clean and iced radome data for in-plane and cross-talk boresight error and one-way power transmission for an azimuth scan at 0-degrees elevation.

Figures 4 and 5 show that severe side lobe degradation can occur with ice accumulation. Main lobe distortion was not measured. The unsymmetrical distortion of the E-plane pattern in figure 5 is probably due to the unsymmetrical application of wax on the radome (figure 3) which was unintentional and not discovered until the wax was removed. A small additional

E-plane asymmetry was the location of the antenna axis approximately 1.5 inches below the radome axis. The sum patterns at 5- and 10-degree antenna scan angles show similar but less severe distortion. In the monopulse difference patterns, null depth changes due to the simulated ice accumulation were also observed.

The data in figure 6 show that there was little boresight error introduced by the clean radome. The maximum measured was approximately 3 milliradians. The iced radome, however, resulted in significant boresight errors for both the in-plane and cross-talk components. The large magnitude of the cross-talk component of the error is probably due to the unsymmetrical wax application. As the antenna was scanned to -5 and -10 degrees elevation, the peaks of the in-plane error decreased as would be expected, while the cross-talk peak remained at approximately the same level. This latter phenomenon is probably due to the combination of the effect of the unsymmetrical wax and the normal increase in peak level expected with the elevation offset of the antenna.

Also shown in figure 6 is the one-way power transmission data taken during the test program. The reference data (clean radome) were taken for one side only, but due to radome symmetry, the transmission through both sides was assumed to be similar. The data show that extremely high losses were experienced looking through the heavy wax concentration. It has been shown in another study that much of the loss in this situation appears as increased side lobe levels. Another significant portion is absorbed in the constrained lens from mismatch at the radome interface.

CONCLUSIONS

This test program showed that ice accumulation on the radome can produce significant perturbations on the performance of a very low side lobe (<-30 db), high-gain antenna operating within a high performance radome (89 percent average transmission). One-way power transmission, boresight shift, and side lobe level were all significantly degraded by the simulated ice.

It should be noted that the results presented in this paper apply to a single configuration of ice accumulation. As the ice thickness increases during accumulation, the effects on antenna performance will vary, passing through maxima and minima with increasing electrical thickness. Additionally, a variety of types and geometries of accumulation can occur under various meteorological conditions, resulting in a variation in the magnitude of the effect on antenna performance. It is therefore suggested that, to determine the significance of the effect of ice accumulation on total radar system performance, tests should be conducted with simulations of a variety of ice types and geometries.

TABLE I. RADOME TEST DATA SUMMARY

Test	Data	"Clean"	"Iced"
Sum Patterns	H-plane peak side lobe level (db)		
	0° azimuth, 0° elevation	26	16
	0 -5	27	22
	0 -10	29	29
	5 0	24	20
	10 0	28	19
	E-plane peak side lobe level (db)		
	0° azimuth 0° elevation	29	24
	0 -5	29	18
	0 -10	29	26
	5 0	29	18
	10 0	27	25
Difference patterns	H-plane null depth (db)		
	0° azimuth, 0° elevation	20	25
	0 -5	22	23
	0 -10	22	22
	5 0	26	25
	10 0	23	31
	E-plane null depth (db)		
	0° azimuth, 0° elevation	28	24
	0 -5	30	15
	0 -10	27	26
	5 0	26	25
	10 0	26	26
Boresight error	In-plane peak (milliradians)		
	0° elevation, azimuth scan	3	18
	-5	2	12
	-10	2	10
	Cross-talk peak (milliradians)		
	0° elevation, azimuth scan	3	11
	-5	2	14
	-10	3	13
One-way power transmission	Minimum (percent)	88	36
	Average (percent)	89	61

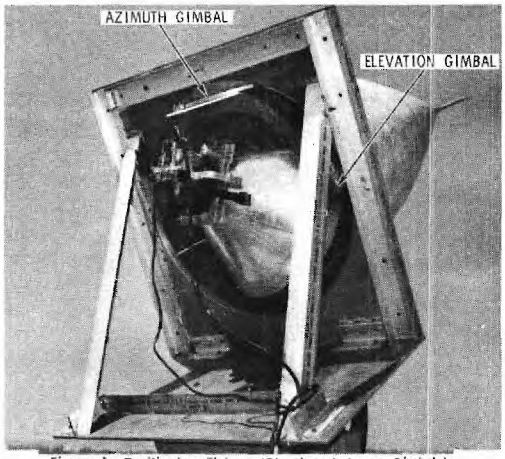

Figure 1. Positioning Fixture (Showing Antenna Gimbals)

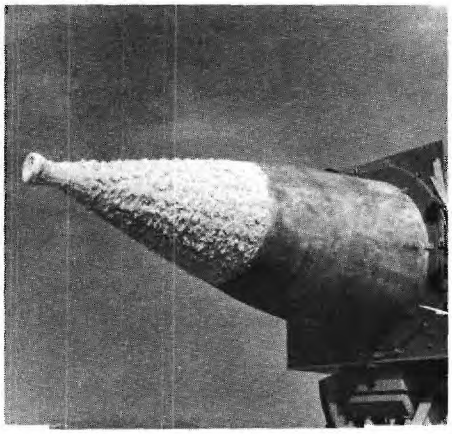
Figure 2. Test Radome With Simulated Ice

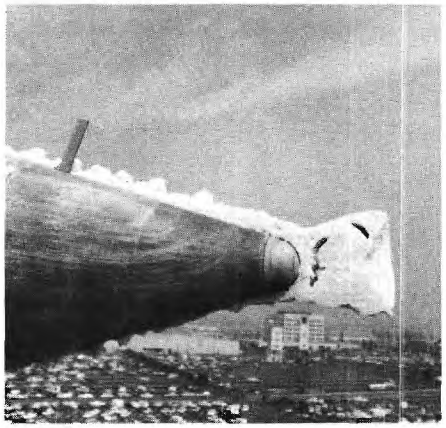
Figure 3. Cross Section of Simulated Ice Near Radome Tip

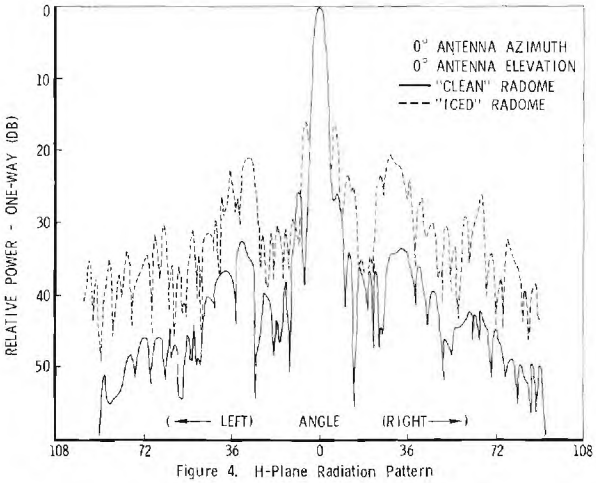

Figure 4. H-Plane Radiation Pattern

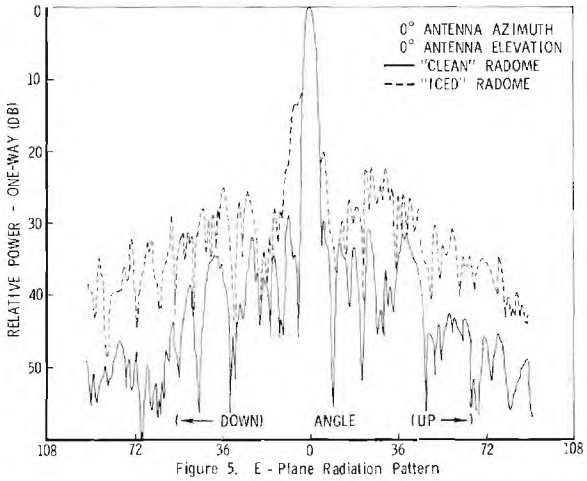

Figure 5. E - Plane Radiation Pattern

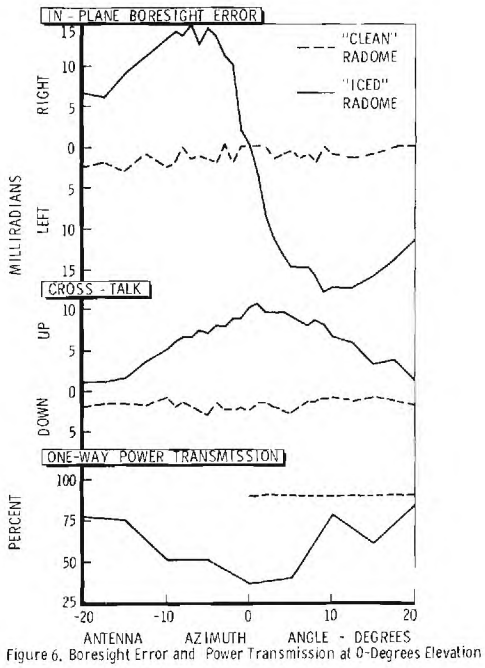

Figure 6. Boresight Error and Power Transmission at 0-Degrees Elevation

MICROWAVE HEATING OF RADOMES

KENNETH D. HILL AND JOHN D. KELLY

THE BOEING COMPANY

I.0 INTRODUCTION

A major factor influencing the choice of dielectric materials for the radome design is the maximum service temperature which is determined by aerodynamic heating in advanced airplane radomes. Recently, an additional source of major heating to radomes has emerged caused by their exposure to high-power microwaves. This source of heating stems from the microwave power dissipated within the radome.

This paper outlines the development of an analytical model to predict the temperatures inside the radome due to microwave heating. The parameters required for the solution of this problem and the method of calculating and utilizing these values are discussed. Temperature predictions made by computerized programs developed by The Boeing Company are shown for various solid-wall and multi-layered radome designs. The temperature sensitivity of radome designs to microwave power density, frequency, dielectric properties, and the environment are shown.

2.0 ANALYTICAL MODEL FOR RADOME TEMPERATURE PREDICTION

The calculation of the temperatures resulting from microwave heating require that the following be completely described at all points or surfaces of the radome: electromagnetic field, power absorption, external heat source and thermal response.

The description of the electromagnetic field throughout the radome requires a physical description of the radome and of the incident electromagnetic fields. Based on this information, internal electromagnetic fields can be described. The electromagnetic power absorption at all points throughout the radome is readily calculated from the internal field description and the dielectric properties of the materials.

The external heat sources to the radome require a relatively simple analytical expression for cases of a well defined environment, such as one of constant temperature. The problem of defining aerodynamic heating is more complex; however, this problem has been worked at Boeing, and the results are adapted for this problem. The description of the thermal response for a radome design requires a knowledge of the physical properties of the radome materials. This description must include the thermal conduction, convection, and radiation properties of each material being considered.

The above steps are combined in a computer program which determines the temperature throughout the radome, given the heat sources and a thermal response description of the radome.

2.1 Description of Electromagnetic Fields Throughout the Radome

The approach for this initial study is based on a simplified radome geometry, consisting of an infinite, flat-sheet, layered radome. The radiation description includes frequency, power density, incident angle, and polarization. The incident radiation for simplicity is assumed to be an uniform, plane wave.

The dielectric materials comprising each of the layers in a radome design have permittivity properties that are a function of temperature. For honeycomb-type materials, these properties are based upon an "equivalent" homogeneous sheet. The "equivalent" characteristics are determined from dielectric measurements of the materials.

The calculation of the electromagnetic fields within each layer of the radome is made by transmission line analysis. Assuming a layered radome geometry consisting of n layers, transmission line analysis is employed to establish the electric field expressions for the forward traveling and backward traveling waves in a given layer.

2.2 Description of the Electromagnetic Power Absorption

The power loss at all points throughout the radome is calculated based upon the expressions for the forward and the backward traveling waves in each layer of the radome. The point-power-loss in terms of the incident power density (PD) is:

$$P_p = \pi f(\varepsilon)^{\frac{1}{2}}(PD)\tan\delta$$

The power loss per unit area in the xy plane for an incremental thickness (z_2-z_1) in the "i layer", P_v is given by:

$$P_v = \text{Real of } \frac{1}{2n_i^*}\{-|{}^{+}E_i|^2\varepsilon^{-\alpha_i z_i}+|{}^{-}E_i|^2\varepsilon^{\alpha_i z_i} -2j\ \text{IMAG}|{}^{-}E_i\,{}^{+}E_i^*\,\varepsilon^{2j\ \text{IMAG}(C_i)z_i}|\}\Big|_{z=z_1}^{z=z_2}$$

where $n_i = (\frac{\mu}{\varepsilon})^{\frac{1}{2}}$, ${}^{+}E_i$ and ${}^{-}E_i$ are the electric fields of the traveling waves in the "i layer", α_i is the attenuation factor, z_1 and z_2 are the positions of depth in the radome and μ, ε are the relative permeability and permittivity, respectively. C_i is given by:

$$C_i = j\frac{2\pi}{\lambda_o}(\mu_i\varepsilon_i-\sin^2\theta)^{\frac{1}{2}}$$

2.3 Aerodynamic Heating Environment

A computer program developed at Boeing for the prediction of the radome aerodynamic heating environment calculates the convective and shock-layer radiation heating rates.

2.4 Radome Thermal Network Description

The required thermal network description of the radome must include data on the thermal conduction, convection, and radiation properties of the radome materials. The Boeing Company has a computer program (BETA) capable of balancing

the thermal energy dissipated by a system through conduction, convection, and radiation with the heat sources present. This program is sufficiently general to solve most heat flow problems.

2.5 Radome Temperature Prediction Using BETA

The Boeing Radome Temperature Distribution Computer Program (RADT) is the tool used for the prediction of the temperature distribution of a radome due to the absorption of microwave power.

This program is based on a transmission line treatment of a flat-sheet, layered radome that defines the radome's electromagnetic field and, subsequently, the power absorbed at all points within the radome. The program makes use of the BETA for the prediction of the radome temperature distribution, treating the microwave absorbed power as heat source terms in the nodal network described to the thermal analyzer. The BETA system provides a thermal analysis with options of transient or of steady-state heat flows. Physical and electrical properties that vary with temperature, time and/or distance can be included.

3.0 APPLICATION TO RADOME DESIGN

The Radome Temperature Distribution computer program was employed for temperature predictions assuming infinite flat-sheet radomes and normally incident, uniform, plane-wave radiation. Studies were made of several typical radome wall designs and the effects of power density, frequency, dielectric properties, and aerodynamic heating.

3.1 Temperature Effects of Various Radome Designs

Temperature predictions were made for a solid wall and for A- and C-sandwich radome designs with 70°F static air on the exterior radome surfaces. The dielectric materials used were epoxy, E-glass skins, and HRP for the sandwich cores (dielectric properties are shown in Figures 1 and 2). The frequencies assumed are in the 14 to 16 GHz region. For the C-sandwich the 0.520 inch core is toward the incident side.

Figure 3 shows the calculated temperature distributions for the λ solid-wall and the A- and C-sandwich radome designs, for a power density of 10 watts/inch^2, as a function of depth within the radome wall, with 0 being the incident surface. The trend of the data shows that the highest temperatures occur for the thicker radome designs.

3.2 Temperature Dependence on Frequency

Temperature dependence on frequency was investigated for frequencies of 9GHz and 14GHz using the C-sandwich of Figure 3. An external environment of 70°F was assumed on the incident surface and 250°F aerodynamic on the transmission side.

The predicted maximum temperatures are presented in Figure 4 for the two frequency cases. These data show that the maximum temperatures increase at slightly higher rate than predicted by a linear relationship with frequency.

3.3 Temperature Dependence on Dielectric Properties
The power absorbed by a dielectric material is a function of the loss-tangent, and the dielectric constant. The temperature dependence for the C-sandwich for the case of an epoxy-HRP core and for the case of polyimide-HRH core is shown in Figure 5. The data of Figure 5 vividly displays the lesser temperatures of the low-loss polyimide radome compared with that of the higher-loss epoxy.

3.4 Temperature Dependence on Aerodynamic Heating
Since aerodynamic heating is a significant heat source, one can expect its presence to affect both the maximum temperature and the temperature distribution in a radome exposed to microwave heating. Two cases were examined, the first is a 70°F static air condition on both sides while the second condition assumed aerodynamic heating of 250°F on the transmission side.

The temperatures are given in Figure 6, for a power density of 20 watts per square inch. It is interesting that the higher temperatures occur for the case of 70°F static air compared with the 250°F aerodynamic case, for power densities above 15 watts/sq. inches. This phenomenon is explained by the greater convective capability of the aerodynamic airflow as compared to static air. The predicted temperature distributions through the radome wall indicate that the general shape of the two curves are nearly the same.

3.5 Temperature Dependence on Power Density
The power absorbed by a given dielectric material is a linear function of the incident power density and the square of the electric field within a dielectric. The temperature dependence with the incident power density can be determined by viewing the temperature data plots in Figure 4, 5 and 6. The temperature plots indicate that the dependence is essentially linear with the power density.

CONCLUSION

Temperature predictions made for typical radome designs exposed to high density microwaves indicate that greater temperatures are encountered with thicker radomes. Multiple sandwich designs such as the C-sandwich are likely to present more of a problem than are an A-sandwich or λ solid wall.

The resulting temperatures from microwave heating can be greatly decreased through the use of low-loss resins, such as the polyimides, and low-loss fibers such as quartz. The maximum temperatures encountered in radomes are approximately linear to the power density and frequency. At high power densities, ground environmental conditions can produce higher temperatures than those of supersonic flight.

REFERENCES

1. Kenneth D. Hill, John D. Kelly, Radome Design For High Power Microwave Systems, The Twenty-First USAF Antenna Symposium, 12-14 October 1971

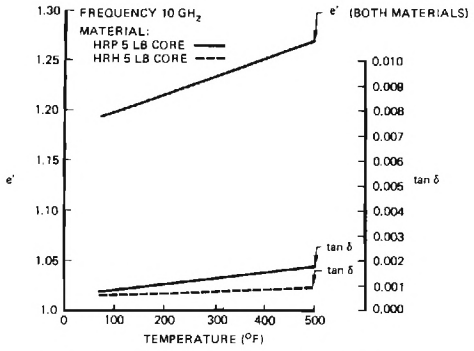

Figure 2 : DIELECTRIC PROPERTIES OF HONEYCOMB CORES

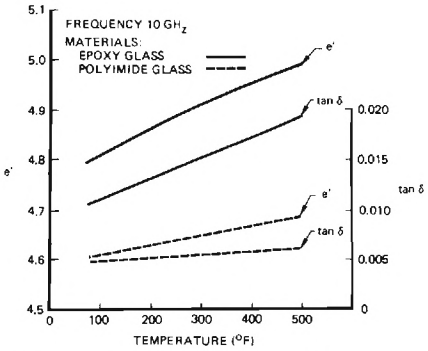

Figure 1 : DIELECTRIC PROPERTIES OF GLASS LAMINATES

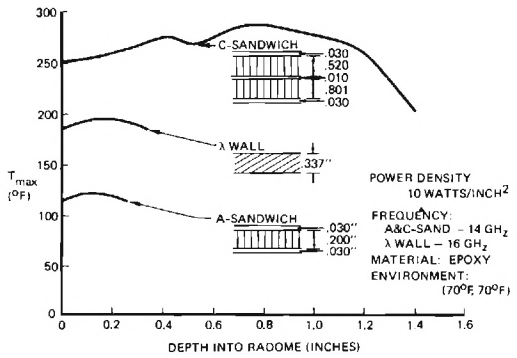

Figure 3 : TEMPERATURE DISTRIBUTION FOR VARIOUS RADOMES

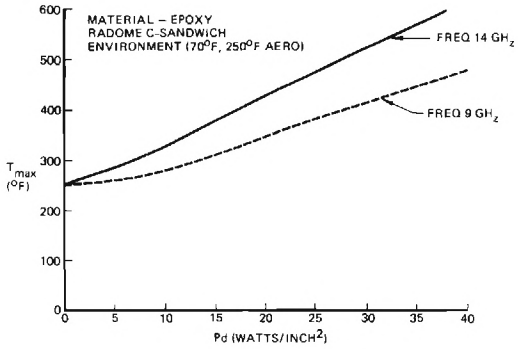

Figure 4 : TEMPERATURE DEPENDENCE ON FREQUENCY

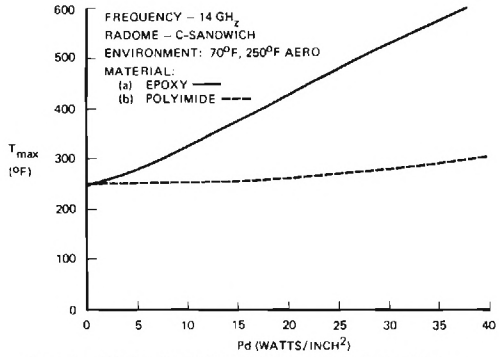

Figure 5 : TEMPERATURE DEPENDENCE ON DIELECTRIC MATERIAL

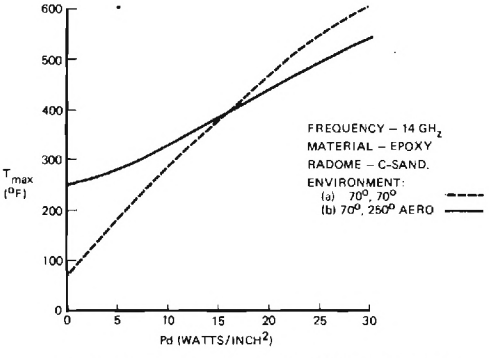

Figure 6 : EFFECT OF ENVIRONMENT ON RADOME TEMPERATURE

$MgAl_2O_4$

A New Material For Electromagnetic Windows, IR Domes, and Radomes

by: D. R. Johnson, D. L. Mann, and D. W. Roy

INTRODUCTION

Magnesium aluminate spinel possesses an unusual combination of optical, dielectric, and physical and mechanical properties that makes it a desirable material for optical, IR, and microwave windows and domes. Excellent transmission in both the IR and microwave regions makes spinel feasible for dual purpose windows.

Spinel is cubic and optically isotropic; thus, polycrystalline shapes may be formed without the problems of poor grain boundary transmission inherent in noncubic materials. In the microwave region the isotropy of spinel prevents localized absorption and heating that occurs in noncubic materials because of differing grain orientation and anisotropic dielectric loss index. Spinel undergoes no polymorphic transformations and is thus free of problems due to thermally induced phase changes. The physical and mechanical properties of spinel are listed in Table I.

OPTICAL PROPERTIES

Coors polycrystalline spinel in reasonably thin shapes exhibits excellent transparency in the visible and IR to 6μm. Figure 1 shows typical transmission data for sintered and hot-pressed parts. The index of refraction, as a function of wavelength, for spinel and other optical materials is given in Figure 2. Transparent parts are obviously free of significant local fluctations in density that would cause severe scattering of radiation in radomes and microwave windows.

DIELECTRIC PROPERTIES

Dielectric data for Coors sintered spinel are given in Table I. The low dielectric constant and extremely low dissipation factor of this material result in a very low loss index. For purposes of comparison the loss index, as a function of frequency, of spinel and other low-loss dielectrics are shown in Figure 3.

THERMAL AND MECHANICAL PROPERTIES

The choice of materials for radomes, irdomes, and electromagnetic windows is limited not only by the optical and dielectric properties of the candidate materials, but also by the ability of the materials to withstand severe thermo-mechanical environments. Particularily important properties include strength, thermal shock resistance, erosion resistance, and toughness. Table II compares the thermal-mechanical properties of spinel and some other optical and dielectric materials.

Resistance to rain erosion is very important to radomes and irdomes. Limited data available indicate that spinel has excellent resistance to rain erosion. On June 6, 1972, a rain erosion test was conducted at the

---

Supported in part by the Air Force Materials Laboratory, Manufacturing Technology Division, Wright-Patterson Air Force Base, Ohio, under Contract No. F33615-72-C-1133; L. Kopell (AFML/LTP), Project Engineer

Naval Weapons Center, China Lake, California. A number of materials were simultaneously tested: spinel; sapphire; yttria-alumina garnet; calcium and magnesium fluoride-with and without sapphire coatings; magnesium oxide; and two glasses-Corning 7913 and 1723. In the accelerated test all the specimens failed mechanically - except the spinel. The spinel showed virtually no damage, the sapphire and YAG failed via a single-line fracture, the others shattered into many pieces.

Table I. Physical and Mechanical Properties of $MgAl_2O_4$

Lattice Parameter (1)		8.0833 Å
Density (1)		3.584 g/cc
Melting Point (1)		2135°C
Coefficient of Lineal Thermal Expansion		
	25-200°C	5.6×10^{-6}/°C
	25-500°C	7.3×10^{-6}/°C
	25-1000°C	7.9×10^{-6}/°C
Thermal Conductivity (1)		
	100°C	0.0357 cal/(sec)(cm)(°C)
	1200°C	0.0130 cal/(sec)(cm)(°C)
Specific Heat (1)		
	20°C	0.200 cal/g °C
	1040°C	0.214 cal/g °C
Index of Refraction		1.71
Dielectric Constant		
	10^3 Hz	8.2
	10^6 Hz	8.2
	9.3×10^9 Hz	8.3
Dissipation Factor		
	10^3 Hz	3.0×10^{-5}
	10^6 Hz	2.0×10^{-5}
	9.3×10^9 Hz	1.3×10^{-5}
Loss Index		
	10^3 Hz	2.5×10^{-4}
	10^6 Hz	2.0×10^{-4}
	9.3×10^9 Hz	1.0×10^{-4}
Strength (1)		
	Ultimate Strength in Four-Point Bending	
	25°C	33,400 psi
	1260°C	33,000 psi
	Yield Stress in Four-Point Benging at 0.005 in/min.	
	25°C	--
	1250°C	11,470 psi
	Ultimate Compressive Strength	
	25°C	390,000 psi
	1550°C	6,220 psi at 5×10^{-4} min^{-1}
Hardness-Knoop	1300 Kg/mm^2 (200 g load)	
Modulus of Elasticity (1)		
	35×10^6 psi Static	
	39.9×10^6 psi Dynamic	
Shear Modulus (1)	15.89×10^6 psi Dynamic	
Bulk Modulus (1)	27.93×10^6 psi Dynamic	
Poisson's Ratio (1)	0.2608	

Table II Thermo-Mechanical Properties of Optical and Dielectric Materials

	σ, psi x 10^3	KHN, Kg/mm^2	E, psi x 10^6	ν	K cal/(cm)(sec)(°C)	α $°C^{-1}$ x 10^{-6}
$MgAl_2O_4$	33.4	1300 (200g)	35	0.26	0.0357	7.9 (25-1000°C)
Y_2O_3 (2)	17.0	875	25	0.30	0.037	7.9 (25-900°C)
Al_2O_3 (9)	41.0	2038 (200g)	57	0.22	0.095	8.0 (25-1000°C)
Al_2O_3 (13)	80.0	1882 (200g)	56	0.22	0.093	8.0 (25-1000°C)
BeO (7)	40.0	980 (200g)	51	0.26	0.67	8.9 (25-1000°C)
MgF_2 (4)	21.8	576	16.6	--	0.034	10.7
MgO (11)	31.5	600	44	0.19	0.091	7.1 (25-1000°C)
SiO_2 (12) Glass	7.2	560 (100g)	10.5	0.16	0.003	0.56 (25-300°C)
Glass-Ceramic (8)	35.0	698 (100g)	17.4	0.25	0.008	0.57 (20-300°C)

Polycrystalline spinel compared favorably with the other optical and dielectric materials. It is exceptionally strong and hard for an optical material, has good thermal shock resistance, moderate thermal expansion coefficient, and is dimensionally and mechanically stable at temperatures up to 1250°C. The polycrystalline structure results in blunting and redirecting of cracks at grain boundaries; thus offering greater toughness than spinel single crystals. The high strength and hardness of spinel makes it feasible to use thinner windows and domes than could be fabricated from lower strength, softer materials. The reduced wall thickness results in lower thermal stresses and improved transmission. The homogeneity, isotropy, and very low dielectric loss index of Coors optically transparent spinel, along with the thermo-mechanical properties, result in an exceptionally stable electromagnetic window.

PRODUCTION

Coors polycrystalline spinel optics are formed by either sintering or hot-pressing. Sintering is accomplished by pressing the spinel powder to a green density of ~65% of theoretical density and then heating to ~1800°C to affect consolidation and removal of porosity. In hot-pressing, a uniaxial pressure of ~10,000 psi is applied to the powder, constrained in a punch-and-die set, while it is being heated. Fully dense, transparent parts can be formed at a lower temperature than with sintering: 1550°C. Optics can be fabricated with greater wall thickness by hot-pressing. Typical microstructures for sintered and hot-pressed parts are given in Figure 4 and 5.

Because of economy, versatility, and larger production capability, sintering is the preferred method of fabrication. At the present time, discs, tubes, rods, and domes having good transmission in the optical and IR can be sintered with up to 0.080" wall thickness. Other dimensions are limited only by furnace capacities. As improved synthesis and fabrication methods are developed, optically clear shapes with thicker walls will become available. Wall thicknesses up to ¼" are envisioned for the future.

Optically clear discs 4" diameter x ¼" thick are presently being fabricated by hot-pressing. Coors is scaling-up the hot-pressed part size to

10" x 10" x½" thick under contract to the Air Force.* Scale-up and process optimization are scheduled to be completed by February 1973.

REFERENCES

1. Hayne Palmour III "Flow and Fracture in Spinel Structured Ceramics", Contract DA31-124-ARD-D-207, Department of the Army Project No. 2001050113700, Army Research Office, Durham N.C. 4932-MC Jan. 1970.
2. Yttralox Ceramic, G.E. Research and Development Center, Schenectady N.Y. R. C. Anderson and J. Barker, "A Unique Optical Ceramic" OPTICAL SPECTRA January/February, 1969, pp 56-60.
3. Lucalox Alumina, General Electric Company.
4. Irtran I, Eastman Kodak Company, Rochester, N.Y. Publication U-72, 1971.
5. Insulation/Circuits Directory/Encyclopedia, Lake Publishing Corp. Libertyville, Illinois, June/July 1971.
6. American Lava Corporation, Chatanooga, Tenn. Chart No. 671
7. Coors BD-995-2 BeO.
8. Corning Glass-Ceramic No. 9606. Corning Glass Works, Corning, N.Y. Materials Handbook, Sixth Edition, April, 1963.
9. Coors VISTAL Alumina.
10. Corning Glass No. 7940, H. E. Busset, et al, "International Comparison of Dielectric Measurements", IEEE Transactions on Instrumentation and Measurement, Vol IM-13, No. 4, pp 305-311, December 1964.
11. Engineering Properties of Selected Ceramic Materials. The Am. Ceram. Soc. Columbus, Ohio, 1966.
12. Corning Glass No. 7940. Corning Glass Works, Corning, N.Y.: Materials Handbook, Sixth Edition, April, 1963.
13. Coors AD-999 Alumina.

*Contract No. F33615-72-C-1133.

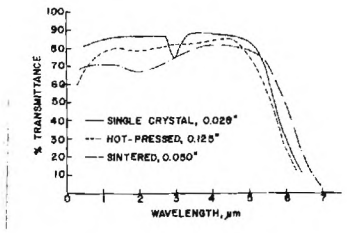

Figure 1. Optical and IR Transmittance of Spinel Parts.

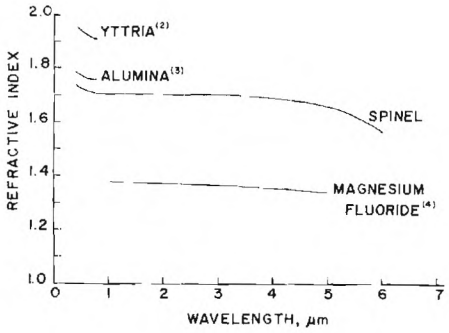

Figure 2. Index of Refraction vs. Wavelength For Optical Materials.

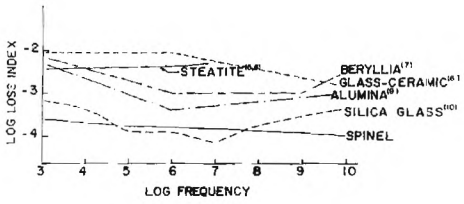

Figure 3. Dielectric Loss Index vs. Frequency For Low-Loss Materials.

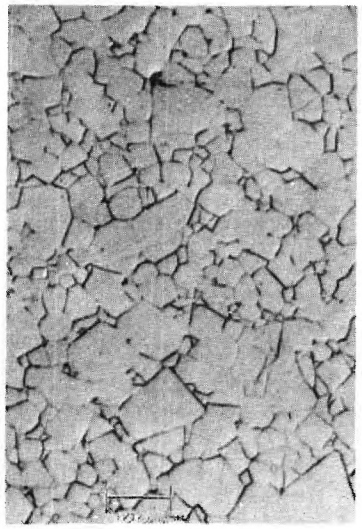

Figure 4. Typical Microstructure of Transparent Hot-Pressed Spinel. Polished and Thermally Etched Surface.

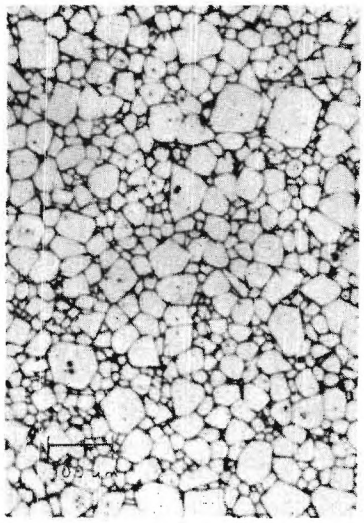

Figure 5. Typical Microstructure of Transparent Sintered Spinel. Polished and Thermally Etched Surface.

HIGH TEMPERATURE EVALUATION OF RADOMES AND RADOME MATERIALS USING THE FRENCH SOLAR FURNACE

By

J. D. Walton, Jr.
Engineering Experiment Station
Georgia Institute of Technology

I. INTRODUCTION

The primary advantage in using a solar furnace for the high temperature evaluation of materials is that the environment is "clean." That is, there are no combustion products or ionized gases in the environment surrounding the material being heated.

Although small parabolic reflectors provide sufficiently high temperatures for a limited study of small specimens, the area of peak heat flux and temperature is only a fraction of an inch in diameter. For many high temperature experiments it is desirable that the high temperature area be many square inches and the temperature over the test area be as uniform as possible. These conditions are most important for the determination of emittance, heat transfer, thermal conductivity, thermal stress and the electrical properties of ceramic materials and for the electrical evaluation of full scale radomes at high temperatures. To provide the thermal environment in which such quantitative data can be obtained, the world's largest solar furnace at Odeillo, France is uniquely suited.

II. THE FRENCH CNRS SOLAR FURNACE

A. Description 1/

The French solar furnace is located in the Pyrenees at Odeillo-Font Romeu (altitude of 5900 feet) about 20 miles east of Andorra. Figure 1 is a schematic of this furnace. The parabolic reflector has a focal length of 59 feet, is 130 feet high and 175 feet wide and is composed of 9500 mirrors 17.7 inches by 17.7 inches. Sixty-three smaller mirrors (heliostats) set in eight tiers follow the sun and reflect its rays in parallel beams onto the parabola. The heliostats are 24.6 feet by 19.7 feet.

B. Thermal Characteristics 1,2/

The solar energy incident on an area of about 23,000 square feet is concentrated by the parabolic reflector into an area about two feet in diameter. The distribution of thermal energy in the focal area of the solar furnace is shown in Figure 2. Curve 0 represents the heat flux at the focal plane. Curve d/2 shows the heat flux incident on a plane removed one-half the diameter of the solar image (about 3.3 inches) behind the focal plane. Curve d shows the heat flux incident on a plane removed one diameter of the solar image (6.6 inches) behind the focal plane. Figure 3 is an energy contour map and shows the distribution of the heat flux in watts/cm^2 at the focal point.

C. Suitability for Materials Evaluation

From Table I and Figures 2 and 3 it can be seen that, in an area about 2 inches in diameter at the focal point of the solar furnace the temperature of the solar radiation is 6840 ± 75° F and the minimum heat flux is approximately 1350 ± 50 Btu-ft^{-2}-sec^{-1} for an incident radiation of 950 W m^{-2}. These data show that the Odeillo solar furnace is capable of providing a relatively constant high temperature, high heat-flux environment (±2.5%) over the surface of a circular sample two inches in diameter. By moving away from the focal plane the heat flux decreases (Figure 2) and the uniformity of heat flux over a given area increases.

The temperatures and heat fluxes available in the solar furnace should be sufficient to melt, vaporize, or decompose most ceramic materials. Therefore, this facility provides an environment in which the effect of the molten surface, decomposition or vaporization products on the heat transfer, emittance and electrical properties can be studied.

III. PROPOSED MATERIALS EVALUATION PROGRAM

A. High Temperature Materials Division Program to Measure Dielectric Properties at High Temperatures

In 1970 the Engineering Experiment Station undertook a program to develop the apparatus and technique for determining dielectric properties of ceramic materials at temperatures to at least 4000° F 3/. A free-space system was selected for electrical measurements at high temperatures under transient heating conditions in order to avoid the deformation and distortion associated with steady state heating using metallic sample holders. The technique developed utilized a system which subjected the dielectric sample to heat from one side only, which enabled measurements to be made on many materials at temperatures above their melting point.

B. Preliminary Evaluation of Materials in Odeillo Solar Furnace

The background and experience gained in the high temperature dielectric measurement program suggested that a similar method might be used to evaluate materials in the high heat-flux, thermal radiation environment provided by the solar furnace at Odeillo, France.

Basically, the proposed program would utilize a 16-inch diameter slip-cast fused silica disc which would hold the test specimens, which would be 2 inches in diameter. Since slip-cast fused silica has a very low thermal conductivity (0.4-0.5 Btu/ft-hr-°F), and will serve as the carrier disc, the edges of the specimens will be insulated and the heat flow into them should be one dimensional.

1. Proposed Test Apparatus. Figure 4 shows the initial design considered for the evaluation of materials in the solar furnace. This design consists of three major components, two thermal shields and a slip-cast fused silica sample holder disc with eight test samples. With the doors of the solar furnace closed, the apparatus shown in Figure 4 will be positioned so that the sample holder disc is in the focal plane of the furnace and the first test sample at the focal point of the furnace.

Thermal Shield No. 1 is designed to limit the solar radiation to a circular area 3 inches in diameter and concentric with the axis of the solar radiation. Thermal Shield No. 2 is designed to block the solar radiation from the test area during the period of time that the solar furnace doors are opened and closed (about 60 seconds for each operation). With Thermal Shield No. 1 positioned as shown in Figure 4, the furnace doors will be opened. Thermal Shield No. 1 will then be removed to expose the first sample to the solar radiation. After the specified exposure time the holder disc will be rotated to expose the next sample. This procedure will be repeated until all eight samples have been exposed, at which time Thermal Shield No. 1 will be replaced in the path of the solar radiation while the furnace doors are closed.

IV. PRELIMINARY TESTS

Fused silica foam was exposed to the peak heat flux during the period of the opening and closing of the furnace doors to simulate Thermal Shield No. 1; and for a continuous period of one minute to simulate Thermal Shield No. 2. Figure 5 shows a 12-inch by 16-inch piece of foamed fused silica after exposure to the peak heat flux of the solar furnace. The hole on the right developed during the period of opening and closing the solar furnace doors. The left side was exposed to the maximum heat flux for a period of one minute. There was evidence of melting or vaporizing of the fused silica foam within the first few seconds of exposure and the thickness of the foam (1 inch) was penetrated in the first 30 seconds of exposure.

A slip-cast fused silica disc was exposed to the peak heat flux for periods of time up to 60 seconds. Melting commenced after about 30 seconds and proceeded to a depth of about one half of an inch at the end of 60 seconds. The disc and the foam sample were supported in the furnace as shown in Figure 6.

V. CONCLUSIONS

The results obtained from the preliminary tests conducted in the solar furnace at Odeillo, France and the background of the high temperature dielectric property measurement program suggest the following conclusions:

1. The focal point of the Odeillo solar furnace provides a uniform ($\pm$ <5%) high temperature (6840 $\pm$ 75° F) high heat flux (1350 $\pm$ 50 Btu-ft^{-2}-sec^{-1}) thermal environment over an area at least 2 inches in diameter.

2. A 2-inch diameter sample in the focal point of the Odeillo solar furnace can be instrumented to obtain quantitative high temperature property data such as emittance, radiant heat transfer, thermal conductivity, thermal stress and dielectric behavior.

3. Slip-cast fused silica can be used as a carrier disc for sample exposure times of up to 30 seconds at maximum heat flux intensities.

4. Foamed fused silica is not suitable for thermal shield applications requiring direct exposure to maximum heat flux intensities.

5. The quantity and distribution of the thermal energy provided by the French solar furnace suggests that full scale radomes of the order of three feet long and fifteen inches in base diameter could be heated to temperatures as high as 3000° F and electrical performance determined during heating.

REFERENCES

1. F. Trombe and A. LePhat Vinh, "Caracteristiques et Performances Energetiques du four solaire de 1000 kW du Centre National de la Recherche Scientifique," C.R. Acad. Sc. Paris, t 272, p 1104-1107 (10 mai 1971).

2. F. Trombe, L. Gion, C. Royere and J.F. Robert, "Traitment d'Oxydes Refractaires au Four Solaire de 1000 kW du Centre National de la Recherche Scientifique," C.R. Acad. Sc. Paris, t 272, p 1971-1973 (14 juin 1971).

3. H. L. Bassett, S. H. Bomar, Jr., G. K. Huddleston and A. C. Merritt, "High Temperature Complex Permittivity Measurements on Reentry Vehicle Antenna Window Materials," Technical Report AFWL-TR-71-189, January 1972.

TABLE I

CHARACTERIZATION OF THERMAL RADIATION AT FOCAL PLANE OF ODEILLO SOLAR FURNACE (1)

Diameter of Radiation (in)		0.79	2.36	6.61 (2)	11.81	15.75
Per Cent of Total Energy in Area of Radiation		0.5	4.50	27	58	75
Energy in Area of Radiation (kW)		5	45	270	580	750
Minimum Heat Flux (3)	Watts-cm^{-2}	1600	1472	912	400	192
	Btu-$ft^{-2}s^{-1}$	1410	1297	804	352	169
Average Heat Flux (3)	Watts-cm^{-2}	1600	1595	1215	820	595
	Btu-$ft^{-2}s^{-1}$	1410	1405	1071	723	524
Temperature of Radiation °F	Min.	6915	6765	5945	4755	3885
	Avg.	6915	6880	6485	5765	5340

(1) For incident energy of 950 W m^{-2} ± 5 per cent.

(2) Diameter of solar image.

(3) Heat flux calculated from water calorimeter and radiometry measurements.

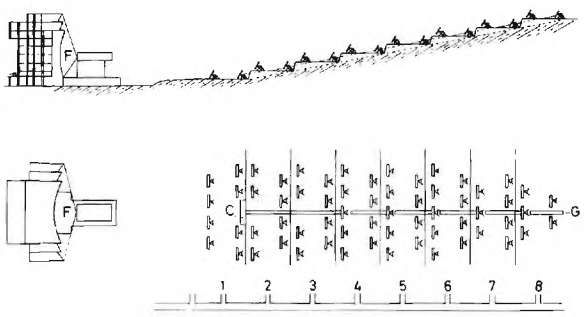

Figure 1. Schematic of Odeillo Solar Furnace.

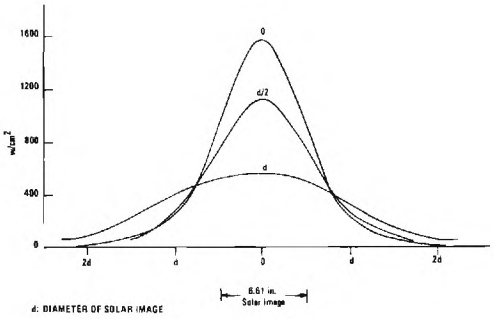

Figure 2. Solar Energy vs Distance from Focal Point in Odeillo Solar Furnace.

Figure 3. Distribution of Thermal Energy in a Plane Inclined at 25° from Vertical at the Focal Point of the Odeillo Solar Furnace.

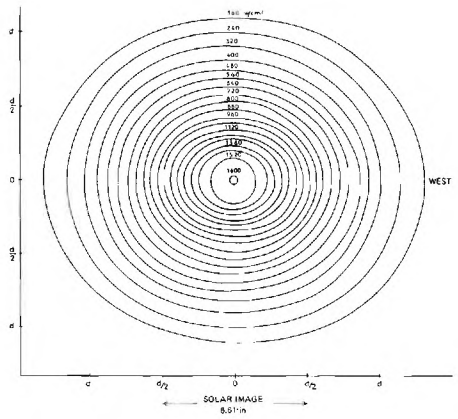

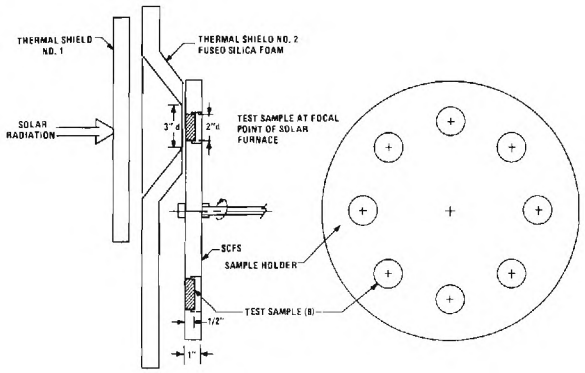

Figure 4. Proposed Slip-Cast Fused Silica Sample Holder and Thermal Shield.

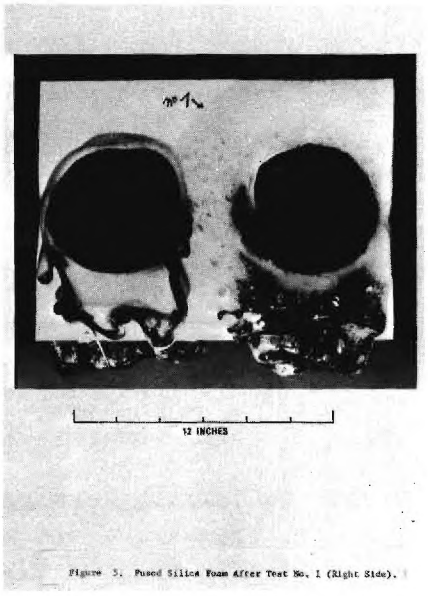

Figure 5. Fused Silica Foam After Test No. 1 (Right Side).

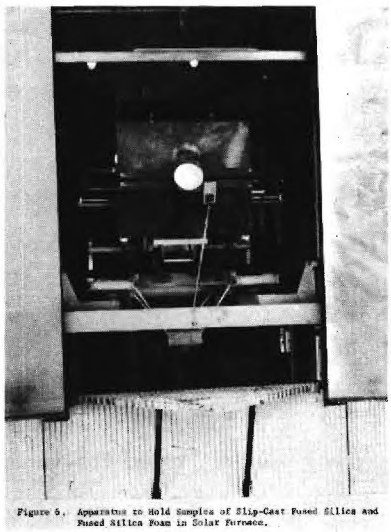

Figure 6. Apparatus to Hold Samples of Slip-Cast Fused Silica and Fused Silica Foam in Solar Furnace.

HIGH-TEMPERATURE COMPLEX PERMITTIVITY MEASUREMENTS ON ANTENNA WINDOW MATERIALS*

S. H. Bomar, Jr. & H. L. Bassett
Engineering Experiment Station
Georgia Institute of Technology
Atlanta, Georgia

ABSTRACT

About three years ago a new technique was developed at Georgia Tech for measurement of the complex permittivity of radar window materials at high temperatures. The new method extended the temperature range of complex permittivity measurements into the 4000° to 4500° F region. The specimen is in the form of a disc which is heated on one side by oxyacetylene flames, then passed through the sample arm of a focused microwave bridge; the specimen is in continuous rotation so that a portion of the revolution is used for heating and the remainder for making microwave and temperature measurements. Experimental data are collected in a transient heating situation; the data are later processed to determine temperature vs. distance profiles at various times during the run, then to determine the dielectric constant and loss tangent vs. temperature functions which must have existed to yield measured microwave phase shifts and transmission coefficients.

This paper describes a research program to modify the original measurement system and to obtain complex permittivity vs. temperature data on six candidate window materials. The objectives accomplished by the modifications were: (1) reduction of sample size to three inches diameter, (2) measurement of up to four sample materials in each experimental run, and (3) substantial improvement of temperature measurement techniques. Complex permittivity data are given for slip-cast fused silica, a quartz fiber composite, hot pressed boron nitride, and isotropic pyrolytic boron nitride.

Both the program for development of techniques and the program to measure several materials were sponsored by the U.S. Air Force Weapons Laboratory.

Section I. Introduction

Conventional high temperature microwave dielectric constant and loss tangent measurements are limited to temperatures tolerated by the mechanical stability of the waveguide or metallic cavity walls. Also, some materials can sinter during thermal equilibration at high temperatures, so that the sample character and dimensions are changed. Problems of this type impose a practical limit of about 2500° F on microwave cavity dielectric constant and loss tangent measurements.

In 1968 a program was begun to develop a free space system capable of making these measurements at temperatures above 2500° F. The free space geometry was chosen to circumvent the problems of containing the sample, and a flame heat source was used in order to achieve temperatures of 4000° to 4500° F. For the required measurements to be made on an unbound sample,

*This work was performed under Contract F29601-70-C-0069 and was administered by the Air Force Weapons Laboratory at Kirtland Air Force Base; part of the funding was furnished by NASA-Langley Research Center. Lieutenant Colonel Walter M. Hart, Jr., Captain David P. Knott and Captain Edward S. Bocian served as technical project officers.

several major experimental problems must be solved. It is necessary to isolate the flame from the sample measurement area to avoid interference with the electrical measurements, and a microwave geometry must be found which allows inclusion of the sample in a bridge in such a way that all losses are accounted for. Another important consideration is the fact that most electromagnetic window materials will either deform in shape or melt if uniformly heated from all sides and allowed to reach temperatures within the 3000° F to 4000° F range. These latter difficulties can be solved by heating the sample from only one side and by operating in a transient mode rather than reaching thermal equilibrium. Measurements can be made on window materials at temperatures far above their melting points, and the experimental conditions approach the actual reentry environment conditions.

The first research program in this area employed samples in the form of discs about 18 inches diameter by 0.7 inch thick. The microwave beam used a 6-inch diameter circular area of the specimen, and the remainder of the sample was heated by oxyacetylene torches. Measurements were made at X-band (9.3 GHz) on slip-cast fused silica specimens. These results have been reported earlier (Ref 1-3).

Section II. Measurement System

A second program was begun in 1970 to further refine the high temperature dielectric measurements technique and to obtain data on six candidate window materials. In this work, the samples were to be circular discs no larger than 3 inches diameter, mounted in a slip-cast fused silica carrier disc. The carrier would be rotated about its center and heated from one side by oxyacetylene torches as before. A microwave measurement area would be kept clear of flame as before, and experimental data would be collected each time a sample passed through the measurement area. Optical pyrometry techniques were to be improved and additional thermocouples were to be provided on the samples. These new requirements led to several significant changes in the original high temperature measurement system: (1) To meet the 3-inch sample diameter requirement, the microwave frequency was changed from 9.3 GHz to 24 GHz and the original prolate spheroidal reflectors replaced by a horn-lens focused system; this reduced the microwave beam diameter at the 20 dB points to less than 3 inches. (2) The mandrel, on which the rotating carrier disc is mounted, was designed with 18 small conduits through which thermocouple leads could be passed. Thermocouple signals are transmitted through brass slip rings and mercury contacts. (3) Two fast-response optical pyrometers operating in the infrared portion of the spectrum were used for measurement of the heated surface temperatures. Infrared pyrometers were chosen to insure that surface rather than in-depth temperatures were measured on silica-based specimens. (4) All instrumentation was arranged to have sufficiently fast response time that data could be collected during the brief period in the carrier revolution when each specimen was in the microwave beam area.

The focused beam system subjects the disc-shaped samples to heating on one side by oxyacetylene torches. During a measurement run the torches are usually operated for about 200 seconds; by the end of this time the front surface temperatures have leveled out in the range of 3500° to 4500° F, depending on the thermal properties of the individual samples. Temperature gradients are established in the samples, but the run is terminated before steady state temperatures are attained. The instrumentation records the following data as functions of run time: heated surface optical temperatures,

internal and back surface thermocouple temperatures, change in sample insertion phase, reflection coefficient phase, sample insertion loss, incident power and reflected power. During the run the sample is continuously moved axially in the microwave beam (± quarter-wavelength longitudinal displacement) so that the average insertion loss can be determined. An event mark signal is placed on all recordings once in each carrier revolution so that the response of each sample can be identified. Thermocouples are mounted on 1.5 inch diameter "thermal samples" which are placed in the carrier disc adjacent to their respective 3-inch diameter "microwave samples."

The microwave measurement system employs the free-space phase-shift bridge and transmission technique described by Redheffer (Ref 4) to determine the complex permittivities of material. The focused beam system forms the sample arm of the microwave bridge. The other arm of the bridge is the reference path for the microwave signal. The material specimen is placed in the focal region of the lenses normal to the beam axis in the sample arm, and the resulting change in electrical path length is measured by a phase detector network. Simultaneously, the attenuation due to the sample is measured. The complex permittivity is later computed from these data. Electrical measurements can be performed either with a static or dynamic thermal environment since the phase and amplitude data are measured and recorded continuously without having to make the usual mechanical phase shifter adjustments. The measurements are made at a frequency of 24 GHz. The focused beam is formed by an 18-inch diameter double convex fused silica lens which is illuminated by a pyramidal feed horn. The material sample is positioned at the focal point of the lens which is located 17 inches from the center of the lens. The incident beam is focused to a 2.6-inch diameter circle (20 dB points) at the focal point. An identical horn-lens system, whose focal point is coincident with that of the transmitting lens, acts as the receiving aperture in the free-space bridge.

The samples are mounted in a 16-inch diameter carrier disc which is enclosed in a furnace and rotated about its axis at about 25 revolutions per minute. The furnace has open windows on each side through which the microwave beam passes; provisions have been made to keep the microwave beam area free of flame and combustion gases. The front section of the furnace, on which the torches are mounted, pivots upward to allow installation of samples and lighting of the torches.

Section III. Processing of Data

Computer programs (Ref 5) are used to obtain smooth temperature profiles from the measured data and to determine the complex permittivity of the materials tested. First, temperature profiles at various times during the experimental run are calculated. The thermal analysis program used for this purpose accounts for density changes due to melting, sintering or expansion and variable heat capacity and thermal conductivity. Sample thickness is calculated with each temperature profile. Next, several of these profiles and thicknesses corresponding to known times in the experimental run are used as input data to an electrical analysis program. Other electrical program input data are measured phase shifts and transmission coefficients of run times matching the temperature profiles, and estimates of the dielectric constant and loss tangent as functions of temperature. The program then divides the sample into 760 layers and based on the temperature profiles and the estimates of dielectric constant and loss tangent, values of transmission coefficients and phase shifts are computed as functions of time.

These computed values are compared to the measured values of transmission coefficient and phase shift; an error term is generated to correct the initial dielectric constant and loss tangent vs. temperature curves; the program recycles until the computed phase shift and transmission coefficient matches the measured phase shift and transmission coefficient as functions of time.

Section IV. Results

Figures 1 and 2 show temperature profiles at various run times for high-purity slip-cast fused silica (SCFS) and HD-0092 hot pressed boron nitride (HPBN) respectively. These profiles are typical of silicas and boron nitrides; the relatively low thermal conductivity of SCFS results in steeper profiles and higher front surface temperatures than are attained with HPBN run under the same experimental conditions. Recalling that the raw electrical data collected during these runs included change in insertion phase and transmission coefficient as functions of run time, it is possible to make rough estimates of radar window transmission characteristics using the temperature profiles and the raw electrical data. The microwave transmission data are given in Reference 5.

Figures 3 through 6 show the final dielectric constant and loss tangents for SCFS, AS-3DX fused quartz fiber composite, HPBN and isotropic pyrolytic boron nitride (IPBN) respectively. The sharp increase in dielectric constant and loss tangent of SCFS and the fused quartz composite in the range of 2800° to 3000° F is associated with densification and melting of the materials in that temperature range. The data in Figures 3 through 6 were verified by short circuit waveguide measurements up to 2000° F; the results of these measurements are given in Reference 5.

References

1. H. L. Bassett and S. H. Bomar, Jr., "Dielectric Constant and Loss Tangent Measurement of High-Temperature Electromagnetic Window Materials," Contract F29601-68-C-0060, Technical Report AFWL-TR-69-92, AD 864731, Dec. 1969.

2. H. L. Bassett, "A Free Space Focused Microwave System to Determine the Complex Permittivity of Materials to Temperatures Exceeding 2000°C," The Review of Scientific Instruments, 42, No. 2, 200-204, Feb. 1971.

3. H. L. Bassett and S. H. Bomar, Jr., "Dielectric Constant and Loss Tangent Measurement of High-Temperature Electromagnetic Window Materials," Proceedings of the Tenth Symposium on Electromagnetic Windows, Georgia Institute of Technology, Atlanta, Georgia, July 1970.

4. R. M. Redheffer, "The Measurement of Dielectric Constants," Technique of Microwave Measurements, ed. C. G. Montgomery, McGraw-Hill, New York, 1947.

5. H. L. Bassett, S. H. Bomar, Jr., G. K. Huddleston and A. C. Merritt, "High-Temperature Complex Permittivity Measurements on Reentry Vehicle Antenna Window Materials," Contract F29601-70-C-0069, Technical Report AFWL-TR-71-189, April 1972.

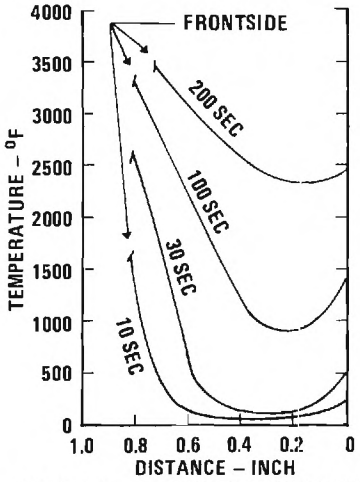

FIGURE 1. PREDICTED TEMPERATURE PROFILES FOR SLIP–CAST FUSED SILICA, CARRIER VI.

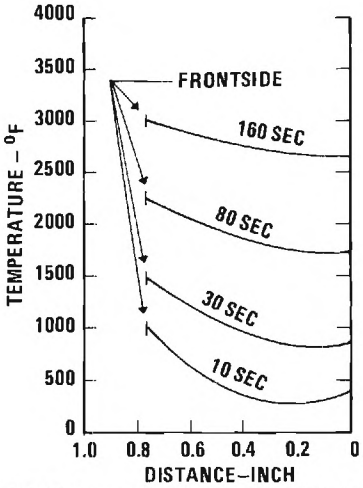

FIGURE 2. PREDICTED TEMPERATURE PROFILES FOR HOT PRESSED BORON NITRIDE (HD–0092), CARRIER II.

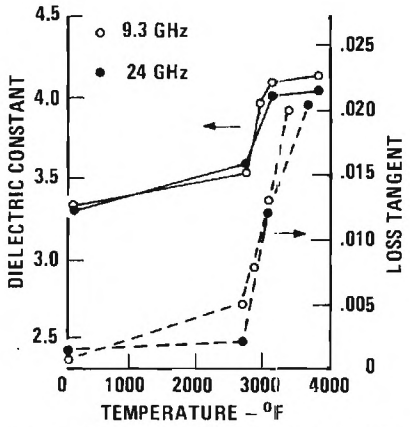

FIGURE 3. DIELECTRIC CONSTANT AND LOSS TANGENT VS. TEM–PERATURE FOR SCFS (DENSITY = 1.93 gm/cm^3).

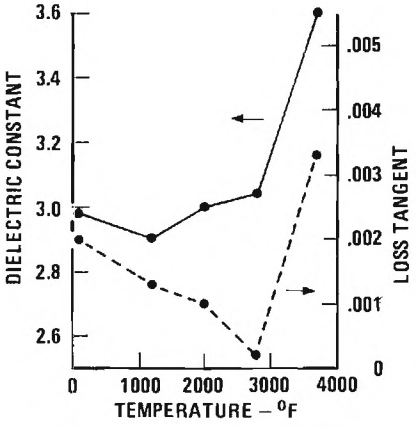

FIGURE 4. DIELECTRIC CONSTANT AND LOSS TANGENT VS. TEM–PERATURE FOR QUARTZ FIBER COMPOSITE (DENSITY = 1.654 gm/cm^3).

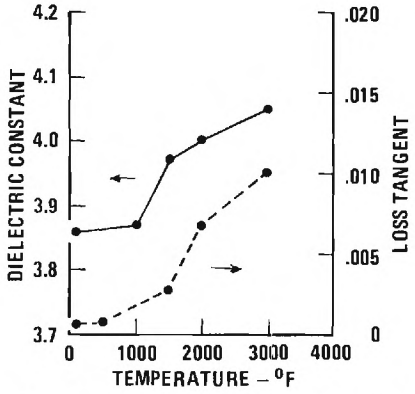

FIGURE 5. DIELECTRIC CONSTANT AND LOSS TANGENT VS. TEM–PERATURE FOR HPBN (DENSITY = 1.945 gm/cm^3).

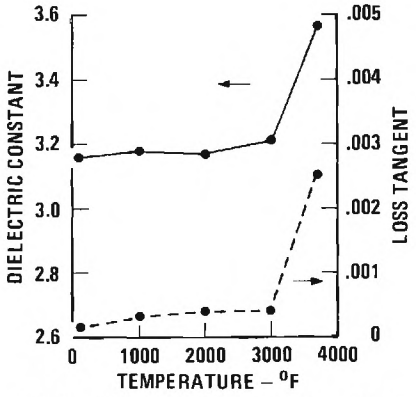

FIGURE 6. DIELECTRIC CONSTANT AND LOSS TANGENT VS. TEM–PERATURE FOR IPBM (DENSITY = 1.274 gm/cm^3).

HIGH-TEMPERATURE DIELECTRIC PROPERTIES OF SEVERAL CANDIDATE SPACE SHUTTLE THERMAL PROTECTION SYSTEM AND ANTENNA WINDOW MATERIALS

M. C. Gilreath and S. L. Castellow, Jr.

NASA Langley Research Center
Hampton, Virginia

INTRODUCTION

The successful operation of the Space Shuttle requires the use of a thermal protection system (TPS) which is reliable, low cost, lightweight, and reusable (up to 100 flights). Several nonmetallic external insulation materials have been developed in an attempt to satisfy these requirements. If a nonmetallic reusable surface insulation (RSI) material is used for the TPS, it would be desirable to also use it as the radome or antenna window material if it has suitable dielectric properties. This would eliminate the problems associated with cutting holes in the RSI material for installing antenna windows of different materials over the many antennas on the Space Shuttle vehicle.

To determine if these candidate RSI materials would be suitable for covering the Space Shuttle antennas, an extensive experimental program was conducted to measure their dielectric properties as a function of temperature from ambient to approximately 2200° F. Several antenna window materials were also evaluated for possible use if the RSI materials were found to be unacceptable as antenna covers. The purpose of this paper is to present the results obtained during this measurement program for both the RSI and antenna window materials.

MATERIAL REQUIREMENTS

The TPS or antenna window material covering the antennas must satisfy several Space Shuttle requirements (Refs. 1 and 2). Among these is the requirement for withstanding repeated exposure to the high temperatures experienced during reentry without degradation of the dielectric properties. The predicted maximum temperatures which the Shuttle Orbiter will encounter during entry are indicated on Figure 1 (Ref. 1). These temperatures are less than those experienced on previous spacecraft during earth entry; however, the duration of the peak Shuttle heating is much longer, as shown on Figure 2 (NASA Contract NAS1-11273 with McDonnell Douglas). This indicates the type of surface temperature profile expected on the Orbiter during entry for an antenna located on the forward bottom center line. Several of the antennas are currently being planned for forward locations. A test program (NASA Contract NAS1-11267 with Georgia Tech) is currently underway to determine the effects on the electromagnetic

properties of several candidate materials during repeated exposure to this type of surface temperature profile.

CANDIDATE MATERIALS

Several candidate antenna window materials were selected for evaluation and these are given in Table I. These materials are primarily in the boron nitride (i.e., Hot Pressed Boron Nitride, Isotropic Pyrolytic Boron Nitride) and silica (i.e., Slip Cast Fused Silica, Silica Composites) classes. An aluminum phosphate foam material was also evaluated. Because of the possibility that the RSI materials might not be developed sufficiently for use on the initial Shuttle Orbiter, requiring the use of an ablative TPS, a typical low-density ablative antenna window material (SLA-220V) was included for evaluation.

Four RSI materials considered as typical of those being developed for Shuttle TPS applications were selected for evaluation. Those evaluated were the Lockheed LI-1500 silica-based material, McDonnell Douglas Mullite HCF, General Electric Mullite MOD1A, and the Grumman Aerospace CPI-35 material. All of these materials are low density (11 to 15 lb/ft^3) except the Grumman CPI-35 which has a density of approximately 35 lb/ft^3. The Lockheed, McDonnell, and General Electric materials are basically silica or fibrous materials that are subject to moisture absorption, damage due to handling and erosion, and poor emissivity properties. Thin surface coatings (10-30 mils) have been developed to provide liquid waterproofing and erosion and handling resistance. Additives to the surface coatings have achieved normal emittance values of 0.8 to 0.9. The materials evaluated in this program did not have the surface coatings. Only the basic material was measured; however, programs are underway to determine the effect of these surface coatings on the transmission properties of the material.

The Grumman CPI-35 material appears to have some advantages over the other materials since it is a closed porosity insulation (CPI) material. It, by definition, cannot absorb moisture and by the use of high emissivity additives to the bulk properties of the material the desired emissivity (0.8 to 0.9) may be achieved, eliminating the surface coating requirement. However, to be more competitive with the other materials, it appears that the density of the CPI material would have to be reduced considerably.

DIELECTRIC PROPERTY MEASUREMENTS

The dielectric constant and loss tangent of each candidate antenna window material was measured initially utilizing rectangular cavities at room temperature. The results of these measurements are presented in Table I along with the measured density of each test sample. The test samples were precured for approximately 5 hours at 392° F prior to conducting the cavity measurements. The frequencies at which the measurements were made were different for each material since a change in the dielectric

constant produced a different resonant frequency of the test cavity. These dielectric constant values were then used to determine the test sample sizes needed for the high-temperature tests.

The high-temperature measurements were conducted at 10 GHz using a short circuited waveguide technique. The sample holder was a section of Platinum/Rhodium waveguide which was heated by a Lindberg Hevi-Duty tubular furnace with an upper temperature limit of approximately 2200° F. The results of the 10 GHz measurements on the antenna window materials at room temperature and 2000° F are presented in Table I. These data were obtained after the test samples had been precured overnight at 392° F. These results are in good agreement with published data for these materials.

The dielectric constants and loss tangents for the RSI materials were also measured at 10 GHz from room temperature to 2192° F and these results are presented in Figures 3-6. Figure 3 shows the results obtained for two samples of Lockheed LI-1500 having different densities. There was very little change in the dielectric constant as a function of temperature for this material. These data presented in Figures 3-5 are averages of several measurements. These data obtained for the McDonnell (Fig. 4) and General Electric (Fig. 5) Mullite materials were similar except the loss tangent of the McDonnell material was approximately a factor of 10 higher. The Grumman CPI-35 test data are presented in Figure 6. Two tests were conducted using the same test sample with the first having a maximum temperature of 1832° F and the second a 2192° F maximum. The loss tangents were essentially the same for both tests; however, the dielectric constant deviated considerably above 1472° F. It is important to note that the dielectric properties returned to the same values after cooling to room temperature; therefore, apparently the high-temperature cycling produced no permanent change in the room-temperature performance of the material. This particular material did exhibit a large change in both the dielectric constant and loss tangent as a function of temperature which is not desirable for an antenna window material.

CONCLUSIONS

The results of the high-temperature tests indicate that some of the RSI materials showed very little change in the dielectric properties as a function of temperature up to approximately 2200° F. Assuming these materials can satisfy all the other Space Shuttle requirements and the addition of the required surface coatings do not degrade the electromagnetic performance considerably, they appear promising as Shuttle antenna window materials. Some of the other materials may also be acceptable when subjected to heating on only one surface.

The antenna window materials performed as expected with very little change as a function of temperature up to 2000° F. Additional tests are planned to evaluate these materials up to approximately 2200° F.

REFERENCES

1. M. W. Vance, "The Manufacture of Mullite Reusable Surface Insulation Materials for Space Shuttle," presented to the Society of Manufacturing Engineers, Westec Conference, March 15, 1972.

2. "Development of a Rigidized, Surface Insulative Thermal Protection System for Shuttle Orbiter," Lockheed Missiles and Space Co. Final Report, NASA MSC Contract No. NAS9-11222, February 16, 1971. (Available as NASA CR-114958.)

TABLE I

PROPERTIES OF ANTENNA WINDOW MATERIALS

Material	Supplier	Density, ρ g/cc	Frequency, GHz*	Dielectric Constant, ϵ_r RT	$2000^{\circ}F$	Loss Tangent, tan δ RT	$2000^{\circ}F$
Slip Cast Fused Silica SCFS	Georgia Tech	1.98	5.375	3.40		0.00089	
			10.000	3.34	3.47	0.00022	0.00223
Boron Nitride HD-0092	Union Carbide	1.99	4.915	4.07		0.00056	
			10.000	4.06	4.15	0.00300	0.00080
Isotropic Pyrolytic BN IPBN	Raytheon	1.22	5.726	3.00		0.00011	
			10.000	2.86	2.88	<0.00010	0.00082
Aluminum Phosphate Foam $AlPO_4$	Whittaker	0.82	7.362	1.82		0.00401	
			10.000	1.81	1.84	0.00327	0.01688
Multidirectional Silica Composite, MARKITE 3 DQ	General Electric	1.89	5.555	3.19		0.00057	
			10.000	3.14	3.23	0.00057	0.00084
Fused Quartz Reinforced Silica Composite AS 3DX	Philco-Ford	1.62	5.841	2.88		0.00612	
			10.000	2.82	2.92	0.00047	0.00284
Silicone Ablator** SLA-220V	Martin	0.25	12.950	1.328		0.00609	
			10.000	1.308	1.302	0.00498	0.00447

*10 GHz measurements after 16 hours precuring at $392^{\circ}F$, other measurements after 5 hours at $392^{\circ}F$.

**Ablation material, maximum test temperature $750^{\circ}F$.

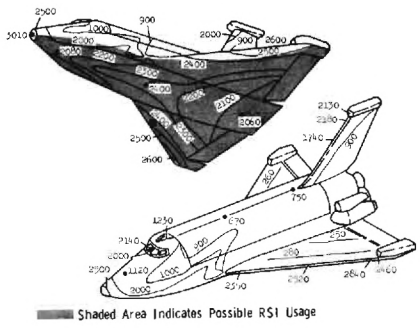

Figure 1. Predicted Maximum Shuttle Orbiter Entry Temperatures.

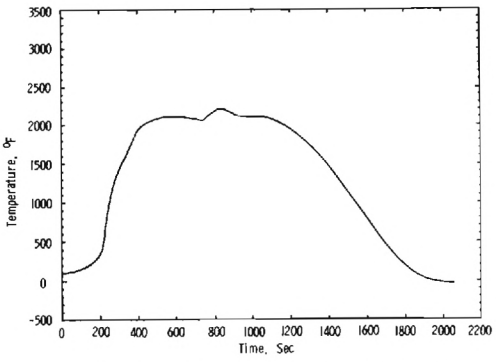

Figure 2. Predicted Surface Temperature Profile for Forward Bottom Centerline Antenna Location (RSI TPS).

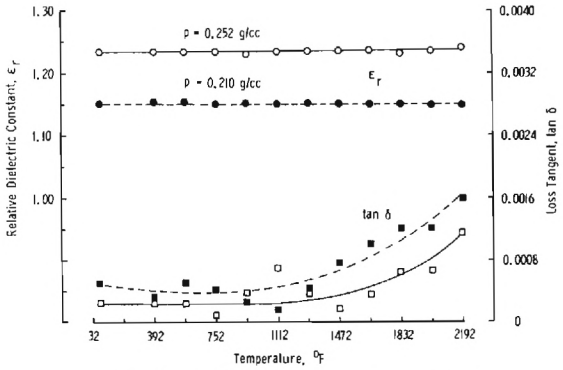

Figure 3. Dielectric Constant and Loss Tangent of Lockheed LI-1500 as a Function of Temperature.

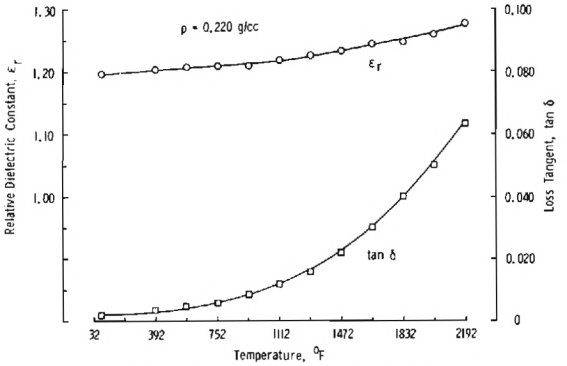

Figure 4. Dielectric Constant and Loss Tangent of McDonnell Mullite HCF as a Function of Temperature.

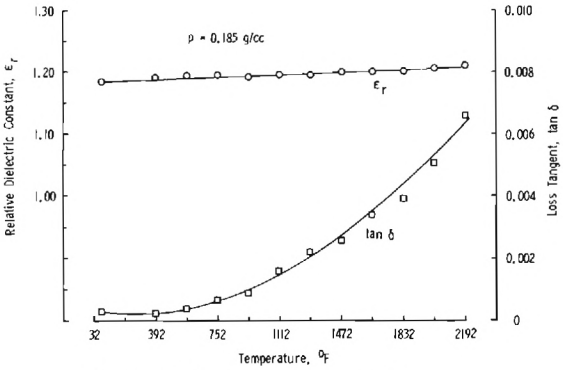

Figure 5. Dielectric Constant and Loss Tangent of General Electric Mullite MOD IA as a Function of Temperature.

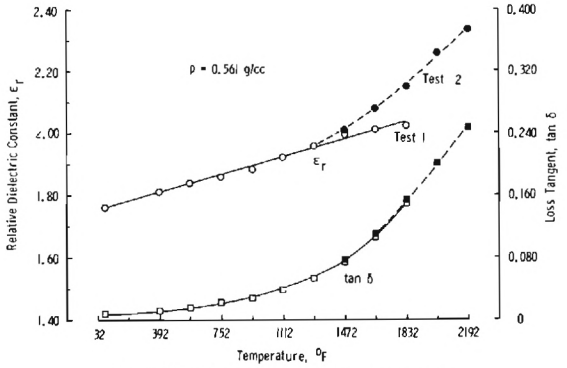

Figure 6. Dielectric Constant and Loss Tangent of Grumman CPI-35 as a Function of Temperature.

TRANSIENT THERMAL AND ELECTRICAL CHARACTERISTICS OF AN ANTENNA WINDOW MATERIAL IN THE PRESENCE OF TWO RETAINERS

by

G. J. HUTCHINS AND R. F. SULLIVAN

Harry Diamond Laboratories, Wash DC

INTRODUCTION

The need for a low-cost antenna window material that can withstand moderate missile aerodynamic heating conditions has led to an investigation into the transient thermal and electrical characteristics of Duroid 5650*, a Teflon-based material with ceramic fibers. Window materials subjected to a thermal environment should have the following characteristics.

1. RF transmission loss through the window/retainer combination must be lower than a specified value at the frequency of interest.

2. The material must possess ablative compatibility with the retainer.

3. Thermal conductivity must be low.

4. The material must be able to withstand a desired heating rate and elevated surface temperatures.

5. The material must be able to withstand moderate bending stresses.

Previous tests (Ref. 1) indicated that Teflon-based materials exhibited excessive attenuation (approximately 20 dB) during the transient heating phase. Conditions imposed on these materials were those expected during re-entry of space vehicles and were considerably more extreme than those of interest in this investigation. In order to determine if Duroid 5650 was acceptable under more moderate conditions, tests were conducted at the NASA-Langley Thermal Facility Unit.**

EXPERIMENTAL CONFIGURATION

A diagram of the experimental configuration is given in Fig. 1. An oscillator produced a 9.3-GHz signal that was 100 percent modulated at a 1-kHz rate. Use of a power monitor enabled power level adjustment, thereby ensuring the same input conditions for each testing cycle. A signal was transmitted from an antenna horn positioned perpendicularly to the test sample. The test sample was comprised of a 2 x 2 x 0.2-in. section of the

---

* Rogers Corporation, Rogers, Connecticut.

** The authors gratefully acknowledge Ross Levin and his highly competent staff at NASA-Langley for providing and operating the necessary testing equipment.

candidate window material surrounded by a 5 x 5 x 0.2-in. section of window-retainer material attached to a wedge-shaped sample holder (Fig. 2). During application of a thermal environment, the leading edge of the copper wedge was water-cooled. Fig. 3 shows the interior of the sample holder. Power received by a section of the open-ended waveguide was detected by a crystal detector. After being amplified by a 1-kHz narrow-band amplifier , the signal was rectified and the dc output continuously recorded by an oscillograph recorder. Temperature readings were obtained using an optical pyrometer and thermocouples (Fig.3) to determine the conditions on the front and back surfaces respectively.

In order to minimize the interference that occurred because of the surrounding metallic structure, it was necessary to position the antenna horn as close as possible to the test sample. This prevented the use of the hydraulically operated insertion arm and necessitated starting the electric arc with the wedge already in its testing position.

TEST CONDITIONS AND RESULTS

Three materials were involved in these tests: (a) Duroid 5650, (b) RPD-41, an asbestos-phenolic retainer material, and (c) RMCP (rubber-modified cotton phenolic) retainer material. Four 30-second tests were made of the Duroid window surround (two tests for each retainer) in an arc-heated airstream with a cold-wall heat flux of 17.5 BTU/FT^2-Sec. and an enthalpy of 3000 BTU/LB. Fig. 4 shows the Duroid 5650/RPD-41 combination after test exposure. The materials in this specimen ablated only slightly in an environment considered more severe than expected flight conditions. Test specimens with a Duroid 5650/RMCP combination exposed to the same conditions resulted in substantially more char and erosion of the RMCP material.

A plot of transmission loss vs. time using both surround materials is presented in Fig. 5. It is believed that the initial loss indicated was the result of either a transmission loss in the window material or a phase change of the signal inside the test chamber. In order to determine which phenomenon was occurring, the sample was removed and an output horn was placed on the far side of the arc chamber. The oscillator was tuned so that a peak signal was obtained by the amplifier and the arc turned on. The resultant signal level decreased. When the same procedure was followed for a null signal, the level increased. For this reason, plus the low surface temperature exhibited by the window material, the initial loss was attributed to a phase change in the test chamber due to the presence of the electric arc. The initial attenuation was therefore considered a "zero" level and the transmission loss in the window/retainer combination was computed as the change from that value.

The considerably greater transmission loss obtained when RMCP was used as a retainer is probably caused by the organic material observed in the glowing flow stream caused by the substantial charring and surface erosion. The presence of these particles is most likely responsible for the possibly high surface temperatures measured by the pyrometer for the Duroid/RMCP combination. A constant temperature rise throughout the cycle (Fig. 6) indicates the absence of ablation effects. The maximum surface temperature (1850^{o}F) for the Duroid 5650/RPD-41 sample occurred after about 17 seconds.

At this point, the ablative effects assumed precedence, and the temperature decreased for the remainder of the cycle. Transmission loss, which can be considered a combination of window-attenuation and particles in the flow stream, was approximately 1.7 dB.

THEORETICAL RESULTS

A computer program was written to determine the amount of aerodynamic heating that occurs for specific flight conditions and to calculate the transfer of the heat to the interior sections of the antenna window/antenna configuration. This program was adapted from a computer code developed in Ref. (2) for stagnation point analysis of nose-cones. The revised code can be used for flow over flat plates or cones for areas away from the stagnation point for both laminar and turbulent flow conditions. Other capabilities include the effects of specific heat, thermal conductivity, and emissivity as functions of temperature.

The following expression for the heat transfer coefficient developed in Ref. 3 for compressible flow was used to calculate the front surface temperature.

$$h = \frac{C}{(T^*)^{.55}} \quad \frac{(P_e V_e)^{0.8}}{(1)^{0.2}} \quad \frac{BTU}{FT^2\text{-Sec-}^oF} \tag{1}$$

where T^* is Eckert's reference temperature, L is the wetted length, P_e and V_e are values of the pressure and velocity at the boundary layer outer edge, and C is a constant denoting laminar or turbulent flow. Fig. 6 indicates that this approximation is indeed valid for the present conditions. Since ablation effects are not considered in the program, the calculated temperature is constantly increasing throughout the cycle, and therefore more closely approximates the Duroid 5650/RMCP results for the latter part of the run.

Interior temperatures were determined using the method of finite differences to solve the first-order differential heat transfer equation. Back-surface temperatures calculated using this procedure are also in close agreement (Fig. 6).

SUMMARY

Excessive attenuation during the transient heating phase of Teflon-based materials found in previous tests did not occur for the heating rate used in this investigation. Duroid 5650 has been shown to possess favorable electrical, thermal, ablative, and mechanical characteristics for moderate missile atmospheric conditions. When used with an asbestos-phenolic retainer, the transmission loss was approximately 1.7 dB. Further investigation is necessary to determine what portion of this attenuation occurs in the antenna window, and what portion results from the retainer material ablating into the flow stream. This investigation indicates that RMCP is an inferior heat shield because of the substantial transmission loss that occurred using this material as a surround.

Finally, a computer program that utilizes an approximate heat transfer coefficient produced results that make it a viable tool for future aerodynamic-heating investigations.

REFERENCES

1. Hank, H., "Antenna Window Investigations," Martin-Marietta Corporation Report (September 1963).

2. Lucey, G. K., Jr., "An Improved Test to Determine Rain-Erosion Resistance in Fuze Nose-Cones," HDL-TR-1559 (July 1971).

3. Buckley, F.T., "Constant-Mach-Number Simulation of Critical Flight Loads on High-Velocity Projectile Fuzes," HDL-TR-1466 (August 1969).

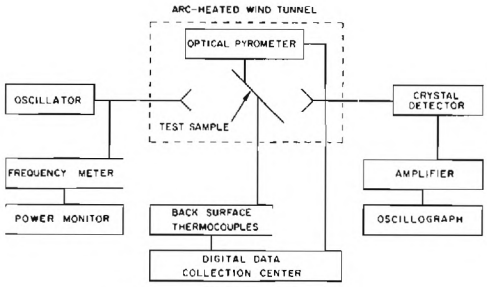

FIGURE I. DIAGRAM OF TEST CONFIGURATION

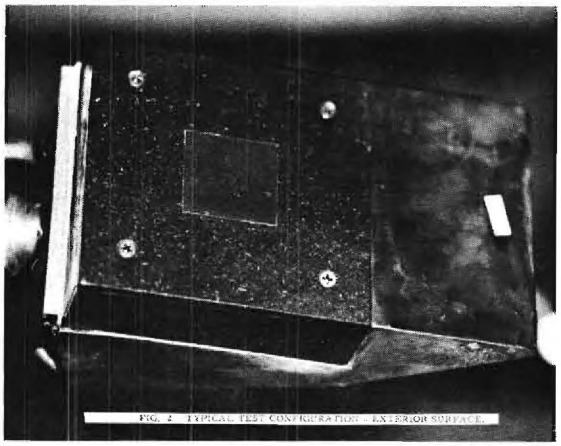

FIG. 2 TYPICAL TEST CONFIGURATION - EXTERIOR SURFACE.

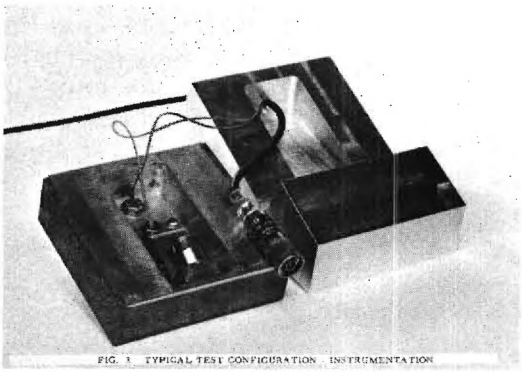

FIG. 3 TYPICAL TEST CONFIGURATION - INSTRUMENTATION

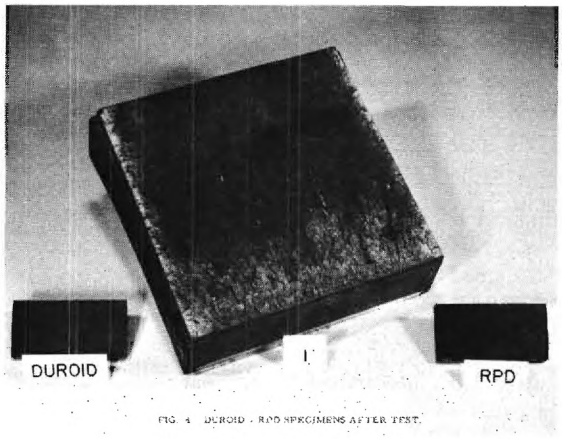

FIG. 4 DUROID - RPD SPECIMENS AFTER TEST.

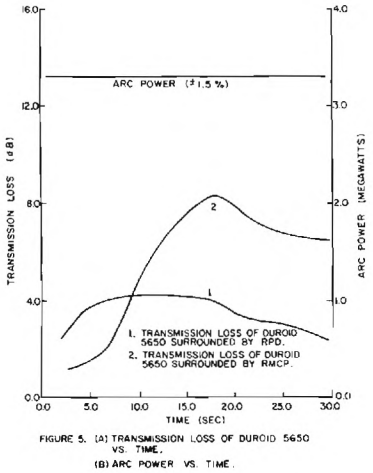

FIGURE 5. (A) TRANSMISSION LOSS OF DUROID 5650 VS. TIME.
(B) ARC POWER VS. TIME.

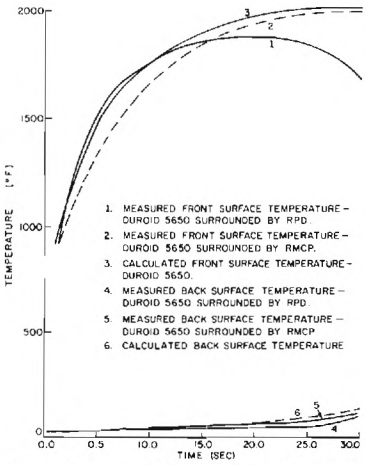

FIGURE 6. FRONT & BACK SURFACE TEMPERATURES OF DUROID 5650 VS TIME

DEVELOPMENT AND CHARACTERIZATION OF SILICONE-SILICA COMPOSITE HARDENED ANTENNA WINDOW MATERIALS BASED ON OMNIWEAVE MULTIDIRECTIONAL REINFORCEMENT[1]

James P. Brazel and Leonard Markowitz
General Electric Company
Re-entry and Environmental Systems Division
Philadelphia, Penna. 19101

A family of hardened antenna window materials based on the General Electric Re-entry and Environmental Systems Division (RESD) Omniweave process was described at the 10th Symposium (ref. 1). The further development of these materials under U. S. Army sponsorship is described in this paper.

Two basic material systems were being developed. The first, designated ADL-10 is a composite of high purity silica omniweave multidirectional reinforcement with a plastic matrix of GE's SR350 silicone resin. The second, designated Markite 3DQ, is an inorganic silica-silica composite derived from pyrolysis of ADL-10. Whereas ADL-10 was limited to heat fluxes of 100 BTU/ft^2-sec (approx. corresponding to 2800°F surface temperature) for loss-free RF transmission, the Markite material was unlimited and had essentially the RF/ablation properties of slip-cast fused silica. ADL-10 had excellent shock resistance but anomolously low strengths in the range 2000-4000 psi in the weakest direction and fractured like a brittle material. Markite also had a low strength which was attributed to the fiber-matrix bonding mechanism. The prognosis for improvement of both materials was to study the matrix-fiber interaction, especially the effects of suspected fiber damage during weaving and the silicone-silica bonding at the time of impregnation. This paper discusses the progress made since the last symposium in carrying out that study.

OMNIWEAVE PROCESS

By a combination of improved fiber combing techniques and the use of teflon-coated Astroquartz roving, Omniweave fabric densities of from 0.7 to 1.1 gm/cc were achieved during this development program. This contrasts with a woven fabric density range of 0.4 to 0.7 gm/cc in the previous program. The finished weaves had a nominal surface projected fiber angle of 40°, which resulted in processed composites of 26 to 38° surface angle. The woven through the thickness fiber angle was close to the nominal 45°, which in the molded specimens ranged between 18 and 36°, depending on molding pressure. The teflon finish was generally removed before impregnation and molding to the composite form. During the early ADL-10 processing studies described in this paper segmented "fingers" of silica omniweave were first produced, in contrast to the large flat "scarves" described in ref. 1. Figure 1 shows a sketch of a finger specimen woven to the nominal 0.9" x 0.4" x 4" tensile specimen geometry. Later weaves were again produced in the large scarf geometry and the various test specimens cut from them.

1. This work was based on funding provided by U. S. Army Materials and Mechanics Research Center under Contract No. DAAG-46-71-C-0053.

ADL-10 SILICA/SILICONE COMPOSITE

MECHANICAL PROPERTIES

The first investigations were directed specifically toward improving the tensile strength properties of ADL-10 by carefully controlling 3 process parameters during fabrication. First, the woven specimens were divided into four groups subjected respectively to etching in HF aqueous solution of 10, 5 and 1% and a control unetched group. Second, these specimens were factored into three groups to which was applied 2 levels of coating by acetoxy ethyl triacetoxy silane in acetone, and a control group uncoated with this "silane coupler" whose purpose is to facilitate tenacious bonding by formation of direct chemical bonds between the silicone matrix and silica fibers. Third, the samples were further factored by molding pressures of 125, 300 and 1000 psi, using the previously developed cure techniques. The details of the processing and of the complete work associated with the materials described at the last symposium are given in ref. 2 and 3, the unclassified final reports under AMMRC sponsorship.

The tensile test results of this "series 1" showed no significantly discernible effect due to either the etching or silane coupling. Only the molding pressure variations showed a discernible trend, apparently optimum at the lowest pressure, 125 psi. However; the overall range of observed strengths was in the range of 5000-18,000 psi (a function of reinforcement angle, see below), and strains to failure of 0.5 to 2.35% occurring in the composite fiber/matrix shear failure mode.

TABLE 1

ADL-10 COMPOSITE PROPERTIES MINIMUM STRENGTH DIRECTION

Material / Property	1000 psi plate molding from low density Omniweave (ref. 1).	Series 1, Segmented Omniweave, 125, 500 and 1000 psi moldings	Series 2, Segmented Omniweave, 125 psi molding	Plate molded for Optimum fiber fraction (molding pressure)
Omniweave fabric density, as woven (gm/cc)	0.4. to 0.7	0.70 to 0.94	0.72 to 0.77	0.79
Molded panel density (gm/cc)	1.38 (cast) 1.8 to 2.0 (1000 psi)	1.55 to 1.68 (125 psi) 1.66 to 1.78 (1000 psi)	1.60 to 1.83	1.68 (125 psi) 1.59 (1000 psi)
Molded panel fiber volume fraction (%)	33 (cast) 67 to 80 (1000 psi)	60 to 70 (125 psi) 67 to 79 (1000 psi)	60 to 80%	67 (1000 psi) 60 (125 psi)
Ultimate Tensile Strength (psi) (axial or minimum)	2000 to 4000	5000 to 18,000	10,000 to 20,000	18,000 (1000 psi) 7,300 (125 psi)
Strain to failure	0.04 to 0.48	1.5 to 2.3 (125 psi) 1.0 to 1.9 (1000 psi)	1.5 to 2.35	0.8 (1000 psi) 0.4 (125 psi)
Elastic Modulus ($x10^6$ psi)	1.7	1.08 to 1.90 (125 psi) 1.22 to 2.18 (1000 psi)	0.8 to 1.7	2.7 (1000 psi) 1.9 (125 psi)

A "series 2" set of similar finger specimens was then fabricated, selecting the 125 psi molding pressure, standardizing on the highest HF etch concentration and two levels of silane coupler. The gratifying results of the tensile testing are summarized in Table 1 where the stages of development of this material can be traced and compared to the earliest versions reported in ref. 1 and 2. Strengths of 10,000 to 20,000 psi were measured in the axial, specimen length direction (fig. 1) with included fiber surface angles of 26^{o} to 34^{o}. Although the same level of elastic modulus as in the weak, earlier material was observed, the precent strain to failure of the series 2 specimens increased from the range 0.04-0.48 to 1.5-2.35. This last result is especially valuable for the intended radome or antenna window role of the material where it would not be intended as a primary load bearing member.

Figure 2 presents these series 2 results in a more rationalized form. The UTS is plotted versus surface (axial projected) reinforcement angle in three groups; 1% and 1% silane and a third factorial group to which Cab-O-Sil was added (ref 3). The effects of machining the edges of the woven tensile specimens was also examined in each group and found to give about 25 % lower strengths. The 1% silane coupling gave the highest strengths of the groups but the spread of the data was relatively larger, reflecting either the difficulty of accurate and representative fiber angle measurement or, as likely, critical performance of the unmatched, near optimal, 1% silane coupled closed-weave specimens.

Figure 3 presents the results of a theoretical analysis of these specimens*. The series 2 data points are plotted against the predicted UTS of the ADL-10 composite with non-machined edge specimens indicated as solid data points. Again, the difficulty of accurately measuring surface fiber angles is a factor, but the composite material is in fact reaching its theoretical strength levels. Measurements of the primary cured SR350 resin elastic properties and unidirectional behavior are discussed in reference 3.

Plate material was also produced from a higher density omniweave fabric. Tensile specimens cut from 2 molding pressures from this plate showed the dominant omniweave parameter to be the fiber volume fraction, optimum and maximum at about 0.68, depending on axial surface angle. The last column of Table 1 shows this result and the equivalence of finger and plate results.

SHOCK RESISTANCE

The mechanical shock resistance of four series 2 test specimens was evaluated by subjecting them to magnetic flyer plate impact. One specimen (in the 10% silane group) was impacted at 2000 taps in the center, gauge section. The apparent result was only a mashing of the matrix, so three specimens from the 1% silane group were then impacted at 4000 taps. These samples are indicated by crossed symbols in figure 2. There was no discernable loss in strength; in fact one of the 4000 tap specimens had the highest strength of any tested, at 21,060 psi. However, the fibers of the "mashed" tensile were allowed to travel 4 to 10 times farther through the crushed matrix before failure. Further testing of ADL-10 hockey puck specimens showed the ability to remain intact at impact levels of 4000 taps. The specimen thickness increased by 15-20% and ultrasonic attenuation from 60 db/cm to somewhat greater than 90 db/cm.

ELECTROMAGNETIC PROPERTIES

The ADL-10 material developed under the second AMMRC-sponsored program had essentially identical RF properties to that reported in ref. 1 and 2. The 100 BTU/ft^2-sec

* This analytic portion of the study was performed by Dr. B. W. Rosen, Materials Sciences, Inc.

heat flux limitation is shown in fig. 4. An analogous heating and RF transmission history is given in ref. 1 for Markite 3DQ which has no flux limitation on transmission. ADL-10 has a thickness direction dielectric constant of 3.0 $\pm$ 0.1 depending on molded density and a loss tangent of 0.004 or less (C-band, 5.47 GHZ).

MARKITE 3DQ SILICA/SILICA COMPOSITE

The etching and silane coupling studies had as their ultimate objective a significant improvement in the strength of the Markite material derived from ADL-10. With achievment of woven omniweave silica fabric densities as high as 1.1 gm/cc (1.2 gm/cc is the maximum useable density, corresponding to the ideal 68% uncrimped fiber volume fraction) all of the postulated requirements for ceramicized composite strength improvement were realized. However, only marginal improvements in strength over the previous work were realized-about 20%, attributable to the increase in woven fabric density. Fig. 5 shows flexure test results of the earlier studies (ref. 2) on repeated pyrolysis and reimpregnation of ADL-10, but with data points from two plates (319-1 and 2) of the latest series. After 3 cycles of densification a maximum ceramic strength of 3000 psi was achieved.

Fig. 6 is a scanning electron micrograph of Markite fiber-matrix bond. The tenacious bonding and filleting is apparent-as is also the cracking. A lower density inorganic matrix is the obvious alternative approach, as is also a less tenacious bond which need only permit the fiber system to realize its strength potential, as did the flyer-plate impacted ADL-10 tensile specimens.

PLANS FOR FUTURE WORK

The current work underway at GE/RESD on low density refractory external insulation (REI) for Space Shuttle applications is serving as a basis for one concept of a ceramic silica-silica antenna window, which aims to achieve a "space-frame" reinforcement (Section 4, ref. 3). Preliminary studies have also been performed on a chemical vapor deposition process for silica but this process appears limited to either an initial deposition into the unimpregnated fabric or a surface hardening or sealing final step.

The most immediately promising process is to continue the reimpregnation-pyrolysis cycle represented in fig. 5, terminating with a final light reimpregnation. The top of the sawtooth ramp does increase to strengths in excess of 5000 psi at 3 complete cycles. A single flexure specimen (319-2 in fig. 5) had a modulus of rupture of 5900 psi after only 2 cycles. Studies of ADL-10 pyrolysis residues have also shown more advantageous methods of converting the silicone matrix to a loss-free silica.

ACKNOWLEDGEMENTS

The authors wish to acknowledge the Omniweave design and fabrication engineering efforts of Mr. M. Wexler and the RF/Ablation tests performed by Mr. J. Hanson (both GE/RESD) and the technical supervision provided by Dr. N. Schneider and Mr. J. Dignam of AMMRC.

REFERENCES

1. Markowitz, L., Brazel, J., Hiltz, A., Hanson, J.; "RF Transparent, Ablative Silica-Silicone Composite", in Proceedings of the 10th Symp. on Electromg. Windows, 1970.
2. Hardened Antenna Window Materials Study, Final Rpt. (U), U.S. Army Mat'ls and Mech. Res. Ctr. Contract Rept. CR-70-15, Sept. 1970.
3. Advanced Hardened Antenna Window Materials Study, Final Rept. (U) U.S. Army Mat'ls and Mech. Res. Ctr., AMMRC CTR-72-1, Feb., 1972.

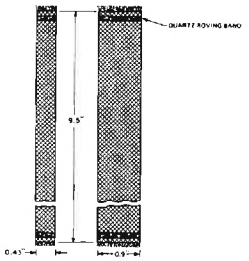

Fig. 1. Woven Omniweave Segment

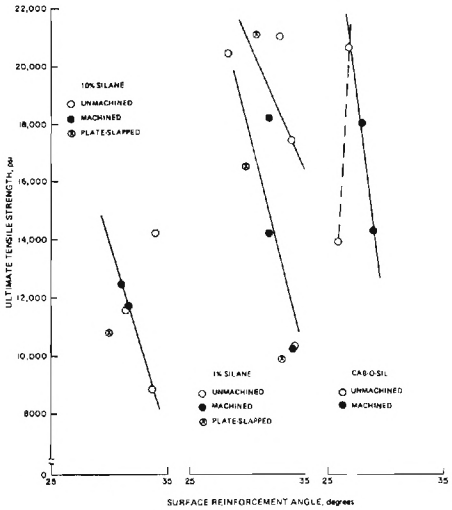

Fig. 2. Ultimate Tensile Strength vs. Surface Reinforcement Angle Series 2 Specimens

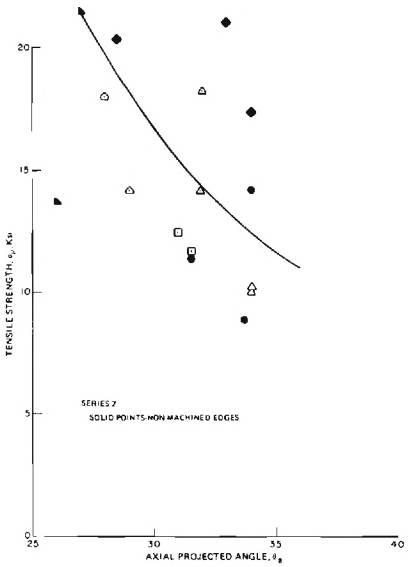

Fig. 3. Theoretical and Experimental Strength Values of ADL-10 Series 2 Specimens

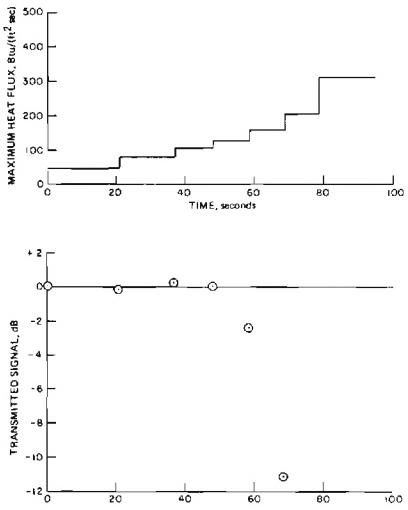

Fig. 4. Specimen 331-I ADL-10

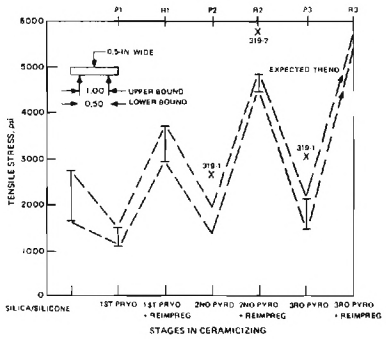

Figure 5. Silica/Silicone Transformation, Short Beam Flexure; Tensile Stress at Failure as a Function of Processing Operations. Latest Values Superimposed on Data from Reference 1

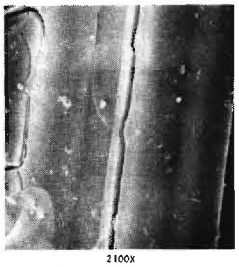

2100X

Figure 6. SEM of Marktite Fiber/ Matrix Interface Showing Filleting and Cracking

RADOME DESIGN: FURTHER DEVELOPMENTS OF THE LIMITED EXPANSION METHOD

BY: F. GASPALOU
Etablissement des Constructions et Armes Navales de RUELLE (FRANCE)

Abstract

The limited expansion method allows in particular to give general formulas for the boresight error slope and for transmission losses using the different parameters defining the combination radome-antenna. The first results of the optimization of the combination radome-antenna are given: influence of the different parameters, theoretic minimum of boresight error slope for a given band of frequency, theoretic largest band of frequency which can be obtained for a given transmission loss, etc.

0. - INTRODUCTION -

The limited expansion method was stated in the Secund International Symposium on Electromagnetic Window (ref. 1) and we invite the reader to refer to the proceedings of the Symposium for detailed explanations (and for the list of hypothesis). We would only like to remind here that this method allows to give general formulas for the boresight error slope and for transmission losses, thus it is a very simple method for radome design. With this method, all the characteristics of electrical analysis cannot be calculated, and the usual method using computers will be necessary for elaborated analysis. But the limited expansion method can help the radome designer and gives answers to such questions as: what is possible with a monolithic radome? Can you obtain 5 per cent of boresight error slope in a band of frequency of 10 per cent? Is it interesting to reduce dielectric constant? What is the influence of the shape of the radome, and for example is it interesting for electrical design to increase the L/D ratio of the ogive? We shall give some results in this summary, without any demonstration.

1. - FURTHER THEORETIC DEVELOPMENTS -

The method has been extended in various ways:

1.1. - Different angle-error sensing techniques -

Initially the method assumed that a monopulse ecartometry technique was used. We have proved that the method could be extended to other angle-error sensing techniques:

- scanning with amplitude comparison: we search the null of the difference fonction.
- scanning with phase comparison: for example, for an electronic scanning made with four phase shifters driven by sine and cosine currents and feeding the four quadrants of the antenna, we have proved that the boresight slope is identical to that obtained when the antenna is used in monopulse (with the two halves of antennas being at plus and minus 90° phase respectively and ecartometry given by the relation: $\vec{S} \cdot j\vec{D} = 0$), i.e. the boresight slope in phase scanning is independant of phase shift.
- theoretic technique using the maximum of the diagram (in analogy with the pencil beam): we have proved we can still write $\vec{S} \cdot j\vec{D} = 0$ with

$$\Sigma\ (z,\varphi) = \Sigma\ (z)$$

$$\Delta\ (z,\varphi) = \Sigma\ (z)^{z \cos \varphi}$$

where Σ et Δ are the fields on the antenna in polar coordinates:
$X = z \cos \varphi$ and $Y = z \sin \varphi$ $(0 \leq z \leq 1)$

1.2. Antenna looking in a non-principal plane: Initially the method assumed that the antenna looked in a principal plane. We have proven that the model given in the conclusion of the communication (ref. 1) was good at any frequency. This model is good only for the boresight error slope when antenna looks in the axe of the radome, and is not good for the boresight error itself.

1.3. Shape with variable thickness: Initially the method assumed that the thickness of the ogive was constant. We have written the formulas for variable thickness. We have proven that for a non-constant thickness the diagram of error slope versus frequency can be deduced from this with constant thickness by a translation along both the axe of frequency and the axe of error slope (and not only along the axe of error slope as it is often said). It is the same for the diagram of transmission losses versus frequency.

1.4. Influence of depolarization angle: Initially the method assumed that the depolarization angle between incident wave and antenna was null. We have started with writing the formulas for a depolarization angle different from zero.

2. EXPERIMENTAL VERIFICATIONS OF THE THEORY -

We have applied the general formulas to real radomes (with scanning or monopulse antennas).

We have to say that the correlation between theory and experimental results is not very good: it seems that the aperture distribution of the antenna is not the one that is indicated by the antenna manufacturer. The theory gives pessimist performances: experimental performances are better than calculated performances. Nevertheless, it is possible to choose an aperture distribution that gives excellent correlation between theory and experience: it is exactly as if an "apparent" aperture distribution was used, different from the real distribution law.

If we apply the general formulas to the same real radomes, but assuming that ecartometry is given by the maximum of the diagram, the correlation between formulas and experimental results is good (formulas give very little optimist performances).

3. INFLUENCE OF THE DIFFERENT PARAMETERS -

3.1 Parametric study:

Let us assume that 1 is the distance between the apex and the center of rotation of antenna
R the radius of curvature of the pointed ogive at the apex
α the half vertex angle of the ogive
d the diameter of antenna
B = 2a the band of frequency
To reduce the boresight slope, 1 should be as little as possible.
When R increases, all other parameters being constant, the slope decreases.

The main parameter characterizing the geometry of radome and antenna system is not the aerodynamic $\frac{L}{D}$ ratio but:

$$u = \frac{1}{R \sin \alpha}$$

and u should be as little as possible. For example, all things being otherwise equal, the cone has better performances than the ogive. For a given diameter D of missile, and for a given aerodynamic $\frac{L}{D}$ ratio, the ogive of Lighthill is better than the parabola, and the parabola is better than the tangent circle. Figure 1 gives u versus $\frac{L}{D}$ ratio for different shapes and for a given $\frac{d}{D}$ ratio.

As for the influence of the angle α, the dielectric constant n^2 and the "apparent" illumination law see figures 2, 3, and 4.

Figure 2 shows the well-known law that says that when the dielectric constant increases, the band of frequency decreases: For example, to a maximum loss of 30% and for $\alpha = 10°$, it is in theory impossible to have a band larger than 5,2% with alumina ($n^2 = 9$) and than 9,5% with silica ($n^2 = 3,5$). Diagrams with maximum loss different from 30% could be drawn.

Figures 3 and 4 give the minimum of boresight error slope p which can be obtained in theory. For example, if $\alpha = 20°$ and $n^2 = 9$ we have $\frac{p}{a} \frac{d}{\lambda} = 7.15$ in monopulse, that is to say for a normalized diameter of antenna $\frac{d}{\lambda} = 9$ we will have at least 0,79% of error slope for a band of 2a = 2% or 3,97% of error slope for a band of 2a = 10%.

Please remember that we deal with monolithic radomes and with pointed radome and not blunted radome (like ogive of vonKarman) and with thickness close to the half wavelength in the dielectric. Figures 3 and 4 show that it is interesting to increase α (contrary to aerodynamic considerations) and to have a low dielectric constant. The minimum error slope given by figure 3 or 5 is theoretic and we get practically twice or more at least.

As for the "apparent" illumination law, we have proven that it exists an optimum illumination law which gives error slope minimum (this optimum law was used to draw figures 3 and 4). We have found that the thickness law, as well as the illumination law and ogive shape, have a great importance, which is a well-known result.

3.2. Influence of little defects and of secondary effects:

At paragraph 3.1 we have assumed that the error slope versus frequency is linear, i.e., we have neglected the second order terms (in other words, we have assumed the band of frequency is not very large). We have begun to study the influence of little defects or secondary effects that can change or lessen the electrical performances:

- manufacturing tolerances upon thickness and dielectric constant (and influence of temperature)

- manufacturing tolerances upon antenna (influence of discontinuity of difference illumination law, influence of a phase not exactly equal to $\frac{\pi}{2}$ between sum and difference channels, etc.)
- influence of a little angle of depolarization between incident wave and antenna
- influence of loss tangent
- influence of effect of curvature and effect of prism (for the radome is not exactly assimilable to a sheet with parallel faces, so that an incident beam is slightly deflected)
- etc...

This study is not completed, thus we refrain from giving other results which are for the moment not definite.

4. CONCLUSION -

The limited expansion method is a very simple method which gives a good approximation to forecast the electrical performances of the combination radome-antenna or which may help the designer to choose the different parameters. We have to complete the optimization study and to see if it is possible to extend this method to blunted radomes or sandwich radomes.

Reference:

(1) Methode de calcul des performances radioélectriques des radomes aéroportés, F. GASPALOU, Deuxieme colloque International sur les fenetres électromagnetiques, Paris 8 au 10 septembre 1971.

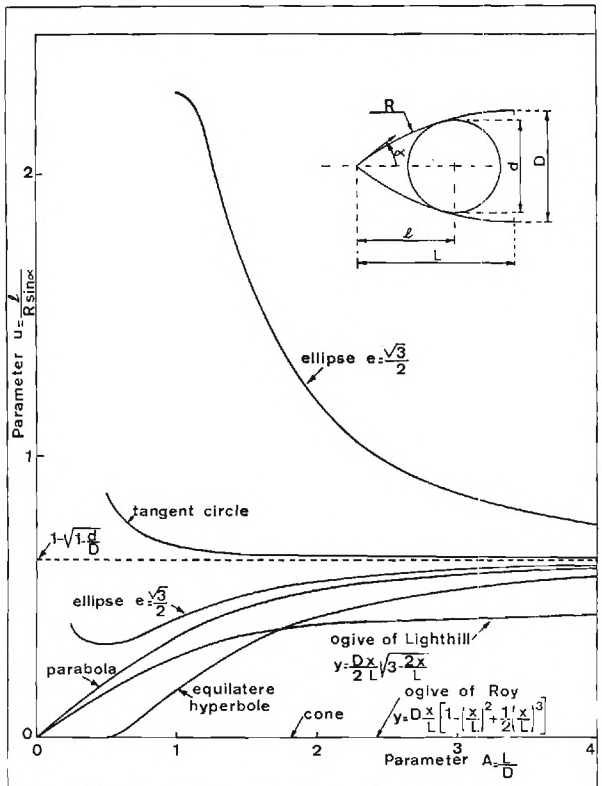

Fig:1 Influence of shape on boresight error slope
(u versus A for $\frac{d}{D}=\frac{200}{230}=0,87$)

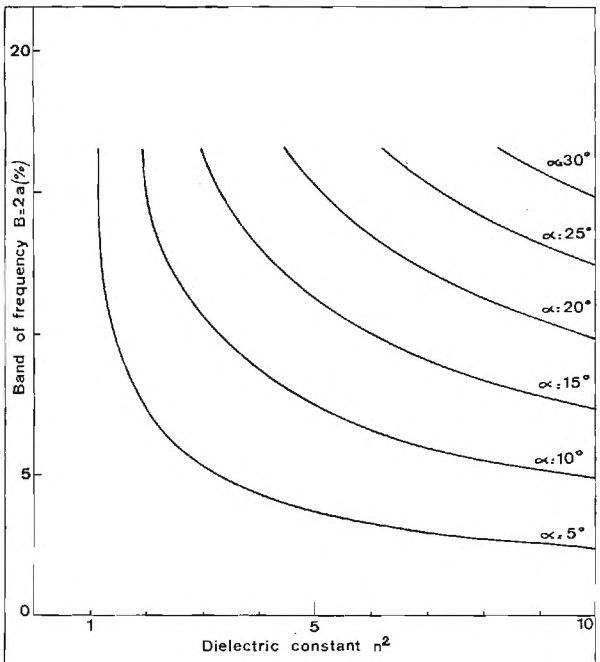

Fig.2 Maximum band of frequency which can be obtained
(for a maximum loss of 30%)

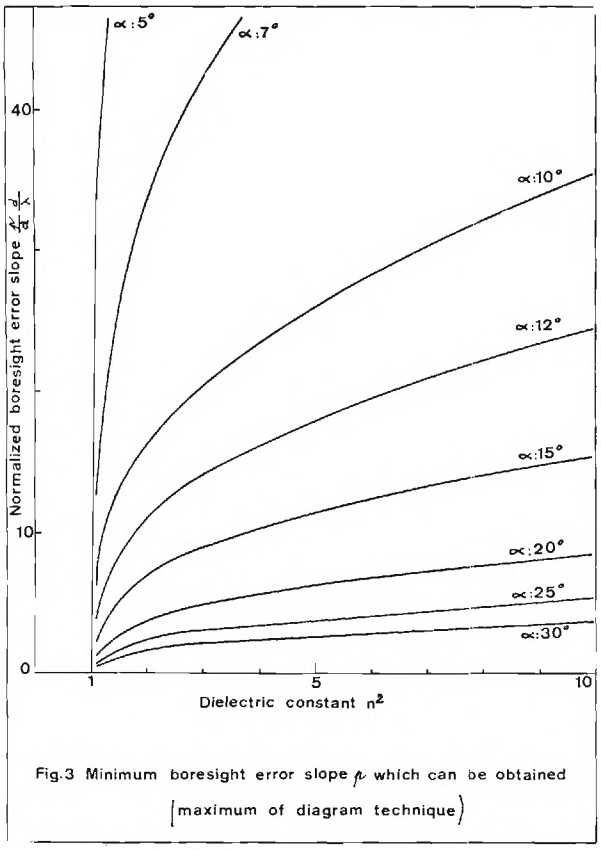

Fig.3 Minimum boresight error slope $\mathcal{P}$ which can be obtained
(maximum of diagram technique)

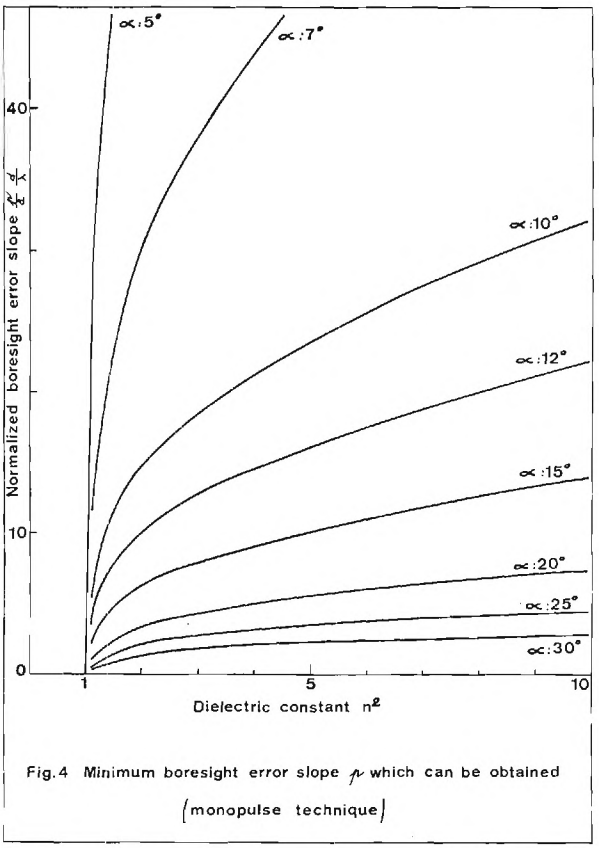

Fig.4 Minimum boresight error slope $\mathcal{P}$ which can be obtained
(monopulse technique)

BROADBAND PANEL DESIGN*

By

H. L. Bassett, D. G. Bodnar, G. K. Huddleston
and J. M. Newton
Systems and Techniques Department
Engineering Experiment Station
Georgia Institute of Technology
Atlanta, Georgia 30332

ABSTRACT

The basic design features of this particular type broadband panel are described in this paper. The inner and outer surfaces of the panels are so designed that the relative dielectric constant is 1.0 at the inner surface, increases to a value at panel center equal to that of the basic panel material, and decreases to 1.0 at the outer surface of the panel. Transmission coefficients of 90 percent or greater have been obtained from 5 GHz to 21 GHz over the incidence angle range 0° to $\pm 60^\circ$ for panel #1. The frequency range was increased to be 5 GHz to 40 GHz on panel #2. Both panels were machined from Rexolite® ($\epsilon_r = 2.54$).

INTRODUCTION

The problems associated with the design of efficient panels are well known, but the basic problem results from two factors:

(1) the panel structure introduces phase perturbations to the incident radiated field, and

(2) the amplitude of the incident wave is reduced by the panel.

The amount of perturbation and/or amplitude reduction depends on the panel type, i.e., a narrowband half-wave panel can be designed to be an efficient EM structure that operates reasonably about a single frequency and over a limited range of angles of incidence. Conventional panels, such as the multilayer and thin-wall structures, can be designed to operate over a much greater bandwidth and incidence angle range than the half-wave panel. But the panel that operates from 5 GHz to 40 GHz, while maintaining a transmission efficiency greater than 80 percent, has little chance of being designed using conventional techniques.

It is the intent to relate a unique panel design feature that will allow panels to be designed that have very broad bandwidths. The uniqueness of the design lies in the fact that both phase and amplitude perturbations can be minimized without resorting to a very costly fabrication process.

PANEL DESIGN

A cross-sectional view of the design of panel #1 is shown in Figure 1. The purpose of tapering the grooves is to provide a gradual transition of dielectric constant as a function of distance through the structure. The dielectric constant of the panel starts at a value equal to that of free space at the inner surface, increases gradually to that of the solid layer, and then decreases gradually to a value of that of free space at the outer

*Supported under AF Contract F33615-71-C-1694, R. A. Ireland, Project Engineer. A patent application has been filed by the U. S. Air Force on disclosures within this abstract.

surface. Such a variation in dielectric constant (assuming a lossless material) yields very high power transmission from 0° incidence angle to the grazing angle. The purpose of running the strips on the outer surface in a direction perpendicular to the strip direction on the inner surface is to reduce the anisotropic effects of this method of obtaining the desired variation in dielectric constant.

A consequence of the above design is that the transmission coefficient is the same for both parallel and perpendicular polarization at any given angle of incidence. Thus, the difference in insertion phase delay of the two polarizations is theoretically zero; this is one criterion which, if satisfied, will result in little antenna sidelobe degradation.

The bandwidth of operation is determined by the dielectric constant of the material, the center-to-center spacing of the strips, and the thicknesses of the two regions containing the tapered strips. For a given dielectric constant, the upper frequency limit is determined by the strip spacing; the lower frequency limit is determined by the thicknesses referred to above. There is good reason to believe that the higher the dielectric constant of the panel material, the narrower the bandwidth.

This method of obtaining broadband panels is an important extension of previous work by J. W. Richmond [1]. In his research, he presented the WKB solution for the field distribution and the transmission coefficient for a plane wave incident on a continuously inhomogeneous plane dielectric slab. His WKB solution for the transmission coefficient is

$$T_{TE} = \frac{\sqrt{(1 - r_e)^2 \ (1 - r_i^2)}}{(e^{\alpha} - r_e r_i \, e^{-\alpha}) \cos \beta + j(e^{\alpha} + r_e r_i \, e^{-\alpha}) \sin\beta} \tag{1}$$

where

$$r_e = \frac{\cos \theta - \sqrt{\epsilon_e - \sin^2\theta}}{\cos \theta + \sqrt{\epsilon_e - \sin^2\theta}}, \quad \text{interface reflection coefficient at exit point,} \tag{2}$$

ϵ_e = complex relative permittivity just within the dielectric slab,

θ = angle of incidence measured from slab normal,

$$r_i = \frac{\cos \theta - \sqrt{\epsilon_i - \sin^2\theta}}{\cos \theta + \sqrt{\epsilon_i - \sin^2\theta}}, \quad \text{interface reflection coefficient at the incident surface} \tag{3}$$

ϵ_i = complex relative permittivity just within the layer at the incident point,

$$\alpha = \frac{K}{2} \int_o^z \frac{\epsilon_r \tan \delta \, dz}{\sqrt{\epsilon_r - \sin^2\theta}}, \quad k = \omega\sqrt{\mu_o \epsilon_o} \tag{4}$$

$$\beta = K \int_o^z \sqrt{\epsilon_r - \sin^2 e} dz \tag{5}$$

By examining Equations (2) and (3) and by inserting a value for ϵ_e and ϵ_1 of near 1.0 (which is correct for the proposed panel design), one obtains interface reflection coefficient values of very near zero. In addition, the magnitude of the transmission coefficient value of Equation (1) would be approximately unity, corresponding to almost perfect transmission. Actually, for the lossless case,

$$T_{TE} = (1)e^{-j\beta} \tag{6}$$

so that a phase variation does exist. With this phase consideration in mind, one can look at the proposed panel design as a two-layered structure. The strips on the inner surface would perturb the phase shift of the parallel rays differently than the perpendicular rays. By the addition of layer 2 or the outer surface strips, one can perturb the rays in such a manner so that equal phase shifts are obtained through the panel for both parallel and perpendicular rays as a function of incident angle.

PANEL DESIGN ANALYSIS

The configuration of the broadband panel is presented in Figure 1. It is the purpose of this section to present the salient design considerations and to relate the physical properties of the panel to its performance in the microwave frequency band.

The method of obtaining the desired variation of the dielectric constant across the panel is an extension of the results of Morita and Cohn [2] and an application of the results obtained from previous research done at Georgia Tech for the Air Force Avionics Laboratory [3]. Appendix I of Reference 3 presents an analysis which determines the effective relative dielectric constants of a flat, infinite array of vertical, parallel dielectric strips of infinite depth for a linearly polarized, uniform plane wave incident on the array in a horizontal and vertical plane of incidence. The method of analysis is attributed to Morita and Cohn [2].

Under appropriate restrictions of the ratio of strip spacing to free space wavelength, $2\ell/\lambda_o$, the dielectric strip array is equivalent to a uniaxial anisotropic medium [3, 4]. In the analysis, the x, y, and z axes of the coordinate system are oriented along the principal axes of the anistropic medium, with the optic axis being along the x axis. The medium is described in terms of a relative dielectric tensor

$$\underline{\epsilon} = \begin{bmatrix} \epsilon_{xx} & 0 & 0 \\ 0 & \epsilon_{yy} & 0 \\ 0 & 0 & \epsilon_{zz} \end{bmatrix} \tag{7}$$

where the nonzero elements of the tensor are given directly from the results of the dielectric strip array analysis as follows:

ϵ_{xx} = Effective relative dielectric constant for the case of horizontal plane of incidence, parallel polarization, at normal incidence.

$\epsilon_{yy} = \epsilon_{zz}$ = Effective relative dielectric constant for the case of horizontal plane of incidence, perpendicular polarization, at normal incidence.

The results of the analysis show that $\epsilon_{xx} < \epsilon_{yy}$ so that the dielectric strip array is equivalent to a uniaxial, negative anisotropic medium.

When a plane wave is incident on the dielectric grating, higher order modes are excited to satisfy boundary conditions. However, if the center-to-center spacing of the strips is restricted by [2]

$$\frac{2\ell}{\lambda_o} \leqq \frac{1}{\sqrt{\epsilon_3} + \sqrt{\epsilon_1}\,|\sin\theta_1|}, \tag{8}$$

the higher order modes do not propagate and a single reflected wave is obtained, corresponding to "correct" operation of the dielectric strip array for the application to broadband panels. Thus, we see that the necessity to prevent higher order grating effects places an upper frequency limit on the simple dielectric strip array; the same restriction is assumed to apply to the structure in Figure 1.

The lower frequency limit of the panel of Figure 1 is determined by the dielectric constant of the panel material and the thickness of the regions containing the tapered strips. Perhaps a more precise statement should embody the phrase "rate of change of dielectric with respect to wavelength." In order that a continuous match be presented to the wave at every point in the panel, the rate of change of dielectric constant with respect to wavelength must be "gradual". At long wavelengths, the lower frequency limit will be reached when the corrugated panel appears, to the wave, to be essentially a flat panel. To date, no explicit relationship between the physical properties of the panel and the lower frequency limit has been established. Work is continuing in this area with some enlightenment being provided by the ongoing measurements on test panels.

A theorectical analysis of the inhomogeneous, anisotropic radome panel has been made for an arbitrary angle of incidence by using an extension of conventional techniques for inhomogeneous panels. The panel is approximated by a series of homogeneous slabs and the fields in each layer expressed in terms of ordinary and extraordinary waves. The propagation constants and directions of propagation are determined successively from the inner surface using Snell's Law and Fresnel's equation for wave normals. For arbitrary orientation of the optic axes from layer to layer, it can be shown that the incident wave would be diffused as it traverses the panel. However, for the orientations of optic axes present in the panels considered, the "integrities" of the ordinary and extraordinary waves are preserved from layer to layer.

MEASUREMENT RESULTS

The transmission properties versus frequency are plotted in Figure 2 thru 5 for panel designs # 1 and # 2. These data will be discussed at the conference.

REFERENCES

1. J. H. Richmond; Trans. IEEE, Vol: AP-10, pp. 472-73, July 1962.
2. T. Morita and S. B. Cohn; Trans. IRE, Vol. AP-3, pp. 33-39, January 1956.
3. H. L. Bassett; AFAL-TR-71-172, Contract No. F33615-70-C-1237, July 1971.
4. O. M. Bucci and G. Franceschetti; Trans. IEEE, Vol. AP-19, No. 1, pp. 96-104, January 1971.

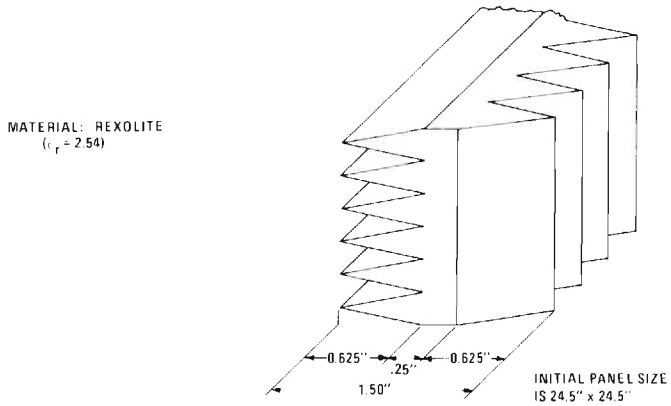

FIGURE 1. INITIAL BROADBAND PANEL DESIGN

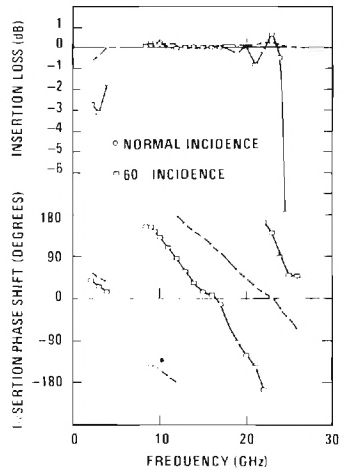

FIGURE 2. TRANSMISSION PROPERTIES – MEASURED DATA – BROADBAND PANEL NO. 1 – VERTICAL POLARIZATION.

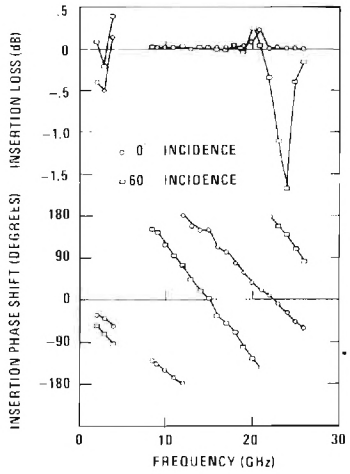

FIGURE 3. TRANSMISSION PROPERTIES – MEASURED DATA – BROADBAND PANEL NO. 1 – HORIZONTAL POLARIZATION.

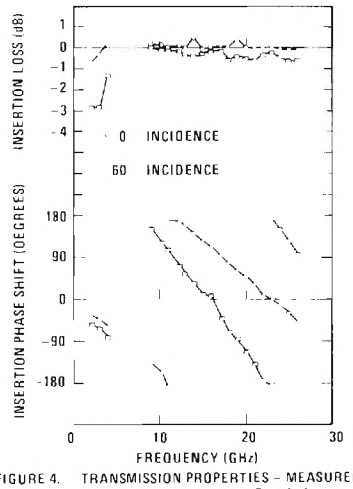

FIGURE 4. TRANSMISSION PROPERTIES – MEASURED DATA – BROADBAND PANEL NO. 2 – VERTICAL POLARIZATION.

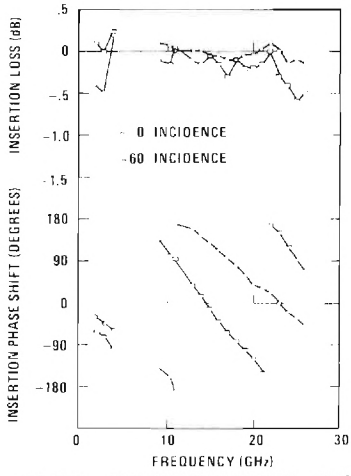

FIGURE 5 TRANSMISSION PROPERTIES – MEASURED DATA – BROADBAND PANEL NO. 2 – HORIZONTAL POLARIZATION.

DEVELOPMENT AND OPERATION OF A GRAPHITE THERMAL RADIATION FACILITY

David B. James, Raytheon Company, Missile Systems Division, Bedford, Mass.

Summary

A high flux thermal radiator, using a graphite heater, has been successfully designed and developed. Thermal flux levels of 100 cal/cm^2 sec have been obtained, radiating uniformly over a 2 1/4" diameter disc. This paper describes the design of the rig, together with solutions to some of the practical operating problems.

Introduction

Electromagnetic window environmental requirements frequently specify exposure to high thermal flux levels. Examples of this include nuclear thermal radiation and aerodynamic heating. High temperature lamps, powered by an Ignitron power supply, had been used to generate a uniform radiant heat flux over an effective test area of 24 in^2, but these were limited to a maximum incident flux of 35 cal/cm^2 sec. With the advent of heating requirements well in excess of this, the need became apparent for a high thermal flux facility, to be built at a minimum of capital expenditure. Designing the facility around a graphite heater was compatible with these requirements. Graphite was selected because its electrical resistance allowed for heating over a substantial heater surface area while utilizing the same power supply.

Design

Rig Layout

Figure 1 shows the graphite resistance heating element. Figures 2 and 3 are photographic and exploded views of the facility. The heater consists of convolutes of 1/4" square cross-sections with an 1/8" air gap between convolutes. An area, approximately the shape of a 4 1/2" diameter circle, contains only these 1/4" square convolutes and comprises the high flux radiating area. Supporting the heater is a pair of 1" diameter graphite rods, which also serve as electrical conductors. Copper plates are positioned front and back of the heater, with gold-plated reflecting surfaces facing the heater. A circular hole in the front plate allows for insertion of a specimen up to 2 1/4" in diameter. A pneumatically-driven, water-cooled shutter can be interposed between the heater and the specimen. Radiant flux levels are measured using a water-cooled calorimeter inserted through an opening in the rear plate. A 1/2" thick steel case encloses the rig and provides structural support.

Heater Design

A design goal was to achieve a flux level of 100 cal/cm^2 sec over a 2 1/4" diameter disc, with 95% uniformity. To allow room for the shutter, the disc opening was located 1" from the heater. Figure 4 shows the predicted distribution of the flux level over the disc radius, as derived from view factor calculations. Also shown is an experimental flux distribution obtained from traversing a calorimeter at the specimen location. The experimental heat flux curve falls below the theoretical curve, but still exceeds the design goal.

To achieve the desired flux level, the heater would be required to operate at a black body surface temperature of 4815°F. The estimated power requirement was 50 - 90 kw, depending on the effectiveness of the plate reflecting surfaces. In practice, a power level of 80 kw was found to maintain a steady-state heat flux of 100 cal/cm^2 sec.

ATJ graphite was selected as being a robust material with a reasonably high electrical resistivity. Highest resistivity occurs across the grain (14 x 10^{-4} ohm cm. at 70°F compared to 11 x 10^{-4} ohm cm. with the grain) and the heater was machined with the grain perpendicular to the main radiating surface. Variation of resistivity with temperature, obtained from Reference (a), is shown in Figure 5. Also shown are temperatures derived from thermal flux levels measured with the calorimeter. This data was deduced assuming a uniform graphite temperature equal to the black body temperature. Despite the considerable discrepancies between the design and the measured resistivity values, the power supply was sufficiently versatile to generate the design power. Design current was 440 amps (slightly less in use), low enough to allow use of uncooled copper leads.

Operational Experience

Pre-Heat

To reduce the proportion of impurities in a new heater, graphite suppliers recommended pre-heating at or above the operating temperature. However, this approach was found to be impractical with operating temperatures near 5000°F. (At 3500°F and above, graphite dust was emitted from the heater, reducing the cross-sectional area of the convolutes, without any improvement in performance.) Instead, it was found beneficial to preheat the heater at approximately 2000°F for 2 minutes prior to running to eject both water vapor and the loosely held solid impurities contained within the graphite.

Thermal Response

With its considerable thermal mass, the heater takes approximately 20 seconds to attain its peak thermal flux of 100 cal/cm^2 sec. The shutter, opening in less than 0.1 sec, can approximate the comparatively rapid increase in flux duringthe initial stage of a typical nuclear thermal pulse. Representation of the slower decay rate of the pulse can often be satisfactorily achieved by allowing the heater to cool without power. A squarewave pulse, terminated by the closing of the shutter, is frequently run. Because of the slow response time of the heater, most pulse shapes cannot readily be achieved by varying the power. A more rewarding approach would be to mount the specimen on a moveable trolley. A programmed heat flux history could be obtained by varying the distance between the specimen and the heater. Incorporation of such a device is anticipated as part of continuing development.

Arcing

During early runs, arcing across the convolutes was observed at an incident flux level of 50 - 60 cal/cm^2 sec. This was accompanied by severe emission of carbon dust from the heater. Fracture of the heater frequently occurred. Visual observation of the phenomenon during running was not possible, but a loud crackling noise, plus jagged identically mating indentations on adjacent convolutes, left little doubt of its nature. Diagnosis suggested the cause as being due to voltage breakdown in the 1/8" hot air gap separating the convolutes.

A solution was attempted by blowing nitrogen over the heater from two ports in the base of the rig. Because nitrogen combines with carbon at high temperatures to form cyanogen, a poisonous gas, a duct was incorporated in the top of the rig, connected to a vacuum blower. The effect of the modification was to delay the arcing flux level to 80 - 100 cal/cm^2 sec with considerable variations in the behavior of individual heater.

A more satisfactory solution was adopted with the incorporation of manifolds above and below the heater. Nitrogen was jetted under pressure through small holes along the manifolds directly to the space between convolutes. Since this modification no arcing has occurred, with flux levels slightly above 100 cal/cm^2 sec.

Carbon Dust Emission and Heater Life

During running, the heater exudes carbon dust, the quantity increasing with increasing emitted thermal flux. Operation of the vacuum blower reduces settling of this dust to a barely discernible amount. It also increases the quantity of dust emitted, thus removing mass from the heater and reducing its life. Typically, the heater will survive six 10-second bursts at full power with the blower off before replacement, compared to two similar bursts using the blower.

The effect of the settled dust is to alter, sometimes radically, the absorptivity of the test specimen. This can be avoided by interposing a sheet of quartz glass in the aperture, at the penalty of a reduction in incident flux. But use of the blower, and acceptance of reduced heater life, is generally found to be the most satisfactory solution.

During the life of the heater, reduction in the cross-sectional area of the convolutes due to the outflow of carbon dust increases its electrical resistance by a factor of up to 1.5 before the heater becomes unusable.

Current Uses

Since its completion in April 1971, the facility has been used extensively, principally in exposing elements of radar antennas to simulated nuclear thermal environments. These elements generally take the form of a ceramic window surrounded by a metal frame, and problems highlighted during testing included window cracking and melting of the frame. With instrumented testing backed up by computerized thermal modeling, determination of the cause of these problems was achieved, leading to eventual solutions.

Another currently active area is the simulation of aerodynamic heating on material samples of high-speed missile radomes. In these cases careful evaluation of the absorbed heat, with a knowledge of the radiation properties of the radome material, is essential to the production of meaningful results.

With the development of high-power laser technology, preliminary knowledge of the thermal effects of the beam on irradiated surfaces is sometimes required, which can be provided using the facility.

Closure

At the outset of the design effort, it was intended to build a rig capable of simulating useful radiant thermal flux levels with a minimum of capital investment and running cost. A fast turnaround time was required, together with ease of maintenance and convenient installation of test specimens. These objects have been satisfactorily achieved, and runs at flux levels of 100 cal/cm^2 sec for up to 20 seconds are now routine. Turn around time between tests is approximately 30 minutes, exclusive of time absorbed on instrumentation set-up.

Brief excursions into flux levels beyond 100 cal/cm^2 sec have generally resulted in rapid heater failure. It is believed that loosening of the bonds, precipitating the massive outflow of carbon dust, is the cause of failure. This therefore represents a practical limit in the attainable flux level of this type of graphite heater.

References: (a) Union Carbide Information Bulletin No. 463-205. "UCAR Premium Graphite Grade ATJ"

Acknowledgement:

The author wishes to acknowledge the assitance of Mr. W. Sweeney in the construction of the facility, and Mr. L. Paradis and Mr. R. Joachim in the preparation of the paper.

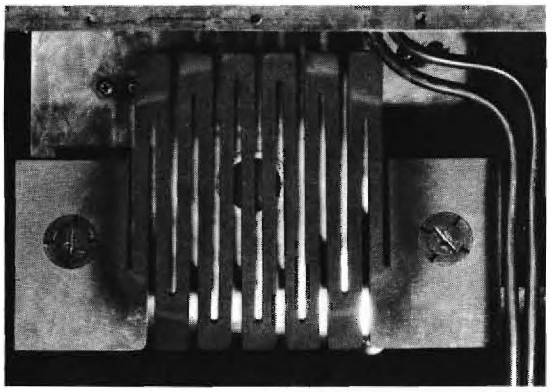

7161404A

FIG. 1 GRAPHITE HEATER

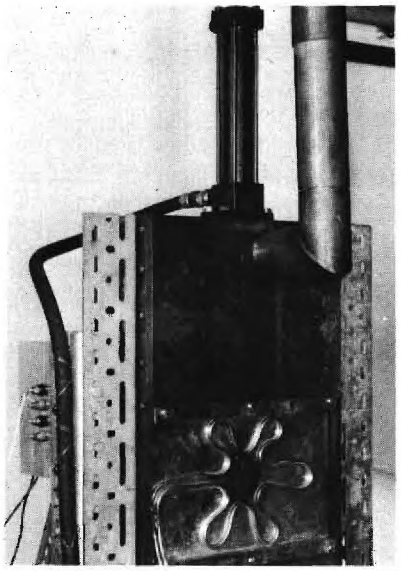

7264909

FIG. 2 GRAPHITE HEAT FACILITY

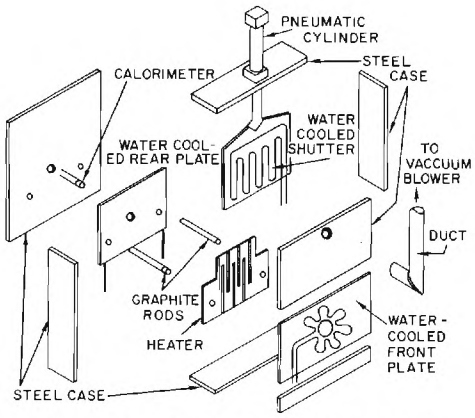

FIG. 3 EXPLODED VIEW OF GRAPHITE HEAT FACILITY

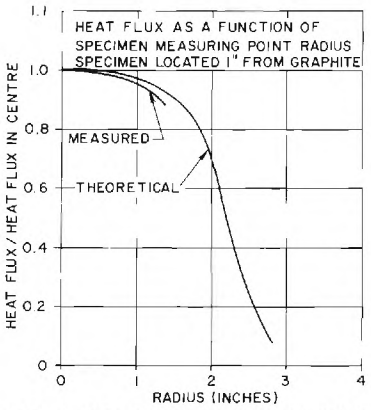

FIG. 4 GRAPHITE HEAT FACILITY

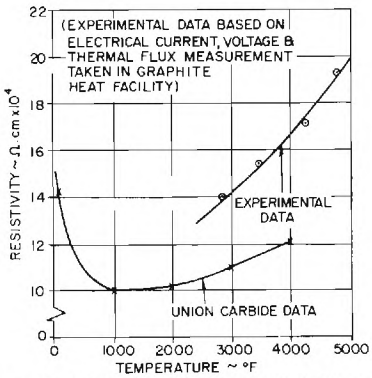

FIG. 5 ELECTRICAL RESISTIVITY OF ATJ GRAPHITE

An Experiment to Correlate the Thermal Stress Failure Level to Modulus of Rupture in Ceramic Materials

Robert Kelly Frazer
Associate Engineer

Johns Hopkins University/Applied Physics Laboratory
Silver Spring, Maryland

In designing radomes for use on high speed missiles, the high temperature strength and dielectric characteristics of ceramic materials become attractive. It has been shown in previous work (Ref. 1) that ceramic radomes most frequently fail in flight due to thermal shock. The design of ceramic radomes should, therefore, be concerned with the definition of allowable levels for thermal stresses during flight. The discussion given here describes an experimental program conducted to correlate the Modulus of Rupture (MOR) to the thermal stress failure level. MOR values obtained with small laboratory specimens are here shown to be a misleading indication of the thermal stress failure level in large bodies of revolution (i.e., radomes). The current work has suggested a method that can be used to predict thermal stress failure levels from properly conducted MOR tests.

To provide a data base for the correlation between MOR and thermal stress, samples of two different ceramic materials were obtained. The first was alumina, (99.5% Al_2O_3) a high strength material with a high coefficient of expansion (4.2 ppm/°F), high elastic modulus (45 x 10^6 psi), and large average grain size (30-40 μm). The second material was cordierite, a solid solution of Al_2O_3, MgO and SiO_2. This material has only moderate strength, but has a low coefficient of expansion (1.24 ppm/°F), a low modulus (18 x 10^6 psi), and a small average grain size (~8 μm). Samples of different sizes were obtained for each of the materials: (a) 6 small MOR bars, 3" x 1/2" x 1/4", (b) 8 large MOR bars, 8" x 1" x 1/2", and (c) 6 cylinders, 5" in outside diameter x 12" long x 1/2" in wall thickness. During the investigation the MOR bars were tested for MOR and elastic modulus (E) using a four-point, quarter span loading fixture. The cylinders (instrumented with strain and temperature measuring devices) were thermal shocked to failure in a specially constructed fixture that provided a well controlled radiant heat flux to the test specimens of 40-50 Btu/ft^2-sec. In addition, it was decided to diamond cut and grind small MOR bars from scrap pieces of the large bars and from cylinder samples. Since MOR samples are often made in this fashion, a brief study was made of the possible effects of surface grinding and cutting on the correlations.

The fracture stress data obtained from all samples tested is summarized in Table I. The dimensions given in Table I are approximate measurements of the central, constant moment section of the bars. Listed in Table I with the failure levels for the cylinders are the times at

which failures occurred in the cylinders, after being subjected to the above mentioned heat flux. The deviations noted for the sample groups indicate an acceptable degree of scatter.

Before the average values of failure level can be compared, a few observations about the nature of the loading and the two types of materials used should be made. During MOR testing, a section of the tested beam is placed in pure bending. This loading produces a uniaxial tensile stress on one surface of the beam and a compressive stress on the opposite side. It is the value of this tensile stress at the time of beam failure that is recorded as the MOR. During the thermal shocking of cylindrical samples, the outer surface is heated rapidly and the inner surface is thereby placed in biaxial tension. For most of the cylinder's length this biaxial stress field is equiaxial, that is, the stress in the circumferential direction is approximately equal to the stress in the meridional direction. When a cylinder fails due to thermal shock it is consequently in a different state of stress than a beam in pure bending. A second item to note is the difference in the sizes of the samples in Table I. The small bars have a test volume of 0.156 in^3, the large bars, 1.75 in^3 and the cylinders ~135 in^3. Also, the microstructure of the two materials differs greatly, as is evidenced in Figures 1 and 2. These figures show the cordierite to have a fine-grained microstructure while the alumina is coarser grained. Additionally, the cordierite contains many small, uniformly sized and oriented flaws while the alumina appears to have fewer flaws but of much larger size. A final difference among the various samples is the rate at which the loads were applied. In the case of the MOR bars, the loads were essentially static; in the case of the cylinders the loading rate was on the order of 3,000 psi/sec.

To resolve the differences in states of stress between bars and cylinders it is noted that, for the same level of stress in bending (σ_B) as in thermal stress (σ_{TS}), the strain energy per unit volume in bending (w_B) is less than the strain energy per unit volume due to thermal stress (w_{TS}). It can be shown that: $w_B/w_{TS} = 1/(2(1-\nu))$, where ν is Poisson's ratio. Conversely, if the strain energy required for unrestricted crack propagation is the same for both uniaxial and biaxial loading then:

$$\frac{\sigma_{B_{max}}}{\sigma_{TS_{max}}} = \sqrt{2(1-\nu)}. \qquad (1)$$

When comparing beam and cylinder data, assuming strain energy is the criterion for failure, failure stresses should be adjusted according to (1) above.

The effect of loading rate on strength is not well understood on a theoretical basis. Results of experimental work by Sedlacek (Ref. 2) where loading rate was examined as it affects overall strength in alumina, has shown that the ratio of strengths between slow loading (σ_s, ~30 psi/sec) and fast loading (σ_f, ~3,000 psi/sec) is $\sigma_f/\sigma_s \cong 1.27$. Consideration

of the failure stress level between bars (slow loading) and cylinders (fast loading) should incorporate this loading rate effect.

Examination of the data in Table I shows standard deviation values for all samples in the range 10% - 15%. This degree of scatter is acceptable and indicates that the mean value is representative of the population sampled. As further evidence to this statement, it was noted that all of the samples in any one group exhibited similar crack patterns in the failure area. Figure 3 shows close-up views of a cordierite and an alumina 8" bar after failure. Each of the fracture patterns is typical of the large MOR bar failure for the respective materials. For the cordierite bar the notable characteristics are the number of small secondary cracks and the shape of the main cracks. The main crack initiates at a location near the tensile surface and propagates perpendicular to that surface for a distance; then, near the compressive surface the crack runs parallel to the surface. This behavior is consistent with crack propagation theories for tensile and compressive loading. For the alumina bar in Figure 3, the same characteristics are noted but to a much lesser degree. The difference between the two characteristic crack patterns can be explained by consideration of the grain sizes for each material. For cordierite, the nominal grain size is about 8μ and for alumina the mean grain size is between 30μ - 40μ. The smaller the grain size the easier it is for a crack to propagate according to the stress field rather than be directed by grain boundaries.

Comparisons between bar and cylinder data in Table I is facilitated if the MOR values are "corrected" for the state-of-stress and loading-rate differences discussed above. In Fig. 4 all of the MOR values plotted have been adjusted in this manner. In considering Fig. 4 a significant size effect between large and small alumina bars is noted; that is, in every instance the MOR values for the 3" bars are higher than either the MOR values for the 8" bars or the failure level of the cylinders. The 3" bars denoted "as cast" are the bars originally acquired from the manufacturer. The 3" bars denoted "cut and ground" are from two sources. The first few of these bars were cut with a diamond wheel from scrap pieces of an 8" bar that showed an MOR of 23,600 psi. This group of small bars showed MOR's that averaged ~31,000 psi. The standard deviations indicate that the data is well grouped and that the smaller bars are significantly stronger than the large bar from which they were cut. This trend is repeated by the second group of "cut and ground" 3" bars. In this case the bars were cut from the end of a cylinder the remainder of which was later tested for thermal shock and failed at 21,880 psi. These 3" bars showed MOR's averaging 30,200 psi. This is very strong evidence for a significant size effect in alumina. Comparing the alumina MOR bars to the alumina cylinders it is seen that the cylinders are not greatly different in strength from the large bars.

It should be noted that in Fig. 4 "size" is relative to the average grain dimension and the curves which have been sketched are intended to be similar in shape to analytical results reported by Glucklich (Ref. 3). Glucklich maintains that in all materials under load the total strain energy, the grain and flaw size, flaw orientation, surface tension, and the overall sample size can combine to allow for strain energy absorption after the initiation of a crack sufficient to arrest the crack process. Glucklich's theory implies that as sample size increases there is a point at which the energy absorbing mechanisms fail to be sufficient to stop the

main crack and overall strengths thereby decrease. After a transition zone of sizes, the size no longer has an effect and failures occur according to flaw severity (the "weakest link" theory).

Glucklich's theory is supported by the size effect noted above and the failure characteristics of the large MOR samples. In the cordierite, the many secondary cracks indicate a considerable amount of strain energy was converted to surface energy (c.f. Figure 3). The large alumina samples show very little secondary cracking and, therefore, a smaller amount of converted strain energy. Conclusion: fine grained cordierite, in spite of its many small flaws, can hold more total strain energy prior to fracture than coarse-grained alumina.

In summary, the current study can be said to focus on one issue, namely a definition of the transition size. A realistic comparison between MOR and thermal stress failure in large bodies can only be made if the MOR samples are above the critical size. Such a correlation can be done with the alumina data presented here because the large bars appear to be past the transition size. The predicted thermal stress value is found by the proposed correlation method:

$$\sigma_{TS_{max}} = MOR_{LB} \times \sigma_f/\sigma_s \times 1/\sqrt{2(1-\nu)},$$

$$\cong 25{,}000 \text{ psi, with } \nu \cong 0.3.$$

The alumina cylinders actually show a failure level of 23,700 psi. While this correlation is fairly good, it is noted that using the small bar data would have predicted a failure level of 37,400 psi for the alumina cylinders, clearly a bad prediction.

The data reported here involve MOR samples of only two different sizes and thereby do not conclusively verify the proposed correlation method. Because the present data do indicate a trend, future work will involve testing different size MOR samples of alumina and cordierite in order to add data points to Figure 4. MOR samples of materials with different microstructure will also be investigated to test the correlation methods' generality. Additional work in the area of MOR-thermal stress correlation should involve determining the loading-rate effect on strength and the strain energy absorbing characteristics of candidate radome materials.

Acknowledgements

The author would like to acknowledge the support of the Naval Ordnance Systems Command, specifically ORD-035 under the direction of Oscar Seidman and Lionel Pasiuk. The supervision of L. B. Weckesser and the assistance of J. R. Kime, were also greatly appreciated. The scanning electron photomicrographs were taken at the Naval Ordnance Laboratory, White Oak, Md. with the assistance of Dr. Mariner Norr.

References

1. Frazer, R. K., Thermal Stress Limitations of Alumina and Pyroceram 9606 A-Sandwich Radomes, APL/JHU TG-1167, September 1971.
2. Sedlacek, R., Processing of Ceramics - Surface Finishing Studies, Stanford Research Institute, April 1970. AD870-158.
3. Glucklich, J., Strain-Energy Size Effect, California Institute of Technology, JPL, August 1970. TR 32-1438, N70-35917.

TABLE 1 SUMMARY OF TEST DATA

	NO. OF SAMPLES	SAMPLE DESCRIPTION	SAMPLE SIZE UNDER LOAD		YOUNG'S MODULUS (PSI)	FAILURE LEVEL (PSI) ± STD DEVIATION	
			DIMENSIONS (INCHES)	VOLUME (IN3)			
ALUMINA	6	3-INCH MOR BARS, SB_1 (AS CAST)	1.25 BY 0.5 BY 0.25	0.156	48.6×10^6	34 840 ± 5100 (STATIC LOAD)	ALUMINA, GRAIN SIZE 30 40 μm
	8	8-INCH MOR BARS (AS CAST)	3.5 BY 1 BY 0.5	1.75	43.2×10^6	23 510 ± 4260 (STATIC LOAD)	
	6	5-INCH OD CYLINDERS	5 OD BY 1/2 THICK BY ≈ 9 LONG	134	45×10^6	23 760 ± 1960 (ACHIEVED IN 8 TO 10 SECONDS)	
	5	3-INCH MOR BAR, SB_2 CUT FROM 8 INCH BAR W/MOR = 23,600	1.25 × 0.5 × 0.25	0.156	46×10^6	31 000 ± 3170 (STATIC LOAD)	
	5	3-INCH MOR BAR, SB_3 CUT FROM CYLINDER W/ FAILURE 21 380	1.25 × 0.5 × 0.25	0.156	48×10^6	30 200 ± 6270 (STATIC LOAD)	
CORDIERITE	8	3-INCH MOR BARS (AS CAST)	1.25 BY 0.5 BY 0.25	0.156	17.66×10^6	20 340 ± 1250 (STATIC LOAD)	CORDIERITE, GRAIN SIZE 8 10 μm
	7	8-INCH MOR BARS (AS CAST)	3.5 BY 1 BY 0.5	156	18.38×10^6	16 960 ± 2200 (STATIC LAOD)	
	5	5-INCH OD CYLINDERS	5 OD BY 1/2 THICK BY ≈ 9 LONG	134	18.0×10^6	10 610 ± 2340 (ACHIEVED IN 6 TO 14 SECONDS)	

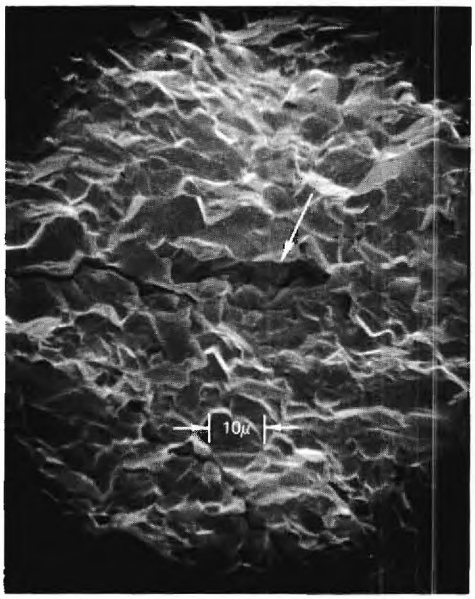

Fig. 1 SEM PHOTO OF ALUMINA FRACTURE SURFACE SHOWING LARGE FLAW

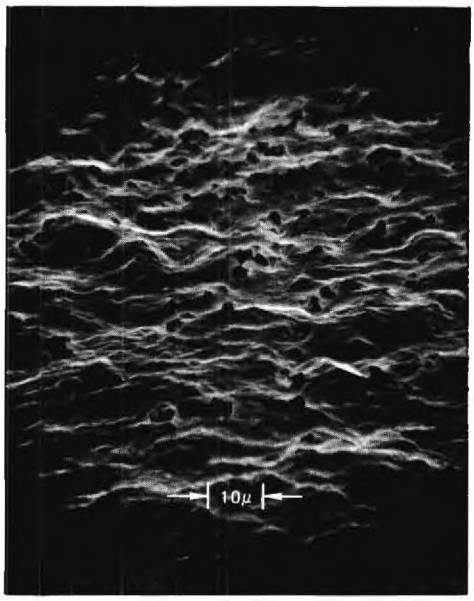

Fig. 2 SEM PHOTO OF CORDIERITE FRACTURE SURFACE

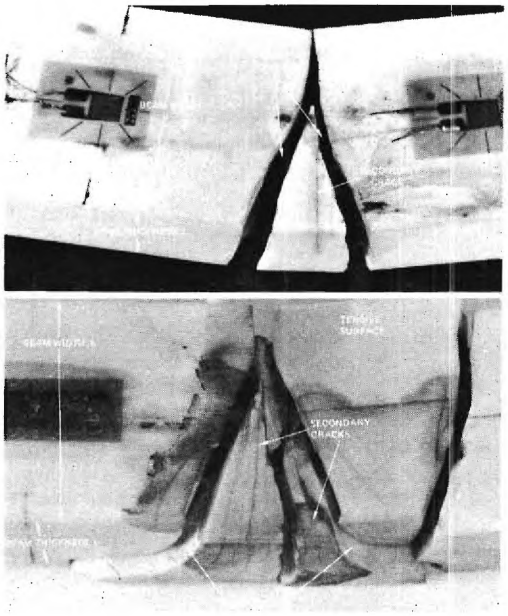

Fig. 3 TYPICAL FAILURE OF 8" MOR BARS,ALUMINA (UPPER), CORDIERITE (LOWER)

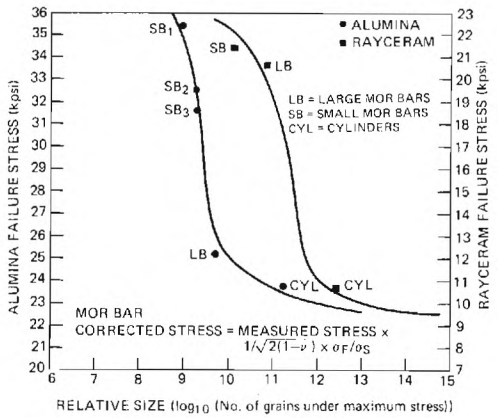

Fig. 4 EFFECT OF SAMPLE SIZE ON STRENGTH OF ALUMINA

COMPUTER CONTROLLED PRECISION GRINDING OF COMPLEX RADOME WALL THICKNESSES

By

H. Nadeau
Raytheon Company
Bedford, Mass.

ABSTRACT

Advanced missile systems require radomes which have low boresight error slopes over relatively large frequency bandwidths. The required character can be attained only if the wall thickness is precisely controlled and varies non linearly in both the axial and circumferential directions (in a manner analagous to a complex lens prescription).

Conventional methods of radome manufacture do not yield the dimensional control required. Thus, the Raytheon Company has developed methods which provide rapid grinding of radomes in production and prototype quantities which are not limited by normal templet production and verification lead times. Experience has shown that fabrication scheme can yield an accurate prototype radome within 1-2 days after availability of a billet.

The techniques developed combine the inherent dimensional accuracy of diamond wheel vertical grinding with numerical control techniques governed by digital computers. Radomes with varying axial thickness and circumferential thickness increments of 1/2 degree are readily fabricated. Grinding times for prescriptions in either fiberglass or ceramic radomes as large as 16 inches outer diameter and 56.5 inches high are less than 4.5 hours. Dimensional accuracy of ± 0.0015-inch has been achieved for production quantities of radomes.

The presentation will include photographs (or motion pictures) of the facility, fixtures and fabrication methods, example wall thicknesses and radomes, and attained dimensional accuracy.

Note: Copies of the presentation of this work can be obtained at the meeting or by making your request to the author.

MULTIOCTAVE BRAODBAND RADOMES

By

Don L. Loyet
Raytheon Company
Bedford, Mass.

ABSTRACT

The optimum wall construction for multiple octave radomes is the gradient dielectric wall. This construction can be attained in several practical ways among which are the use of discrete layers and mechanical gratings. The former technique is based on a stepwise approximation to the desired gradient while the latter method employs grooves ground into the wall. Alternate design techniques such as the multiple layered sandwich walls (including the trivial cases of single and two layered walls) are used for all present production radomes.

Practical design limitations such as rain resistance, thermal and structural loadings and materials selection dictate that the attainment of the unity dielectric constant required at the external faces is not feasible. Studies of the trade-off of electrical characteristics as a function of design constraints show several significant constructions for bandwidth as large as 1 to 40 GHz.

Analyses were conducted using digital computer techniques wherein the best possible combination of dielectric properties and wall thicknesses were determined based on specified number of layers, minimum transmission efficiency, and maximum reflection levels.

Studies conducted by the author during the past several years for high power systems will be summarized and significant wall constructions presented with their characteristics.

Note: Copies of the presentation of this work can be obtained at the meeting or by making your request to the author.

AWACS RADOME MATERIALS AND CONSTRUCTION

By

James E. Barbee
The Boeing Company

ABSTRACT

The AWACS radome design trades resulted in the requirement for a single-piece, C-sandwich structural shell that was one-half of an ellipsoid, 30 feet in diameter and 6 feet thick at the center of rotation. This radome presented a fabrication challenge because of the size and stringent electromagnetic requirements.

The AWACS radome materials and processes development work required evaluation and optimization of construction materials to permit accurate structural and electrical analysis of the design, consistent with fabrication of a flight worthy radome.

Materials were evaluated primarily for their electrical, structural, elevated temperature and environmental properties, in addition the physical thickness of component materials and overall C-sandwich cross-section were precisely measured and controlled. High strength-high modulus "S" glass/epoxy-novolac laminate was chosen as the sandwich skin material to meet these requirements.

Process problems dealing with laminate porosity, HRP honeycomb core contour and thickness control, sandwich adhesive bond properties, scale-up effects, and shape distortion were identified and resolved. A four-stage construction process with process controls, environmental controls, tooling requirements, and NDI techniques are described.

Note: Copies of the presentation of this work can be obtained at the meeting or by making your request to the author.

APPENDIX I

AUTHOR INDEX

AUTHOR INDEX